

**In-situ Jet Calibration and Electro-Weak Induced Production of $W\gamma$ in
Association With Two Jets at ATLAS**

A thesis submitted to the University of Manchester for the degree of
Doctor of Philosophy
in the Faculty of Science and Engineering

2024

Benjamin Honan
Department of Physics and Astronomy

Contents

| | |
|---|-----------|
| Contents | 2 |
| Abstract | 5 |
| Declaration of originality | 6 |
| Copyright statement | 7 |
| Acknowledgements | 8 |
| 1 Introduction | 9 |
| 2 Theory | 11 |
| 2.1 The Standard Model | 11 |
| 2.1.1 Quantum Mechanics and Classical Field Theory | 11 |
| 2.1.2 Quantum Electrodynamics (QED) | 13 |
| 2.1.3 Spontaneous Symmetry Breaking | 16 |
| 2.1.4 Non-Abelian Gauge Symmetries | 17 |
| 2.1.5 Electroweak Unification | 18 |
| 2.1.6 The Standard Model Lagrangian | 20 |
| 2.2 Physics of Hadron-Hadron Collisions | 22 |
| 2.2.1 Scattering Amplitudes and Cross-sections | 22 |
| 2.2.2 Calculations of Cross-sections in pp Collisions | 27 |
| 2.2.3 Formation of Hadronic Final States | 28 |
| 2.3 Vector Boson Scattering | 32 |
| 3 The LHC and ATLAS Experiment | 37 |
| 3.1 The Large Hadron Collider | 37 |
| 3.1.1 Detector Luminosity | 39 |
| 3.1.2 Pile-up | 39 |
| 3.2 The ATLAS Experiment | 41 |
| 3.2.1 Inner Detector | 41 |
| 3.2.2 Calorimeters | 44 |
| 3.2.3 Muon Spectrometer | 46 |
| 3.2.4 ATLAS Trigger and Data-acquisition | 48 |
| 3.2.5 Data Processing | 51 |
| 3.2.6 ATLAS Object Reconstruction | 52 |

| | |
|--|-----------|
| 4 Insitu Calibration of Large-R Jets Using Direct Balance in Z+Jet Events | 66 |
| 4.1 Introduction | 66 |
| 4.2 Jet Calibration | 66 |
| 4.3 Data and MC samples | 70 |
| 4.4 Jet definitions | 71 |
| 4.5 Object Selections | 72 |
| 4.5.1 Electrons | 72 |
| 4.5.2 Muons | 72 |
| 4.5.3 Jets | 73 |
| 4.5.4 Overlap Removal | 73 |
| 4.6 Event Selection | 73 |
| 4.7 Nominal Response Calculation | 74 |
| 4.8 Systematic Uncertainties | 76 |
| 4.9 Results | 80 |
| 4.10 Insitu combination | 80 |
| 4.11 Small-R Insitu Calibration Cross-check | 81 |
| 4.11.1 Samples, object definitions, and event selection | 81 |
| 4.11.2 Results | 81 |
| 5 Differential Cross-section Measurement of $W\gamma jj$ EW Production at $\sqrt{s} = 13 \text{ TeV}$ | 89 |
| 5.1 Signal and Background Processes | 90 |
| 5.1.1 Signal | 90 |
| 5.1.2 Backgrounds | 91 |
| 5.2 Interference Sample Generation and Validation Studies | 93 |
| 5.3 Object and Event Selections | 95 |
| 5.3.1 Derivations and Triggers | 95 |
| 5.3.2 Object Selections | 96 |
| 5.3.3 Event Selections | 99 |
| 5.4 Data-driven Background Estimates | 100 |
| 5.4.1 Jets Faking Leptons | 100 |
| 5.4.2 Jets Faking Photons | 101 |
| 5.4.3 Electrons Faking Photons | 102 |
| 5.5 Expected Yields and Events in Data | 103 |
| 5.6 Signal Extraction Methodology | 103 |
| 5.6.1 Choice of Model Parameters | 107 |
| 5.7 Shape Dependence of $N_{\text{jets}}^{\text{gap}}$ and $\xi_{l\gamma}$ | 108 |
| 5.8 Construction of the Asimov Dataset | 108 |
| 5.9 Binning Determination | 110 |
| 5.9.1 Detector Resolution with Bin Width | 110 |
| 5.10 Symmetrising of the $\Delta\phi_{l\gamma}^{\text{signed}}$ and $\Delta\phi_{jj}^{\text{signed}}$ Templates | 110 |
| 5.11 Testing of the Binned Likelihood Fit | 112 |
| 5.12 Choice of Function for the Residual Correction | 115 |

| | |
|---|------------|
| 5.12.1 $f(x_i) = 1$ | 116 |
| 5.12.2 $f(x_i) = mx_i + c$ or $f(x_i) = c$ | 117 |
| 5.13 Uncertainties | 120 |
| 5.13.1 Data Statistical Uncertainties | 120 |
| 5.13.2 MC Statistical Uncertainties | 120 |
| 5.13.3 Treatment of Systematic Uncertainties | 122 |
| 5.13.4 Experimental Systematic Uncertainties | 124 |
| 5.13.5 Non-prompt Background Uncertainties | 126 |
| 5.13.6 Theoretical Uncertainties | 127 |
| 5.13.7 Summary of the Systematic Uncertainties | 134 |
| 5.14 Prefit and Postfit Distributions | 140 |
| 5.15 Cross-checks | 147 |
| 5.15.1 Changes to the Likelihood Fit | 147 |
| 5.15.2 Signal Injection Test | 148 |
| 5.16 Correction for Detector Effects | 149 |
| 5.16.1 Unfolded Differential Cross-section Results | 151 |
| 5.16.2 Validation of the Unfolding Procedure | 152 |
| 6 Conclusions | 156 |
| References | 158 |
| Appendices | 177 |
| A Large-R $Z+jets$ Insitu Calibration | 178 |
| B Differential Cross-section Measurement | 182 |

Abstract

Differential cross-section measurements of the electroweak production of $W\gamma$ in association with two jets are made using proton-proton collision data with an integrated luminosity of 140fb^{-1} and a centre-of-mass energy of $\sqrt{s} = 13\text{ TeV}$, recorded by the ATLAS detector. Six different observables are used to present the differential cross-sections, where these observables are chosen due to their anticipated sensitivity to anomalous quartic gauge couplings and CP-violating interactions.

The differential cross-section measurements are presented at particle-level after applying corrections to account for detector inefficiencies. These corrections are applied to differential signal yields which are obtained through a minimum log-likelihood fit of the data to simulations and data-driven background estimates. The measured differential cross-sections are compared to predictions from simulation, and are found to be compatible within statistical and systematic uncertainties.

Correction factors to the jet energy scale calibration for large-radius jets are presented. These residual insitu corrections account for detector mismodelling in applying the simulation derived jet energy scale to data. The calibration is performed using $Z+\text{jets}$ events in both the electron and muon decay channels, and are found to be most relevant in the kinematic range of $200\text{ GeV} \leq p_{\text{T}}^{\text{jet}} \leq 500\text{ GeV}$, where $p_{\text{T}}^{\text{jet}}$ represents the jet transverse momentum. The total uncertainty on the insitu calibration factor is found to range from $0.5 - 1.5\%$ depending on the decay channel and $p_{\text{T}}^{\text{jet}}$ bin.

Declaration of originality

I hereby confirm that no portion of the work referred to in the thesis has been submitted in support of an application for another degree or qualification of this or any other university or other institute of learning.

Copyright statement

- i The author of this thesis (including any appendices and/or schedules to this thesis) owns certain copyright or related rights in it (the “Copyright”) and s/he has given The University of Manchester certain rights to use such Copyright, including for administrative purposes.
- ii Copies of this thesis, either in full or in extracts and whether in hard or electronic copy, may be made *only* in accordance with the Copyright, Designs and Patents Act 1988 (as amended) and regulations issued under it or, where appropriate, in accordance with licensing agreements which the University has from time to time. This page must form part of any such copies made.
- iii The ownership of certain Copyright, patents, designs, trademarks and other intellectual property (the “Intellectual Property”) and any reproductions of copyright works in the thesis, for example graphs and tables (“Reproductions”), which may be described in this thesis, may not be owned by the author and may be owned by third parties. Such Intellectual Property and Reproductions cannot and must not be made available for use without the prior written permission of the owner(s) of the relevant Intellectual Property and/or Reproductions.
- iv Further information on the conditions under which disclosure, publication and commercialisation of this thesis, the Copyright and any Intellectual Property and/or Reproductions described in it may take place is available in the University IP Policy (see <http://documents.manchester.ac.uk/DocuInfo.aspx?DocID=24420>), in any relevant Thesis restriction declarations deposited in the University Library, The University Library’s regulations (see <http://www.library.manchester.ac.uk/about/regulations/>) and in The University’s policy on Presentation of Theses.

Acknowledgements

I would like to start by giving a huge thank you to my supervisor Andy for always being available to answer my questions, providing endless valuable feedback, and generally keeping me on the right track. I really believe you have gone above and beyond your duty as a supervisor, and it is clear that you care a great deal about your students.

The process of completing my PhD has been made so much easier by the constant support of my friends and family. In particular, Jordan who was my housemate when I moved to Manchester, and let me live with his family in Pembrokeshire for over a month! Our many bike rides in and around the depths of the peak district definitely helped me in maintaining my sanity during the COVID-19 pandemic. Lastly, thanks for introducing me to surfing, although I'm not entirely sure if I should be grateful for this. Perry, I am forever grateful for letting me live with you in Liverpool near the end of the pandemic. I can always confide in you and Arun when things are not going my way. Another big thank you to Arun for coming to see me when I completed my viva. Zak, thank you for being such a good housemate whilst on LTA in Switzerland, and for helping me stay sane whilst I was writing up. Rhys, I will always strive to reach your level of life optimisation. Thanks for visiting me many times in Cornwall and Switzerland, and for always being such a good friend. To all my other friends in the Imperial College Caving Club, the occasional weekend trips were a nice respite from thesis writing and intense analysis work particularly in the final years of my PhD, and the Slovenia expedition remains a consistent yearly highlight. Thanks for all the memories. To my family, thank you for putting up with my grumpiness during the last few months of thesis writing. You are always there for me, through thick and thin. The whole PhD process was made so much easier with the constant support of my caring family.

Lastly, a big thank you to everyone that proof read sections of my thesis, and Dr. William Barter and Prof. Justin Evans for being my examiners.

Chapter 1

Introduction

The Standard Model (SM) of particle physics is a quantum field theory which describes the interactions of six quarks and six leptons along with their anti-particles in addition to four vector bosons, and a scalar boson. Even though many predictions of the SM have stood up to experimental scrutiny [1], the theory has a number of shortcomings which indicate it is not a complete description of nature. To name a few of these, the SM does not explain the origin of neutrino masses [2], the reason why there are three generations of fermions [3], and the origin of electroweak symmetry breaking [4, 5]. It is possible that the resolution to some of these problems lie in the idea that the SM is a low-energy effective theory, which is completed at some higher energy scale [5, 6]. It is through precision measurements of SM interactions that this hypothesis can be tested. The study of Vector Boson Scattering (VBS) in particular is of interest due to the presence of quartic EW boson interactions which are potentially sensitive to beyond-the-standard-model (BSM) contributions. Additionally, the scattering cross-sections of VBS processes diverge at high centre-of-mass energies without the presence of delicate cancellations in the form of Higgs boson interactions [7, 8]. Measurements of VBS processes therefore also provide an insight into the nature of the Higgs mechanism.

Experimental measurements of VBS processes are extremely challenging because these represent some of the rarest SM processes measurable with the 140fb^{-1} ATLAS Run-2 dataset [9]. This means that the accuracy of these measurements are usually limited by the statistical precision of the dataset. Furthermore, these measurements are often accompanied by a large irreducible background which dominates over the signal process. Measuring the signal therefore requires precise modelling of this background, in addition to the careful derivation of data-driven background constraints.

The work presented in this thesis focusses on the differential cross-section measurements of $W(\rightarrow \ell\nu)\gamma$ in association with two jets in the electroweak production mode (no strong coupling vertices at leading order). Separating the signal from the dominant strong irreducible background is facilitated by performing the measurement in a phase-space optimised for sensitivity to VBS processes. Such a phase-space is constructed using knowledge of the characteristic event topologies of VBS processes, which is summarised by the presence of two jets with large longitudinal momenta and a large separation in rapidity. Furthermore, the lack of colour flow between the partonic initial states results in an absence of hadronic activity in the rapidity interval between these two jets.

The shape and normalisation of the signal and the strong background predictions are constrained via a binned log-likelihood fit of the data to simulation. The construction of three background-enriched control regions, and careful consideration of the floating parameters in the likelihood help to constrain the background. Differential cross-sections in six observables are obtained after applying corrections for detector effects to the extracted signal yields.

In addition to the measurements of differential cross-sections, this thesis presents work on the calibration of large-radius jets. The hadronic decays of high transverse momentum heavy particles such as top quarks and W or Z bosons result in a highly collimated decay product, where the angular separation of the outgoing partons is often not large enough to enable the resolution of the individual jets. In these situations, the hadronic decay product can be reconstructed as one large-radius jet. Up until recently, the reconstruction of large-radius jets has been performed using inputs constructed solely from topologically grouped clusters of calorimeter cells [10, 11]. Recent advancements have lead to jet definitions derived using inputs from combined track and calorimeter information, which results in jets with improved pileup stability, energy/mass resolution, and substructure performance [12–14]. This thesis outlines the calibration of large-radius jets reconstructed using one of these improved inputs known as “unified flow objects” (UFO) [14].

The jet calibration work in this thesis pertains to the derivation of residual corrections to the jet energy scale (JES), known as the insitu calibration. This correction is applied at end of a chain of calibration steps, where the initial steps are primarily responsible for bringing the energy scale of reconstructed jets to that of simulated *truth* particles. The insitu calibration uses data-to-simulation ratios to primarily correct for detector effects not captured by simulation when applying the JES to data [10]. The insitu calibration itself is derived from the statistical combination of a number of different methods which all exploit the transverse momentum balance of a well measured reference object against a probe jet to define a response which should be close to unity. The calibration presented in this thesis is derived using events where the reference system is comprised of a reconstructed $Z \rightarrow e^+e^-$ or $Z \rightarrow \mu^+\mu^-$ decay.

The chapters in this thesis are outlined as follows. Chapter 2 begins with an introduction to the SM, and culminates in a description of the SM Lagrangian. Subsequently, a section on the formation of hadronic final states begins with an introduction to matrix-elements, Feynman diagrams, and cross-sections, and ends with a description of the techniques employed by event generators to model the non-perturbative physics. The final section outlines the defining theoretical and experimental features of VBS, in addition to a summary of recent VBS measurements made at ATLAS. Chapter 3 introduces the LHC and the ATLAS experiment, and contains a detailed description of the subsystems comprising the ATLAS detector. Additionally, this chapter describes the ATLAS trigger and data acquisition systems along with the reconstruction algorithms which go into defining the objects used in ATLAS analyses. Chapter 4 describes the author’s work on the insitu calibration of large-radius jets, and Chapter 5 outlines the authors work on the differential cross-section measurements of the electroweak production of $W(\rightarrow \ell\nu)\gamma$ in association with two jets. Finally, Chapter 6 concludes this thesis.

Chapter 2

Theory

2.1 The Standard Model

This section is primarily based on quantum field theory undergraduate lecture notes from Tim Evans [15], David Tong [16] and lecture notes on unification by Arttu Rajantie.

The standard model (SM) is the best description of fundamental physics at the quantum scale. It is a *quantum field theory* (QFT) that describes the interactions of the fundamental particles, which emerge as quantised excitations of fields. In order to understand the details of this theory, one must first be introduced to the concepts of quantum mechanics and classical field theory.

2.1.1 Quantum Mechanics and Classical Field Theory

The equations of motion of a classical system are determined by the *principle of least action*. This states that the trajectory $x(t)$ of a particle is the one that extremises the *action* S :

$$S = \int dt L(x, \dot{x}), \quad (2.1)$$

where $L(x, \dot{x})$ is called the *Lagrangian*. In this *Lagrangian formulation*, a particle trajectory is parametrised by its coordinates x and their time derivative \dot{x} .

In the equivalent Hamiltonian formalism of classical physics, a point particle is parametrised by coordinates and momenta (x, p) . A function called the Hamiltonian (H) is defined which describes the evolution in the space of coordinates and momenta, called *phase space*. The equations of motion are given by Hamilton's equations:

$$\dot{x} = \{x, H\}, \quad \dot{p} = \{p, H\}, \quad (2.2)$$

where $\{, \}$ are the Poisson brackets, and a dot denotes the partial derivative with time. The Poisson brackets for coordinates and momenta are:

$$\{x, p\} = 1, \quad \{x, x\} = 0, \quad \{p, p\} = 0, \quad (2.3)$$

and the time evolution of any function $F(x, t)$ can be expressed in terms of the Poisson bracket

ets:

$$\frac{dF}{dt} = \{F, H\}. \quad (2.4)$$

The probability of being in $d\mathbf{p}dx$ is denoted through a probability density function $w(p, x, t)$:

$$w(p, x, t)d\mathbf{p}dx, \text{ where } \int d\mathbf{p}dx w(p, x, t) = 1. \quad (2.5)$$

Quantum Mechanics (QM) can be defined through the direct quantisation of a classical dynamical system of particles, in a process known as canonical quantisation. In this process, the system is *quantised* by replacing Poisson bracket relations with a commutator relation times i/\hbar , and replacing the conjugate variables x, p with operators \hat{x}, \hat{p} . For a finite system of point particles, the canonical commutation relations are written as:

$$[\hat{x}_i, \hat{p}_j] = i\hbar\delta_{ij}, \quad [\hat{x}_i, \hat{x}_j] = [\hat{p}_i, \hat{p}_j] = 0. \quad (2.6)$$

There are many interpretations of quantum mechanics, one of the most used ones is the *Copenhagen Interpretation*, which proposes that the state of the system is described analogously to equation 2.5 by a *wave function*, $\psi(\mathbf{x})$, where the probability density $p(\mathbf{x})$ of finding the system in a given state is described by the *Born rule*:

$$p(\mathbf{x})d^3x = |\psi|^2d^3x, \text{ where } \int d^3x |\psi(\mathbf{x})|^2 = 1. \quad (2.7)$$

This description of reality has a number of problems. First, the universe is assumed to be split into quantum and classical regimes, where classical physics emerges at larger scales (lower energies). Secondly, QM only describes a finite number single-particle states – this can be seen from equation 2.7, which states that a particle exists with probability 1. This is problematic since this is at odds with the principle of matter-energy equivalence from special relativity. Namely, single-particle states don't allow for the creation of particle-antiparticle pairs. Additionally, a multi-particle theory is necessary from the standpoint of causality. This is less obvious, but a good description of causality violation is given in [17].

In classical field theory, single particle states are replaced by a *fields* which are functions defined at every point in space and time. This formalism describes the dynamics of continuous systems with an infinite number of degrees of freedom. Examples of classical fields are the electric and magnetic fields in Maxwell's theory of electromagnetism. The equations of motion are again determined through the principle of least action, where the Lagrangian is replaced by its continuous generalisation, the *Lagrangian density*, \mathcal{L} – in the rest of this chapter \mathcal{L} will simply be referred to as the Lagrangian. The action is written as:

$$S = \int d^4x \mathcal{L}(\phi, \partial_\mu \phi), \quad (2.8)$$

where the index μ runs over one time coordinate (x^0) and three space coordinates (x^1, x^2, x^3) and $\partial_\mu \equiv \frac{\partial}{\partial x^\mu}$. One of the most important aspects of a field theory is the invariance of the action under a set of symmetries. If a given transformation leaves the laws of physics unchanged,

the Lagrangian must be left unchanged up to a total derivative. In particular, a relativistic field theory requires that the Lagrangian is invariant under Lorentz transformations. Fields which transform under the trivial representation of the Lorentz group (the value of the field at any spacetime point remains unchanged) are called *scalar fields*¹. These fields don't come with a *Lorentz index*, μ . Fields with a Lorentz index are called *vector fields*, and the components of these fields change under non-trivial Lorentz transformations. The Lagrangian can also have *internal symmetries*, which specifies the invariance of the theory under some symmetry group. Demanding a number of internal symmetries, limits the form of \mathcal{L} , and therefore limits the theory by, for example, only allowing certain interactions.

To introduce QFT, it is useful to start with the simple classical field theory of a real, non-interacting scalar field. After enforcing the theory to be invariant under the group of spacetime symmetries (Poincare group), the only possible Lagrangian is of the form:

$$\mathcal{L} = \frac{1}{2}(\partial_\mu\phi)^2 - \frac{1}{2}m^2\phi^2. \quad (2.9)$$

This corresponds to the equations of motion:

$$\partial_\mu\partial^\mu\phi + m^2\phi = 0, \quad (2.10)$$

which is the Klein-Gordon equation, and describes a relativistic spin-zero field of mass m . This field theory can be quantised in a similar procedure to the canonical quantisation. This is done by promoting the field and its conjugate momentum-density $\pi(x) \equiv \frac{\partial\mathcal{L}}{\partial\dot{\phi}}$ to operators and enforcing the axioms:

$$[\hat{\phi}(\mathbf{x}, t), \hat{\pi}(\mathbf{y}, t)] = i\hbar\delta^{(3)}(\mathbf{x} - \mathbf{y}), \quad [\hat{\phi}(\mathbf{x}, t), \hat{\phi}(\mathbf{y}, t)] = [\hat{\pi}(\mathbf{x}, t), \hat{\pi}(\mathbf{y}, t)] = 0, \quad (2.11)$$

where $\delta^{(3)}(\mathbf{x} - \mathbf{y})$ is the Kronecker delta function. These are called the *equal time commutation relations*. In going from QM to QFT, the coordinates \mathbf{x} no longer represent quantised operators, but are arguments of the field. This is a big conceptual shift – fields represent deviations in a *field space*. This is very different to QM, where the equations of motion describe the dynamics of single particles in coordinate space.

2.1.2 Quantum Electrodynamics (QED)

Maxwell's theory of electrodynamics can be described as a classical field theory using the *scalar potential* ϕ and the *vector potential* \mathbf{A} . The electric and magnetic fields are given in terms of the potentials by:

$$\mathbf{E} = -\frac{\partial\mathbf{A}}{\partial t} - \nabla\phi, \quad \mathbf{B} = \nabla \times \mathbf{A}. \quad (2.12)$$

These scalar and vector potentials can be combined into a real Lorentz vector field, the *four-vector potential* $A^\mu = (\phi, \mathbf{A})$.

¹In the SM, scalar fields are spin-zero fields, and their excitations represent Bosons.

Let's assume the Lagrangian of classical electrodynamics involves A^μ and its derivative $\partial_\mu A_\nu$. The general form of the Lagrangian can be derived from the knowledge that \mathcal{L} must be (i) a Lorentz scalar, (ii) *renormalisable*, and (iii) invariant under *gauge transformations*. Renormalisation is a concept from QFT which limits the energy dimensions of the terms in the Lagrangian. Namely, renormalisable terms are those with energy dimensions of at most 4, since the introduction of higher dimension terms leads to divergent cross-sections. Gauge invariance is simply the statement that certain changes to the scalar and vector potentials ϕ and \mathbf{A} leave the electric field \mathbf{E} and the magnetic field \mathbf{B} invariant. These gauge transformations are given by:

$$A_\mu \rightarrow A_\mu - \partial_\mu \lambda(x) \quad (2.13)$$

where λ is an arbitrary scalar function. It is immediately clear that terms like $A_\mu A^\mu$ and $\partial_\mu A^\mu$ are not invariant under gauge transformations, and are therefore not allowed. The only renormalisable Lorentz scalar term which is invariant under gauge transformations is:

$$\mathcal{L} = -\frac{1}{4}F_{\mu\nu}F^{\mu\nu}, \quad (2.14)$$

where $F_{\mu\nu}$ is the anti-symmetric tensor known as the *field strength tensor* $F_{\mu\nu} = \partial_\mu A_\nu - \partial_\nu A_\mu$, and the normalisation of $-\frac{1}{4}$ is chosen by convention. The equations of motion corresponding to this Lagrangian reproduce all of Maxwell's equations but with no charge-density and current-density terms. This describes the dynamics of massless, non-interacting spin-1 fields, which can be identified as photons in the quantised theory.

Scalar and vector fields give rise to spin-0 and spin-1 particles, respectively. To describe leptons and quarks, which have spin-1/2, requires the concept of *spinor* fields ψ . The Lagrangian which describes the dynamics of fermions in the SM is given by the Dirac Lagrangian:

$$\mathcal{L} = \bar{\psi}(i\gamma^\mu \partial_\mu - m)\psi, \quad (2.15)$$

where γ^μ are the gamma matrices, which are a set of four 4×4 matrices which satisfy the *Clifford Algebra*, and $\bar{\psi} \equiv \psi^\dagger \gamma^0$. The equations of motion are given by the Dirac equation:

$$i(\not{\partial} - m)\psi = 0, \quad (2.16)$$

where a slash indicates contraction with the gamma matrices. The Dirac equation is a first-order equation which replaces the Klein-Gordon equation for spin-1/2 particles. The plane-wave solutions to the Dirac equation represent particles and antiparticles with energies given by $E^2 = \mathbf{p}^2 + m^2$.

The Dirac Lagrangian has a global² U(1) symmetry, i.e. it is invariant under the transformation $\psi \rightarrow e^{i\theta}\psi$. As a consequence of Noether's theorem, which states that every continuous symmetry of the action has a corresponding conservation law, this symmetry results in a conserved *current*, j^μ , which satisfies the continuity equation. This gives rise to an associated

²A *global* symmetry transformation is not position-dependent, whereas a *local* symmetry transformation is position-dependent.

conserved *charge*. The current is given by:

$$j^\mu = -e\bar{\psi}\gamma^\mu\psi, \text{ where } \partial_\mu j^\mu = 0, \quad (2.17)$$

where $-e$ is the charge of the electron. In the quantised Dirac theory, this gives rise to the conserved charge given by:

$$Q = \int -e \sum_s (\hat{N}_a^s - \hat{N}_b^s) \frac{d^3 p}{(2\pi)^3}, \quad (2.18)$$

where \hat{N}_a^s and \hat{N}_b^s are the number operators for fermions and anti-fermions, respectively, in spin state s . The global U(1) symmetry of the Dirac Lagrangian therefore gives rise to particle number, and as a consequence, electric charge conservation [17].

The description of QED given by the Dirac Lagrangian (2.15) and the Maxwell Lagrangian (2.14) does not give the full picture. First, the Maxwell term does not reproduce Maxwell's equations for non-zero electric charge, and there is still no description of interactions between photons and fermions. Both of these issues are solved by adding an extra interaction term, $-j^\mu A_\mu$, where j^μ is the conserved current in equation 2.17. With this additional term, the QED Lagrangian is given by:

$$\mathcal{L} = -\frac{1}{4}F_{\mu\nu}F^{\mu\nu} + \bar{\psi}(i\cancel{D} - m)\psi + e\bar{\psi}\gamma^\mu\psi A_\mu. \quad (2.19)$$

This is equivalent to:

$$-\frac{1}{4}F_{\mu\nu}F^{\mu\nu} + \bar{\psi}(i\cancel{D} - m)\psi, \text{ where } D_\mu \equiv \partial_\mu + ieA_\mu. \quad (2.20)$$

D_μ is referred to as the *covariant derivative*. In going from the sum of the Maxwell (Equation 2.14) and Dirac Lagrangians (Equation 2.15) to Equation 2.20, a global U(1) symmetry is replaced by a local U(1) symmetry. This process of turning a global symmetry into a local symmetry through the introduction of the covariant derivative has given rise to interactions between fields.

The Dirac Lagrangian (Equation 2.15) is invariant under parity transformations defined by $(t, \mathbf{x}) \rightarrow (t, -\mathbf{x})$ if the spinor ψ transforms as $\psi \rightarrow \gamma^0\psi$. However, this contradicts experimental observations of parity violation in beta decay [18]. The generalisation of *Dirac spinors* to left- and right-handed *Weyl spinors* allows parity to be violated. By introducing a fifth gamma matrix γ^5 which anti-commutes with all other gamma matrices, Hermitian “Left” and “Right” projection operators can be defined

$$P_L = \frac{1}{2}(\mathbb{1} - \gamma^5), \quad P_R = \frac{1}{2}(\mathbb{1} + \gamma^5), \quad (2.21)$$

which are then used to construct the Weyl spinors

$$\psi_L = P_L\psi, \quad \psi_R = P_R\psi, \text{ where } \psi = \psi_L + \psi_R. \quad (2.22)$$

It can be shown that left (right) handed Weyl spinors transform into left (right) handed Weyl spinors under Lorentz transformations, which implies it's possible to construct a Lorentz invariant theory using Weyl spinors. Under parity transformations, however, left-handed Weyl spinors turn into right-handed Weyl spinors, and vice-versa, giving rise to parity violating theories. The Dirac Lagrangian (Equation 2.15) can be written in terms of Weyl spinors as

$$\mathcal{L} = \bar{\psi}_L i\partial^\mu \psi_L + \bar{\psi}_R i\partial^\mu \psi_R - m(\bar{\psi}_L \psi_R + \bar{\psi}_R \psi_L), \quad (2.23)$$

where the spinors decouple at $m = 0$. The handed-ness is interpreted as the helicity of the particle, i.e. whether the spin is parallel or anti-parallel to the momentum. This is only well-defined in the $m = 0$ case as here a Lorentz boost to the centre-of-mass frame (where the momentum is zero) is not possible.

2.1.3 Spontaneous Symmetry Breaking

Equation 2.20 describes a theory of a massless photon, massive fermions and interactions between photons and fermions. However, there is still no theory of massive vector bosons. To realise this, it is necessary to introduce the concept of *spontaneous symmetry breaking* (SSB). This describes the situation where the Lagrangian has an internal symmetry, but there exists a ground state which is not invariant under the full symmetry group of the Lagrangian.

Let's introduce the concept of SSB with the Lagrangian of complex scalar field

$$\mathcal{L} = \frac{1}{2}\partial_\mu\phi^*\partial^\mu\phi - V(\phi^*, \phi), \quad V(\phi^*, \phi) = -\mu^2\phi^*\phi^* + \frac{1}{2}\lambda(\phi^*\phi)^2, \quad (2.24)$$

with $\mu^2 > 0$. Notice that this is simply the Klein-Gordon Lagrangian (Equation 2.9), where the scalar field is now complex, and with the addition of a ϕ^4 term, which can be added by virtue of it being renormalisable. This Lagrangian has a global U(1) symmetry, i.e. is invariant under

$$\phi \rightarrow e^{i\theta}\phi, \quad \theta \in [0, 2\pi]. \quad (2.25)$$

The ground state is described by the minima of the potential $V(\phi^*, \phi)$, which are

$$\phi = \frac{v}{\sqrt{2}}e^{i\theta}, \quad \text{where } v^2 \equiv \mu^2/\lambda. \quad (2.26)$$

This describes a circle of identical minima, and we have the freedom to choose the vacuum state $\phi = v/\sqrt{2}$, where $v \in \mathbb{R}$. The value of the field at the minimum is called the *vacuum expectation value* (vev). Expanding $\phi(x)$ around the vev gives

$$\phi(x) = \frac{1}{\sqrt{2}}(v + \varphi(x) + i\chi(x)), \quad \varphi, \chi \in \mathbb{R}. \quad (2.27)$$

Up to quadratic order, this results in the Lagrangian

$$\mathcal{L}^{(2)} = \frac{1}{2}(\partial_\mu\varphi)^2 + \frac{1}{2}(\partial_\mu\chi)^2 - \mu^2\varphi^2, \quad (2.28)$$

from which it is clear that there is no mass term for the field $\chi(x)$. Therefore, as a result of SSB, the theory contains a massless scalar particle known as a *Goldstone boson*. This is a general consequence of SSB known as *Goldstone's theorem*: every generator³ of the global symmetry group that changes the vev (known as an *broken generator*) results in a massless boson. Spontaneous symmetry breaking when applied to a local symmetry is known as the *Higgs Mechanism*. In the application of the Higgs mechanics to the theory of electroweak unification (Section 2.1.5), the available degrees of freedom are reassigned to allow the W^\pm and Z bosons to become massive. Furthermore, all massless goldstone modes can be removed through a gauge choice.

Up until this point, only theories with a U(1) symmetry have been considered. This is an example of an Abelian⁴ group. The theory of electroweak unification is invariant under an additional group called SU(2), which is an example of a non-Abelian group. The next section gives a brief overview of the mathematical tools required for the application of the Higgs mechanism to a theory with a non-Abelian gauge symmetry.

2.1.4 Non-Abelian Gauge Symmetries

Each element of a non-Abelian group corresponding to a local symmetry transformation has a *representation* $M(x)$, which is an $N \times N$ matrix. Each group element can also be expressed as $M = e^{i\theta^a t^a}$, where θ^a are real coefficients, and t^a are a set of basis matrices called *generators*. The number of generators is given by the *dimensionality* of the group, D . For the group of traceless, Hermitian matrices, SU(N), the dimensionality is given by $D = N^2 - 1$.

Under a local non-Abelian transformation, the components ϕ_i of an N -component complex scalar field $\begin{pmatrix} \phi_1 \\ \vdots \\ \phi_N \end{pmatrix}$ transform as

$$\phi_i(x) \rightarrow M_{ij}(x)\phi_j(x). \quad (2.29)$$

In order for the Lagrangian in equation 2.24 to be locally gauge invariant, the derivatives should be replaced with covariant derivatives $D_\mu \equiv \partial_\mu + igA_\mu$. This Lagrangian is gauge invariant only if A_μ transforms as:

$$A_\mu \rightarrow MA_\mu M^\dagger + \frac{i}{g}(\partial_\mu M)M^\dagger. \quad (2.30)$$

Invariance under this transformation only holds if A_μ can be expressed as a linear combination of group generators $A_\mu^a t^a$, where A_μ^a are real coefficients. This implies that A_μ is a D component vector field. The group generator t^a is a *broken generator* if $t^a\phi_0 \neq 0$ and t^a is an *unbroken generator* if $t^a\phi_0 = 0$, where ϕ_0 is the vev.

³Group generators are defined in Section 2.1.5.

⁴An *Abelian* group is one where the group elements commute. Conversely, transformations that do not commute are called *non-Abelian*.

It is useful to define a $D \times D$ matrix

$$S^{ab} = \frac{1}{2}\phi_0^\dagger\{T^a, T^b\}\phi_0. \quad (2.31)$$

It can be shown that unbroken generators are eigenvectors of S^{ab} with zero eigenvalue. The eigenvectors c^A can be used to define a new set of generators

$$\hat{T}_{ij}^A = (c^A)^a T_{ij}^a, \quad (2.32)$$

with $A \in \{1, \dots, D\}$ and where the eigenvectors are ordered so that the zero eigenvalues come first. Then

$$\begin{aligned} \hat{T}_{ij}^A \phi_{0j} &= 0 \quad \text{for } A \leq D', \\ \hat{T}_{ij}^A \phi_{0j} &\neq 0 \quad \text{for } D' < A \leq D. \end{aligned} \quad (2.33)$$

The generators for $A \leq D'$ generate a subset of the original group, and generate the group of residual symmetries after symmetry breaking.

2.1.5 Electroweak Unification

The theory of electroweak unification is invariant under the symmetry $SU(2) \times U(1)$ and contains one complex doublet scalar field (the Higgs field), $\phi = (\begin{smallmatrix} \phi_1 \\ \phi_2 \end{smallmatrix})$; a three-component vector field $A_\mu = A_\mu^a t^a$ which transforms under $SU(2)$ ⁵; and a one-component vector field B_μ which transforms under $U(1)$. The transformation law for ϕ goes as

$$\phi \rightarrow e^{i\theta^a t^a + i\eta} \phi, \quad a \in \{1, 2, 3\}, \quad (2.34)$$

where ϕ^a and η are real numbers and t^a are the generators of $SU(2)$ which are 2×2 matrices. The $SU(2)$ and $U(1)$ gauge couplings are given by g_2 and $g_1/2$, respectively. The Lagrangian for this theory is given by

$$\mathcal{L} = -\frac{1}{4}F_{\mu\nu}^a F^{\mu\nu a} - \frac{1}{4}B_{\mu\nu} B^{\mu\nu} + (D_\mu \phi)^\dagger D^\mu \phi + \mu^2 \phi^\dagger \phi - \frac{1}{2}\lambda(\phi^\dagger \phi)^2 \quad (2.35)$$

where

$$F_{\mu\nu}^a = \partial_\mu A_\nu^a - \partial_\nu A_\mu^a + g_2 \epsilon^{abc} A_\mu^b A_\nu^c, \quad a \in \{1, 2, 3\}, \quad (2.36)$$

and ϵ^{abc} is the levi-cevita symbol and the covariant derivative is

$$D_\mu \phi = \partial_\mu \phi + ig_2 A_\mu^a t^a \phi, \quad a \in \{1, \dots, 4\}, \quad (2.37)$$

where a fourth generator and gauge field component is introduced for convenience. These are defined as $t^4 \equiv \frac{g_1}{2g_2} \mathbb{1}$ and $A_\mu^4 \equiv B_\mu$.

The kinetic terms in the Lagrangian are similar to the theory of free non-interaction photons (Equation 2.14). However, this theory would not be invariant under a non-Abelian transfor-

⁵ A_μ has three components since the dimensionality of $SU(2)$ is equal to three.

mation (Equation 2.30). It turns out that the trace of the field strength tensor is invariant, however, which explains the form of the first term in Equation 2.35.

By expanding ϕ around the vev

$$\phi(x) = \phi_0 + \frac{1}{\sqrt{2}}\varphi(x), \text{ where } \phi_0 = \frac{1}{\sqrt{2}} \begin{pmatrix} 0 \\ v \end{pmatrix}, \quad (2.38)$$

and expressing the gauge fields in terms of the generators in Equation 2.32, i.e. $A_\mu = A_\mu^A \hat{T}^A$, the covariant derivative can be written as

$$D_\mu \phi = \frac{1}{\sqrt{2}} \partial_\mu \varphi + g_2 A_\mu^A \hat{\phi}^A + \frac{i}{\sqrt{2}} g_2 A_\mu^A \hat{T}^A \varphi, \quad (2.39)$$

where we have defined $\hat{\phi}^A \equiv i \hat{T}^A \phi_0$. To quadratic order, the derivative term in the Lagrangian becomes:

$$(D_\mu \phi)^\dagger (D^\mu \phi)^{(2)} = \frac{1}{2} (\partial_\mu \varphi)^\dagger \partial^\mu \varphi + g_2^2 \sum_A \lambda^A A_\mu^A A^{\mu A} + \mathcal{O}((\partial_\mu \varphi) \hat{\phi}^A A^{\mu A}), \quad (2.40)$$

where we have used the fact that the vectors $\hat{\phi}^A$ are orthogonal

$$(\hat{\phi}^A)^\dagger \hat{\phi}^B = \lambda^B \delta_{AB}, \quad (2.41)$$

and λ^B are the eigenvalues of the matrix S^{ab} in Equation 2.31. Finally, the mixing term in Equation 2.40 and the $\phi_0^2 \varphi^2$ potential term can be eliminated through a gauge choice called the *unitary gauge*. Up to quadratic order, the Lagrangian becomes:

$$\begin{aligned} \mathcal{L}^{(2)} = & -\frac{1}{4} (\partial_\mu A_\nu^A - \partial_\nu A_\mu^A) (\partial^\mu A^{\nu A} - \partial^\nu A^{\mu A}) \\ & + g_2^2 \sum_A \lambda^A A_\mu^A A^{\mu A} + \frac{1}{2} (\partial_\mu \varphi)^\dagger \partial^\mu \varphi + \mu^2 \varphi^\dagger \varphi, \end{aligned} \quad (2.42)$$

from which the particle spectrum can be read off⁶. There is one scalar particle, the Higgs boson, with mass $\sqrt{2}\mu$ and four gauge bosons with mass $g_2 \sqrt{2\lambda^A}$, with $A \in \{1, \dots, 4\}$. Therefore calculating the eigenvalues of the matrix S^{ab} gives the masses of the gauge bosons. It turns out that the Lagrangian after symmetry breaking has a residual U(1) symmetry, which has dimensionality one. Therefore, according to equation 2.33, there is one eigenvalue which satisfies $\lambda^A = 0$, which means there is one massless gauge boson, i.e. the photon. The other three eigenvalues are non-zero implying that the other gauge bosons are massive. It is worth noting that the residual U(1) symmetry group is not the original U(1), but rather a linear combination of a subgroup of SU(2) and the original U(1) group. This means that the gauge fields corresponding to the W^\pm and Z bosons are linear combinations of the SU(2) and U(1) gauge fields.

⁶Calculating the equations of motion using the Euler-Lagrange equations would lead to 4 separate massive Klein-Gordon equations for the gauge field components A_μ^A . This calculation is omitted here for brevity.

2.1.6 The Standard Model Lagrangian

The SM has $SU(3) \times SU(2) \times U(1)$ gauge symmetry, where the $SU(3)$ gauge fields are given by $G_{\mu\nu}$. After spontaneous symmetry breaking, the residual symmetry group is $SU(3) \times U(1)$, meaning that $SU(3)$ is not a broken gauge symmetry, and hence the $SU(3)$ gauge fields do not gain mass under the Higgs mechanism. Hence this theory contains eight (since $SU(3)$ has dimensionality eight) massless gauge bosons called gluons, which are the mediators of the strong interaction. With the extra gauge field, the covariant derivative becomes

$$D_\mu = \partial_\mu + ig_3 G_\mu^c T_{SU(3)}^c + ig_2 A_\mu^a T_{SU(2)}^a + ig_1 Y B_\mu \mathbb{1}, \quad c \in \{1, \dots, 8\}, a \in \{1, 2, 3\}, \quad (2.43)$$

where Y is the $U(1)$ *hypercharge* which is just a real coefficient which changes depending on how a particular field transforms under $U(1)$. The SM also contains three left-handed Weyl spinors representing the lepton fields ℓ_L^f , $f \in \{1, 2, 3\}$, which are neutral under $SU(3)$ as leptons do not interact with the strong force

$$\ell_L^1 = \begin{pmatrix} \nu_{eL} \\ e_L \end{pmatrix}, \quad \ell_L^2 = \begin{pmatrix} \nu_{\mu L} \\ \mu_L \end{pmatrix}, \quad \ell_L^3 = \begin{pmatrix} \nu_{\tau L} \\ \tau_L \end{pmatrix}. \quad (2.44)$$

Charged leptons and neutrinos are known to interact via the weak force, hence the doublet lepton fields should be charged under $SU(2)$ and since they are doublets they should transform under the 2×2 matrices which make up the *fundamental representation*⁷ of $SU(2)$. The SM scalar field is the complex doublet discussed in Section 2.1.5, which means that it is in the trivial representation of $SU(3)$ (meaning that $T_{SU(3)}^c = 0$ for the Higgs field), the fundamental representation of $SU(2)$, and that the hypercharge is $Y = \frac{1}{2}$. The theory also contains three right-handed lepton fields which are neutral under $SU(3)$ and $SU(2)$

$$\ell_R^1 = e_R, \quad \ell_R^2 = \mu_R, \quad \ell_R^3 = \tau_R. \quad (2.45)$$

To identify the $e_{L/R}, \mu_{L/R}, \tau_{L/R}$ fields as the electrically charged left and right-handed leptons and $\nu_{eL}, \nu_{\mu L}, \nu_{\tau L}$ as the electrically neutral neutrinos, the hypercharge is required to be $Y = -\frac{1}{2}$ for the left-handed spinors and $Y = -1$ for the right-handed spinors. The Lagrangian cannot have a mass term like in equation 2.23 since this is not gauge invariant as left- and right-handed spinors transform differently under $SU(2)$ and $U(1)$. The lepton mass term in the SM goes as

$$\mathcal{L} \supset -y_l^e (\bar{\ell}_L^1 \phi \ell_R^1 + \bar{\ell}_R^1 \phi^\dagger \ell_L^1) - y_l^\mu (\bar{\ell}_L^2 \phi \ell_R^2 + \bar{\ell}_R^2 \phi^\dagger \ell_L^2) - y_l^\tau (\bar{\ell}_L^3 \phi \ell_R^3 + \bar{\ell}_R^3 \phi^\dagger \ell_L^3), \quad (2.46)$$

where y_l^f , $f \in \{1, 2, 3\}$ are the Yukawa couplings for leptons. There are no cross-generational terms since these can be removed via *singular value decomposition* which diagonalises the matrix of Yukawa couplings without affecting the lepton kinetic terms. After SSB, using the Higgs vev ϕ_0 from Equation 2.38, this reduces to the mass term from Equation 2.23 with mass $m_\ell = y_l^f v / \sqrt{2}$. There is also no neutrino mass term in the broken phase. Therefore the

⁷The fundamental representation is the original representation of $D N \times N$ matrices.

SM predicts massless neutrinos.

Quarks are represented by left and right handed Weyl spinors which are charged under SU(3) and are in the fundamental representation. This means that the quark fields come with three (since, in the fundamental representation, the generators of SU(3) are 3×3 matrices) *colour* indices, which are omitted here for brevity. Since the weak interaction can change quark flavours, the left handed fields are assumed to be charged under SU(2) and are in the fundamental representation. Just like with leptons, quarks come in three generations. For a given generation $f \in \{1, 2, 3\}$ and colour index, the left handed fields are therefore doublets of the form

$$q_L^f = \begin{pmatrix} u_L^f \\ d_L^f \end{pmatrix}, \quad (2.47)$$

where u_L^f refer to *up-type* and d_L^f refer to *down-type* quarks. Left handed quark fields also need to be charged under U(1) with $Y = -1/6$ for the up-type and down-type quarks to have an electric charge of $+\frac{2}{3}e$ and $-\frac{1}{3}$, respectively. The SM also contains right-handed quarks which are in the fundamental representation of SU(3) and are neutral under SU(2) and have hypercharge $Y = +\frac{2}{3}$ and $Y = -\frac{1}{3}$ for up and down-type quarks, respectively. The SM Yukawa term for quarks is given by

$$\mathcal{L} \supset -y_d^{fg} \bar{q}_L^f \phi d_R^g + (y_d^{fg})^* \bar{d}_R^g \phi^\dagger q_L^f + y_u^{fg} \bar{q}_L^f \tilde{\phi} d_R^g + (y_u^{fg})^* \bar{d}_R^g \tilde{\phi}^\dagger q_L^f, \quad (2.48)$$

where $\tilde{\phi} = i\sigma_2 \phi^*$ and σ_2 is the Pauli matrix with imaginary components. This redefinition is necessary for the last term to have the correct transformation properties under SU(2). The matrix of quark Yukawa couplings can be diagonalised just like with leptons, however this affects the kinetic term for the quark fields since the left-handed up-type and down-type quark fields are rotated differently, resulting in interactions between the W-boson and the quarks that can change the quark generation. This is summarised by the CKM matrix

$$V_{CKM} \equiv V_{uL}^\dagger V_{dL}, \quad (2.49)$$

where V_{uL} and V_{dL} are the singular value decomposition matrices applied to the left handed quark fields. Similarly to the lepton case, the quark field mass terms appear after SSB, where the masses are given by $\frac{y_d^f v}{\sqrt{2}}$ and $\frac{y_u^f v}{\sqrt{2}}$ for down-type and up-type quarks, respectively. Finally,

the SM Lagrangian is given by

$$\begin{aligned}
\mathcal{L} = & -\frac{1}{4}G_{\mu\nu}^a G^{\mu\nu a} - \frac{1}{4}W_{\mu\nu}^b W^{\mu\nu b} - \frac{1}{4}B_{\mu\nu} B^{\mu\nu} \\
& + (D_\mu \phi)^\dagger D^\mu \phi + \mu^2 \phi^\dagger \phi - \frac{1}{2}\lambda(\phi^\dagger \phi)^2 \\
& + \sum_f [\bar{\ell}_L^f i\cancel{D} \ell_L^f + \bar{\ell}_R^f i\cancel{D} \ell_R^f + \bar{q}_L^f i\cancel{D} q_L^f + \bar{d}_R^f i\cancel{D} d_R^f + \bar{u}_R^f i\cancel{D} u_R^f] \\
& - \sum_{fg} [y_d^{fg} \bar{q}_L^f \phi d_R^g + (y_d^{fg})^* \bar{d}_R^g \phi^\dagger q_L^f + y_u^{fg} \bar{q}_L^f \tilde{\phi} d_R^g + (y_u^{fg})^* \bar{d}_R^g \tilde{\phi}^\dagger q_L^f] \\
& - \sum_f [y_l^f \bar{\ell}_L^f \phi \ell_R^f + \bar{\ell}_R^f \phi^\dagger \ell_L^f], \quad a \in \{1, \dots, 8\}, \quad b, f, g \in \{1, 2, 3\},
\end{aligned} \tag{2.50}$$

where $G_{\mu\nu}^a$, $W_{\mu\nu}^b$ are the SU(3) and SU(2) field strength tensor components, respectively, and $B_{\mu\nu}$ is the U(1) field strength tensor. The SM has 19 parameters which have all been experimentally measured. These are the 3 gauge couplings, Higgs self-coupling λ and mass parameter μ , the 3 lepton Yukawa couplings, 6 quark Yukawa couplings, 3 CKM mixing angles and one complex phase, and finally an additional parameter called the strong CP angle, θ .

2.2 Physics of Hadron-Hadron Collisions

This section is primarily based on the textbook “Practical Collider Physics” [19], undergraduate lecture notes on quantum field theory by Tim Evans [15], in addition to lecture notes from the 2020 STFC HEP summer school. The review “General-purpose event generators for LHC physics” [20] was used in writing the subsection on Monte-Carlo generators.

2.2.1 Scattering Amplitudes and Cross-sections

The equations of motion for a free, real scalar field are given by the Klein-Gordon (KG) equation. The KG equation can be solved by taking a trial solution for $\phi(x)$ as the Fourier transform, i.e. a sum over plane waves. Substituting this into Equation 2.10 gives the usual relativistic dispersion relation $m^2 = k^2$, where $k^2 = k_0^2 - \mathbf{k}^2$, and k denotes the four-momentum. Therefore the general solution is⁸

$$\begin{aligned}
\phi(x) &= \int d^4k \delta(k^2 - m^2) (\theta(-k^0) A_k e^{-ikx} + \theta(k^0) B_k e^{ikx}) \\
&= \int \frac{d^3k}{2\omega_k} (A_k e^{-i\omega_k t + i\mathbf{k}\cdot\mathbf{x}} + B_k e^{i\omega_k t - i\mathbf{k}\cdot\mathbf{x}}), \quad \text{where } \omega_k = \sqrt{\mathbf{k}^2 + m^2},
\end{aligned} \tag{2.51}$$

A_k and B_k are general functions of k , $d^4k \equiv \frac{d^4k}{(2\pi)^4}$, and the Heaviside step function $\theta(\pm k^0)$ is used to separate the $k_0 < 0$ and $k_0 > 0$ solutions. Equation 2.51 motivates the following

⁸The notation is used where k or x without bold font are four-vectors. The Minkowski metric of (+1,-1,-1,-1) is assumed.

form of the quantum field operator $\hat{\phi}(x)$

$$\hat{\phi}(x) = \int \frac{d^3 k}{\sqrt{2\omega_k}} (e^{-ikx} \hat{a}_{\mathbf{k}} + e^{ikx} \hat{a}_{\mathbf{k}}^\dagger), \text{ where } kx = \omega_k t - \mathbf{k} \cdot \mathbf{x}. \quad (2.52)$$

The field operator can be interpreted as creating one quantum at $x^\mu = (\mathbf{x}, t)$, and the *raising* operator $\hat{a}_{\mathbf{k}}^\dagger$ creates one quantum at 3-momentum \mathbf{k} . The raising (and lowering) operators act on *states* which are momentum eigenstates of the free Hamiltonian. These states are vectors in a *Hilbert space* of all possible momentum eigenstates. An n -particle state is denoted in terms of n creation/annihilation operators acting on a single vacuum state $|0\rangle$

$$|\mathbf{p}_1, \mathbf{p}_2, \dots, \mathbf{p}_n\rangle = \hat{a}_{\mathbf{p}_1}^\dagger \hat{a}_{\mathbf{p}_2}^\dagger \dots \hat{a}_{\mathbf{p}_n}^\dagger |0\rangle. \quad (2.53)$$

In the *Schrödinger picture*, states evolve in time and operators are fixed. States evolve according to the time-dependent Schrödinger equation (TDSE)

$$i \frac{d|\psi\rangle_S}{dt} = H|\psi\rangle_S, \quad (2.54)$$

where H is the Hamiltonian, and a subscript S denotes the Schrödinger picture. In the *Heisenberg picture*, states are fixed, and operators \mathcal{O} evolve in time

$$\begin{aligned} \mathcal{O}_H(t) &= e^{iHt} \mathcal{O}_S e^{-iHt}, \\ |\psi\rangle_H &= e^{iHt} |\psi\rangle_S, \end{aligned} \quad (2.55)$$

where a subscript H denotes the Heisenberg picture. The *interaction picture* is a hybrid of the Heisenberg and Schrödinger pictures. The Hamiltonian is split up into the free Hamiltonian H_0 and the interacting part H_{int} ⁹

$$H = H_0 + H_{\text{int}}. \quad (2.56)$$

In the interaction picture, the time dependence of the operators is according to Equation 2.55 but with the Hamiltonian replaced with the free Hamiltonian H_0 . The states in the interaction picture evolve according to the TDSE with the Hamiltonian replace with H_{int} . A corollary of this is that states are evolved in time from t_0 to t through the unitary time evolution operator $U(t, t_0)$

$$|\psi(t)\rangle_I = U(t, t_0) |\psi(t_0)\rangle_I, \quad (2.57)$$

where the subscript I denotes the interaction picture. $U(t, t_0)$ is given by *Dyson's formula*

$$U(t, t_0) = T \exp \left(-i \int_{t_0}^t H_I(t') dt' \right), \quad (2.58)$$

where T denotes the *time ordering* of the operators such that later times are on the left.

We want to calculate the probability P for a scattering processes which has some initial state

⁹In principle this is an arbitrary split, but it useful for the discussion of matrix elements for the split to correspond to the free part and the interacting part of the Hamiltonian.

$|i\rangle$ and a final state $|f\rangle$. This is given by

$$P = \frac{|\mathcal{M}|^2}{\langle f|f\rangle\langle i|i\rangle}, \quad (2.59)$$

where \mathcal{M} is called the *matrix element*. To determine the form of \mathcal{M} , we make the following assumptions. The scattering process happens at some time t , $t_- < t < t_+$ and the interactions happen on very short time scales. Therefore at $t_\pm \rightarrow \pm\infty$ there are no interactions, which means the initial and final states $|i\rangle$ and $|f\rangle$ are simply the eigenstates of the free theory. The matrix element is given by

$$\mathcal{M} = \lim_{t_\pm \rightarrow \pm\infty} \langle f|U(t_+, t_-)|i\rangle \equiv \langle f|S|i\rangle, \quad (2.60)$$

where $U(t_+, t_-)$ is the unitary operator which evolves the state $|i\rangle$ in time to the state $|f\rangle$, where these are now eigenstates of H_0 , and S is the operator known as the *S-matrix*. By Taylor expanding S , the matrix element can be written as

$$\mathcal{M} = \delta_{if} + i(2\pi)^4 \delta^{(4)} \left(\sum_i p_i - \sum_f q_f \right) \mathcal{A}, \quad (2.61)$$

where the factor of $(2\pi)^4$ comes from the normalisation of the states, the first term describes the case where there is no scattering, and the delta function in the last term imposes overall energy-momentum conservation. The remaining quantity \mathcal{A} is called the *amplitude*, and is like the matrix element \mathcal{M} but without the energy-momentum conservation and only includes the pure scattering terms.

Scattering amplitudes can be explicitly calculated through writing the matrix element as a product of *Green's functions*, which are time-ordered vacuum expectation values of the field operators that define the initial and final states. Perturbatively expanding the S-matrix gives the amplitude at a given order, and the time-ordered product of fields can then be computed using Wick's theorem [17]. The method of using *Feynman diagrams* simplifies this procedure by representing each term in the perturbative expansion of $\mathcal{M} - \delta_{if}$ as a diagram. The specific set of rules which defines the correspondence between terms and the diagrams is dependent on the interacting part of the theory. These rules are called the *Feynman rules*.

Feynman diagrams consist of *external legs* which correspond to initial or final state (real) particles; *internal legs* which correspond to virtual particles; and *vertices* which correspond to interaction points between particles. Feynman diagrams are constructed as follows

1. Draw an external line for every particle in the initial state and in the final state.
2. Write down all possible combinations of n vertices if calculating \mathcal{A} at order n .
3. Connect the legs corresponding to the same particle together in all possible ways.

The simplest diagrams that contribute to a given process give the Leading Order (LO) diagrams. The addition of diagrams with extra radiation amounts to an increase in the number

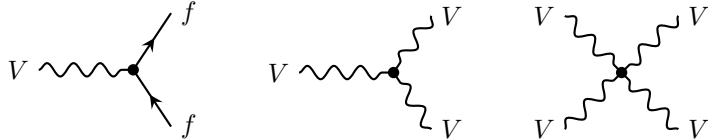


Figure 2.1. The types of possible EW interaction vertices at tree-level (no loops), omitting the diagrams involving a Higgs boson. V represents an EW gauge boson (γ, Z, W^\pm), f represents a fermion. Care must be taken in the choice of particle, as there are many interactions with the configurations listed here which are not allowed.

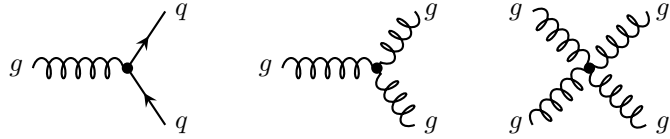


Figure 2.2. The types of possible QCD (strong) interaction vertices at tree-level, omitting the diagrams involving a Higgs boson. g represents a gluon and q a quark. Since gluons carry colour charge, they can self-interact.

of vertices, which comes with additional factors in the coupling constants. Considering only diagrams up to a given order in the coupling is called *perturbation theory*. The simplest corrections to the LO diagrams are called next-to-leading order (NLO).

The types of possible vertices for the EW interactions are shown in Figure 2.1. Care must be taken to ensure that vertices involving a γ must involve charged particles, and therefore vertices like γZZ are not allowed. Since, it is only through interactions with the W -boson that quarks can change families, *flavour changing neutral current* vertices like $Zd\bar{s}$ are not allowed, and vertices which do involve an interaction between a W -boson and quarks from different families are suppressed by off-diagonal factors from the CKM matrix. Additionally, diagrams like $\gamma\gamma\gamma$, ZZZ , $ZZZV$, and $\gamma\gamma\gamma V$ are not allowed. Finally, charge and lepton number must be conserved at each vertex, where lepton (and baryon) number conservation are accidental symmetries of the $U(1)$ gauge invariance.

The types of possible QCD interaction vertices are shown in Figure 2.2.

From Equation 2.59, the probability of an interaction is proportional to the square of the matrix element. Ignoring factors of 2π , this is given by

$$|\mathcal{M}|^2 = |\mathcal{A}|^2 \delta^{(4)} \left(\sum_i p_i - \sum_f q_f \right) \delta^{(4)}(0), \quad (2.62)$$

where $\delta^{(4)}(0)$ comes from the square of the delta function, and results in an infinite interaction probability. This infinity is resolved if a finite space-time volume VT is considered

$$\delta^{(4)}(0) = \int d^4x e^{-ipx} \Big|_{p=0} = \int d^4x = VT. \quad (2.63)$$

After summing over all possible momentum states, the interaction probability per unit time

reduces to [19]

$$\sum_{\text{momenta}} \frac{P}{T} = \frac{(2\pi)^4}{4E_1 E_2 V} \left(\prod_{k=3}^n \int \frac{d^3 \mathbf{p}_k}{2E_k} \right) \delta^{(4)} \left(\sum_i p_i - \sum_f q_f \right) |\mathcal{A}|^2, \quad (2.64)$$

where E_1 and E_2 are the energies of the initial and final state particles.

pp collision experiments don't directly measure scattering probabilities since the interaction rate depends on factors which are specific to the experiment, such as the focus, shape, and intensity of the particle beams. Instead, a quantity known as the *cross-section* is measured, which is related to scattering amplitudes but is not dependent on the properties of the beam.

Cross-sections

In a scattering event it is useful to think of one of the particles as being the incident particle, and the other as being the target. Then, there is some region of space around the target particle, such that an interaction occurs if the incident particle is within that region. Therefore the target particle has an effective cross-sectional area for interaction, which is referred to as the scattering *cross-section*, σ .

The number of scattering events N in a given amount of time is directly related to σ and satisfies

$$\frac{dN}{dt} = \mathcal{L}(t)\sigma, \quad (2.65)$$

which defines the quantity known as the *instantaneous luminosity* $\mathcal{L}(t)$ (this is discussed in more detail in Section 3.1.1), which carries the dependence on the beam parameters. Linking the interaction cross-section to an event rate requires knowledge of some properties of the incident and target particles, specifically

$$\sigma = \frac{1}{N_b \mathcal{F}_a} \frac{\delta N}{\delta t}, \quad \text{where } \mathcal{F}_a = n_a(v_a + v_b), \quad (2.66)$$

and n_a is the number of incident particles per unit volume; N_b is the total number of target particles; v_a, v_b correspond to the incident and target particle speeds; and \mathcal{F}_a is the *flux* of the incoming particles.

Scattering processes are described by Poisson statistics since the interaction probability is constant in a given amount of time. For Poisson processes, the total probability per unit time is equal to the event rate. Therefore scattering amplitudes can be linked to cross-sections by taking Equation 2.64 and dividing by a flux factor. This gives

$$\sigma = \frac{1}{F} \int d\Phi |\mathcal{A}|^2, \quad \text{where } F = 4(E_1|\mathbf{p}_2| + E_2|\mathbf{p}_1|), \quad (2.67)$$

and

$$\int d\Phi = (2\pi)^4 \left(\prod_k \int \frac{d^3 \mathbf{p}_k}{2E_k} \right) \delta^{(4)} \left(\sum_i p_i - \sum_f q_f \right), \quad (2.68)$$

where F is referred to as the Lorentz invariant flux, the product is over final state particles, and $\int d\Phi$ is the phase-space integral. The calculation of a scattering cross-section is therefore performed by (i) calculating the square modulus of the scattering amplitude \mathcal{A} , (ii) performing the phase-space integral, and (iii) dividing by a flux factor.

Chapter 5 outlines the measurement of a *differential* cross-section. This describes the dependence of σ with a some observable \mathcal{O} , and is denoted $\frac{d\sigma}{d\mathcal{O}}$. Experimentally, this is determined through measuring the number of scattering events in a given bin of the observable, and normalising by the integrated luminosity (Section 3.1.1).

2.2.2 Calculations of Cross-sections in pp Collisions

The methods described above allows for the calculation of cross-sections for the scattering of two fundamental particles. However, it is not immediately obvious how to extend this prescription to pp collisions. A proton is a bound state of three quarks, uud , where the binding force is the strong interaction, or QCD. One of the properties of QCD is that the interactions become asymptotically weaker at higher energies (equivalently, smaller times or distances), this is called *asymptotic freedom*. Hence, for the high-energy collisions at the LHC, protons interact as if their constituents are not in a bound state at all.

Due to the Heisenberg uncertainty principle, the constituent valence quarks¹⁰ of the proton have non-zero momenta, even in the rest frame of the proton. In the proton rest frame, the extreme case can be considered where the energy of one of the valence quarks is equal to half of the proton mass. A Lorentz boost to the lab frame then reveals that the quark momentum can take any value between zero and the total proton momentum. Therefore it is useful to think of colliding partons as having a momentum collinear with the proton p_i which is some fraction x_i of the total proton momentum P_i

$$p_i = x_i P_i, \quad 0 \leq x_i \leq 1. \quad (2.69)$$

Individual cross-sections for quarks and gluons can then be combined in the following way to give the total cross-section σ corresponding to a pp collision

$$\sigma = \sum_{i,j \in \{q,\bar{q},g\}} \int_0^1 dx_1 \int_0^1 dx_2 f_i(x_1) f_j(x_2) \hat{\sigma}_{ij}, \quad (2.70)$$

where the sum is over all combinations of partons, and $\hat{\sigma}_{ij}$ is the cross-section for a given parton scattering process, referred to as the *partonic cross-section*. The functions $f_i(x_k)$ are called parton distribution functions (PDFs) which are probability distributions that give the probability of there being a parton i with momentum fraction x_k in proton k . The total cross-section σ is therefore split up into a part which can be calculated using perturbation theory – the partonic cross-sections – and a part which cannot be calculated using perturbation theory,

¹⁰The valence quarks are the real uud quarks that make up the proton. However, the proton mass is much larger than the sum of the valence quark masses. Therefore it is useful to think of a proton as consisting of *partons*, which describes a valence quark, gluon, or a virtual quark (known as a *sea quark*).

and must be determined from the particle collision data – the PDFs. It is worth pointing out that this treatment of PDFs is a simplification, and in particular, PDFs can be negative at next-to-leading and higher orders. The true form of the hadronic cross-section is written as

$$\sigma = \sum_{i,j \in \{q,\bar{q},g\}} \int_0^1 dx_1 \int_0^1 dx_2 f_i(x_1, \mu_F^2) f_j(x_2, \mu_F^2) \hat{\sigma}_{ij}(x_i, \mu_F^2, \{p_i \cdot p_j\}) + \mathcal{O}\left(\frac{\Lambda_{\text{QCD}}^2}{Q^2}\right), \quad (2.71)$$

which includes a momentum transfer scale describing the partition between the perturbative and non-perturbative physics, the factorisation scale μ_F (more detail in Section 2.2.3). Equation 2.71 also contains a dependence on the energy scale of the hard scattering process, Q^2 , and the scale at which the strong coupling becomes large, Λ_{QCD} . Variations in the PDFs and factorisation and renormalisation¹¹ scales are used to estimate uncertainties in theory predictions, for more details refer to Section 5.13.6.

2.2.3 Formation of Hadronic Final States

Even if it is possible to calculate the partonic cross-section for a given scattering process at a fixed order in perturbation theory and combine these with PDFs to get a hadronic cross-section, there are still a substantial number of complexities to consider before arriving at a result which can be compared with experimental data. It turns out it is not possible to describe the hadronic final state solely using perturbation theory. In practise then, the hadronic final states are simulated using *Monte Carlo* (MC) event generators, where MC refers to a class of statistical techniques used in the simulations.

In any given pp collision at the LHC, the incoming partons can radiate gluons and since those gluons are colour charged, they can go to radiate even further. There is therefore a huge amount of QCD radiation from the incoming partons prior the hard interaction (i.e. the process where a large momentum transfer occurs or where heavy objects are created) in addition to radiation from the outgoing partons. Calculating the Feynman diagrams corresponding to each emission is clearly not practical. In practise, MC event generators employ *parton shower* algorithms to model this QCD radiation. At a certain point, the partons cease to radiate. Since free partons cannot exist due to a property of QCD known as *confinement*, they go on to form colour neutral (singlet) bound states, hadrons, before they can be observed. The formation of hadrons from partons is called *hadronisation*, and occurs when the momentum transfer scale is small. This in turn means that the value of strong coupling α_s is large. In this regime, perturbation theory breaks down as it relies on α_s being small. Hadronisation, therefore, is intrinsically non-perturbative. In describing the hadronic final state, MC generators employ hadronisation models to describe this non-perturbative physics.

¹¹The renormalisation scale is a factor which enters into the running of the masses and the coupling constant in QCD. For more detail refer to [19] and Section 5.13.6.

The description of parton showers begins with the observation that partonic cross-sections tend to diverge when we consider soft or collinear (small-angle) radiation. Consider a $q\bar{q}$ scattering process where there is additional gluon radiation off of an incoming external quark leg. If the quark has momentum p_1 and the radiated gluon has momentum k , there is an additional internal quark leg whose propagator¹² contains the factor

$$\frac{1}{(p_1 - k)^2} = \frac{1}{-2|\mathbf{p}_1||\mathbf{k}|(1 - \cos \theta)}, \quad (2.72)$$

where the last equality holds when we consider the lab frame at a pp collider, and the gluon momentum is parametrised in terms of a qg scattering angle θ , i.e.

$$p_1^\mu = (|\mathbf{p}_1|, 0, 0, |\mathbf{p}_1|), \quad k^\mu = (|\mathbf{k}|, 0, |\mathbf{k}| \sin \theta, |\mathbf{k}| \cos \theta). \quad (2.73)$$

The scattering amplitude diverges in the soft and collinear limit. The problem here lies in that this calculation pertains to a scattering amplitude for a process where the final state has a fixed number of partons. This amplitude is not *infrared safe* (IR safe) as it does not include a sum over all physically indistinguishable states. For the case of pp collisions, all partonic cross-sections are not IR safe by themselves. This is because there are divergences associated with not summing over all possible initial states. The total hadronic cross-section is IR safe however, as the IR divergences are absorbed by the PDFs by defining a momentum transfer scale μ_F , called the factorisation scale which effectively divides the perturbative from the non-perturbative physics. In simulating scattering events μ_F must be set at some fixed choice.

Let's consider the case where a final state parton i radiates and therefore splits into other partons, j and k . It turns out that in the collinear limit, the partonic differential cross-section for the $n + 1$ parton production factorises into the differential cross-section for n parton production multiplied by a factor that includes a sum over all partons that give final state parton j .

$$d\hat{\sigma}_{n+1} = d\hat{\sigma}_n \sum_i \int_{k_{\min}}^{k_{\max}} \frac{d|\mathbf{k}_T|^2}{|\mathbf{k}_T|^2} \int_{z_{\min}}^{z_{\max}} \frac{dz}{z} P_{ji}(z), \quad (2.74)$$

where \mathbf{k}_T is the transverse momentum of the parton k relative to j , P_{ji} are *splitting functions* which are different depending on the specific parton splitting vertex and depends on α_s and z , which is the fraction of the momentum of parton i carried by parton j . Equation 2.74 makes it possible to calculate the differential partonic cross-section for any number of collinear splittings. Even if the splittings are not exactly collinear, this will give a reasonable approximation since radiation is enhanced in the collinear limit.

With each emission, the emitting parton gets progressively closer to satisfying

$$t \equiv p_i^2 = 0, \quad (2.75)$$

¹²In the QCD Feynman rules an internal leg corresponds to a factor of $\frac{i(p+m)}{p^2-m^2+i\epsilon}$, where $\epsilon \ll 1$ insures the correct causal properties. This factor is called the propagator. For the calculation in this section, the quark is assumed to be massless.

where the *virtuality* t is defined as the square of the momentum of parton i , and the parton is assumed to be massless. This means that the parton gets progressively closer to being on-shell. However, because of colour confinement, the parton will never be precisely on-shell, therefore the parton ceases to emit at a certain virtuality, t_0 . The probability of an emission between virtualities t_n to t_{n+1} for momentum fractions z_n and z_{n+1} is given by the probability of no (resolvable) emissions in the virtuality range multiplied by the probability of a (resolvable) emission which is related to the splitting function for the pair (z_n, z_{n+1}) . The probability for a whole cascade of partons is just given by repeated products of these terms. Therefore a parton shower algorithm can simulate QCD radiation through randomly generating a set of virtualities and momentum fractions.

Thus far we have only considered radiation in the small angle limit, but Equation 2.72 shows that soft radiation is also enhanced. For wide-angle soft radiation, the differential cross-section does not factorise like in Equation 2.74. However, the resolution to this is relatively straightforward. By ordering the parton shower in emission angle θ rather than virtuality, the effects of soft emissions are correctly accounted for – this is called *angular ordering*. Another resolution is to replace the notion of radiation recoiling off a single parton with recoil against a pair of partons. This is called a *dipole shower*. Depending on the MC generator, either transverse-momentum ordered dipole showers or angular ordering are used in parton shower algorithms.

In the current description of the formation of the partonic final state is an unaddressed ambiguity relating to whether the additional partonic radiation should be generated from the matrix element or from the parton shower. Since the parton shower is only exact for collinear radiation, it does not provide a good description of wide-angle radiation. Therefore it is preferable not to leave the generation of additional partons entirely up to the parton shower. On the other hand, the matrix element calculations contain collinear singularities, meaning that additional small-angle radiation is not well described by higher order calculations in the matrix element. The PYTHIA8 user manual [21] defines the procedure of combining one matrix element calculation with the parton shower as *matching*, and combining several matrix element calculations with each other and the parton shower as *merging*.

The formation of final state hadrons from a collections of partons is modelled through hadronisation algorithms. The two primary models are called the *Lund string model* and the *cluster* hadronisation model. The Lund string model is predicated on the fact that the strong force between a quark-antiquark pair is constant with the distance between them if they are sufficiently far apart. The gluon field lines between the quarks are called *flux tubes* (or *strings*) with uniform energy per unit length. At a large enough separation, the flux tube breaks resulting in the formation of another quark-antiquark pair. Hadrons are formed by the grouping of quarks when a string splitting is no longer kinematically possible. The model depends on a number of parameters which affect the functions describing the momenta of the quarks after a string break and the probability distributions governing a string break. In the cluster model, the gluons at the end of the parton shower split up into quark-antiquark pairs. Subsequently, colour neutral clusters are formed from neighbouring quark-antiquark pairs, which then go

on to decay into hadrons.

The description of a hadronic scattering process given here still does not include a number of complexities such as the interactions between multiple incoming partons – called multi-parton interactions (MPI) – and effects of the proton remnants. Such additional complexities which are not considered in the hard scatter, parton shower, or hadronisation are collectively referred to as the *underlying event* (UE). Accurate modelling of the UE is often very important in comparing predictions with experimental data [20].

Jet Formation

The hadrons produced as a result of the pp collisions at the LHC are grouped into collimated streams of hadrons called jets. The reason for this is that the hard interaction gives rise to high transverse momentum partons which then go on to emit approximately collinear radiation. The kinematics of the resulting jet is then closely related to that of the original hard parton [22]. Jets are defined using by a specific *jet algorithm*, which is a set of rules that govern the grouping of partons. Simulated and measured collision events can then be readily compared if the same algorithm is used for both. The primary requirement of a jet algorithm is that it should be IR safe, meaning that the addition of soft and/or collinear emissions should not change the results.

The jet algorithm that is primarily used at the LHC is the anti- k_t algorithm [23]. This algorithm falls under a class of IR safe algorithms known as *sequential recombination* algorithms which both find jets and assign a clustering sequence to an event. In these algorithms, pairs of particles are grouped together according to the value of a distance parameter. In the anti- k_t algorithm, the distance parameter is based on the transverse momenta of the particles. This choice is motivated by the observation that the parton multiplicity of a jet depends on its transverse momentum [24–26].

The anti- k_t algorithm uses a particle distance parameter d_{ij} and an additional beam distance parameter d_{iB} .

$$d_{ij} = \min(p_{t,i}^{2p}, p_{t,j}^{-2}) \frac{\Delta R_{ij}^2}{R^2}, \quad \Delta R_{ij}^2 = (y_i - y_j)^2 + (\phi_i - \phi_j)^2, \quad (2.76a)$$

$$d_{iB} = p_{t,i}^{-2}, \quad (2.76b)$$

where the R parameter is related to the radius of the jet and is usually set at $R = 0.4$ at ATLAS. ϕ_i and y_i denote the azimuthal angle and rapidity (defined in Chapter 3) of the particle.

The anti- k_t algorithm favours clustering around hard seeds and produces circular jets [27]. This is attractive because soft hadrons which are produced from the emissions of a hard parton ought to be assigned to the jet of the nearest hard parton [26]. Circular jets are desired since any jet that points at least a distance R from the edge of the center of the detector will then be fully contained within it [22].

Monte-Carlo Event Generators

The generation of simulated events in Monte-Carlo (MC) event generators begins with the matrix element calculation of a user-selected hard process at a given order in perturbation theory which is typically at NLO. In order to calculate a cross-section, the square of the matrix element needs to be derived for every phase-space point (the set of incoming and outgoing momenta). There is the possibility of relying on analytical results for LO matrix elements for low multiplicity final states (usually 1-3 particles), and all multi-purpose MC event generators rely on such a list of LO matrix elements. Alternatively, dedicated matrix-element and phase-space generators exist for the calculations involving more complex final states. Some examples are the ALPGEN [28], AMEGIC [29], or COMIX [30] programs.

After the construction of the matrix element, the phase-space integrals are usually computed using algorithms which rely on phase-space sampling. Examples of such algorithms are *sequential* algorithms which rely on the pole structure of one of the Feynman diagrams contributing to the matrix element [31] and *multi-channel* integrators which utilise combinations of several sampling algorithms [32]. Because of the large dimensionality of the phase-space, numerical techniques such as quadrature integration are not typically not practical for the computation of phase-space integrals [20].

Subsequent to the simulation of the hard interaction, MC event generators are also responsible for simulating the parton showers associated with incoming and outgoing partons, performing hadronisation algorithms, simulating underlying-event activity, and modelling the decays of unstable particles.

The primary event generators used for event simulation in the analyses described in Chapters 4 and 5 are PowHEG [33–35], PYTHIA8 [21, 36], SHERPA [37, 38], and MADGRAPH [39]. For the MC samples used in this thesis, when matrix elements are calculated using PowHEG and MADGRAPH, they are interfaced with PYTHIA8 for parton showering and hadronisation, whereas samples generated using SHERPA use the same program for parton showering and hadronisation. PYTHIA8 and SHERPA both have p_T -ordered dipole showers, but PYTHIA8 uses the lund string model for hadronisation, whereas SHERPA uses the cluster model. MADGRAPH, SHERPA, and PowHEG all use different schemes for the matching and merging of matrix elements with parton showers [40–42], where for NLO matching and merging, MADGRAPH uses the MC@NLO implementation [43], SHERPA uses a variant of this [44], and PowHEG has its own dedicated approach [35].

2.3 Vector Boson Scattering

Precision measurements of processes involving Vector Boson Scattering (VBS) and Vector Boson Fusion (VBF) have become experimentally measurable only very recently, with the first measurements by ATLAS and CMS in LHC Run-1 [45–51]. The defining feature of VBS and VBF processes is the t-channel exchange of an EW gauge boson in a quark/anti-quark

scattering processes. The presence of one (two) EW boson(s) in the final state is referred to as VBF (VBS). The two final-state quarks are manifested as hard *tagging* jets in the forward and backward regions of the detector. Moreover, these events are characterised by the lack of hadronic activity in the rapidity interval of the tagging jets, centrally produced EW bosons, and a large dijet mass m_{jj} of the tagging jets.

Measurements of VBS processes are of particular interest because the production cross-section is sensitive to Feynman diagrams which include quartic EW boson (Z, W, γ) self-interactions.¹³ The scattering cross-section in VBS processes also include contributions from trilinear interactions, but since these can be probed through more common diboson processes, the primary goal in measuring VBS is to study the quartic vertices. These cross-sections are usually of the order of fb, and therefore represent some of the rarest processes which are still measurable at the LHC.

Chapter 5 outlines the differential cross-section measurement of $W\gamma$ production in association with two jets. This process is sensitive to VBS interactions, and occurs with electroweak (EW) and strong production modes. The EW production mode is defined by tree-level diagrams calculated at $\mathcal{O}(\alpha_{EW}^4)$, and include diagrams with the t-channel exchange of an EW boson and (s-channel) triboson production. The strong production mode has tree-level diagrams at $\mathcal{O}(\alpha_s^2 \alpha_{EW}^2)$ and includes diagrams where quarks and gluons are exchanged in the t-channel. Some examples of tree-level diagrams for the EW and strong production modes are shown in Figure 2.3. The rate of the strong production mode is significantly higher than the EW production mode because of the appearance of two powers of the strong coupling constant and the larger number of subprocesses that contribute to the total cross-section. It is for this reason that the dominant systematic uncertainties associated with VBS measurements usually pertain to the modelling of the strong background. A precise measurement of the EW production mode therefore requires this background to be carefully constrained.

The lack of central hadronic activity for VBS processes is a feature of perturbative QCD, and is a consequence of the colour structure [52]. In the tree-level VBS diagrams in Figure 2.3, it is only colour singlet states that are exchanged through the rapidity difference of the two partons. Therefore the dominant contributions to the EW process are the t-channel diagrams which do not have any colour exchange between the partons. This results in the outgoing quarks being only slightly deflected, and the emission of any partons will be therefore be along the beamline. For the strong diagrams (for example diagram (f) in Figure 2.3), a colour charge is accelerated through the rapidity difference of the incoming partons, which will generate parton radiation away from the beamline. A central jet veto is therefore paramount in separating the VBS signal from large strong backgrounds. Because of the lack of central hadronic activity, the outgoing quarks in a VBS interaction will have a back-to-back geometry with large longitudinal momenta. This motivates the requirements of a large dijet mass and rapidity separation.

¹³It is important to note that the full gauge invariant set of Feynman diagrams contributing to the scattering cross-section includes those contributions from non-VBS interactions. Therefore, it is not possible to solely measure the VBS interactions.

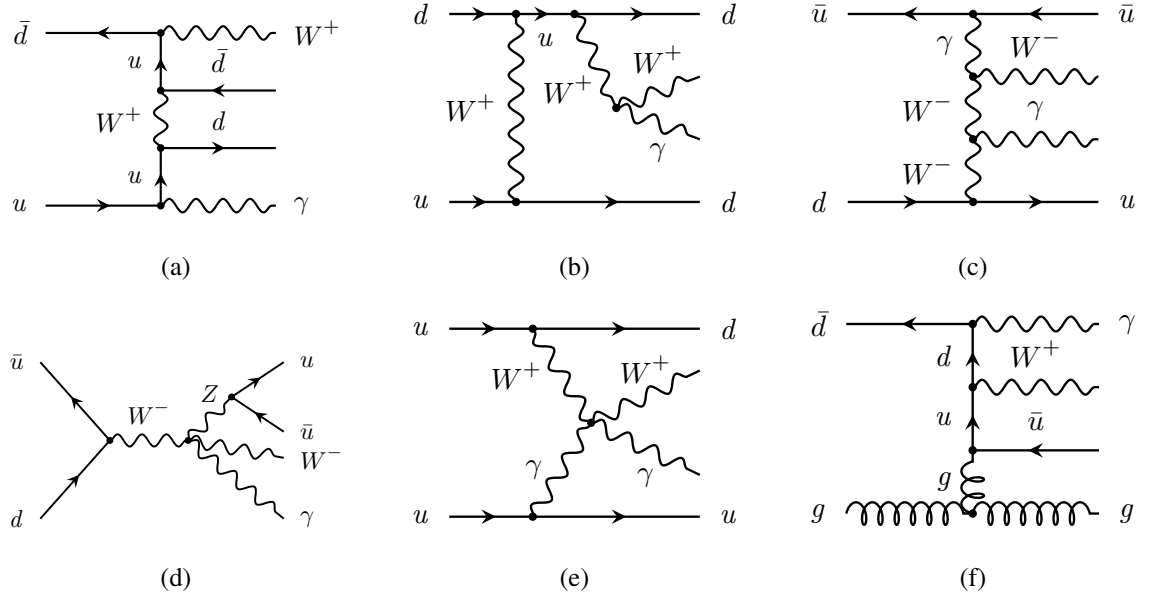


Figure 2.3. (a) EW- $W\gamma jj$ production involving no gauge boson self-interactions; (b) bremsstrahlung EW- $W\gamma jj$ non-VBS production involving trilinear gauge boson interactions; (c) EW- $W\gamma jj$ VBS involving trilinear gauge boson interactions; (d) EW- $W\gamma jj$ non-VBS production through s-channel triboson interaction involving EW quartic gauge boson interactions; (e) EW- $W\gamma jj$ VBS involving quartic gauge boson interactions; (f) strong- $W\gamma jj$ production. Diagrams produced by author apart from (b) and (e), which are from [53].

Status of VBS Measurements at ATLAS

A summary of the standard model fiducial and total cross-section measurements derived at ATLAS are shown in Figure 2.4. From this figure it is clear that the VBS and VBF measurements correspond to some of the rarest standard model processes measured at ATLAS. In addition to electroweak $W\gamma jj$, some of the most recent VBS-sensitive measurements include

- The fiducial cross-section measurement and observation of electroweak $W^\pm W^\mp jj$ production [54];
- The electroweak and inclusive differential cross-section measurements of $W^\pm W^\pm jj$ production [55];
- Electroweak and inclusive differential cross-section measurements of $ZZ(\rightarrow 4\ell)jj$ [56].

A summary of all public VBF, VBS, and triboson cross-section measurements, and their agreement with theory are shown in Figure 2.5.

Standard Model Production Cross Section Measurements

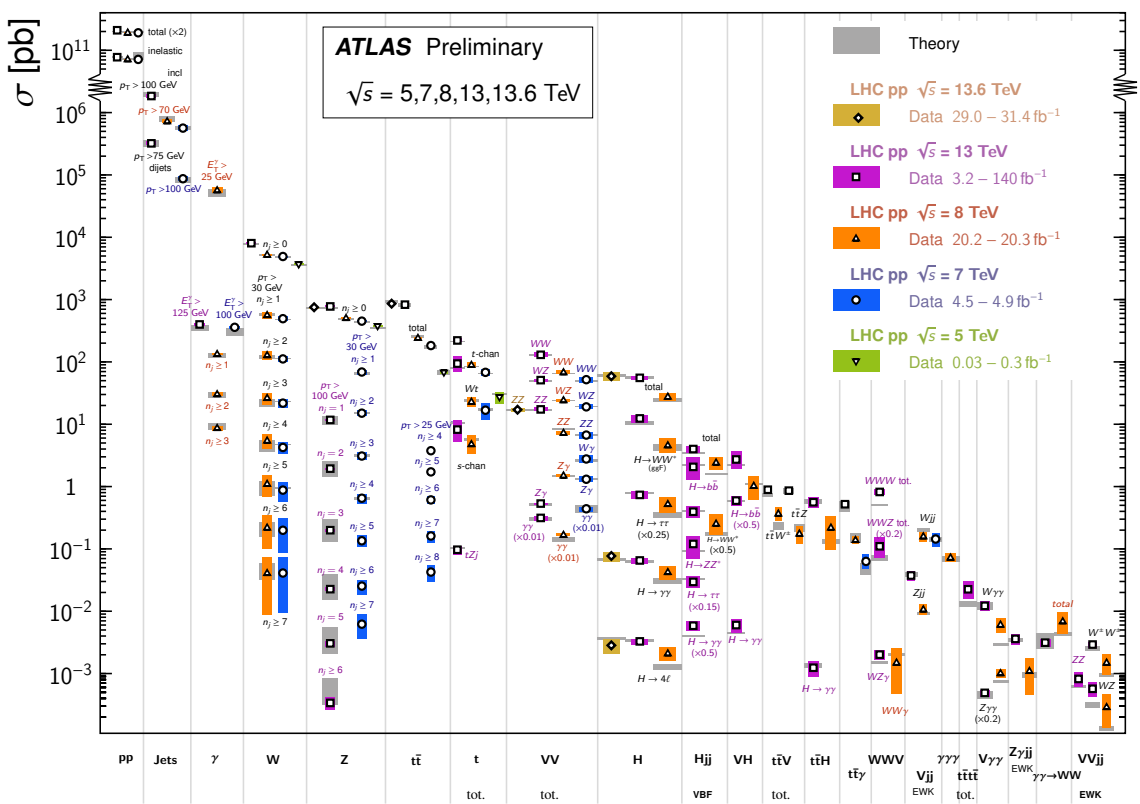


Figure 2.4. Overview of standard model total and fiducial cross-section measurements made at ATLAS. Total cross-sections are corrected for branching fractions. Figure from [9].

VBF, VBS, and Triboson Cross Section Measurements

Status: October 2023

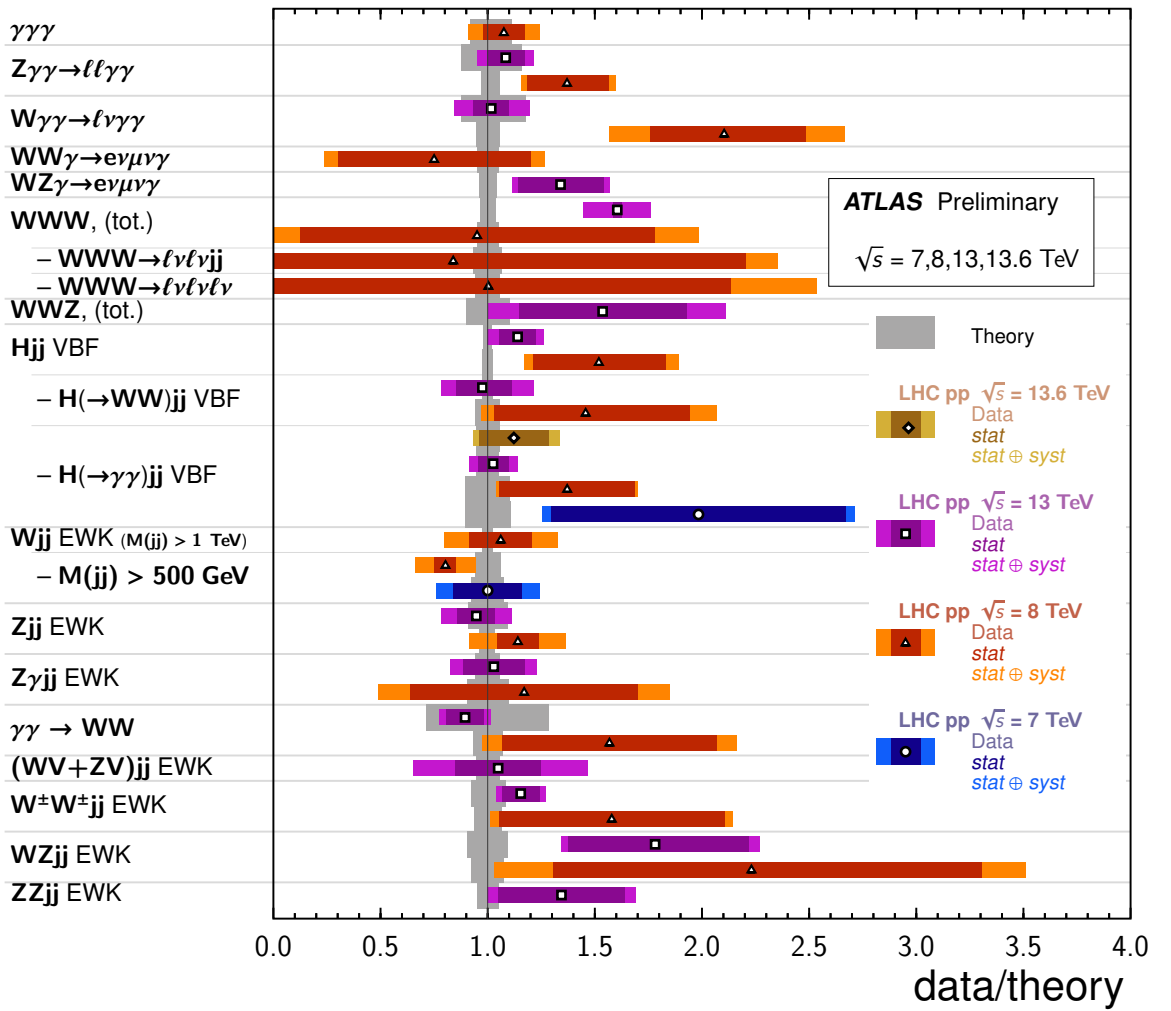


Figure 2.5. Overview data-to-theory ratios for a selection of ATLAS cross-section measurements for VBS, VBF, and triboson production. Measurements of these processes gives rise to an increasingly large body of constraints to quartic electroweak interactions. Figure from [9].

Chapter 3

The LHC and ATLAS Experiment

3.1 The Large Hadron Collider

The Large Hadron Collider [57] (LHC) is a two-ring proton-proton and Pb-Pb ion collider installed into the 27km long LEP tunnel at CERN. The primary discovery goal of the LHC was the observation of the Higgs boson which was achieved in July 2012 [58]. The LHC has two high-luminosity experiments, ATLAS [59] and CMS [60] with a design peak luminosity of $10^{34}\text{cm}^{-2}\text{s}^{-1}$, in addition to TOTEM [61], LHCb [62], and ALICE [63].

The proton source for the LHC is a bottle of hydrogen gas. The hydrogen is ionised by an electric field before they are accelerated to around 50 MeV by Linac 2. The Proton Synchrotron (PS) PS accelerates protons to 25 GeV and provides them as bunches with a 25ns spacing to the Super Proton Synchrotron (SPS). The SPS accelerates the bunches to an energy of 450 GeV. The acceleration of proton bunches in the LHC itself is achieved through the radio frequency (RF) system. The RF system is comprised of 16 RF cavities housed in 4 cryomodules. Each RF cavity delivers an oscillating longitudinal electric field of 5MV/m, delivering an accelerating voltage of 2MV at a frequency of 400MHz. The RF cavities serve two primary purposes, first to accelerate the protons with every pass of the RF system, and second to group the packets of protons from the PS into even tighter bunches, to ensure a high luminosity at the collision points. The proton injection is timed such that the center of a packet of protons is located just after the oscillating field maximum. Hence, protons just before the center of the bunch (closer to the field maximum) will be accelerated more than protons just after the center of the bunch (further from the field maximum). This results in protons away from the center of the bunch to be moved towards the center, creating stable, tight, bunches. The number of possible stable bunches (h) is therefore equal to the number of possible synchronised protons. A proton is synchronised if the RF frequency (f_{RF}) is an integer multiple of the revolution frequency (f_{rev})

$$f_{\text{RF}} = h \times f_{\text{rev}}. \quad (3.1)$$

Therefore dividing the two frequencies gives the number of possible bunches. With $f_{\text{rev}} = c/27\text{km}$ and $f_{\text{RF}} = 400\text{MHz}$, this gives the value of h as approximately 35640. These are called RF buckets. Not every RF bucket is filled, and the number of occupied buckets in the LHC is 2808. Each bunch contains $\sim 1.15 \times 10^{11}$ protons [64–66]. A schematic of the CERN

The CERN accelerator complex Complexe des accélérateurs du CERN

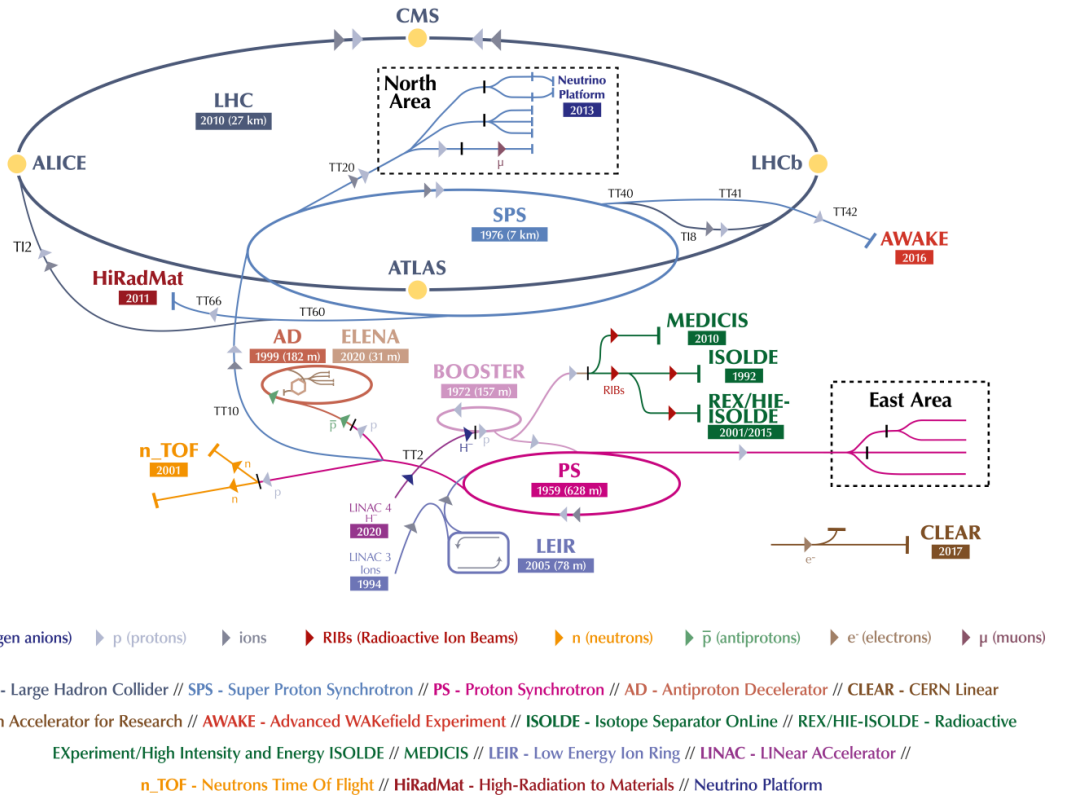


Figure 3.1. The CERN accelerator complex. Figure taken from [67].

accelerator complex is shown in Figure 3.1.

As protons carry electric charge, the particle beam will naturally diverge. In the curved sections of the LHC (arcs), the beam must be focused such that its width and height are constrained to be within the vacuum chamber. At the interaction Points (IPs), to enhance the interaction probability for each bunch crossing, the beams are focussed to a size of $16\mu\text{m}$ in the $x - y$ plane for CMS and ATLAS. The focussing in the arcs is achieved by collections of superconducting quadrupole, dipole, and other multipole magnets organised into twenty-three LHC cells per arc, resulting in a total of 858 quadrupoles and 1232 dipoles. For the 1232 superconducting dipoles to operate reliably at the 8.33T magnetic field required for 7 TeV beams, the magnet system must operate in a bath of superfluid helium at a temperature of 1.9K. Dispersion suppressors, comprised of four quadrupoles separated by two dipole magnets, are located at the boundaries between the beam insertion regions (IRs) and the arcs, and reduce the machine dispersion (momentum spread of particles within a bunch). Reducing the machine dispersion at the IPs to zero requires two additional quadrupole magnets at each side of the arc. The focusing of the bunches at the IP is achieved using 8 sets of superconducting “inner triplet” magnets [64, 68, 69].

3.1.1 Detector Luminosity

The instantaneous luminosity (Equation 2.65) depends on a number of beam parameters, and is given by

$$\mathcal{L}(t) = \frac{N_b^2 n_b f_{rev} \gamma_r}{4\pi \epsilon_n \beta^*}, \quad (3.2)$$

where N_b is the number of particles per bunch, n_b the number of bunches per beam, f_{rev} the revolution frequency, γ_r the relativistic gamma factor, ϵ_n the normalized transverse beam emittance (this reflects the beam quality, and is roughly defined as the smallest opening the beam can be squeezed through), β^* the beta function (the width of the beam, squared, divided by the emittance) at the collision point and F a geometric luminosity reduction factor. The linear dependence on γ_r and square dependence on N_b implies that a large luminosity requires beams of high energy and high intensity. Separate dipole magnetic fields and vacuum systems are required for the two beams, as both beams contain positively charged protons. At the IRs the two beams share a common 126m (for ATLAS and CMS) long beam pipe.

Integrating Equation 2.65 yields the integrated luminosity L

$$L = \int_0^T \mathcal{L} dt, \quad (3.3)$$

which is a measure of how much data has been taken in time T . Equation 2.65 can be written in terms of L as

$$N = \sigma L. \quad (3.4)$$

The luminosity in the LHC is not constant over a physics run. The beam intensities and emittances of the circulating beams degrade primarily due to the collisions themselves, leading to a decay in the luminosity. This is quantified with the luminosity lifetime, τ_L .

The expected integrated luminosity of the LHC of a luminosity run is given by

$$L = L_0 \tau_L (1 - e^{-T_{run}/\tau_L}), \quad (3.5)$$

where the assumption is made that the time for beam injection, ramping up the beam energy, ramping down the magnets, and programmed main systems checks total a turnaround time of $T_{turnaround} \approx 70\text{min}$. Assuming that the LHC is taking data 200 days a year for an optimum run time of 12h, the total maximum luminosity per year is about 120fb^{-1} [64].

The Run-2 total integrated luminosity is shown in Figure 3.2. The Run-2 integrated luminosity recorded by ATLAS with good data quality is 140.1 fb^{-1} [70].

3.1.2 Pile-up

All LHC analyses need to contend with the harsh experimental conditions which come about due to the very large number of interactions per bunch crossing. The mean number of inter-

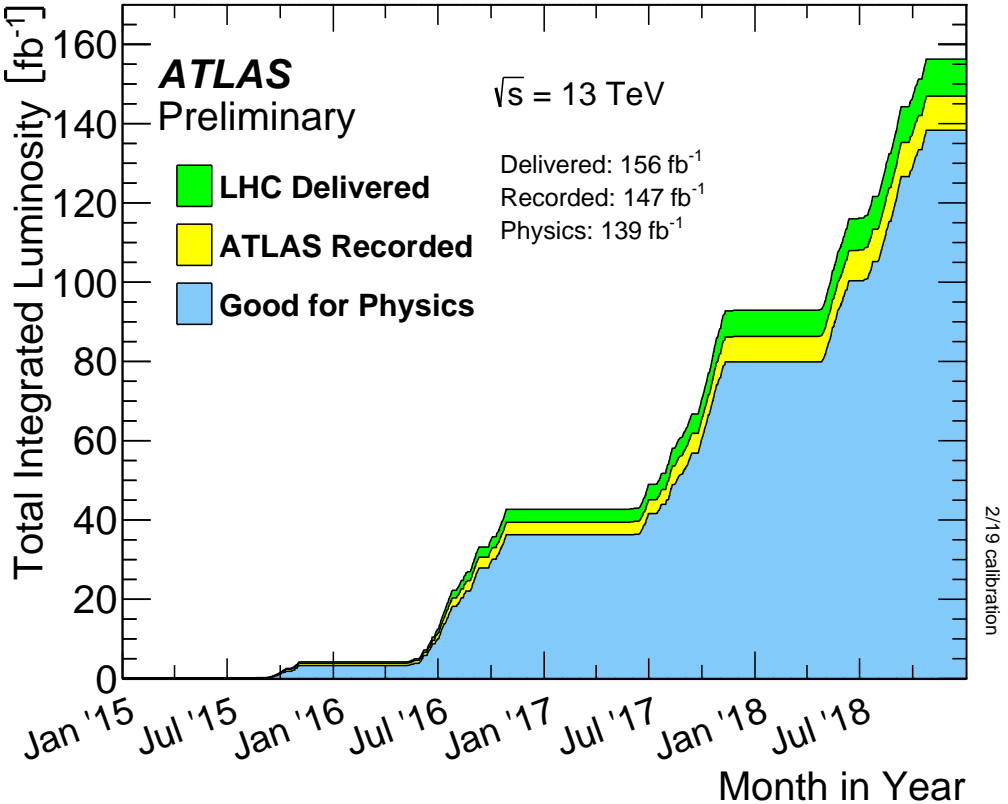


Figure 3.2. The total integrated luminosity for Run-2 versus time. The green curve shows the luminosity delivered to ATLAS by the LHC. The yellow curve shows the luminosity recorded by ATLAS. The blue curve shows the luminosity of the dataset certified to be good data quality. Since this plot has been produced, the most accurate assessment of the total integrated luminosity certified good for physics has been updated to 140 fb^{-1} [70]. Figure from [71].

actions per bunch-crossing (averaged over luminosity) $\langle\mu\rangle$ in Run-2 was $\langle\mu\rangle = 33.7$. The largest momentum transfer happens in the primary hard scatter interaction, all other secondary interactions are referred to as pile-up interactions and consist mainly of soft-QCD processes. There are two types of pile-up. In-time pileup refers to pp collisions from the same bunch-crossing as the interaction of interest, whereas out-of-time pileup refers to pp collisions occurring in bunch-crossings just before and after the interaction of interest.

Pileup is responsible for a large number of soft hadrons distributed throughout the detector. Therefore the reconstruction of jets and Missing Transverse Energy (MET) are especially effected. Without pileup mitigation techniques, the energies of jets will in general be overestimated, and spurious jets not associated with the hard scatter will be included in the event leading to changes in the MET measurement. In addition to these biases, pileup also results in the degradation of the resolution of reconstructed quantities. The reason for this is that the pileup activity itself is not a fixed quantity, which therefore results in fluctuations of the bias due to pileup. The challenges associated with pileup in the context of object reconstruction is discussed in more detail in Section 3.2.6 [19, 72].

3.2 The ATLAS Experiment

The design of the ATLAS detector was initially motivated by the search for the Higgs boson and physics beyond the Standard Model (SM). The challenging experimental conditions at the LHC require fast, radiation-hard electronics and sensors. Large particle fluxes require a good detector granularity. An almost 4π acceptance is necessary to access the rich physics contained in the forward regions, such as the Vector Boson Scattering (VBS) process targeted in this thesis. Excellent electromagnetic (EM) calorimetry is a requirement for accurate electron and photon identification. The need for accurate jet and MET reconstruction dictates the energy resolution requirements for the hadronic calorimeter systems. Muon identification and momentum resolution must be able to determine the charge of high transverse momentum muons. Finally, a highly efficient trigger and data acquisition system is required to be able to select signal events of interest whilst rejecting backgrounds.

Figure 3.3 shows the different nested subsystems of the ATLAS detector. From the IP, the products of inelastic p-p collisions travel outwards through the detector subsystems. The origin of the coordinate system is defined as the IP. The beam direction defines the z -axis, whereas the $x - y$ plane is transverse to the beam direction. The positive x -axis points from the IP to the LHC ring centre, and the positive y -axis points upwards. The azimuthal angle ϕ is measured around the beam axis; and the polar angle θ is the angle from the beam axis. The rapidity is defined (in natural units) as

$$y = 1/2 \ln[(E + p_z)/(E - p_z)], \quad (3.6)$$

where E is the energy, and p_z is longitudinal component of the momentum \mathbf{p} . In the $|\mathbf{p}| \gg m$ limit, the rapidity can be approximated by the pseudorapidity, $\eta = -\ln \tan(\theta/2)$. The distance between two particles i and j can be quantified using a metric, ΔR_{ij} , which combines the rapidity separation $\Delta y_{ij} \equiv |y_i - y_j|$ and the azimuthal separation $\Delta\phi_{ij} \equiv |\phi_i - \phi_j|$

$$\Delta R_{ij} = \sqrt{\Delta y_{ij}^2 + \Delta\phi_{ij}^2}, \quad \Delta R_{ij}^\eta = \sqrt{\Delta\eta_{ij}^2 + \Delta\phi_{ij}^2}. \quad (3.7)$$

The coordinate system used to describe the kinematics of particles detected at the ATLAS detector is represented schematically in Figure 3.4. The three-momentum of the final-state particle is denoted by \vec{p} . The transverse momentum, p_T , is defined by projecting \vec{p} onto the $x - y$ plane and taking the magnitude.

3.2.1 Inner Detector

The Inner Detector (ID) is comprised of three independent sub-detectors contained within a cylindrical envelope in a 2T solenoidal magnetic field. As charged particles travel through the ID, they ionise the material and leave behind a trail of electrical signals which are reconstructed to form tracks through the inner part of the ATLAS detector. The momentum can be inferred with high resolution from the curvature of the tracks. The ID also provides

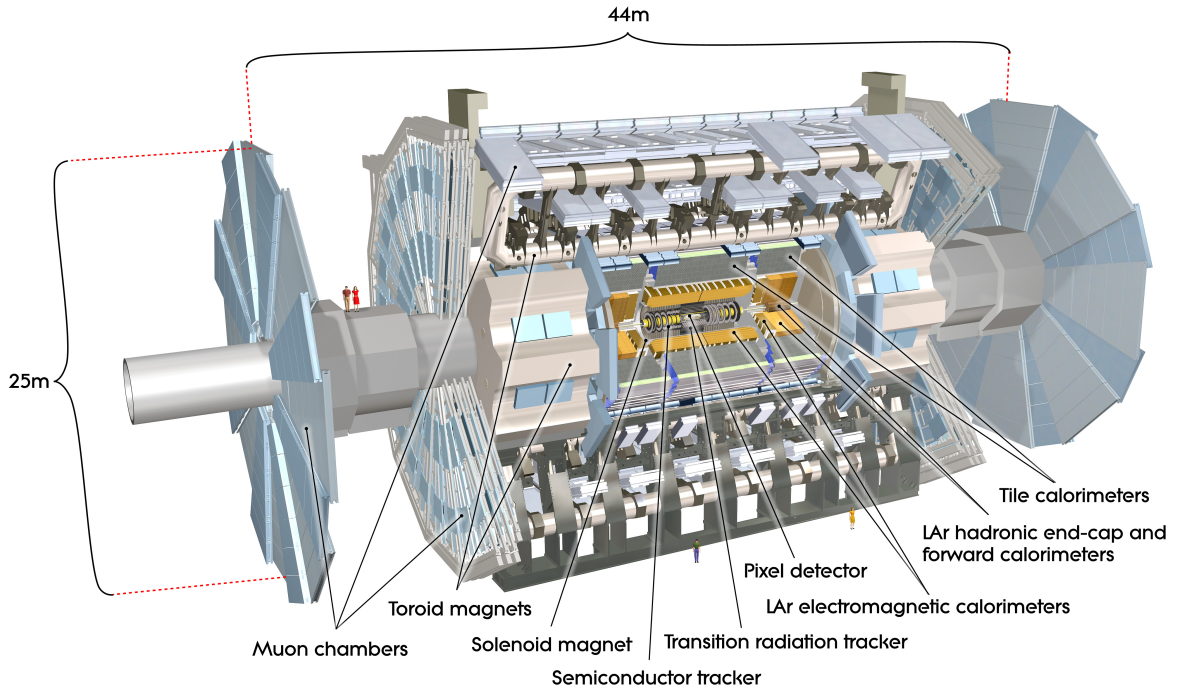


Figure 3.3. A cut-out of the ATLAS detector showing the tracking, calorimeter, muon, and magnet systems. Figure from [73].

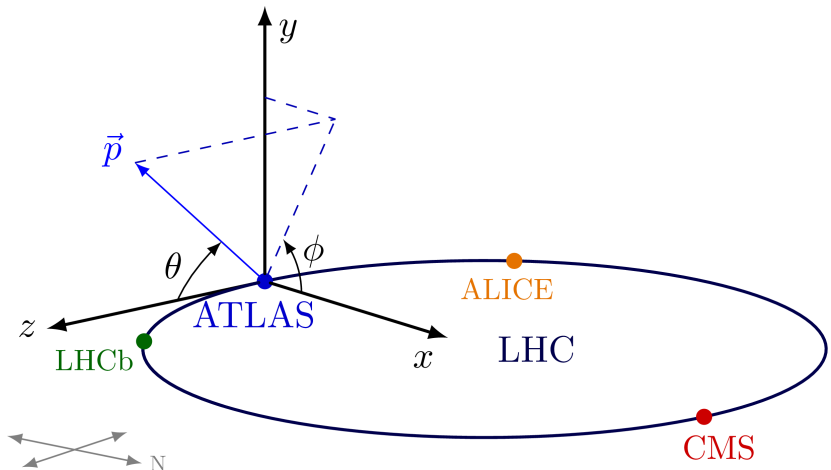


Figure 3.4. The ATLAS coordinate system. Figure from [74].

primary vertex (PV) and secondary vertex measurements (vertices are defined and discussed in Section 3.2.6), and provides electron identification complimentary to the calorimeter. The ID covers the pseudorapidity range of $|\eta| < 2.5$. In order of radial distance from the IP, the subdetectors consist of silicon pixel layers (Pixel detector), silicon microstrip layers (SCT detector), and layers of gaseous straw-tube elements called the Transition Radiation Tracker (TRT detector).

The Pixel Detector

At the inner radii, the highest resolution silicon sensors are required due to the difficulties in resolving tracks close to the IP. As such, the Pixel detector consists of three cylindrical silicon layers with individual sensor elements of $50 \times 400 \mu\text{m}^2$. The Pixel sensor elements are

made up of 16 Front-End (FE) readout ASICS connected to a thin ($250\mu\text{m}$) layer of silicon. When a charged particle travels through one of the pixel sensor elements, silicon atoms are ionised and liberated electrons travel through the bump bonds to the FE electronics. There are 2880 readout cells per FE ASICS chip. The readout cells of the FE amplify the sensor charge signal and compare it to a programmed discriminator threshold. For each readout, the hit pixel address, time stamp and amplitude information is transferred to buffers at the bottom of the FE.

The top of the sensor elements contain a layer of kapton film onto which a Printed Circuit Board (PCB) is mounted containing a number of Surface Mounted Devices (SMDs) such as a temperature sensor, decoupling capacitors, and the Module Controller Chip (MCC). The MCC is responsible for Timing, Trigger and Control (TTC) logic tasks such as rejecting events where there are too many (> 15) hits triggered in the FEs. The MCC is also responsible for extracting ordered hits from the FE and preparing them for transmission out of the pixel module [75].

The Semi-Conductor Tracker (SCT)

The SCT enhances the high-resolution pattern recognition abilities of the ID at high radii, and consists of 4088 modules, arranged in four cylindrical layers in the barrel region and two end-caps, each containing nine disk layers. Each module consists of four sensors, with two sensors each on the top and the bottom side. A hybrid¹ assembly bridges the sensors on each side. The top and bottom sensors are rotated through a relative “stereo” angle. In order to achieve the design azimuthal (the $R\text{-}\phi$ plane) and radial (R) resolutions of $17\mu\text{m}$ and $580\mu\text{m}$ respectively, the sensors are rotated at an angle of 40mrad. The silicon sensors are connected to binary signal readout chips. The readout hybrid on each SCT module contain 12 ASICs, with a total of 1536 readout channels. For each channel, there is a pre-amplifier, signal discriminator, and a shaper (splits each signal into overlapping channels, and applies a filter to optimise the signal/noise ratio). A buffer stores the hit information for approximately $3.2\mu\text{s}$, to allow for the L1 trigger decision (discussed in Section 3.2.4).

The Transition Radiation Tracker (TRT)

The TRT enhances the performance of the ID at large radii, and consists of a barrel section and two end-cap sections. The basic elements of a TRT detector module are 4mm diameter polyimide straw tubes reinforced using carbon fibre bundles which stabilise the straw geometry by providing protection against environmental factors such as humidity and temperature. The straw tube walls are comprised of two multi-layer $35\mu\text{m}$ thick films bonded back-to-back. Each tube contains a $31\mu\text{m}$ diameter positively charged tungsten wire plated with $0.5\text{-}0.7\mu\text{m}$ gold, directly connected to the front-end electronics. The tubes are filled with a mixture of 70% Xe, 27% CO₂, and 3% O₂ gas. The gold plated wires act as anodes, attracting electrons

¹Here, hybrid technology refers to the use of carbon-fibre substrates that have been directly interfaced with thin-film (polyamide) circuits to produce low-mass, thermally conductive, and radiation hard devices [76]

liberated by charged particles and photons interacting with the gas mixture. The films contain a layer of aluminium, ensuring the sufficient electrical conductivity of the tube which acts as a cathode attracting positively charged ions [77].

3.2.2 Calorimeters

The ATLAS calorimetry system consists of electromagnetic (EM) and hadronic calorimeters. These are *sampling* calorimeters, meaning that they are comprised of separate materials for inducing particle showers and for detecting the energy of the particles. Due to superior energy resolution, the energy measurements of most charged and neutral particles are provided by the calorimeters (rather than the tracking system). The electromagnetic calorimeters primarily make measurements of electrons and photons. The energy measurements of hadrons are primarily derived from signals in the hadronic calorimeter system.

The EM Calorimeters

The EM barrel and end-cap calorimeters have an accordion geometry and are comprised of lead and stainless-steel absorbers, LAr active material, and copper readout electrodes, which are positioned in the gaps between the absorbers. There are three active layers in the central region ($0 < |\eta| < 2.5$), and two in the forward regions ($2.5 < |\eta| < 3.2$). The first layer is read out front, which is defined as the inner radius of the EM barrel, and the small- z region of the end-cap. Conversely, the second and third layers are read out from the back. The barrel EM calorimeter is made up of two halves covering $|\eta| < 1.475$. The cell granularity in $\Delta\eta \times \Delta\phi$ is $0.025/8 \times 0.1$, 0.025×0.025 , and 0.050×0.025 in the first, second, and third layers respectively, for $|\eta| < 1.40$. In the $|\eta| > 1.40$ region, the cell granularity is significantly coarser. The end-cap regions cover the $1.375 < |\eta| < 3.2$ range. The cell granularity in this region is the finest in the central part of the coverage range. The first layer has a granularity of $0.025/8 \times 0.1$ at $1.5 < |\eta| < 1.8$, and the granularity becomes coarser towards the limits of the end-cap coverage. There is a crack region at $1.37 < |\eta| < 1.52$ where the transition between the barrel and end-cap calorimeters takes place. There is also a small crack at $|\eta| = 0$ due to the fact that the calorimeter half-barrels are separated by 6mm at $z = 0$.

When electrons and photons interact with the stainless-steel absorbers, narrow particle showers are produced as a result of a combination of bremsstrahlung, $e^\pm \rightarrow e^\pm\gamma$, and $\gamma \rightarrow e^+e^-$. Repeated interactions of the produced particles results in a cascade of particles with decreasing energy, which continues up until the pair production energy threshold. Below this threshold, photon energy losses occur primarily via compton scattering and the photo-electric effect, and the shower ceases. The characteristic amount of matter traversed by a particle before undergoing bremsstrahlung or pair production is the radiation length X_0 , which is used to quantify the amount of material used in the calorimeter layers. The expectation values of the energies of the electrons $E(x)$ and intensity of the photons $I(x)$ in the shower follow

exponential decay laws, with the decay constant determined by the radiation length

$$\langle E(x) \rangle = E_0 e^{-\frac{x}{X_0}}, \quad \langle I(x) \rangle = I_0 e^{-\frac{7}{9} \frac{x}{X_0}}, \quad (3.8)$$

where x is the distance of the traversed material. The EM calorimeters are complemented by pre-samplers which provide measurements of energy losses incurred by particles in the inner detector, i.e. before they interact with the calorimeter material.

The Hadronic Calorimeters

Hadrons interact with the nuclei of the absorbers via the strong force, resulting in the production of hadrons, especially pions. Each hadron undergoes additional interactions to form a cascade. Through nuclear de-excitation, lower energy neutrons, protons, α -particles and photons are also produced. The hadronic shower also has a substantial electromagnetic component, which comes about primarily due to the decays of neutral pions [78]. Hadronic showers are characterised by the nuclear interaction length λ , which is a function of the inelastic cross-section of the scattering process. Nuclear interaction lengths are typically an order of magnitude larger than radiation lengths, which explains why the ATLAS hadronic calorimeter system is larger than the EM calorimeter system [19].

Hadronic showers represent a number of challenges. There are a considerable number of sources of energy leakage, such as backscattering and nuclear excitation processes, which do not result in an observable signal. In this way, the ATLAS calorimeter system is *non-compensating*. This means that the calorimeter response (the ratio of the average calorimeter signal to the energy of the particle) is smaller for non-EM components of hadron showers than for EM components. Additionally, there are large fluctuations in the fraction of the EM and non-EM components of the larger hadronic shower. All of this degrades the hadronic energy resolution.

The three hadronic calorimeters correspond to the Tile, the Hadronic End-Cap (HEC), and the Forward Calorimeters (FCal). The Tile calorimeter is comprised of an array of steel absorbers and scintillator sheets as the active medium. The Tile calorimeter comprises three layers, and covers the region $|\eta| < 1.7$, behind the EM calorimeter, and has a radial depth of about 7.4λ . The $\Delta\eta \times \Delta\phi$ cell granularity in the first two layers is 0.1×0.1 , and 0.2×0.1 in the last layer. The scintillator signals are read out by photomultiplier tubes coupled to each tile edge through a series of fibres. The Tile calorimeter has a total of 187456 readout channels [59].

The HEC calorimeter uses copper as the absorber and liquid-argon as the active material. The HEC comprises four layers, which cover the range $1.5 < |\eta| < 3.2$. The HEC calorimeter has a radial depth of about 9.7λ . The $\Delta\eta \times \Delta\phi$ cell granularity is 0.1×0.1 at $1.5 < |\eta| < 2.5$, and 0.2×0.2 at $2.5 < |\eta| < 3.2$. The gaps between the plates that comprise the HEC modules contain the readout modules, which are made up of three electrodes separated by honeycomb spacers. The central electrodes contain readout cells of size $\Delta\eta \times \Delta\phi = 0.1 \times 0.1$ in the $|\eta| < 2.5$ region and 0.2×0.2 for larger values of $|\eta|$. The HEC calorimeter contains 5632

readout channels [59, 79].

The FCal extends the calorimeter coverage into the forward regions ($3.1 < |\eta| < 4.9$), and has a radial depth of about 10λ . The FCal comprises one electromagnetic module (FCal1) and two hadronic modules (FCal2, FCal3). The $\Delta\eta \times \Delta\phi$ cell granularities are 3.0×2.6 , 3.3×4.2 , and 5.4×4.7 in the central cells of the FCal1, FCal2, and FCal3, respectively, and the granularities are around four times finer around the coverage limits. Copper is used as the absorber for FCal1 to optimise the energy resolution of measurements of EM showers, and tungsten is used as the absorber in FCal2 and FCal3 to contain the lateral spread of hadronic showers. Each of the FCal modules contain readout electrodes which are connected to the module faces. Signals are read out from the side nearer to the interaction point for FCal1, and from the side furthest from the interaction point for FCal2 and FCal3. The FCal calorimeter contains 1762 readout channels [59].

Energy Resolution

The energy resolution defines the most important attributes of the ATLAS calorimeter system and is often quoted as follows

$$\frac{\sigma(E)}{E} = \frac{a}{\sqrt{E}} \oplus \frac{b}{E} \oplus c\%, \quad (3.9)$$

where \oplus denotes addition in quadrature. The a term is the *stochastic* term, which primarily arises due to fluctuations in the number of particles produced in the shower. This term limits the low-energy performance of the calorimeters. The b term describes electronic noise primarily from readout electronics, and the c term is a constant term which dominates in the high energy limit. Measurements of the calorimeter energy resolutions are made using lepton and hadron test-beams. Results from these measurements are shown in Figure 3.5. Note that for the LAr energy resolutions results using electron test-beams are fitted with equation 3.9, without the $\frac{b}{E}$ term. This is because a noise-subtraction step is implemented for every energy measurement since the noise here depends on the gain of the LAr calorimeter cells. The pion test-beam results for the combined calorimetry shown in Figure 3.5 utilises the full functional form of equation 3.9.

3.2.3 Muon Spectrometer

The muon spectrometer (MS) covers the pseudorapidity range of $|\eta| < 2.7$. The MS measures charged particles (primarily muons) that penetrate the barrel and end-cap calorimeters. The primary purpose of the MS is to identify and measure high momentum muons. The MS is designed to measure the transverse momentum of muons with $p_T > 1 \text{ TeV}$ to an accuracy of 10%. The MS is also capable of triggering on muon tracks, and is designed to trigger in the region of $|\eta| < 2.4$. The precision momentum measurements of the MS system are provided by Monitored Drift Tube (MDT) chambers and Cathode-Strip Chambers (CSC).

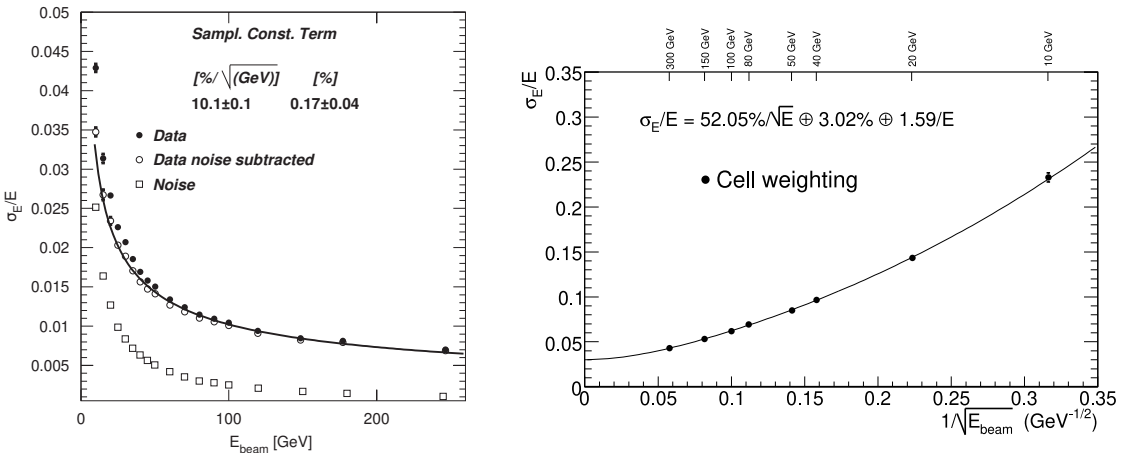


Figure 3.5. Fractional energy resolution in the ATLAS EM barrel calorimeter as a function of the beam energy obtained from electron test-beams at $|\eta| = 0.687$ (left). Fractional energy resolution obtained using pion test beams for combined LAr and tile calorimetry at $|\eta| = 0.25$ (right). The energy resolution for pion test-beams is shown as a function of $1/\sqrt{E_{\text{beam}}}$. Markers corresponding to E_{beam} are shown at the top of this plot for the ease of comparison. 100 GeV electrons have an energy resolution of about 1.1% in the central region of the calorimeter system, compared to about 6.2% for hadrons. Note that in regions where the forward calorimetry (FCal) system is in use ($3.1 < |\eta| < 4.9$), the energy resolution increases to about 5% for 100 GeV electrons, and to about 8% for 100 GeV pion test-beams [59, 80].

This is complemented by Resistive Place Chambers (RPC) and Thin Gap Chambers (TGC) which provide fast triggering capabilities to clarify events of interest.

The MS is partitioned in the barrel and endcap regions into three layers referred to as the inner, middle, and outer layers. Two MDT chambers are housed in each of the layers. There are a total of twelve MDT segments in radially consecutive stations (collection of segments in a layer) spanning three layers. The CSCs are located in the inner endcap layer. Both the CSCs and MDTs are segmented into large and small chambers. The RPC system is layered into three trigger stations and is comprised of large and small small segments. The RPCs are located in the middle and outer layers of the barrel. The TGC system is comprised of seven layers in the EM layer, and two layers in the inner endcap layer.

The MDTs cover the pseudorapidity range of $|\eta| < 2.7$ in all but the inner most layer. The MDTs are drift tubes with a diameter of about 3cm, and are pressurised with a mixture of Ar and CO₂ gas. The centers of the tubes contain a 50 μm diameter tungsten-rhenium wire. When a charged particle enters the tube, the gas is ionised, and liberated electrons drift to the wire and the ions drift to the walls of the tube.

The MDTs provide a position resolution of 80 μm . The position measurements are determined by the drift time of the charges deposited in the MDTs. Muon tracks are reconstructed using these measurements, and this is discussed in more detail in Section 3.2.6. The p_{T} of the muon is directly inferred from the radius of curvature of the tracks. For the required momentum resolution, a sagitta ² along z of about 500 μm needs to be known with a resolution better than 50 μm .

The CSC system covers the forward $2 < |\eta| < 2.7$ region. The CSC system are two disks of eight wire chambers. Each chamber is filled with an ArCO₂ gas mixture and contains an

²The perpendicular distance between the apex of the arc of the track, and the chord intersecting the inner and outer layers of the MDT.

array of high voltage anode wires and cathode planes at ground potential. Precision position measurements in both R and z are obtained with a resolution of $60\mu m$ via measurements of the charge distributions on the cathodes.

The muon trigger system consists of RPCs and TGCs. The RPCs are used in the barrel region ($|\eta| \leq 1.05$), and TGCs in the end-cap region ($1.05 \leq |\eta| \leq 2.4$). Different technologies are used in different regions due to different requirements on spatial and timing resolution as well as considerations of trigger rate. The RPCs are gaseous parallel electrode-plate detectors. These are comprised of two parallel dielectric plates separated by 2mm. In the 2mm gap is a gas mixture, and a high electric field is applied (4kV/mm) between the plates. When a charged particle travels through the gas gap, the gas is ionised, and the positive ions travel towards the cathode, and the electrons towards the anode. The liberated electrons are accelerated by the high electric field to a sufficient extent such that they go on to liberate additional electrons from the gas medium resulting in a chain reaction of ionisation events. This process is known as a Townsend avalanche [81]. The electrical signals from the avalanches are read out via metallic strips mounted on the outer faces of the resistive dielectric plates. TGCs operate on the same principle as the wire chambers of the CPC. The primary function of the RPCs and TGCs are to facilitate triggering on muon events, but they also complement the MDT tracking data. Through the additional measurement of the track coordinates in the non-bending ϕ plane, which complement the measurement in the bending η plane, the MDT and RPC (and TGC in the end-cap region) measurements can be combined in an unambiguous way [59, 82].

3.2.4 ATLAS Trigger and Data-acquisition

The ATLAS trigger and data-acquisition (TDAQ) system is responsible for deciding which events from of the 40×10^6 bunch-crossings per second at the ATLAS interaction point to save for physics analyses, calibrations, monitoring, and performance measurements. The trigger system is comprised of two stages. These are the Level-1 (L1) and HLT triggers.

The hardware based Level-1 trigger is principally responsible for making the trigger decision to reduce the event rate from 400MHz to maximally 100kHz by processing signals from the calorimeters and MS. The L1 trigger consists of the L1Calo, L1Muon, L1Topo, and Central Trigger subsystems. The L1Calo comprises the Cluster Processor (CP) and Jet/Energy-sum Processor (JEP), which receive calibrated calorimeter signals in parallel to identify physics object candidates. Tile calorimeter and MS information is passed to the L1Muon, where searches are performed for signals consistent with muons originating from the interaction point. The L1Topo receives object candidates from the L1Calo and L1Muon in order to reconstruct topological observables such as invariant masses and angular observables. The outputs from the L1Calo, L1Muon and L1Topo are processed by the Central Trigger Processor (CTP) which makes the L1 trigger decision. The CTP is also responsible for applying a preventative *dead-time* mechanism to moderate the L1 accept rate. For every L1 trigger decision, “Regions Of Interest” (RoIs) are identified using η and ϕ information [19, 83, 84].

After a L1 trigger accept, the events are processed by the software-based High-Level Trig-

ger (HLT). Events processed by the HLT use fine-granularity calorimeter and precision MS information, as well as tracking information from the ID. The HLT performs the event reconstruction within the L1 RoIs or the full detector, as needed. In most cases, the HLT performs a fast first-pass reconstruction using a sequence of *feature-extraction* algorithms. A trigger decision is then subsequently made by the *hypothesis* algorithms. Afterwards, more precise and computationally expensive algorithms reconstruct high level physics objects in greater detail – this is called the *online reconstruction*. The online reconstruction of objects is less precise, but nevertheless similar to the offline reconstruction (Section 3.2.6). Events passing the HLT decision are saved to the CERN Tier-0 computer centre for offline reconstruction, this occurred at a rate of approximately 1.2kHz during the 2018 data taking for Run-2 for triggers dedicated to physics analyses [83, 85].

Each combination of L1 and HLT event selections has an associated set of *prescale* factors, which take values of at least 1. A prescale value of n means that an event has probability of $1/n$ of being kept. Prescales are defined for both L1 and HLT, but the prescale is implemented slightly differently in each case. For L1 prescales, since the CTP is fast, the trigger decision is still computed for every event, but for each event that passes the trigger decision, a random number generator determines whether it is passed to the HLT. Since the online reconstruction is expensive, HLT prescales are applied before the trigger decision is computed. The reason for applying prescales is to prevent saturating the allowed bandwidth. This is possible for certain processes, such as minimum bias, which have very loose triggers and therefore very high event rates [19].

A combination of L1 and HLT prescales and event selections comprises an item in the *trigger menu*, which consists of a list of:

- *Primary* triggers: used for physics analyses, usually unprescaled.
- *Support* triggers: used for monitoring, performance, and efficiency measurements. These are usually prescaled, and have small HLT rates of around 0.5Hz
- *Alternative* triggers: used in the commissioning of new triggers. These use alternative reconstruction algorithms, and are complimentary to primary triggers
- *Backup* triggers: used in case CPU usage or output rate of primary triggers too high. These are similar to primary triggers but with tighter selections.
- *Calibration* triggers: used for detector calibrations, and run at high rates.

All items in the trigger menu are connected to an HLT data stream. The *Main* physics stream contains events for physics analyses, and a small fraction of these events are written to the *Express* stream which is used to derive offline calibrations soon after data taking. There are about twenty additional streams for calibration, monitoring and detector performance studies in addition to specialised *Trigger-Level Analysis* and *debug* streams. The physics *Main* stream events are partitioned into categories called trigger signatures, for example “single leptons”. Each trigger signature is split up into multiple items giving the L1 and HLT trigger

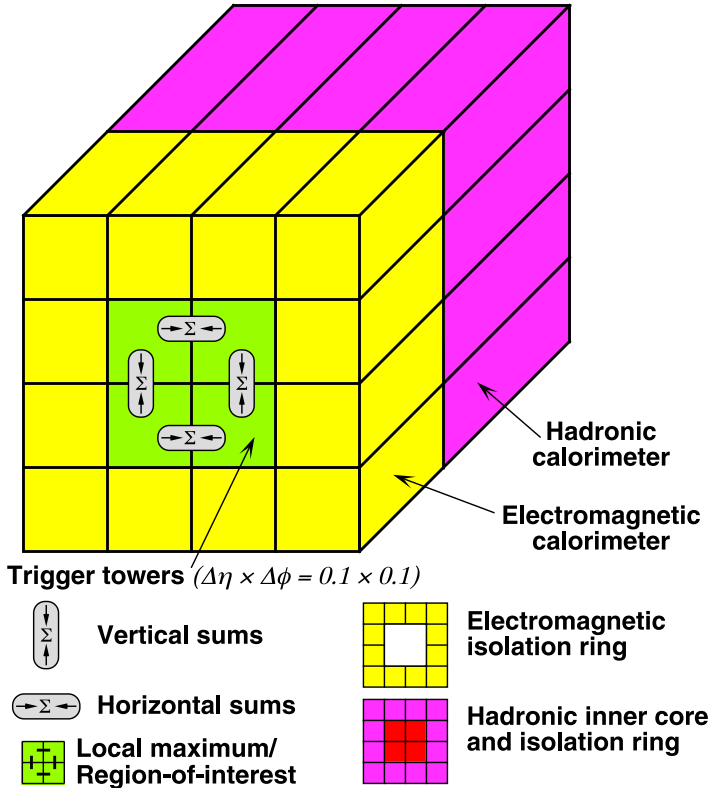


Figure 3.6. Layout of the trigger towers used in the L1 trigger electron and photon reconstruction. The EM calorimeter cells are colored in yellow, and the magenta cells denote the hadronic calorimeter cells. Figure from [85].

thresholds, object multiplicities, online object isolation requirements, as well as peak trigger rates. For example, for an offline selection of a single isolated muon with $p_T > 27 \text{ GeV}$, the corresponding trigger in the 2018 trigger menu corresponds to a 20 GeV single muon requirement at L1, a 26 GeV isolated muon at HLT, with a peak L1 trigger rate of 16kHz, and peak HLT trigger rate of 218kHz. The values of the offline p_T values in the trigger menu are usually defined as the value where the trigger efficiency³ plateaus [87].

Photon and Lepton Triggers

Electron and photon candidate RoIs are identified in the L1 trigger using only calorimeter information in the central ($|\eta| < 2.5$) region. The identification works by iterating over groups of EM calorimeter cells, called “trigger towers”, of size 2×2 ($\Delta\eta \times \Delta\phi = 0.1 \times 0.1$). Within each 2×2 region, the E_T of all the four possible 1×2 and 2×1 pairs of towers is calculated. If the maximum E_T among these pairs passes the L1 E_T threshold (nominally 22 GeV), the 2×2 region is identified as an ROI. An additional hadronic activity veto can be applied, where candidates are rejected if the 2×2 hadronic calorimeter trigger towers behind the EM cluster have an E_T above a given threshold. An isolation requirement can also be defined by a threshold on the energy of the EM isolation ring around the 2×2 ROI. Figure 3.6 shows a schematic view of the EM and hadronic trigger towers [85, 88].

The reconstruction of electrons and photons at the HLT is performed in each ROI identified

³The trigger efficiency is the number of correctly identified objects divided by the actual number of objects above a certain p_T threshold. At the LHC, typically trigger efficiencies of $> 90\%$ (10% accuracy) are deemed acceptable [86].

by the L1 trigger. For the fast stage of the HLT decision, a cut-based algorithm is used for electrons below 15 GeV and for the reconstruction of all photons. Objects are identified based on the E_T of the cluster and the shape of the EM shower. After the initial fast HLT decision, information from outside the ROI may be used, and the precision online-reconstruction is performed in a similar manner to the offline electron and photon reconstruction outlined in Section 3.2.6.

At the precision stage, there are optional requirements on the calorimeter-only isolation used in the photon triggers denoted by *icalvloose* or *icaltight* in the trigger menu. These operating points differ in the size requirements of the isolation cone around the photon candidate used for noise subtraction, and in the fraction of topo-cluster energy required to originate from the photon candidate. For the noise subtraction, the *icalvloose* working point uses a cone size of $\Delta R = 0.2$, and *icalvloose* uses $\Delta R = 0.4$. The ratio of the total topo-cluster E_T to the photon-candidate E_T is required to be $< 10\%$ for *icalvloose* and $< 3\%$ for *icaltight*.

For identifying electrons at the precision stage, a likelihood discriminant is constructed in a similar way to the offline-reconstruction. The likelihood discriminant operating points are: *lhvloose*, *lhloose*, *lhmedium*, and *lhtight*. For some electron triggers, the transverse impact parameter d_0 , and its significance $|d_0/\sigma(d_0)|$ are not used in constructing the online discriminant. Such triggers are labelled with the suffix “nod0”. A tracking-only isolation requirement called *ivarvloose* is also available for electron triggers [88].

3.2.5 Data Processing

What happens upstream of the offline physics object reconstruction steps is different depending on whether real collider data or simulated event generator data is being processed. With real data, particles interact with the ATLAS subdetectors, and the data are retrieved from the detector readout hardware, after the Level1 and HLT trigger decisions, through the DAQ system. These raw signals are then passed through the offline reconstruction algorithms. For the case of simulated data, a detector simulation is used on the information from the MC event generator event record. ATLAS makes use of the GEANT4 [89] program to perform this step. The output from this step is a collection of simulated energy deposits in the detector, called “hits”. The raw hit information cannot be used to reconstruct physics objects, as these algorithms rely on information from the detector subsystem readout electronics. The process of “digitization” turns the hits into simulated detector responses (digits), which correspond to the electrical signals from the readout system.

After the building of physics objects via the offline reconstruction step, the output is a highly detailed collection of event data containing the physics objects as well as information pertaining to the raw detector readout or digits in the case of simulated events. This is called Event Summary Data (ESD). ESD is not used directly in a physics analysis. Instead, a reduced format called Analysis Object Data (AOD) provides the necessary physics object information. Since different analyses and calibrations have varying needs for information on the reconstructed objects, the AODs require filtering into smaller subsets which are actually used at an

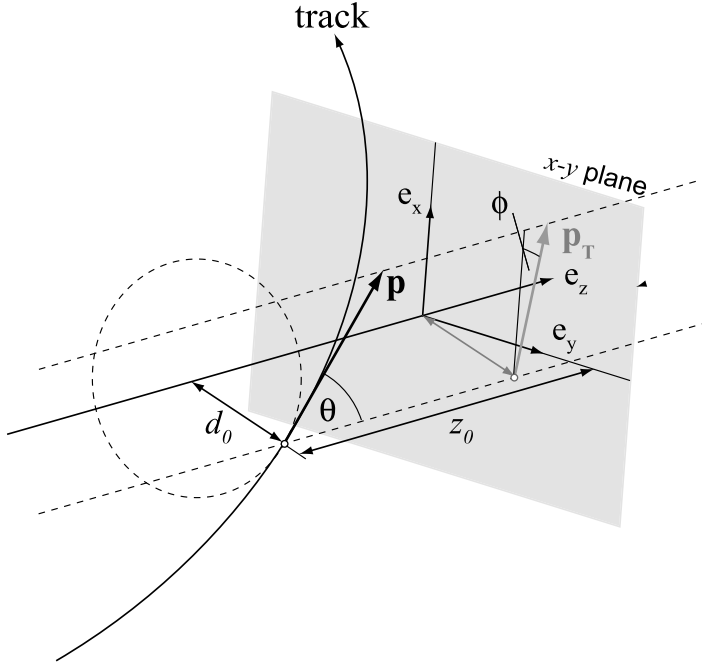


Figure 3.7. Schematic of the track coordinates defined using the perigee of the track. Figure from [90].

analysis level. These subsets are called derived AODs, or DAODs (also “derivations”). At ATLAS, each combined performance and analysis subgroup have their own set of DAODs which are targeted at specific calibrations or physics analyses. The following terms are often used in the context of derivation production:

- **Skimming:** where physics object cuts and trigger requirements are used to remove events.
- **Slimming:** the removal of unrequired computed quantities.
- **Thinning:** the removal of containers of physics objects [19].

3.2.6 ATLAS Object Reconstruction

Tracks and primary vertices

Tracks are described by five parameters relative to a reference point, as shown in Figure 3.7. The transverse and longitudinal impact parameters (d_0 and z_0) are defined using the perigee (point of closest approach) of the track relative to the reference point. d_0 and z_0 are then the transverse and longitudinal distances of the perigee to the reference point, respectively. The other three parameters are the angles ϕ and θ , which are the azimuthal and polar angles of the track momentum relative to the reference point, and the ratio $\frac{q}{|\mathbf{p}|}$, which is the ratio of the electric charge divided and the magnitude of the track momentum. The reference point for track reconstruction is defined as the “beamspot” position, i.e. the average position of the pp interactions. See Figure 3.7 for a schematic view.

Track reconstruction is partitioned into a primary tracking chain of algorithms followed by a back-tracking chain. The primary tracking chain starts with track seed formation. Track

seeds consist of a triplet of space-points (SP) in the pixel or SCT layers, which are consistent with originating from a charged particle track. Next, for each seed, a set of detector modules in the path of the track are identified. The seeds are extended using SCT and pixel clusters contained within those modules using a Combinatorial Kalman Filter [91]. This results in a set of potentially overlapping track candidates. Fake tracks also are reconstructed, which are incorrect combinations of unrelated pixel and SCT clusters [92].

A dedicated ambiguity resolution step is performed to reduce contributions from fake tracks. In this step, a score is given to each track candidate based on a number of criteria, and lower quality candidates are rejected if there are a large number of shared hits with higher quality tracks. After the ambiguity resolution, a global χ^2 fit is performed to obtain the final track parameters. Finally, if an extension of the track into the TRT is possible, tracks are extended, and a re-fit of the entire track is performed. For electron and converted photon tracks, there is an additional refitting procedure using a “Gaussian-sum Filter” (GSF) which is a generalisation of the Kalman filter. The GSF method takes into account non-linear effects related to bremsstrahlung [93].

To increase the acceptance of the tracking to particles produced away from the beamline, such as electrons originating from photon conversions, tracks are reconstructed from the outside-in (seeded by the TRT) using detector hits not already associated with tracks from the primary pass. To avoid large contributions from falsely reconstructed tracks backtracking is only performed in regions seeded by energy deposits ($E_T > 6$ GeV) in the EM calorimeter [94].

With the mean number of interactions per bunch-crossing being $\langle \mu \rangle = 33.7$ for Run-2 [95], precisely identifying the specific pp interactions, called primary vertices ⁴, is an important task. An iterative vertex finding algorithm, which takes all tracks as input parameters, is used for vertex reconstruction. The hard-scatter vertex is usually identified amongst many pileup vertices as the vertex which has the largest $\sum p_T^2$ of contributing tracks. The assumption here is that the charged particles produced in the hard-scatter interaction have a harder p_T spectrum than those produced in pile-up interactions [94, 97].

Electrons and Photons

Electrons and photons can be identified by the presence of a shower in the EM calorimeter. The showers of electrons and photons are almost indistinguishable, since electrons emit photons through bremsstrahlung, and photons produce electron-positron pairs. However, since the ID only responds to charged particles, photons and electrons can be distinguished through the presence or absence of a track.

Electrons are experimentally defined as objects consisting of a cluster built from energy deposits in the calorimeters and one or more matched tracks. Converted photons are defined as calorimeter clusters matched to a photon conversion vertex. Unconverted photons are defined as clusters without either a matched conversion vertices or an electron track.

⁴“Primary” refers to pp interactions. Secondary vertices are defined as the spatial locations of hadronic interactions from primary (pp) collision products. From here on, the term “vertex” will be used to refer to a primary vertex [96].

Electron and photon reconstruction starts with a topological cluster (topo-cluster) formation algorithm. Topo-clusters are topologically connected collections of EM and hadronic calorimeter cells, calibrated at the EM scale⁵. The algorithm starts with the formation of seed cells, which are required to have a cell energy of at least four times the expected cell noise. Neighbouring cells are then connected if the cell energies are at least twice the expected cell noise. These clusters of cells then go on to become the seed cells for the next iteration, and proto-clusters are merged if they share cells. In the final splitting step, proto-clusters are split into separate clusters if they contain two or more local maxima ($E_{\text{cell}} > 500 \text{ MeV}$ and ≥ 4 neighbours with a smaller signal).

Topo-clusters contain both EM and hadronic calorimeter cells, however, only the energy measured from cells in the EM calorimeter are used for photon and electron reconstruction. Energy measurements in the hadronic calorimeter are still important, however, since they are used to quantify the fraction of the EM calorimeter energy to the total cluster energy, f_{EM} . Topo-clusters with $f_{\text{EM}} > 0.5$ are called EM topo-clusters. Each topo-cluster is interpreted as a massless pseudo-particle, and the energy and momentum components are calculated from the cluster energy at the EM scale and the angular coordinates of the cluster. The reason for defining clusters as massless is because there is no physically meaningful mass without a corresponding particle hypothesis for the origin of the signal [98]. The reconstruction is finalised with the matching of tracks and conversion vertices to clusters using a ΔR criteria [99].

After reconstruction, electrons and photons are calibrated to account for energy losses in material upstream of the calorimeter, energy deposited outside of the clusters, and energy losses beyond the EM calorimeter. The electron/photon energy scale⁶ is determined in a calibration chain, where the response of electrons and photons is derived from simulated samples [100, 101]. After the simulation-based correction is applied, additional corrections are derived using data to account for response variations not included in simulation, and non-linear behaviour of the electronics [102]. Finally, a residual energy scale correction factor, called the in-situ calibration, is applied to data so that it agrees with the expectation from simulation. Additionally, a correction factor is applied to simulation so that the energy resolution agrees between data and simulation. These factors are derived using the m_{ee} invariant mass distribution in $Z \rightarrow ee$ events, where a χ^2 minimisation simultaneously solves for the energy scale and resolution parameters in bins of η . For photons, there is an additional correction to account for the mis-modelling of out-of-cluster leakage. This is only derived for photons since the mis-modelling is found to be lower than 0.1% for electrons. The photon energy scale calibration is cross-checked using $Z \rightarrow ee\gamma$ decays, and the electron energy scale is validated with $J/\psi(c\bar{c}) \rightarrow ee$ events in data [101, 102]. The calibration chain used for correcting the full 140 fb^{-1} Run-2 dataset is shown as a schematic in Figure 3.8.

Electrons and photons can be mimicked by other objects, particularly jets, converted photons

⁵The EM Scale is derived using electron test beams and is defined as the mean calorimeter response measured as the ratio of de-positioned charge to test-beam energy. The EM scale therefore corrects the measured calorimeter signal to the correct energy for EM showers.

⁶The energy scale is numerical factor that corrects the measured energy to that of simulated truth particles as a function of η and E_{T} or p_{T} .

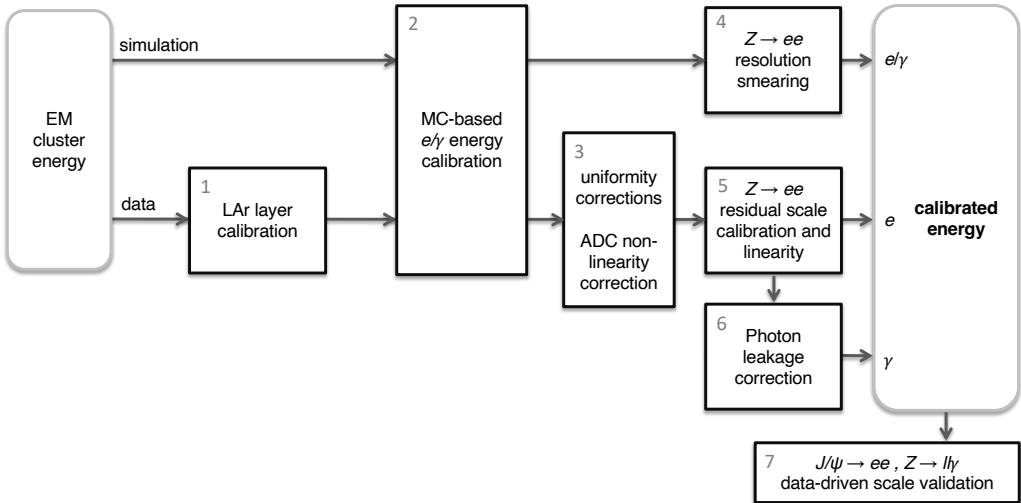


Figure 3.8. The e/γ calibration chain used to correct the full Run-2 ATLAS dataset. Figure from [102].

and heavy-flavour hadron decays. It is actually very rare for a jet to be collimated in addition to being almost entirely contained in the EM calorimeter [100]. After reconstruction and calibration, identification algorithms based on shower shape variables are calculated to separate prompt⁷ electron/photons from jets. These variables quantify the degree to which the shower is collimated (the lateral shower development), how deep the shower penetrates the calorimeters (the longitudinal shower development), and in the case of electrons, the spatial compatibility of the track with the cluster.

Prompt electrons entering the central region ($|\eta| < 2.47$) of the detector are selected using a likelihood-based (LH) identification (ID) discriminant [99]. By cutting on values of this discriminant, a given electron candidate can pass or fail *Tight*, *Medium*, *Loose*, or *VeryLoose* ID criteria. An electron satisfying a tighter working point has lower reconstruction efficiency but is more likely to correspond to a prompt electron. The likelihood discriminant is determined from signal and background probability density functions (pdf⁸). The signal pdfs are derived from $Z \rightarrow ee$ and $J/\psi \rightarrow ee$ events with a strict requirement on one of the reconstructed electrons and a very loose requirement on the other electron. The background pdfs are derived in a dijet enriched, prompt electron deficient fiducial region.

For photon identification within the region of $|\eta| < 2.37$, $1.37 < |\eta| < 1.52$ excluded, a cut-based, selection is implemented. Photon ID criteria are designed to select prompt, isolated photons, and reject backgrounds from jets. Eleven shower shape variables are used to define *Tight*, *Medium*, and *Loose* (the latter two are used in the trigger) working points. Additionally,

⁷The definition of a prompt lepton are those not from hadron decays. Prompt photons are those not from hadron or τ lepton decays [103].

⁸pdf refers to probability density function, and PDF (capitalised) refers to parton distribution function.

there are multiple photon ID working points for variations of the *Tight* selection, where a number of shower-shape variable cuts have either been removed, or relaxed. These are called *LoosePrime2-5*. These working points are useful for estimating systematic uncertainties on non-prompt photon estimates [99, 100].

The degree to which reconstructed electrons or photons are surrounded by other particles can be quantified using calorimeter or track based isolation variables. The calorimeter-based isolation energy ($E_{\mathrm{T}}^{\mathrm{coneXX}}$) is calculated by summing up the energy of topo-clusters whose barycentre⁹ falls within a fixed-size cone of size ΔR of the EM particle cluster barycentre ($E_{\mathrm{T},\mathrm{raw}}^{\mathrm{isolXX}}$), and subtracting the energy contributed by the electron or photon which is taken to be a fixed $\Delta\eta \times \Delta\phi = 5 \times 7$ cluster around the barycentre of the EM particle cluster ($E_{\mathrm{T},\mathrm{core}}$). An additional leakage correction ($E_{\mathrm{T},\mathrm{leakage}}$) is required to account for the fact that not all of the EM particle energy is subtracted. Finally, there is a correction to account for pileup and underlying-event¹⁰ ($E_{\mathrm{T},\mathrm{pile-up}}$). The full calorimeter-based isolation energy is expressed as:

$$E_{\mathrm{T}}^{\mathrm{coneXX}} = E_{\mathrm{T},\mathrm{raw}}^{\mathrm{isolXX}} - E_{\mathrm{T},\mathrm{core}} - E_{\mathrm{T},\mathrm{leakage}}(E_{\mathrm{T}}, \eta, \Delta R) - E_{\mathrm{T},\mathrm{pile-up}}(\eta, \Delta R), \quad (3.10)$$

where XX refers to the size of the cone, $\Delta R = \mathrm{XX}/100$. The track isolation variable ($p_{\mathrm{T}}^{\mathrm{coneXX}}$) is calculated by summing the p_{T} of tracks within a cone centered around the electron track or photon cluster direction, whilst excluding the tracks matched to the electron or converted photon. Track-based isolation has better resolution and lower pile-up dependence and provides a superior p_{T} resolution. However, calorimeter-based isolation includes neutral particles and particles below the ID track p_{T} threshold. Hence, both variables provide complimentary information, and the combination of selections on both variables generally results in improved performance over cutting on one variable [99].

Electron isolation working points include the *Gradient* working point which is defined such that the selection efficiency is 95% at $p_{\mathrm{T}} = 20 \, \mathrm{GeV}$ and 99% at $p_{\mathrm{T}} = 60 \, \mathrm{GeV}$, as well as *Loose*, *Tight*, and *HighPtCaloOnly* which implement a cut on the calorimeter or track isolation variables as a function of p_{T} . The *HighPtCaloOnly* working point gives the largest rejection of all the working points at high p_{T} , and only uses the calorimeter-based isolation variable. There are three photon isolation working points: *Loose*, *Tight*, and *TightCaloOnly*. These all cut on the isolation variables as a function of E_{T} , and the *TightCaloOnly* working point only uses the calorimeter-based isolation variable.

Differences between data and simulation can arise due to imperfect detector modelling (see Section 3.2.5 for more details), mismodelling of the shower shape variables, as well as the modelling of complex objects such as the beamspot. The ratios of the data-to-MC efficiencies are referred to as ID or isolation efficiency scale factors, or just scale factors, and correct the MC simulations so that they closely resemble the data. Systematic variations in these scale factors are propagated through to the analysis-level objects [105].

⁹The barycentre of a topo-cluster is the average position of the cluster, weighted by energy deposits.

¹⁰The underlying event (UE) is usually defined as all particles from a single particle collision except those from the process of interest. The UE is not equivalent to minimum bias events, but they are related [104].

Muons

Muons can be reconstructed solely using the MS (stand-alone muons), or a combination of detector subsystems. Stand-alone muons are of use in the reconstruction of ID + MS combined muons and when operating in the forward region $2.5 < |\eta| < 2.7$, which is not covered by the ID. Stand-alone muon reconstruction starts with track reconstruction in the MS, where preliminary track candidates are formed through the identification of short straight-line track segments from hits in individual MS stations. The tracks are then built using all MS sub-detectors, taking into account detector-misalignment, particle-detector interactions, outlier hits, track overlaps, and calorimeter energy losses. Track candidates are finalised after being extrapolated to the IP [106].

In most cases, it is advantageous to combine the signals from the MS with other detector subsystems. Since muons are the only standard model particle that leave signatures in the MS, usually the combination of ID and MS information is sufficient. However, in some special cases it is advantageous for the full detector information to be used. There are four classes of reconstructed muons where detector information beyond the MS is used:

1. Combined muon (CB) tracks are formed from a successful combination of stand-alone MS muons and ID tracks.
2. Inside-out combined (IO) muons are reconstructed with an algorithm that extrapolates ID tracks to the MS whilst using the ID track, the calorimeter energy losses, and the MS hits in a combined fit. IO muons have some performance improvements over CB muons as they do not rely on the independently reconstructed MS track. Most analyses only select for combined (either CB or IO) muons as the combination of two tracks results in the best possible precision.
3. Segment Tagged (ST) muons are required to have a tight angular matching of an ID track to at least one reconstructed MS segment, and the muon parameters are taken solely from the ID track fit. ST muons are of use when there is no fully reconstructed MS track, but only segments in layers of the MS. This can be the case with low p_T muons.
4. Calorimeter-tagged (CT) muons require an ID track which is extrapolated into the calorimeters. Energy deposits compatible with a minimum ionising particle are used to tag the ID track as a muon, and the muon parameters are taken directly from the ID fit. CT muons are only of use when there is no MS track, which is possible for cases where there are known holes in the MS. The signatures for these muons are easily caused by other particles and hence CT muons have low purity (one minus hadron misidentification rate).

Muon identification working points (*Loose*, *Medium*, and *Tight*) are defined to moderate the prompt muon purity and reconstruction efficiency trade-off. This is achieved through requirements on the number of hits in ID layers and MS stations, track properties, and ID-MS compatibility variables. Non-prompt muons can come about due to semileptonic decays of

light hadrons as well as heavy-flavour hadron decays. Since light hadron decays result in lower-quality muons, the working points are optimised to reject muons from light-flavour hadrons. Non-prompt muons from heavy flavour decays result in higher quality muon tracks and can usually therefore be distinguished from prompt muons through the association with the primary vertex and the isolation of the ID tracks or calorimeter deposits. In addition to the standard working points, *Low- p_{T}* and *High- p_{T}* working points are optimised to select for low and high p_{T} muons.

The track and calorimeter-based isolation variables for muons are defined in a similar way to electrons and photons (Section 3.2.6). p_{T} requirements on the calorimeter and track-based isolation variables as well as a requirement on the track p_{T} give an array of isolation working points. These are *Loose* and *Tight*, in addition to more specialised working points such as the *particle-flow* working points which are optimised to reject muons from heavy-flavour hadrons, as well as a set of track-only working points [19, 106].

Jets

The vast majority of pp collisions at the LHC result in the production of quarks and gluons of which the observable signatures are collimated streams of hadrons, *jets*. A number of algorithms for the clustering of observed detector outputs into jet objects exist, where the primary one for ATLAS jet reconstruction is the anti- k_t algorithm (Section 2.2.3). The most common anti- k_t distance parameter is $R = 0.4$ (small-R jets), however, jets reconstructed with $R = 1.0$ (large-R jets) are used in cases where high p_{T} jets originate from the hadronic decays of massive particles like H/W/Z bosons and top quarks. Since the angular separation of their decay products scales as $1/p_{\mathrm{T}}$, i.e. $\Delta R \approx \frac{2m}{p_{\mathrm{T}}}$, they become collimated (highly Lorentz-boosted) [107]. In these situations, these decay products can be reconstructed in a single large-R jet.

The inputs to the anti- k_t algorithm are four-momentum vectors called *input objects*, which can be derived from various sources. These are either tracks, calorimeter deposits organised into topo-clusters, or a combination of track and calorimeter information. Jets reconstructed solely from tracks are referred to as *track-jets*. The acceptance limitations of the ID ($|\eta| < 2.5$), and the inability for the ID to measure neutral particles limits the usefulness of track-jets. For this reason, jets in most ATLAS analyses are reconstructed solely using calorimeter topo-clusters, or a combination of topo-clusters and tracks.

The formation of topo-clusters for jet reconstruction is identical to the description given in Section 3.2.6. Calorimeter jets reconstructed at the EM scale are called *EMTopo jets*. Calorimeter jets can also be reconstructed at the *Local hadronic Cell-Weighting* (LC) scale, where an additional calibration factor is applied to topo-clusters consistent with hadronic energy deposits. These jets are called *LCTopo jets*. The LC weighting is derived from simulations of single pion events, and corrects for signal losses and calorimeter non-compensation.

In Run-1 and in early Run-2 analyses, jets were reconstructed solely using topo-clusters. How-

ever, using a combination of ID and calorimeter information is preferable for the reasons that:

- The calorimeters provide measurements of both charged and neutral particles.
- The superior angular resolution of the ID means that tracks can be associated with vertices.
- The momentum resolution of the ID at low E_T is superior to that of the calorimeters.
- The energy resolution of the calorimeters at high E_T is superior to that of the ID.
- The calorimeters cover the forward $2.5 < |\eta| < 4.9$ regions.

Different algorithms are used for the complimentary use of both track and calorimeter information. These algorithms are classified under the umbrella term of *particle-flow*, or PFlow, algorithms [108]¹¹. The PFlow algorithm described in [12] was developed at ATLAS to combine tracking and calorimetric information for hadronic jet and soft activity¹² reconstruction. At the heart of this algorithm is the ability to distinguish charged from neutral particle deposits in the calorimeters and furthermore to subtract the energy deposited by charged particles from the topo-clusters and to replace them with the momenta of tracks matched to the topo-clusters. The output of the algorithm is a list of tracks, a list of unmodified topo-clusters, and a list of modified topo-clusters. These outputs are often referred to as a Particle Flow Objects (PFOs). The pion mass is assumed, since pions dominate the charged component of the jet, and to take up an average of approximately two-thirds of the visible jet energy [12, 109, 110].

The steps of the PFlow algorithm are as follows:

1. **Track selection:** Well-measured tracks are selected: 9 hits in the Pixel + SCT; no pixel holes; ID acceptance $|\eta| < 2.5$; and $0.5 \text{ GeV} < p_T < 40 \text{ GeV}$. The lower bound p_T threshold is chosen to allow for tracks from particles below the topo-cluster energy threshold. The upper bound selects against poorly isolated tracks. Tracks matched to electrons or muons with *medium* ID are rejected since the algorithm is optimised for hadronic showers.
2. **Matching tracks to topo-clusters:** For each track, an attempt is made to find a match with a single topo-cluster. In some cases tracks are determined to not have formed a topo-cluster. These tracks are retained in the algorithm output list of tracks and steps 3-6 are not performed.
3. **Expected deposited particle energy:** The mean deposited energy of a track of measured momentum p^{trk} , denoted $\langle E_{\text{dep}} \rangle$, is determined using single-pion samples without pileup. Additionally, the spread in the expected single-pion energy deposition ($\sigma(E_{\text{dep}})$) is determined. These are important quantities for steps 4-6 of the algorithm.

¹¹In this thesis, the terms *particle/PFlow jets* and *the particle/PFlow algorithm* will be used to refer to the particle flow algorithm described in [12]. However, particle flow is a broader concept which can also be used to describe other input object algorithms. These are the TCC and UFO algorithms, and are described further on in this chapter.

¹²Soft activity is the additional hadronic recoil below the energy threshold used for jet reconstruction (this is important for missing transverse momentum reconstruction).

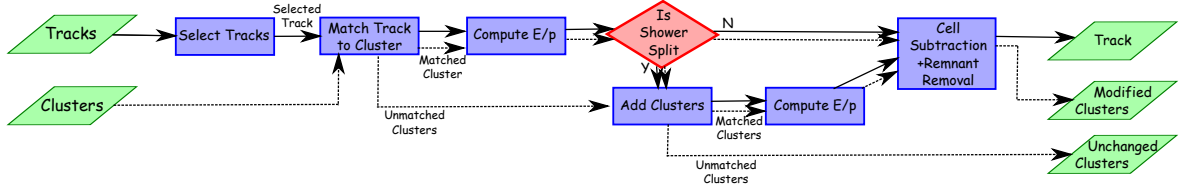


Figure 3.9. Flow chart showing the algorithm used in the construction of particle flow jet input objects.
Figure from [12].

4. **Split-shower recovery:** For each track/topo-cluster system, a discriminant $S(E^{\text{clus}}) \equiv \frac{E^{\text{clus}} - \langle E_{\text{dep}} \rangle}{\sigma(E_{\text{dep}})}$, where E^{clus} is the energy of the topo-cluster, is calculated to distinguish between cases where the particle energy is entirely deposited in a single topological cluster, and cases where the energy is split across multiple topo-clusters. This is actually very common, especially where the shower is split across two topo-clusters. A value of $E^{\text{clus}} > -1$ indicates that more than 90% of clusters have the large majority ($> 90\%$) of the particle's true energy deposited in the topo-cluster. Hence a discriminant value of -1 is used in performing the split-cluster recovery. The algorithm extrapolates the track to the EM calorimeter and expands the set of matched clusters using a simple $\Delta R = 0.2$ criteria around the extrapolated track.
5. **Cell-by-cell subtraction:** It is possible that particles unrelated to the track (for example neutral particles) deposit their energy in close proximity to the clusters matched to the track. Hence simply removing every topo-cluster matched to a track would potentially remove energy deposits made these close-by particles. For this reason, the energy of the total set of topo-clusters is compared to $\langle E_{\text{dep}} \rangle$, and if it is less than $\langle E_{\text{dep}} \rangle$, the topo-clusters are removed. If total topo-cluster energy is larger than $\langle E_{\text{dep}} \rangle$, a cell-by-cell subtraction procedure is implemented to remove calorimeter cells around the extrapolated track.
6. **Remnant removal:** If the cell-by-cell subtraction is implemented, it is likely that there will be some remaining energy from the cells that were not subtracted (if there are energy deposits from neutral particles, for example). A procedure is implemented to determine whether this energy is consistent with shower fluctuations, or whether the energy is consistent with close-proximity particle deposit(s). The remnant topo-clusters are removed if the former case, and retained in the latter.

Figure 3.9 shows a flow chart of this PFlow algorithm.

In the presence of pileup, where jets can arise from particles not produced in the primary hard scatter interaction, the performance benefits of PFlow jets can clearly be observed. This is shown in Figure 3.10a, where the average number of pileup jets (referred to as “fake jets” in the figure) are compared between LCTopo jets and PFlow jets. The fake-rate is an order of magnitude lower for PFlow jets in the region of tracker acceptance, and there are no large deviations in performance outside of the tracker acceptance. Figure 3.10b shows the efficiency of reconstructing a hard-scatter jet, and improvements to the hard-scatter jet reconstruction efficiency can be seen in the comparison of PFlow jets to LCTopo jets.

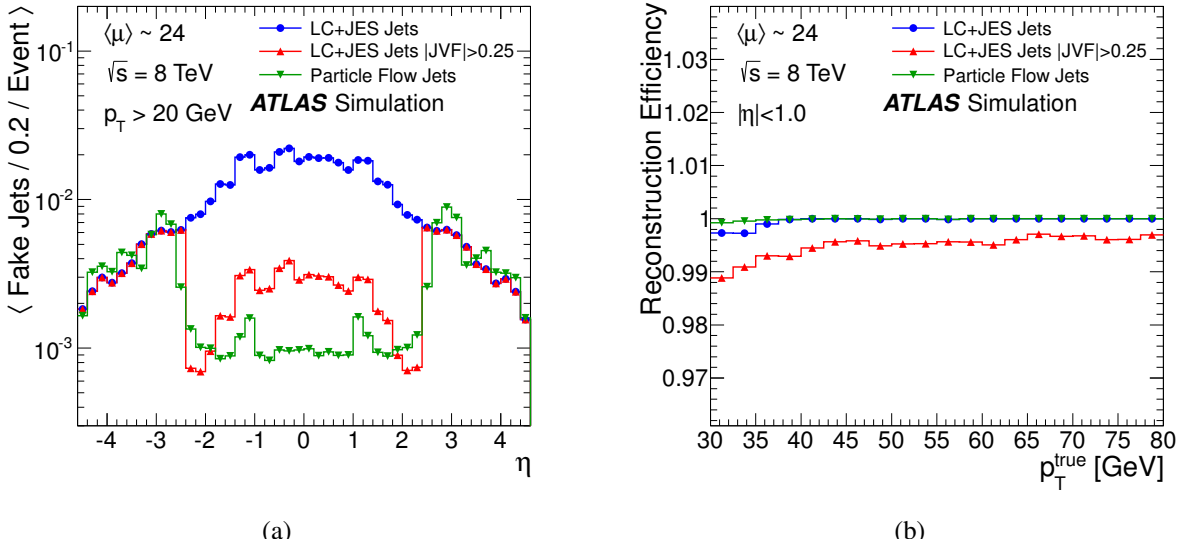


Figure 3.10. Performance improvements of PFlow jets over calorimeter jets. Figures from [12], with and without a jet vertex fraction (JVF) cut applied. JVF is the ratio of two scalar sums, where the numerator is the scalar sum of the p_T of tracks associated to the jets which are matched to the hard-scatter vertex; and the denominator is the scalar sum of p_T of all tracks associated with the jet.

In spite of the performance benefits shown in Figure 3.10, the algorithm does have some shortcomings, particularly at high p_T . Since the lateral shower width of a jet scales as $1/p_T$, high p_T jets have a dense core. The presence of a dense core degrades the accuracy and efficiency of track reconstruction. Additionally, the angular resolution of the calorimeter limits the degree to which the cell subtraction step can be performed reliably in the presence of close proximity showers. It is because of these reasons, that tracks with $p_T > 40 are excluded from the algorithm in the track selection step [108].$

Another PFlow algorithm called the Track-Calorimeter Cluster (TCC) algorithm [13] was developed at ATLAS for improved jet substructure reconstruction performance, and hence tagging performance in very high p_T jets. Since the energy resolution of the calorimeters is superior to that of the ID at high p_T , the TCC algorithm directly uses the energy information from topo-clusters and the angular information from tracks. The output of the TCC algorithm is a set of four-momenta (p_T, η, ϕ, m), where m is the invariant mass of the object¹³. The TCC algorithm works as follows:

- All *loose* tracks matched to primary vertices (including pileup) are matched to topo-clusters calibrated at the LC scale, and each track forms its own TCC object. In cases where one track matches one topo-cluster, the p_T of the TCC object is taken from the topo-cluster, and the η and ϕ coordinates from the track.
- If multiple tracks match to multiple topo-clusters, the cluster p_T is split amongst the tracks, and the track angular coordinates are taken from the seed track.
- In cases where there is a topo-cluster (track) unmatched to a track (topo-cluster), the four-momentum of the TCC object is taken as that of the topo-cluster (track).

¹³TCC objects are massless if ≤ 1 topo-clusters are matched to the seed track, and have non-zero mass if multiple clusters are matched to the seed track

A particle flow algorithm called the Unified Flow Object (UFO) algorithm was designed as a solution to the problem that no single jet input object definition, be it PFlow, TCC or LC/EMTopo, is optimal for any given measure of performance. TCC jets, while having excellent tagging performance at high p_T , perform worse than LCTopo jets at low p_T . PFlow jets outperform LCTopo jets across the entire p_T range, particularly when it comes to pileup sensitivity. However, PFlow jets have significantly worse tagging performance than TCC jets at high p_T .

The UFO algorithm combines the PFlow algorithm in [12] and the TCC algorithm [13] in such a way as to optimise the performance across the kinematic range. In this algorithm, the $p_T^{\text{trk}} < 40 \text{ GeV}$ cut is replaced with a method to gradually switch from the PFlow cell subtraction to the TCC cell subtraction depending on p_T^{trk} , and on the measured calorimeter activity [111]. The switch is made if the energy E^{clus} in a cone of size $\Delta R = 0.15$ around the extrapolated particle satisfies:

$$\frac{E^{\text{clus}} - \langle E_{\text{dep}} \rangle}{\sigma(E_{\text{dep}})} > 33.2 \times \log_{10}(40 \text{ GeV}/p_T^{\text{trk}}). \quad (3.11)$$

In this way, the PFlow cell subtraction algorithm is not implemented for cases where the track momentum is high, and in cases where the measured calorimeter activity is high, such as in very dense environments. Additionally, charged PFOs (tracks selected by PFlow algorithm) which are not matched to the hard-scatter vertex are removed in order to suppress contributions from pileup. This procedure is called ‘‘Charged Hadron Subtraction’’ (CHS). The neutral PFOs (modified or unmodified topo-clusters) have constituent-level (before jet building with anti- k_t) pileup mitigation algorithms applied that go by the names of ‘‘Constituent Subtracton’’ (CS) and SoftKiller (‘‘SK’’). These pileup mitigation algorithms are applied for both small-R and large-R jets. The full UFO algorithm is outlined in Figure 3.11. UFO jets will be the default for small-R and large-R jet definitions in Run-3 analyses.

Jet Flavour Tagging

Identifying jets containing b - and c -hadrons is very important in the context of precision electroweak measurements (for example [112, 113]). In the VBS measurement discussed in Chapter 5, b -tagging is of importance due to large backgrounds from top quarks, which decay to a W -boson and a b -quark.

Because third generation quarks have a large CKM Suppression (little mixing between quark families), b -hadrons tend to have a large decay length. Furthermore, b -hadrons formed from the fragmentation of b -quarks tend to carry a large fraction of the intial quark momentum. This means that b -hadrons are likely to have a large Lorentz boost. The combination of these effects results in prominent displaced vertices. This detector signature is exploited in b -jet tagging algorithms, such as the *DL1r* multivariate algorithm used for the $W\gamma$ VBS measurement [114]. When implementing b -tagging in an analysis, a tagging efficiency (the rate at which a true b -jet is identified correctly) working point needs to be selected depending on

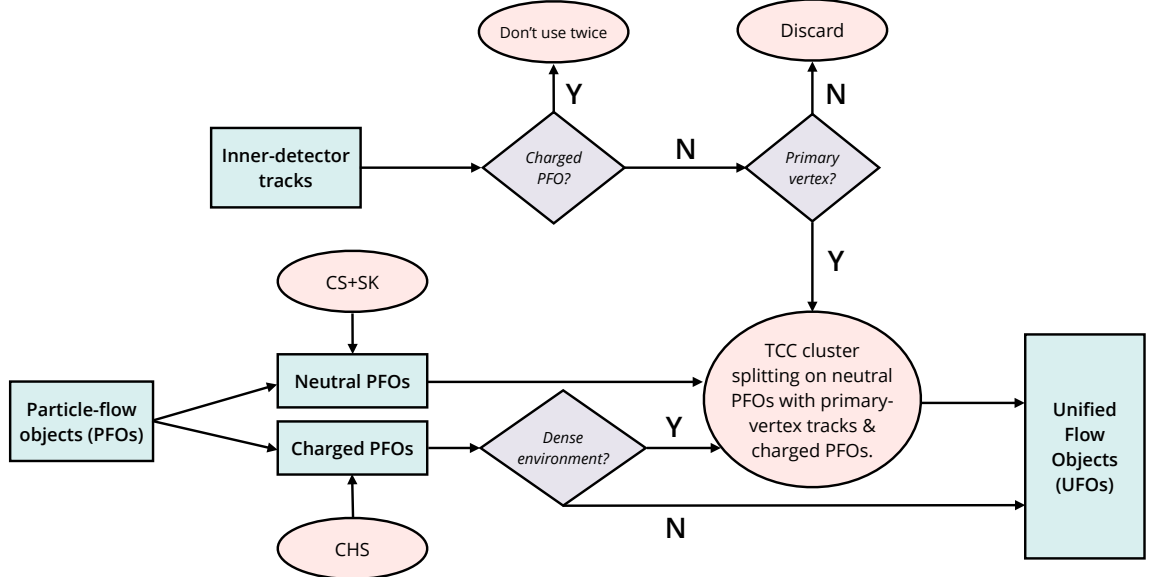


Figure 3.11. A flow chart outlining the construction of UFO jet input objects from PFOs and ID tracks. The “dense environment” decision is defined by equation 3.11, and results in the TCC algorithm being applied to track and topo-cluster combinations with high p_T tracks or very energy-dense calorimeter environments.

efficiency and purity requirements [19].

Missing Tranverse Energy

Since protons travelling along the LHC beamline carry no momentum component in the transverse plane, the p_T in any collision must be conserved. However, in many processes, an imbalance in momentum is expected due to the production of neutrinos which don’t interact with the ATLAS detector, but can carry significant p_T . The missing transverse momentum $\mathbf{p}_T^{\text{miss}}$ is given by $\mathbf{p}_T^{\text{miss}} \equiv (p_x^{\text{miss}}, p_y^{\text{miss}})$ and quantifies the momentum balance in the transverse plane. The magnitude of the vector $\mathbf{p}_T^{\text{miss}}$ is referred to as the *missing transverse energy* (MET), E_T^{miss} :

$$E_T^{\text{miss}} = \sqrt{(p_x^{\text{miss}})^2 + (p_y^{\text{miss}})^2}. \quad (3.12)$$

The direction of the $\mathbf{p}_T^{\text{miss}}$ in the transverse plane is defined as

$$\phi^{\text{miss}} = \text{atan}2(p_y^{\text{miss}}, p_x^{\text{miss}}), \quad (3.13)$$

where the $\text{atan}2(y, x)$ function is defined to return the argument of the complex number $x+iy$, and is used over the \arctan function as it covers the interval $(-\pi, \pi]$, rather than the $[-\frac{\pi}{2}, \frac{\pi}{2}]$ interval covered by the \arctan function.

The components $p_{x(y)}^{\text{miss}}$ are given by the negative vector sum of *hard objects* and *soft signals* in the event:

$$p_{x(y)}^{\text{miss}} = - \sum_{i \in \{\text{hard objects}\}} p_{x(y),i} - \sum_{j \in \{\text{soft signals}\}} p_{x(y),j}. \quad (3.14)$$

The *hard objects* refer to electrons, photons, muons, τ leptons, and jets, with a set of kinematic

and object reconstruction quality requirements. The *soft signals* refers to all detector signals for the triggered event which do not contribute to the hard objects. They include non-collision backgrounds such as scattered soft particles from the UE as well as signals from objects which do not satisfy the hard object selection criteria.

The mutual exclusivity of the detector signal requires a well defined sequence of contributions as well a way of rejecting signals where overlaps are present. The usual reconstruction sequence for the hard objects is electron reconstruction, followed by photons, hadronically decaying τ s, muons, and finally jets. Each of these objects are fully calibrated before they enter the $\mathbf{p}_T^{\text{miss}}$ calculation, such that contributions to $\mathbf{p}_T^{\text{miss}}$ do not arise due to incorrect energy scales. All electrons passing some selection criteria are included in the $\mathbf{p}_T^{\text{miss}}$ reconstruction first, and particles further in the sequence are rejected if there is a shared calorimeter signal with an earlier particle in the sequence.

The contributions from soft signal are calculated in the following way. Good quality tracks in p_T range of $400 \text{ MeV} < p_T < 100 \text{ GeV}$ are selected. The tracks are then extrapolated to a high granularity region of the EM calorimeter, and a ΔR check is performed to assess whether the track is associated with an calorimeter deposits. Those tracks which do not have calorimeter deposits are retained in the soft term, and those which do match to a topo-cluster, are also retained, but the topo-cluster is removed in order to take advantage of the improved p_T resolution of the ID. For cases where multiple topo-clusters are matched to a given track, the highest energy cluster is retained. Any left over topo-clusters which have not been matched to tracks or discarded are also added to the soft term. The performance of E_T^{miss} and $\mathbf{p}_T^{\text{miss}}$ reconstruction is assessed using $Z \rightarrow ee/\mu\mu$ events, where selections of the dilepton invariant mass around the Z invariant mass peak provide clean signal with no expected contributions for E_T^{miss} . Events involving leptonic W decays in association with jets are used to study cases with true E_T^{miss} [19, 115].

Taus

Tau leptons decay (decay length $87\mu\text{m}$) either leptonically or hadronically before reaching the active parts of the ATLAS detector. About 35% of the time, taus decay to a tau neutrino, electron/muon, and lepton neutrino mediated via an off-shell W boson. 65% of the decay modes involve the tau decaying hadronically, where in 72% and 22% of the time one or three charged pions are produced, respectively. Additionally, 68% of hadronic tau decays involve the production of a neutral pion. Leptonic tau decays cannot be distinguished from electrons or muons at the interaction point, however hadronic tau decays have a very specific signature. Firstly, the invariant mass of the system of jets must be less than the tau invariant mass of around 1.8 GeV , and the predictable production of charged pions result in either one or three tracks in the ID [116]. Taus also have very collimated showers compared to QCD jets, this is because QCD jets are initiated by partons carrying colour charge, where the hadronisation process results in multiple quark and gluon emissions due to them being colour-connected to the initial parton. Additionally, tau tracks tend to have large impact parameters due to the

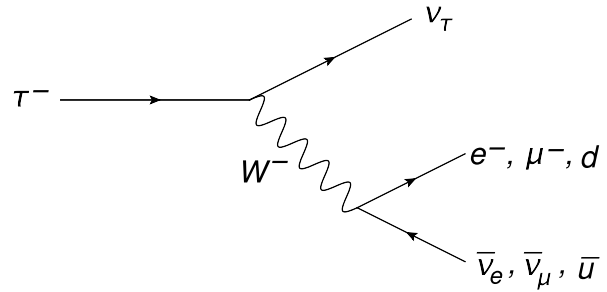


Figure 3.12. Feynman diagram for tau decays via off-shell W boson. From [19].

significant decay length of the tau. Taus are reconstructed initially as jets using the anti- k_t with $R = 0.4$. Afterwards, a multivariate analysis uses various jet properties to tag the taus [19, 117].

Chapter 4

Insitu Calibration of Large-R Jets Using Direct Balance in Z+Jet Events

4.1 Introduction

This chapter describes the methods used to derive the first Jet Energy Scale (JES) insitu calibrations for large-R jets using Z +jets events, for jets that have been reconstructed using UFO input objects (Section 3.2.6). The JES is derived in the region $|\eta| < 0.8$, for large-R jets with $152.2 \text{ GeV} < p_T < 754.6 \text{ GeV}$ for $Z \rightarrow e^+e^-$ events and $156.9 \text{ GeV} < p_T < 745.4 \text{ GeV}$ for the $Z \rightarrow \mu^+\mu^-$ events. The calibration was derived using the “InsituBalance” framework, which is a software package originally created for the MultiJet-Balance calibration [10], but was adapted by the author for the Z+jet insitu calibrations.

4.2 Jet Calibration

After reconstruction, jets are calibrated so that the average reconstructed jet p_T and mass, m , is restored to that of particle-level (also called *truth*) jets. These are simulated jets which have not gone through detector simulation. The correction factors are known as jet energy/mass scale (JES,JMS) factors. The JES+JMS calibration consists of a series of steps outlined in Figure 4.1, where the steps are slightly different for small-R and large-R jets.

After anti- k_t jet building of the detector-level (also called *reco*) jets - these are simulated jets which have gone through detector simulation - a reference set of truth jets are reconstructed and geometrically matched to the reco jets using a ΔR matching requirement. Small-R jets then have a pileup correction applied in the first stage of the calibration chain. The purpose of this step is to correct for the contribution to the jet energy due to pileup. The correction consists of two steps: the jet area-based correction and the residual pileup correction. The area-based corrections subtracts the expected contribution from pileup based on the area of the jet and the median p_T density in the event. After this correction there is still a dependence of the difference between the reco jet and truth jet p_T on the pileup activity. A residual correction is therefore implemented, parametrised in the number of PVs (N_{PV}), and μ which quantify in-time and out-of-time pileup¹ respectively.

¹in-time pileup refers to pp collisions from the same bunch-crossing as the interaction of interest, whereas out-of-time pileup refers

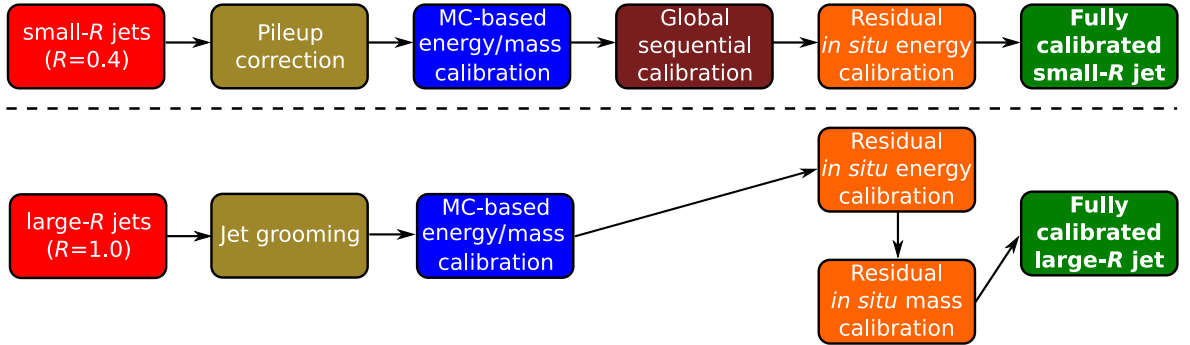


Figure 4.1. Jet calibration chain for small-R and large-R jets. Adapted from [11].

Large-R jets do not have a pileup correction applied in the same way as small-R jets. Since the jet volume of large-R jets encloses a larger fraction of the calorimeter than small-R jets, they are significantly more sensitive to pileup. In spite of the fact that large-R jets represent high p_T objects, and pileup is typically low p_T , the angular structure of large-R jets can be affected, limiting the jet substructure performance. For this reason, “grooming” algorithms are applied to large-R jets. Grooming algorithms remove jet constituents, and rebuild the jets from the remaining constituents. The “trimming” algorithm was prevalent for large-R jets in early Run-2 analyses, where regions of the jet with small relative contributions to the jet p_T are removed. The latest recommendations use variations of the “Soft-Drop” algorithm, which is a technique for removing soft and wide-angle radiation from a jet. With the reconstruction of large-R truth jets, the same grooming algorithm is applied as the reco jets.

In the next step of the calibration chain, the MC-based JES and JMS corrections are derived using dijet events. The p_T and mass responses are defined as $R_{p_T} = \langle p_T^{\text{reco}} / p_T^{\text{true}} \rangle$ and $R_m = \langle m^{\text{reco}} / m^{\text{true}} \rangle$, where the averages are determined from Gaussian fits (recently, small-R UFO jets were calibrated using a “numerical inversion” technique which uses piecewise polynomials called “splines” to fit the response [118]). For the JES calibration, the response fits are performed in bins of jet energy and detector pseudorapidity (pseudorapidity relative to the geometrical center of the ATLAS detector, rather than the hard scatter PV). The JES factor, $c_{\text{JES}} = 1/R_{p_T}$ is then smoothed in energy and η_{det} . A correction to η , $\Delta\eta$ is also derived. After c_{JES} is calculated, a correction to the jet invariant mass is derived². Jet mass corrections are derived using the same procedure as the JES, and in bins of E_{reco} , η^{det} , as well as $\log(m_{\text{reco}}/E_{\text{reco}})$. The JMS calibration factor ($c_{\text{JMS}} = 1/R_m$) is applied only to the mass of the jet while keeping the energy fixed, and allowing the p_T to vary. The ϕ coordinate is not affected by the calibration. The calibrated kinematic variables are thus given by:

$$E_{\text{reco}} = c_{\text{JES}} E_0, \quad m_{\text{reco}} = c_{\text{JES}} c_{\text{JMS}} m_0, \quad \eta_{\text{reco}} = \eta_0 + \Delta\eta, \quad p_T^{\text{reco}} = c_{\text{JES}} \frac{\sqrt{E_0^2 - c_{\text{JMS}}^2 m_0^2}}{\cosh(\eta_0 + \Delta\eta)}, \quad (4.1)$$

where the quantities with a 0 subscript refer to those prior to any calibration, but after jet grooming (for the large-R case) [10, 119].

to pp collisions occurring in bunch-crossings just before and after the interaction of interest.

²Corrections to the large-R jet mass in particular are important since the mass is more sensitive than the p_T to soft, wide-angle contributions, calorimeter geometry and topo-cluster merging and splitting. Moreover, the large-R jet mass is a powerful substructure variable used for discriminating between QCD jets and hadronically decaying massive particles.

For small-R jets, there is an additional step after the MC-based calibration, which is the Global Sequential Calibration (CSC). This step aims to improve the relative p_T resolution given by $\frac{p_T^{\text{JES+JMS}}/p_T^{\text{true}}}{\langle p_T^{\text{JES+JMS}}/p_T^{\text{true}} \rangle}$, where $p_T^{\text{JES+JMS}}$ is the jet transverse momentum after the MC-based calibration. The GSC also corrects for differences in the p_T response for gluon initiated and quark initiated jets. This correction is derived based on global jet observables such as the longitudinal shower structure, and tracking information, and takes the form of a sequence of multiplicative corrections. Recently a neural network approach (Global Neural Network Calibration) has been explored which is an alternative to this sequential correction and allows for correlated global observables to be used in deriving the calibration [120].

The final calibration stage is the *in situ* calibration. Differences in the jet response can arise between data and simulation due to imperfect detector modelling, pileup, particle-detector interactions, the UE, and jet formation. The *in situ* correction factor is defined as the double ratio of the response in data divided by the response in MC:

$$c = \frac{\mathcal{R}_{\text{in situ}}^{\text{data}}}{\mathcal{R}_{\text{in situ}}^{\text{MC}}}, \quad (4.2)$$

where the response is defined as:

$$\mathcal{R}_{\text{in situ}} = \left\langle \frac{p_T^{\text{jet}}}{p_T^{\text{ref}}} \right\rangle, \quad (4.3)$$

and p_T^{ref} is defined as the p_T of a well-measured reference object, and p_T^{jet} is the transverse momentum of the jet being calibrated. $\mathcal{R}_{\text{in situ}}$ is transformed from a function of p_T^{ref} to a function of jet transverse momentum through a process of numerical inversion (see Section 4) prior to the double ratio c calculation. The response $\mathcal{R}_{\text{in situ}}$ is sensitive to secondary effects such as out-of-cone radiation, where jets from QCD radiation are not captured by the jet cone. The expectation is therefore that $\mathcal{R}_{\text{in situ}}$ is skewed below 1, and these effects are partially mitigated through the event selection. The double ratio c , however, is robust to such effects, so long as they are not mismodelled in simulation.

There are three stages of the insitu calibration which are performed sequentially. First, the inter- η calibration uses dijet events to correct the energy scale of forward jets ($0.8 < |\eta_{\text{det}}| < 4.5$) to that of central jets ($|\eta_{\text{det}}| < 0.8$). The reason for deriving this correction is that the *in situ* calibrations that follow are derived solely in the central region as forward jets have increased response variations due to the more complicated detector structure in the forward regions. The η -inter calibration requires two back-to-back jets in the transverse plane from different η_{det} regions. All insitu calibration steps exploit the momentum balance of the system. In the case of the η -inter calibration, the two jets are required to have equal and opposite p_T to satisfy the momentum balance. A quantity called the momentum asymmetry is constructed, which is the difference of the jet transverse momenta divided by the average jet p_T , and quantifies the response difference between the two detector regions. For a given pair of η_{det} , the asymmetry can be used to define the calibration factors.

The next step of the calibration chain exploits the p_T balance in $\gamma/Z(\rightarrow ee/\mu\mu)$ +jet events. Electrons and photons are accurately calibrated as described in Section 3.2.6, and the muons are calibrated using $Z \rightarrow \mu\mu$, $J/\Psi \rightarrow \mu\mu$ and $\Upsilon \rightarrow \mu\mu$ events. These methods benefit from the accurate knowledge of the energy scale and resolution of leptons and photons. These in situ calibrations are called the direct-balance (DB) calibrations. The DB response is:

$$\mathcal{R}_{\text{DB}} = \langle \frac{p_T^{\text{j1}}}{p_T^{\text{ref}}} \rangle, \quad p_T^{\text{ref}} = p_T^{Z\gamma} |\cos(\Delta\phi)|, \quad (4.4)$$

where p_T^{j1} is the p_T of the leading jet, and $\Delta\phi$ is the azimuthal separation between the photon or the reconstructed Z . The reason for the $|\cos \Delta\phi|$ factor is to reduce the effect of “out-of-cone” (OOC) radiation, which is additional QCD radiation from the jet which is not captured in the jet cone during jet building. The reference object is colour neutral, hence there is more QCD radiation in the jet hemisphere resulting in a bias which takes the response below unity. This $|\cos \Delta\phi|$ factor reduces the effect of this bias by balancing the momentum of the reference object onto the jet axis in the transverse plane.

Events are selected by requiring low p_T jet veto, and a minimum requirement on the $\Delta\phi$ between the leading jet and the reference system. Independent calibration factors are derived for $Z(\rightarrow ee)$ +jet, $Z(\rightarrow \mu\mu)$ +jet and $Z\gamma$ +jet DB. The Z +jet calibration is limited to the statistically significant p_T range of Z boson production, and is therefore only relevant at low and medium p_T in the range of around $17 < p_T < 800$ GeV. The complementary γ +jet measurements which are limited by small numbers of events at high p_T and by dijet contamination, are relevant at around $30 < p_T < 2000$ GeV with a limited precision at $p_T < 100$ GeV.

For the calibration of small-R jets, an additional insitu calibration called the Missing Momentum Fraction (MPF) method is also used to complement the DB calibrations. The MPF method measures the p_T balance between the reference object and the full hadronic recoil (i.e. including any QCD OOC radiation). This method is very robust against pileup and the UE, and covers a similar kinematic range to γ +jet DB. In the final stage of the insitu calibration, a p_T balance method using multijet events is implemented to extend the kinematic range of the calibration to larger transverse momenta than what could be achieved by γ +jet. Recent developments in the insitu calibration have allowed for a precision of the correction factor at level of 1%. Additionally, recent developments have allowed for measurements of the JES for b-tagged jets at the level of 1% using γ +jet direct balance. These measurements have the potential to improve the precision of analyses which are very sensitive to the b-jet JES such as $H \rightarrow b\bar{b}$ and top mass measurements [10, 120, 121].

For the case of large-R jets, an in situ calibration for the JMS is also calculated. Two independent methods are used to derive these corrections. The R_{trk} method uses calorimeter-to-tracker response ratios. This method was used for calibrating large-R LCTopo jets for Run-2 analyses, where the fact that tracker and calorimeter provide independent measurements is exploited in order to validate the modelling of large-R jet properties. The forward folding method uses a high purity, high p_T large-R jet sample from $t\bar{t}$ events, where one of the top quark decays hadronically ($t \rightarrow b + W(\rightarrow \text{jets})$), and the other decays via a leptonically

| | Year | Level1 | HLT |
|--------------------|----------------|--|---|
| Dielectron trigger | 2015 | $E_T > 10 \text{ GeV}^(*);$ Hadronic activity veto | $E_T > 12 \text{ GeV};$ loose ID |
| | 2016 | $E_T > 13 \text{ GeV}^(*);$ Hadronic activity veto | $E_T > 15 \text{ GeV};$ vloose ID, $d0$ unused |
| | 2017/2018 | $E_T > 15 \text{ GeV}^(*);$ Hadronic activity veto; Isolated | $E_T > 17 \text{ GeV};$ vloose ID, $d0$ unused |
| Dimuon trigger | 2015 | $E_T > 10 \text{ GeV}$ | $E_T > 10 \text{ GeV}$ |
| | 2016/2017/2018 | $E_T > 10 \text{ GeV}$ | $E_T > 14 \text{ GeV}$ |

Table 4.1. An η -dependence of the L1 trigger threshold is denoted by (*).

decaying W ($t \rightarrow b + W(\rightarrow l\nu)$). The response is obtained from fits to the top and W mass peaks in the invariant mass distribution of the large-R jet of the hadronically decaying top candidate. The W mass peak is present when a large-R b-jet veto is applied, and the top mass peak is present when the large-R jet is b-tagged. Two independent methods for calculating the large-R jet mass are implemented. These are the calorimeter jet mass, m^{calo} , and the track-assisted jet mass (m^{TA}). For a large-R calorimeter jet J with topo-cluster constituents i with energy E_i and momentum \mathbf{p}_i , the calorimeter-based jet mass is defined as:

$$m^{\text{calo}} = \sqrt{\left(\sum_{i \in J} E_i\right)^2 - \left(\sum_{i \in J} \mathbf{p}_i\right)^2}, \quad (4.5)$$

and the track-assisted jet mass is defined as:

$$m^{\text{TA}} = \frac{p_{\text{T}}^{\text{calo}}}{p_{\text{T}}^{\text{track}}} \times m^{\text{track}}, \quad (4.6)$$

where the track invariant mass, m_{trk} , is assumed to be the pion mass. The values for the response in data and MC are extracted simultaneously in a fit known as *forward folding* [10].

4.3 Data and MC samples

Proton-proton collision data at a centre-of-mass energy of $\sqrt{s} = 13 \text{ TeV}$ are used in the in-situ calibration. The data are required to pass unprescaled dielectron or dimuon triggers depending on whether the Z -boson decays to electrons or muons, respectively. These triggers are shown in Table 4.1, and depend on the year the data were recorded. The dataset corresponds to an integrated luminosity of 139 fb^{-1} [122]. The data are required to pass data-quality criteria to ensure the data were taken during periods where the detector subsystems were fully functioning. This is achieved via “GoodRunsLists (GRLs)”, which are provided by the ATLAS Data Quality group.

The nominal sample of Z +jets events is generated using PowHEG-Box v1 [33–35], with NLO matrix-element (ME) accuracy in perturbative QCD for inclusive Z production. The CT10 PDF set is used in the ME calculation [123]. The parton-level final state is interfaced with

PYTHIA8 (v8.186) [36] for generating the parton shower (PS), hadronisation, and multi parton interactions (MPI), utilising the AZNLO tuned parameter set [124]. The PHOTOS++ program [125] is used for the modelling of QED emissions from electroweak vertices and charged leptons. EvtGen 1.2.0 [126] is used for the properties of b - and c -hadron decays.

For evaluating the systematic uncertainty due to MC generator choice, a second $Z+jets$ sample is generated using SHERPA2.2.1 [37, 38] and is subdivided (sliced) into discrete regions of $\max(H_T, p_T^V)$, with boundaries at $[0, 70, 140, 280, 500, 1000, 6500]$ GeV, where H_T is defined as the scalar sum of all partonic jet transverse momenta, and p_T^V is the mass of the dilepton system. NLO-accurate matrix elements for up to two jets, and LO-accurate matrix elements for up to 4 jets are calculated with COMIX [30]. The b - and c -quarks are treated as massless at the ME calculation, and massive in the parton shower. The parton showering is conducted by CSShower [127], which is based on Catani-Seymour dipole factorisation [128]. Virtual QCD corrections to the ME are derived with OPENLOOPS [129]. The NLO matrix elements for any given jet multiplicity is matched to parton shower, and different jet multiplicities are then merged according to the CKKW matching procedure [40, 41] and extended to NLO accuracy using the MEPS@NLO prescription [130]. The NNPDF3.0NNLO PDF set [131] is used with dedicated parton shower tuning developed by the SHERPA authors. The invariant mass of the dilepton system is required to be at least 40 GeV [132]. The MC event simulations are interfaced with the GEANT4 toolkit [89] for detailed modelling of the ATLAS detector response [133].

4.4 Jet definitions

The large- R jets, which are the subject of the insitu calibration described in this chapter, are built from UFO jet input objects [14] using the anti- k_t algorithm [23] with radius parameter $R = 1.0$. Constituent-level pile-up mitigation is applied using the Constituent Subtraction (CS) [134] and SoftKiller (CS) [135] algorithms. To remove soft contributions from the reconstructed jet, the Soft-Drop (SD) grooming algorithm [136] is implemented. Additionally, fully calibrated small- R jets [111, 137] are used for p_T balancing and jet veto purposes. These jets are built from Particle Flow (PFlow) [12] input objects using the anti- k_t algorithm with radius parameter $R = 0.4$. An overview of the definitions of the different jet objects is shown in Table 4.2. The specific implementation of the jet clustering algorithm is taken from the FASTJET package [138, 139].

Large- R jets are calibrated in both data and simulation up the MC-based JES and JMS (MC JES+JMS) calibration scale [10]. Small- R jets are fully calibrated in both data and simulation, as described in Section 4.2.

| | Algorithm | R | Settings |
|-------------------------------|-------------------------|-----|--|
| Jet input objects | Particle-Flow | 0.4 | N/A |
| | Unified Flow Objects | 1.0 | N/A |
| Pile-up mitigation algorithms | Constituent Subtraction | 1.0 | $A_g = 0.01$ $\Delta R_{\max} = 0.25$ $\alpha = 0$ |
| | SoftKiller | 1.0 | $\ell = 0.6$ |
| Jet grooming algorithms | Soft-Drop | 1.0 | $z_{\text{cut}} = 0.1$ $\beta = 1$ |

Table 4.2. Summary of the jet input object algorithms used for small- R ($R = 0.4$) and large- R ($R = 1.0$) jets, in addition to the specific pile-up mitigation and grooming algorithms used for the large- R jets. Since different versions of the pile-up and grooming algorithms exist, the exact parameters used relevant to these algorithms is shown in the last column. See [134–136] for further details on the parameters..

4.5 Object Selections

4.5.1 Electrons

Electrons are reconstructed from ID tracks and calorimeter information as described in section 3.2.6. Electrons are calibrated using the “EgammaCalibrationAndSmearingTool” with the ESMModel “es2018_R21_v0” configuration using the decorrelation model setting “1NP_v1”, which results in one non-zero scale and resolution systematic variation. Electrons are required to satisfy *Loose* ID, and *FCLoose* isolation requirements³, and are reconstructed within $|\eta| < 2.47$, excluding the gap between the barrel and endcap EM calorimeters ($1.36 < |\eta| < 1.52$). Electrons are required to satisfy $p_T > 20 \text{ GeV}$. Electrons are constrained to originate from the primary hard-scatter vertex through the requirements $|d_0|/|\sigma_{d_0}| < 5$ and $|z_0 \sin \theta| < 0.5 \text{ mm}$, where the impact parameters are defined in Section 3.2.6.

4.5.2 Muons

Muons are reconstructed from MS tracks matched to ID tracks as described in Section 3.2.6. Muons are calibrated using the “MuonCalibrationAndSmearingTool” and the “correctData_ID MS” scheme which gives muon track resolution and momentum scale systematic variations on the separate ID and MS components of the combined (CB) muon. Muons are required to satisfy *Loose* ID, and *FCLoose* isolation requirements, and must be reconstructed within $|\eta| < 2.4$ with $p_T > 20 \text{ GeV}$. Muons are constrained to originate from the primary hard-scatter vertex through the requirements $|d_0|/|\sigma_{d_0}| < 3$ and $|z_0 \sin \theta| < 0.5 \text{ mm}$, where the impact parameters are defined in Section 3.2.6. The η cut, ID quality, and track selections are performed by the “MuonSelectionTool”, which also facilitates vetoing events containing mis-reconstructed muons, as these objects tend to have significantly worse momentum resolution. Muons consistent with cosmic ray backgrounds are removed.

³“FC” refers to “FixedCut”, i.e. that a cut is put on the isolation variables themselves, rather than using cut maps to achieve a target selection efficiency.

4.5.3 Jets

As described in Section 4.2, the $Z+jets$ insitu calibration is designed to provide residual corrections to jets measured in the central detector region. Therefore, large-R jets are selected to be in the region $|\eta| < 0.8$ and with $p_T > 100 \text{ GeV}$. Small-R jets are selected with $p_T > 10 \text{ GeV}$ and $|\eta| < 4.5$ and are required to be $\Delta R > 1.4$ from the leading large-R jet, to ensure no overlap. Small-R jets with $p_T < 60 \text{ GeV}$ and $|\eta| < 2.4$ are required to satisfy the *Tight Jet Vertex Tagger* (JVT) [140] working point in order to reject additional jets originating from pileup. The *Medium* JVT working point is used as a systematic variation to assess the impact of the JVT selection on the calibration.

4.5.4 Overlap Removal

To prevent detector signals from one object being used in the reconstruction of a different object, an object overlap removal procedure is applied according to the ATLAS standard overlap removal tool [141] in the following order:

- If two electrons share the same track in the ID, the electron with the lowest p_T is rejected.
- Calorimeter muons are rejected against electrons if they share the same track in the ID.
- Electrons are rejected against muons if they share the same track in the ID.
- Small-R jets are rejected against electrons if $\Delta R < 0.2$.
- Electrons are rejected against small-R jets if $\Delta R < 0.4$.
- Small-R jets are rejected against muons if there are < 3 tracks and either the jet and the muon are ghost-associated⁴ or $\Delta R < 0.2$.
- Muons are rejected against small-R jets if $\Delta R < 0.4$.
- Large-R jets are rejected against electrons if $\Delta R < 1.0$.

4.6 Event Selection

Event selection criteria are applied such that the analysis is performed in a region that is populated by event topologies in which the reconstructed Z -boson’s momentum is balanced by the momentum of the large-R jet (a so-called $2 \rightarrow 2$ topology). Furthermore, to ensure the leptons are consistent with a Z -boson decay, lepton pairs are required to have the same flavour and opposite charge. The invariant mass of the dilepton system is required to be consistent with the invariant mass of the Z -boson, i.e. $66 \text{ GeV} < m_{ll} < 116 \text{ GeV}$. The $2 \rightarrow 2$ topology selection is enforced by a veto on events in which (i) there is a small-R jet that carries a significant amount of the total jet momentum, and (ii) the large-R jet and the dilepton system

⁴With “ghost-association” particles can be associated to jets by treating them as particles with negligible p_T and clustering them within the jet [142].

| Variable | Nominal Selection | Up Variation | Down Variation |
|----------------------|--|---|---|
| $p_T^{j_1}$ | $< \max(0.1 p_T^{\text{Ref}}, 15 \text{ GeV})$ | $< \max(0.15 p_T^{\text{Ref}}, 20 \text{ GeV})$ | $< \max(0.05 p_T^{\text{Ref}}, 10 \text{ GeV})$ |
| $\Delta\phi(Z, J_1)$ | > 2.8 | > 2.9 | > 2.7 |
| m_{ll} | $66 \text{ GeV} < m_{ll} < 116 \text{ GeV}$ | — | — |
| Lepton charge | Opposite charge pairs | — | — |

Table 4.3. Event selection criteria and corresponding systematic variations. The large-R jet with the highest p_T (hardest) is given the label J_1 . The hardest small-R jet is given the label j_1 (not capitalised).

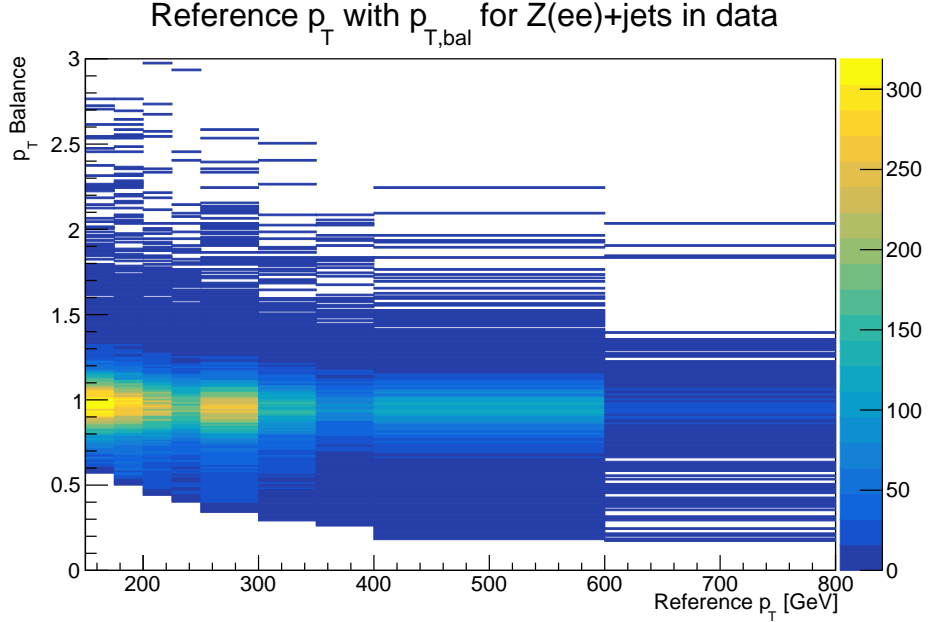


Figure 4.2. p_T^{Ref} with p_T^{Bal} for $Z \rightarrow e^+e^-$ events in data. The response distributions in bins of p_T^{Ref} are y-axis slices of this 2D histogram.

are separated by $\Delta\phi(Z, J_1) \approx \pi$. The event selections and their variations for evaluating systematic uncertainties are listed in Table 4.3.

4.7 Nominal Response Calculation

Measurements of R_{DB} are carried out separately in the electron and muon channels. These measurements are later combined in the insitu combination effort to provide a single insitu correction. R_{DB} is measured using a 2D histogram of p_T^{Ref} and $p_T^{\text{Bal}} \equiv \frac{p_T^J}{p_T^{\text{Ref}}}$ for every event passing the selection criteria. The binning of p_T^{Ref} is chosen to be [150, 175, 200, 225, 250, 300, 350, 400, 600, 800] GeV to match the previous calibration effort for EMTopo large-R jets [10]. The p_T^{Bal} variable has a fine binning to facilitate a Gaussian fit of the response curves. The 2D histogram is shown for $Z \rightarrow e^+e^-$ events for the response calculation in data in Figure 4.2.

The 2D histogram is sliced in bins of p_T^{Ref} , and the average response R_{DB} is determined from the mean of a Gaussian fit. The error on the mean is used to quantify the statistical uncertainty on p_T^{Bal} .

Before performing the fit, each p_T^{Ref} distribution is uniformly re-binned in accordance to Scott's normal reference rule [143], which states that the bin width should be as close as pos-

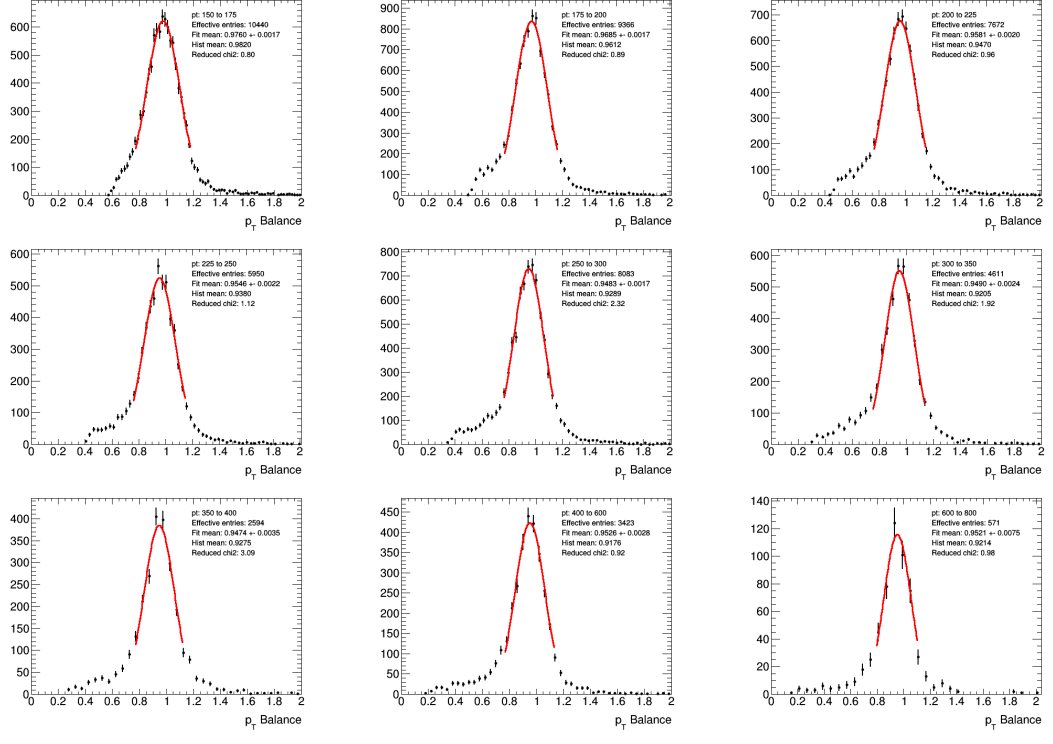


Figure 4.3. Gaussian fits to p_T^{Bal} in slices of p_T^{Ref} in the electron channel. The y -axis shows the number of events per bin.

sible to $\frac{3.5\sigma_{\text{hist}}}{\sqrt{N}}$ (σ_{hist} is the standard deviation of the histogram and N is the number of events). After re-binning, a Gaussian distribution is fit using a minimum log-likelihood method, where the likelihood is built assuming a Poisson probability density function for each bin [144]. This fit is performed over the range $x_{\text{max}} \pm \frac{x_{\text{max}}}{8}$, where x_{max} is the x value corresponding to the bin with the maximum histogram content. After the fit, the range is adjusted to $\mu_{\text{fit}} \pm 1.6\sigma_{\text{fit}}$, where μ_{fit} is the mean of the Gaussian, and σ_{fit} is the width⁵. In this way approximately 90% of the events contribute to the fit. A second Gaussian fit is then performed over the new fit range, now using χ^2 minimisation. The fit range is adjusted again in the same way, and a third Gaussian fit is performed, again using χ^2 minimisation. This fit method results in lower reduced χ^2 values than a single fit with a static fit range [145].

The response fits are shown for data in the electron channel in Figure 4.3 and the muon channel in Figure 4.4. See Appendix A.1 for the Gaussian fits from simulated events for both channels.

The 18 Gaussian fits in Figures 4.3 and 4.4 qualify the average jet response, R_{DB} , as a function of p_T^{Ref} . However, since the final insitu calibration is applied to large-R jets, the p_T^{Ref} values need to be mapped to p_T^J . To derive the mapping, a 2D histogram of p_T^{Ref} vs p_T^J is produced. For a given p_T^{Ref} slice, the p_T^J bin center is given by the histogram mean over the range $[0.4p_{T,\text{ref},i}^{\text{low}}, 1.6p_{T,\text{ref},i}^{\text{high}}]$, where $p_{T,\text{ref},i}^{\text{low}}$ and $p_{T,\text{ref},i}^{\text{high}}$ are the lower and upper bin edges for bin i of p_T^{Ref} , respectively. The p_T^J midpoint values for each p_T^{Ref} bin are shown in Figure 4.5.

⁵The reason for not fitting over the entire histogram range is because of the non-Gaussian nature of the low p_T^{Bal} tail. This non-Gaussian tail comes about due to the 100 GeV cut on the large-R jet p_T , and the maximum value of the p_T^{Ref} bin. For example, in the 150-175 GeV bin, the minimum value p_T^{Bal} can take is $100/175 = 0.57$. There is no such upper limit for p_T^{Ref} , leading to a slight bias at low p_T^{Ref} .

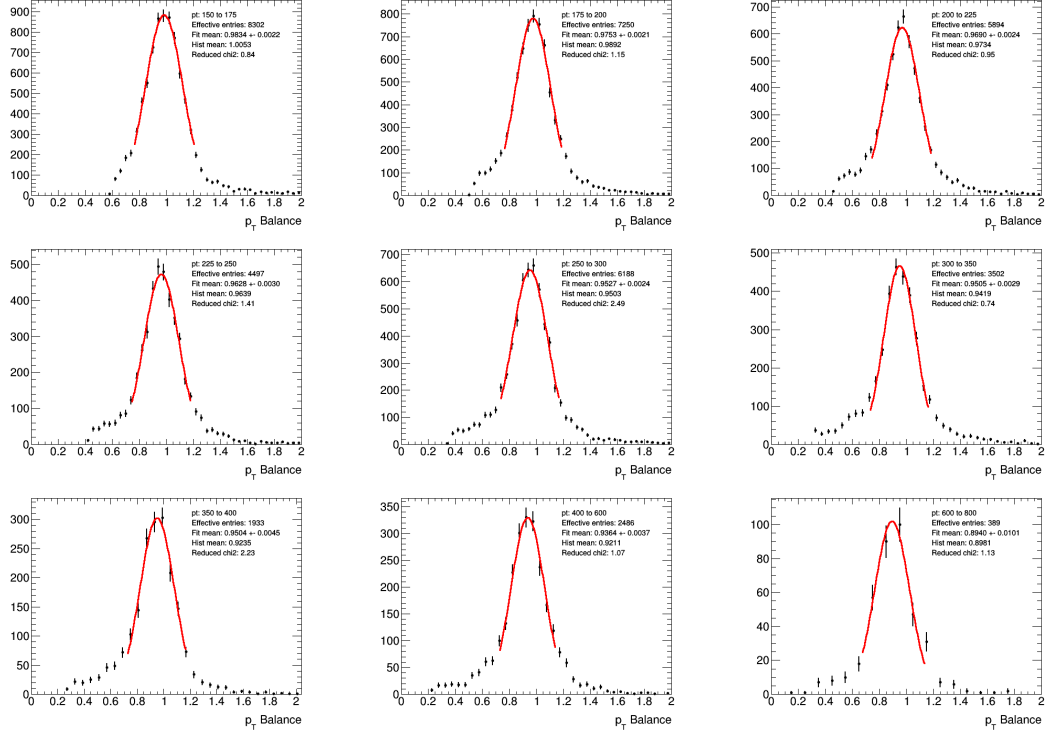


Figure 4.4. Gaussian fits to p_T^{Bal} in slices of p_T^{Ref} in the muon channel. The y -axis shows the number of events per bin.

4.8 Systematic Uncertainties

Systematic uncertainties in the insitu correction arise from the reconstruction and calibration of the leptons, the choice of event generator used to calculate the double ratio c , the JVT working point, and the variations in the event selection criteria (given in Table 4.3). JES and JER systematic uncertainties on the small-R jet used in the radiation veto, and lepton reconstruction, ID, isolation and trigger efficiency scale factors, are not considered. These uncertainties were found to be negligible in previous large-R jet calibration efforts at ATLAS [10]. The statistical uncertainties from the number events in data, and the number of simulated events are included in the final uncertainty.

There are 64 independent sources of uncertainty which contribute to the electron energy scale variations. These include uncertainties in the material upstream of the calorimeter, cell readout non-linearity, transitions between higher and lower gains in the EM calorimeter, presampler calibration, intercalibration of first and second accordion layers, $Z \rightarrow e^+e^-$ energy scale calibration, pileup modelling, and lateral shower shape development [102].

The sources of uncertainty contributing to the electron energy resolution are: shower and sampling variations in the calorimeter, fluctuations in the energy loss upstream of the calorimeter, electronics and pileup noise, and residual non-uniformities affecting the measurement of the energy in the data [100]. For the muon p_T scale and resolution uncertainties, the sources include: the $J/\psi \rightarrow \mu^+\mu^-$ and $Z \rightarrow \mu^+\mu^-$ fits, reweighting simulated Z samples to improve agreement with data, decay and final state radiation modelling, $J/\psi/Z$ p_T template range, $J/\psi/Z$ mass binning, $J/\psi/Z$ mass window, J/ψ alternate background parametrisation function, the closure test, and statistical uncertainty [146].

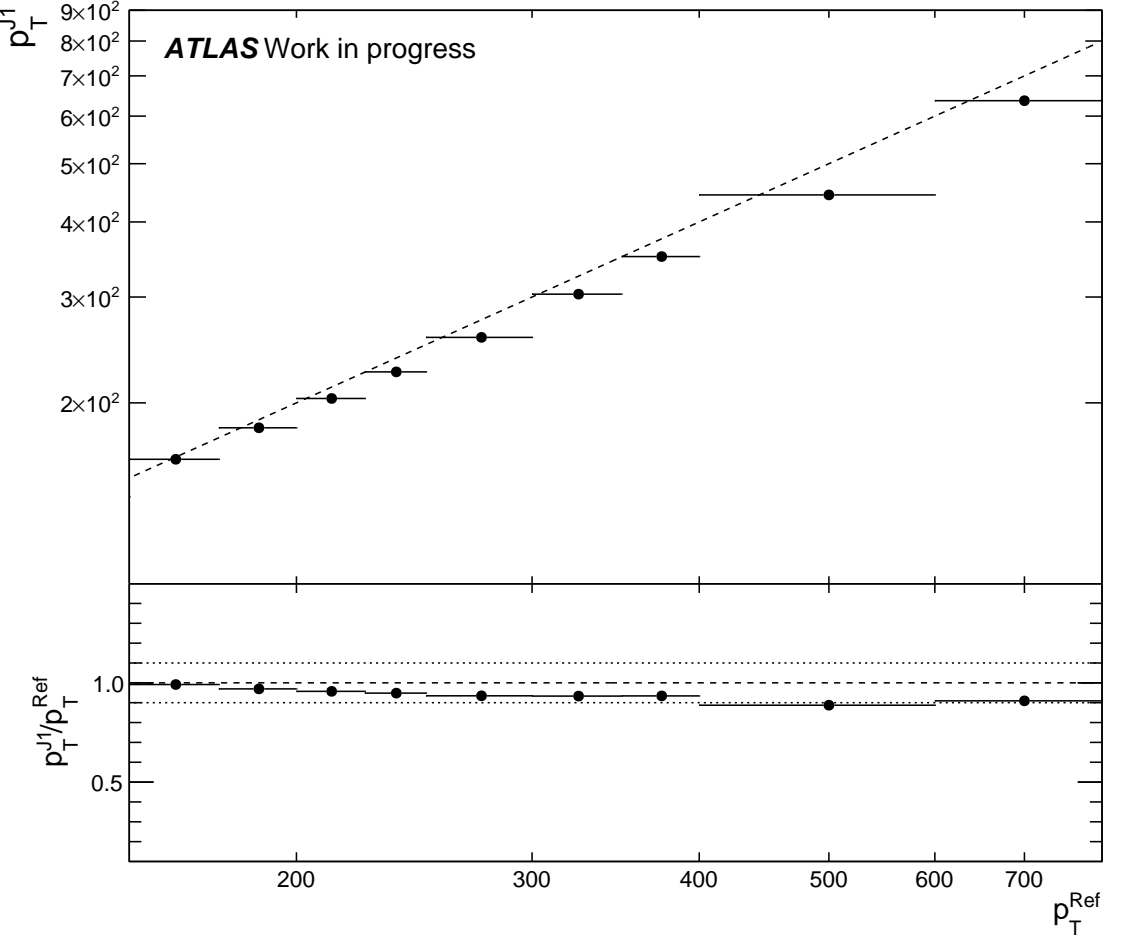


Figure 4.5. p_T^{Ref} with midpoint p_T^J values on a log scale. The horizontal bars represent the bin edges of the original p_T^{Ref} binning. The black dots in the top canvas shows the p_T^J midpoints for a given p_T^{Ref} slice. The diagonal line is $p_T^J = p_T^{\text{Ref}}$. The ratio plot shows the ratio of the midpoints of the p_T^J bins with the midpoints of the p_T^{Ref} bins. It is evident from this plot that the bins at higher p_T^{Ref} have a larger correction than the bins at lower p_T^{Ref} .

Up and down variations in the each of the scale and resolution systematic uncertainties are propagated independently through the analysis chain and are later symmetrised (with the exception of MC modelling and JVT). Systematic variations in the electron and muon calibration are applied only to simulation when calculating the systematic uncertainty on the double ratio c . Each source of uncertainty for the e/μ scale and resolution is considered as fully correlated across η and p_T , and are all added in quadrature (independently for electrons, and MS and ID components for muons)

The MC modelling uncertainty is evaluated by performing the response measurements separately for the SHERPA and Powheg+PYTHIA samples. The double ratio is calculated for both response measurements, and the difference between the nominal values defines the uncertainty. Sherpa is chosen as the nominal MC generator because a significantly larger degree of mismodelling is seen in the Powheg-Pythia samples as a function of jet p_T as shown in Figure 4.6.

For uncertainties associate with JVT, the *Medium* working point is used. The default *Tight* working point is defined by the threshold $JVT > 0.5$, and the *Medium* working point is

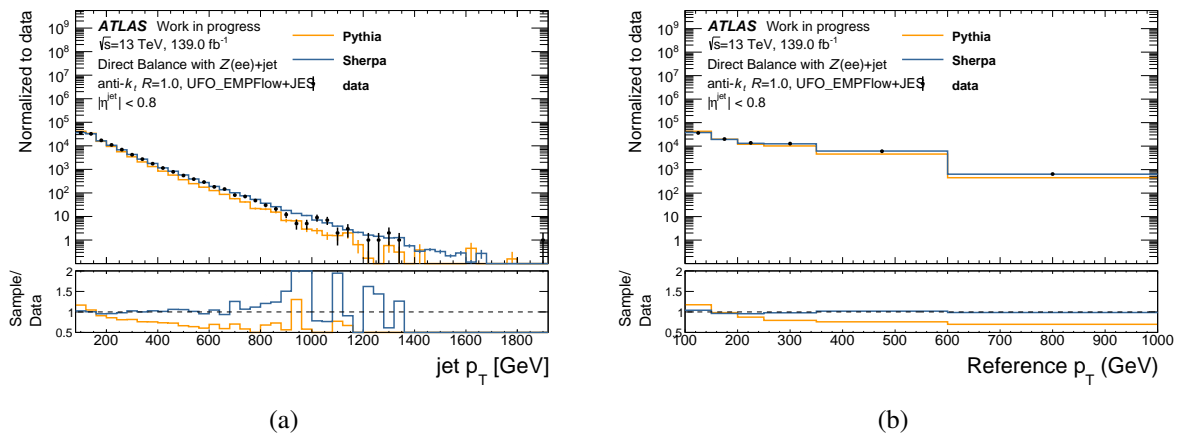


Figure 4.6. Data to MC distributions for the p_T^J (a) and p_T^{Ref} (b). The MC distributions are normalised to the data distribution. It is clear that there is a large degree of mismodelling in the POWHEG+PYTHIA MC sample which cannot be explained by the lack of an insitu calibration, as this is of the order of a few %. For this reason the POWHEG+PYTHIA sample is only used to quantify a systematic modelling uncertainty of c , and is not used in the calculation of the nominal value.

$JVT > 0.2$. The cut values refer to the output values of the JVT likelihood-based discriminant derived from simulated dijet events [140].

Systematic variations in the event selection criteria are carried out to test the assumption of a $2 \rightarrow 2$ topology. The $\Delta\phi(J, Z)$ variations are defined by varying the default selection by ± 0.1 radians. Table 4.3 gives the variations in the radiation veto. Event selection and JVT systematic variations are performed simultaneously in data and MC.

Each source of uncertainty is considered as fully correlated across η and p_T . Each uncertainty is evaluated by propagating each source through the analysis chain and calculating its effect on the double ratio, c . The final uncertainty is taken to be the quadrature sum of the individual uncertainties.

To prevent large statistical fluctuations in the systematic uncertainties, a *bootstrapping* procedure is used to determine a statistically significant re-binning for every source of uncertainty. In this procedure, 100 bootstrap replicas are created, where each replica has a copy of the nominal 2D distribution (Figure 4.2) and each systematically varied 2D distribution. For each event in the dataset, 100 event weights are chosen by sampling a Poisson distribution with mean of one. These represent a modified set of event weights, one for each bootstrap replica. Each replica histogram is then filled with its corresponding set of event weights. The sampling of the Poisson distribution depends on a random number uniquely determined from the run and event number. In this way, nominal events, and events corresponding to systematic variations remain correlated for every replica. The nominal R_{DB} response values for one of the p_T^{Ref} bins in data for 100 replicas is shown in Figure 4.7.

The re-binning procedure works by iterating over each p_T^{Ref} bin, and determining the double ratio c for each replica of the systematic variation (c_i^{sys}), and for each nominal replica (c_i^{nom}). The value of the systematic uncertainty for a given replica, i , is then given by:

$$\delta_{\text{sys},i} = \frac{c_i^{\text{sys}} - c_i^{\text{nom}}}{c_i^{\text{nom}}}. \quad (4.7)$$

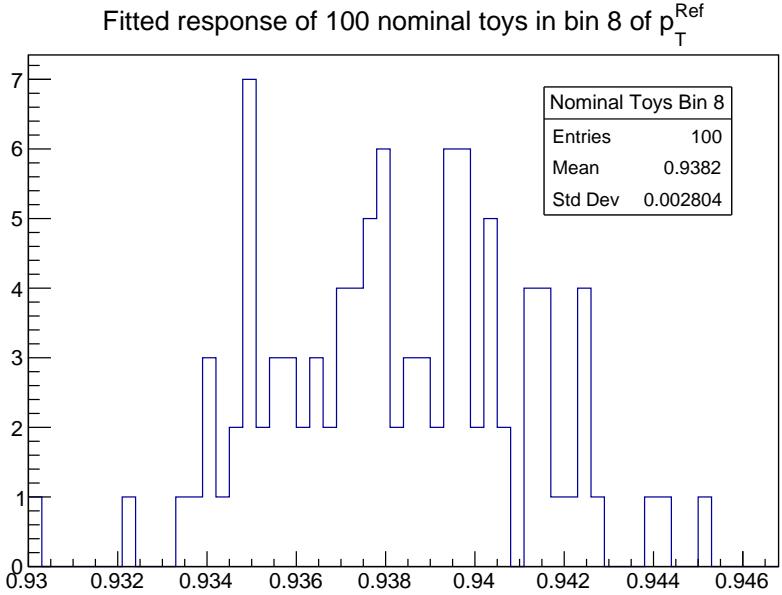


Figure 4.7. The R_{DB} response derived from 100 nominal replica distributions in bin 8 of p_T^{Ref} in the electron channel. Every entry in this histogram has a corresponding value for any given systematic uncertainty. By calculating the spread in the differences between these correlated values, the statistical significance of the systematic variation for a given bin can be ascertained. The x -axis shows p_T^{Ref} and the y -axis shows the number of replica instances per bin.

Table 4.4. Sources of uncertainty on the double ratio in the $Z+\text{jets}$ insitu correction.

| Component | Description |
|--------------------------------|--|
| e E scale | Uncertainty in the electron energy scale |
| e E resolution | Uncertainty in the electron energy resolution |
| μ p_T resolution ID | Uncertainty in muon p_T resolution in the ID |
| μ p_T resolution MS | Uncertainty in muon p_T resolution in the MS |
| μ p_T scale res. & comb. | Muon p_T scale uncertainties from (residual and combined) charge-dependent corrections |
| μ p_T scale | Uncertainty in the muon p_T scale from charge-independent corrections |
| MC modelling | Difference between MC event generators |
| Pile-up (JVT) | Jet vertex tagger uncertainty |
| $\Delta\phi$ | Variation of $\Delta\phi$ between the jet and Z boson |
| Small-R jet veto | Radiation suppression through second-jet veto |
| Statistical | Total MC and data Statistical uncertainty |

The statistical significance of the systematic variation is given by the ratio of the systematic uncertainty calculated from the un-fluctuated dataset, δ_{sys} , and the standard deviation of the replica systematic uncertainties. The systematic uncertainty is deemed to be statistically significant if this ratio is larger than 2. If this criteria is met, the bin is kept as it was. Otherwise, the p_T^{Ref} bin is combined with the next bin, and the nominal and systematic responses are re-fit with the combined bins. If the significance threshold is still not reached, the next p_T^{Ref} bin is added, and the responses are subsequently re-fit. To prevent over-binning, only a maximum of 5 bins are allowed to be combined. An example of a systematic uncertainty which is rebinned (MC modelling) and one which is not rebinned (electron energy scale) is shown in Figure 4.8.

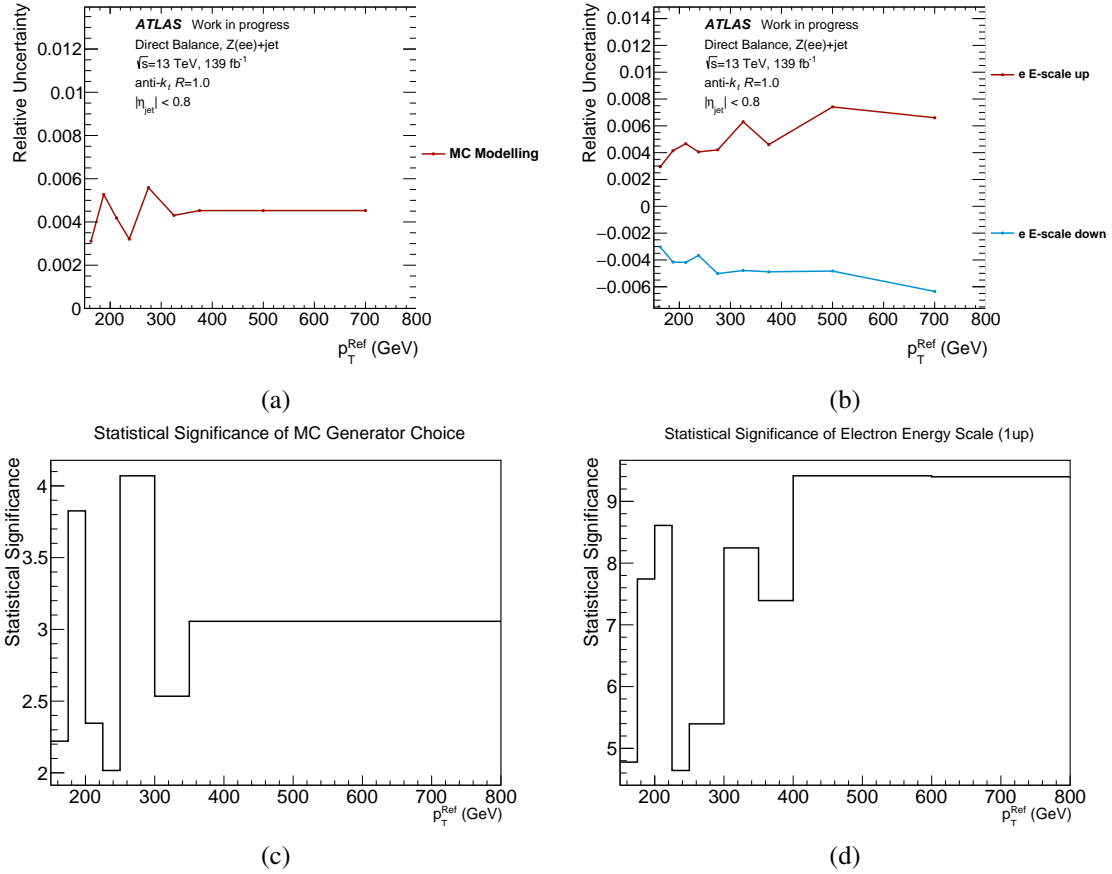


Figure 4.8. MC modelling uncertainty on R_{DB} prior to the mapping to p_T^J (a). Electron energy scale uncertainties on R_{DB} prior to mapping to p_T^J . Statistical significance of the MC modelling uncertainty is shown in (c), and the up variation of the electron energy scale in (d). In (a), the last two bins (bins 7 and 8) were not statistically significant, but were made statistically significant with the addition of bin 6. In (b), all uncombined bins are statistically significant, and no rebinning has taken place.

4.9 Results

The responses R_{DB} for the electron and muon channels after the p_T^{Ref} to p_T^J mapping are shown in Figure 4.9. The systematic uncertainties on the double ratio with p_T^{Ref} prior to symmetrising are shown in Figure 4.10. The final systematic uncertainties on p_T^J are shown in Figure 4.11. From the response distribution it is evident that the jets require a quasi-flat 2% correction in both electron and muon channels. The size of this correction is very similar to the one derived for large-R LCTopo jets [10]. However, the shape of the R_{DB} distribution is very different in that there is a clear up-turn at low p_T^J , this was not seen for large-R LCTopo jets. This upturn was seen in all the insitu calibrations (γ +jets, Z +jets, and MJB) for the UFO large-R insitu JES measurements [147].

4.10 Insitu combination

The results in Figures 4.11 and 4.9 were used in the insitu combination [147] to derive the precision recommendations for Athena Release-21 large-R UFO jets. In the combination, the η -intercalibration [149], γ +jets [150], Z +jets [151], and MJB results [152] are combined to form the final insitu correction factor (c) to the JES. The combination of all the c factors and

uncertainties is shown in Figure 4.12.

4.11 Small-R Insitu Calibration Cross-check

As an additional cross-check for the small-R EMPflow Z +jets insitu calibration, the InsituBalance software framework was used to derive the nominal insitu calibration. This was compared with the nominal insitu calibration derived using the software framework which is usually used for the small-R calibration in ATLAS (the MPF framework).

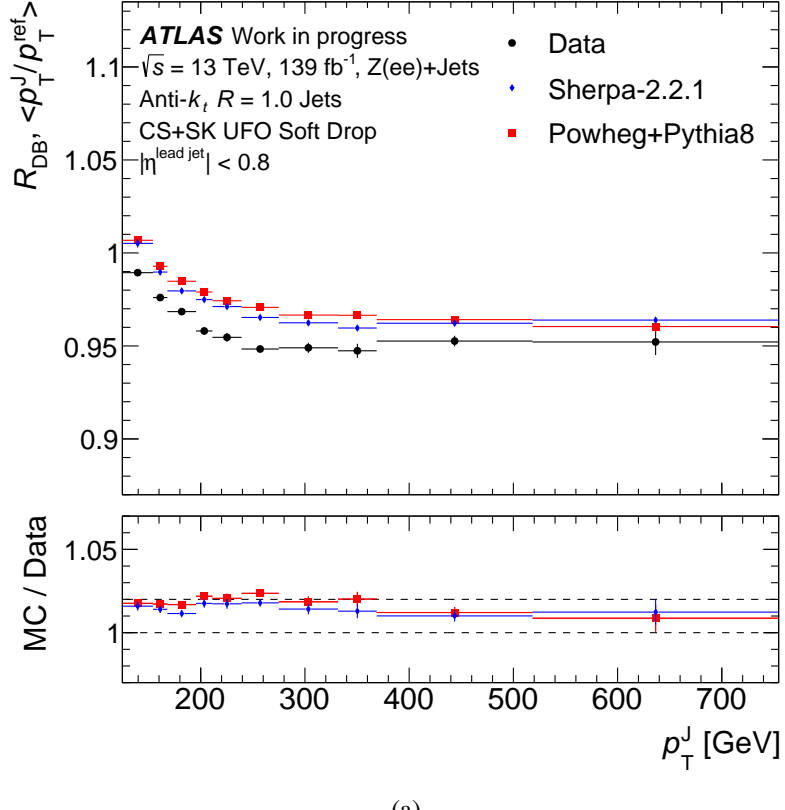
4.11.1 Samples, object definitions, and event selection

The comparison was done using 2018 data in the electron channel. Small-R EMPFlow jets are used in the calibration. The 2018 dielectron trigger described in Table 4.1 is used. Electrons are required to satisfy “Loose” ID and “Loose” isolation criteria. Jets are selected in the central $|\eta| < 0.8$ region. Jets are calibrated up to the MC JES + GSC (Global Sequential Calibration) level using the 2019 consolidated recommendations. Electrons are calibrated using the same prescription as in Section 4.5. Jets are required to satisfy $p_T^j > 10 \text{ GeV}$, and events are selected such that $\Delta\phi(j, Z) > 2.8$. In order to reduce contamination from events with large hadronic recoil, a sub-leading jet veto is applied such that $p_T^{\text{second}} < \max(20 \text{ GeV}, 0.1 \times p_T^{\text{Ref}})$, where p_T^{second} is the p_T of the sub-leading jet. The *Tight* JVT working point is used for jets with $p_T < 60 \text{ GeV}$ and $\eta < 2.4$. The only overlap removal requirement is that jets are required to satisfy $\Delta R(j, Z) > 0.2$.

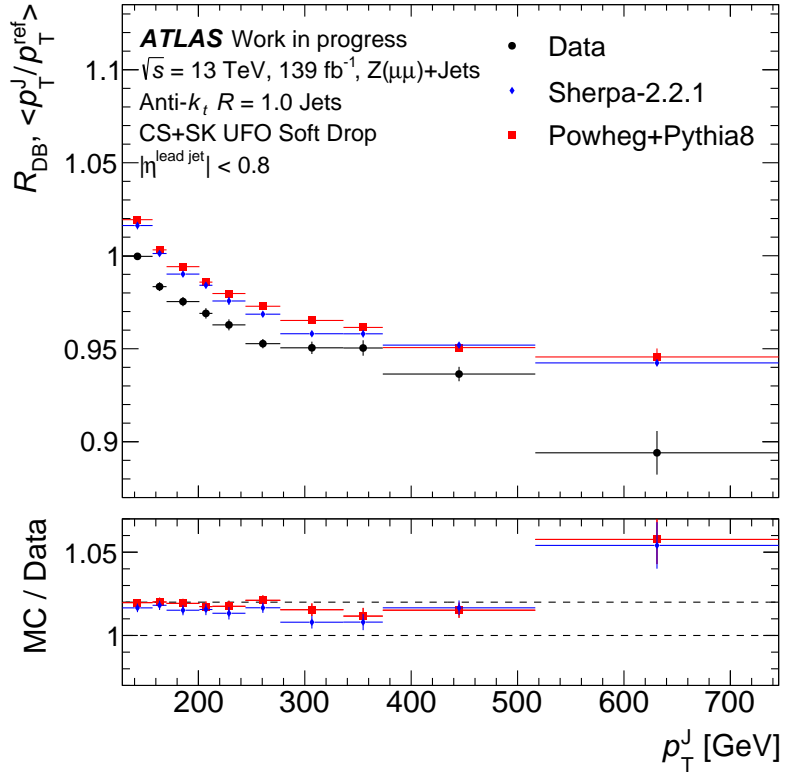
4.11.2 Results

The responses agree very well between the two frameworks, as shown in Figure 4.13. This serves as a cross-check for the small-R jet calibration, but indeed also gives confidence in the large-R calibration in that the software machinery is behaving as expected.

The slight differences between the response in Figures 4.13a and 4.13b can be attributed to differences in the fit range, fitting function, and binning of p_T^{Bal} . The InsituBalance framework uses a Gaussian fit over the fit range given by 1/8 times the maximum bin, and the MPF framework uses a modified Poisson distribution (a continuous generalisation of the Poisson distribution defined using the gamma function) with a dynamic, asymmetric p_T^{Bal} range. This was confirmed by explicitly checking the calibrated p_T^{Ref} and p_T^{Bal} values for individual events in the 2018 data sample in the two software frameworks, and equivalent values were obtained. The p_T^{Bal} fits in p_T^{Ref} bins for the InsituBalance framework and MPF framework are shown in Figures 4.14 and 4.15, respectively.

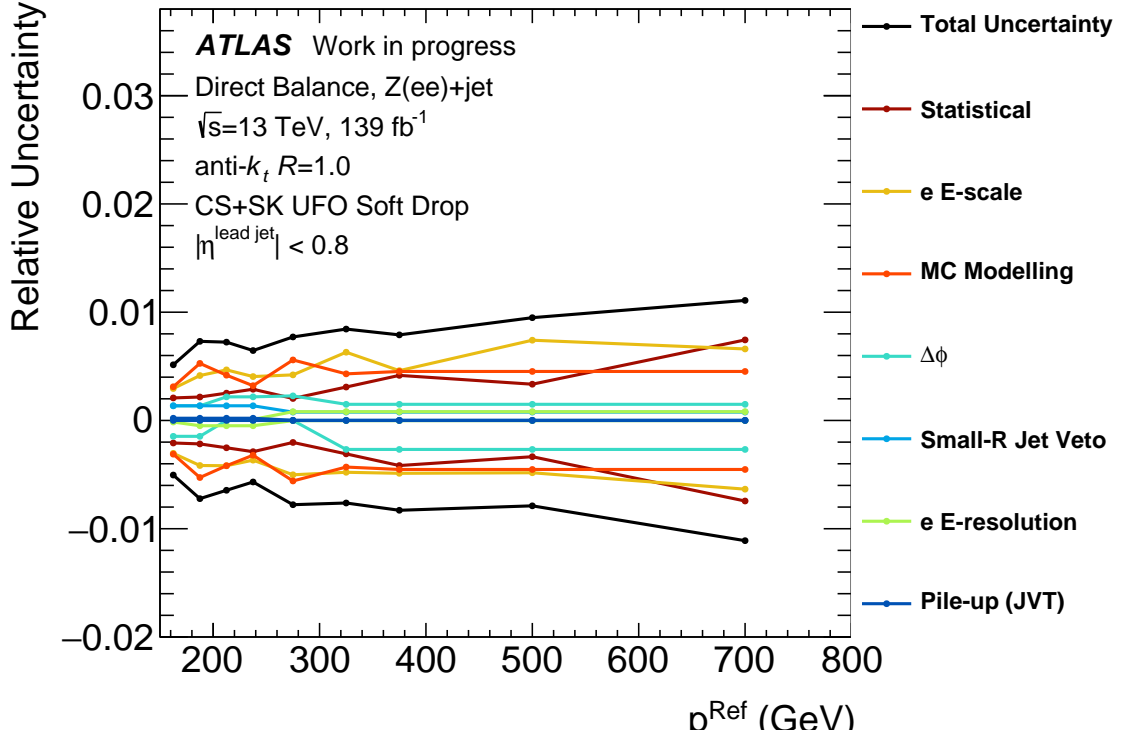


(a)

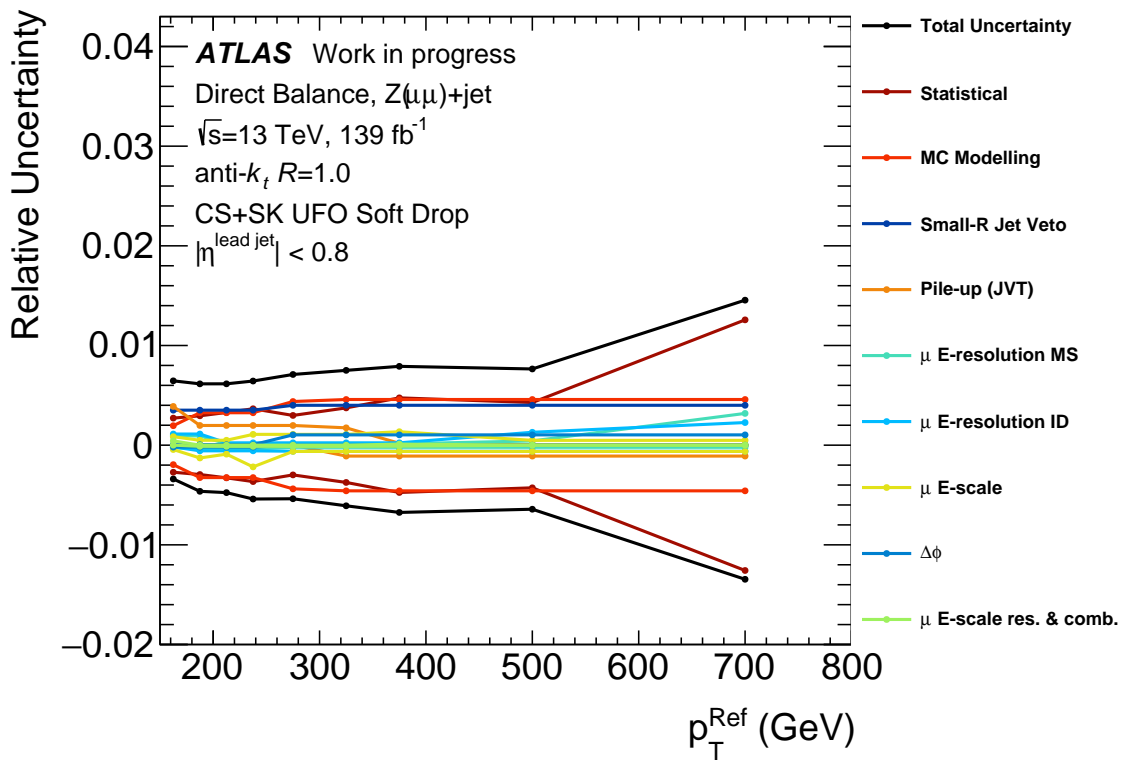


(b)

Figure 4.9. Direct balance response, R_{DB} , and the double ratio “MC/Data” ($1/c$), with leading large-R jet pt p_T^J . The error bars only show statistical uncertainties. (a) shows the response for the electron channel, and (b) shows the muon channel. In the final calibration, the final bin in the muon channel is omitted due to large statistical uncertainty on the response. This comes about because fewer events are selected in the muon channel (also seen in MPF results [148]).

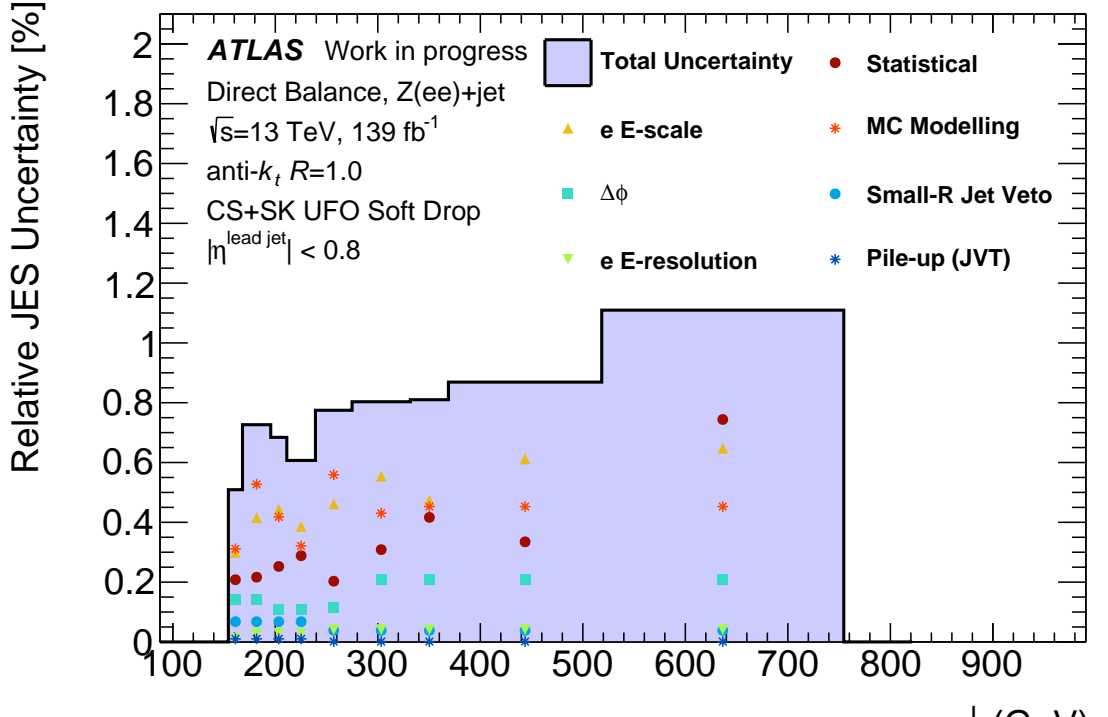


(a)

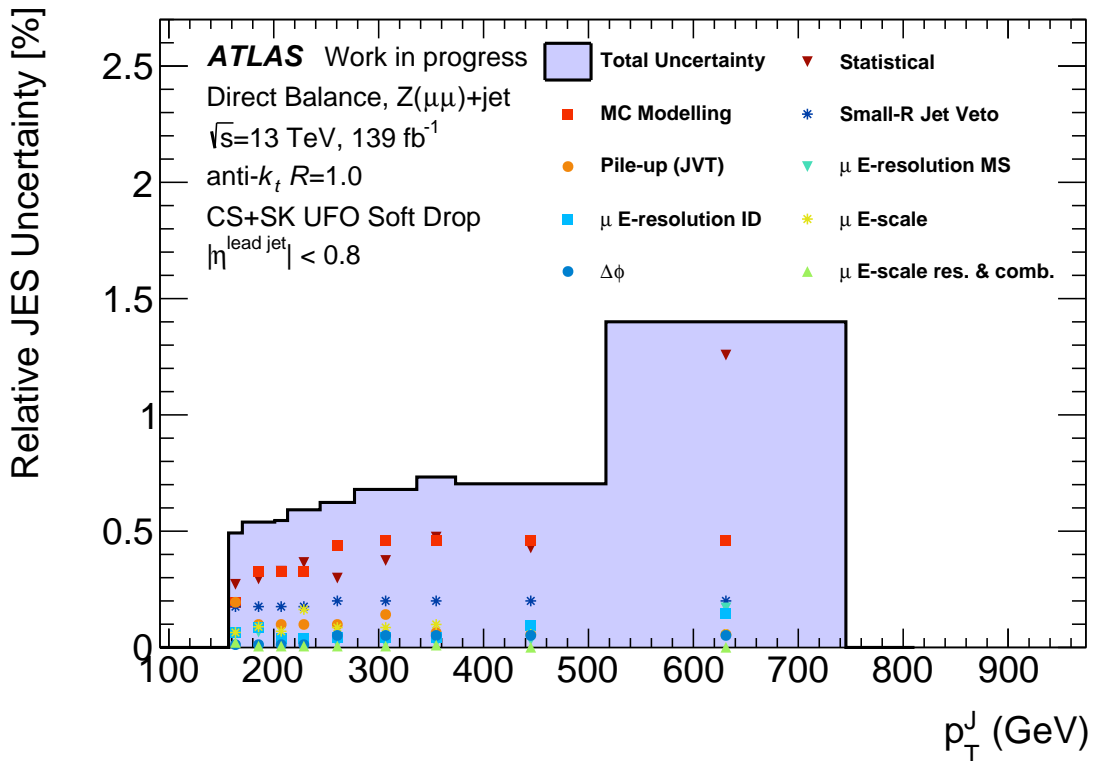


(b)

Figure 4.10. Uncertainties on the double ratio in the electron (a) and muon (b) channels with p_T^{Ref} before the mapping to p_T^J , and before symmetrising of the uncertainties. For uncertainties which do not have a down variation (for example statistical, MC modelling), a down variation is plotted by simply inverting the sign, this is done only for aesthetic reasons.



(a)



(b)

Figure 4.11. The final uncertainties on the insitu JES correction with p_T^J and symmetrised uncertainties in the electron (a) and muon (b) channels. Uncertainties are symmetrised by subtracting the down variations from the up variations and dividing by two.

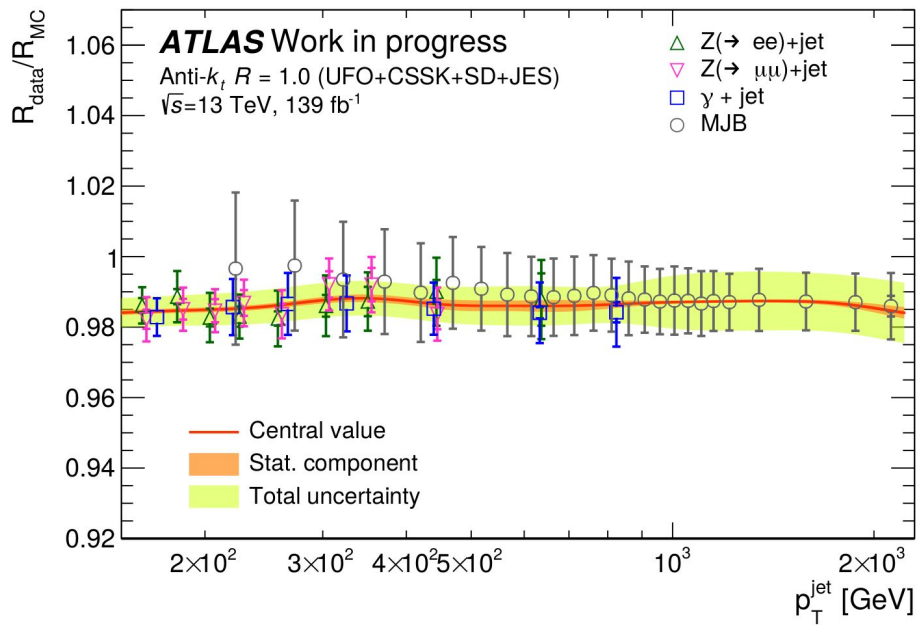
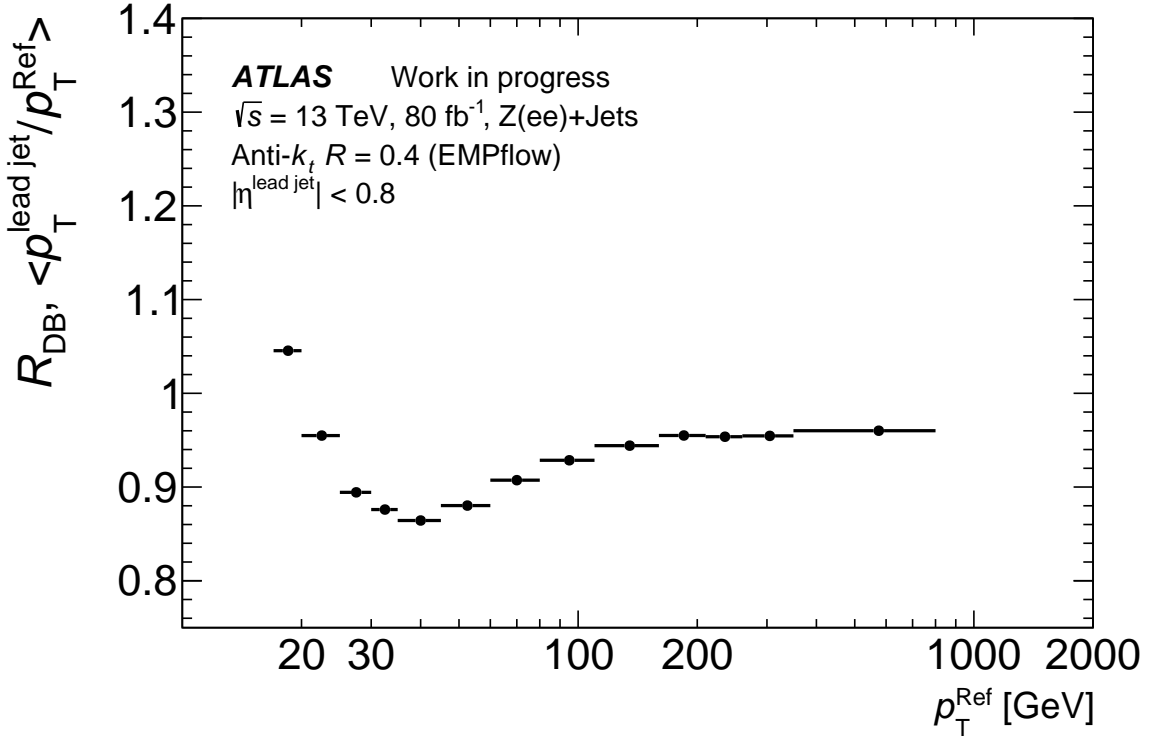
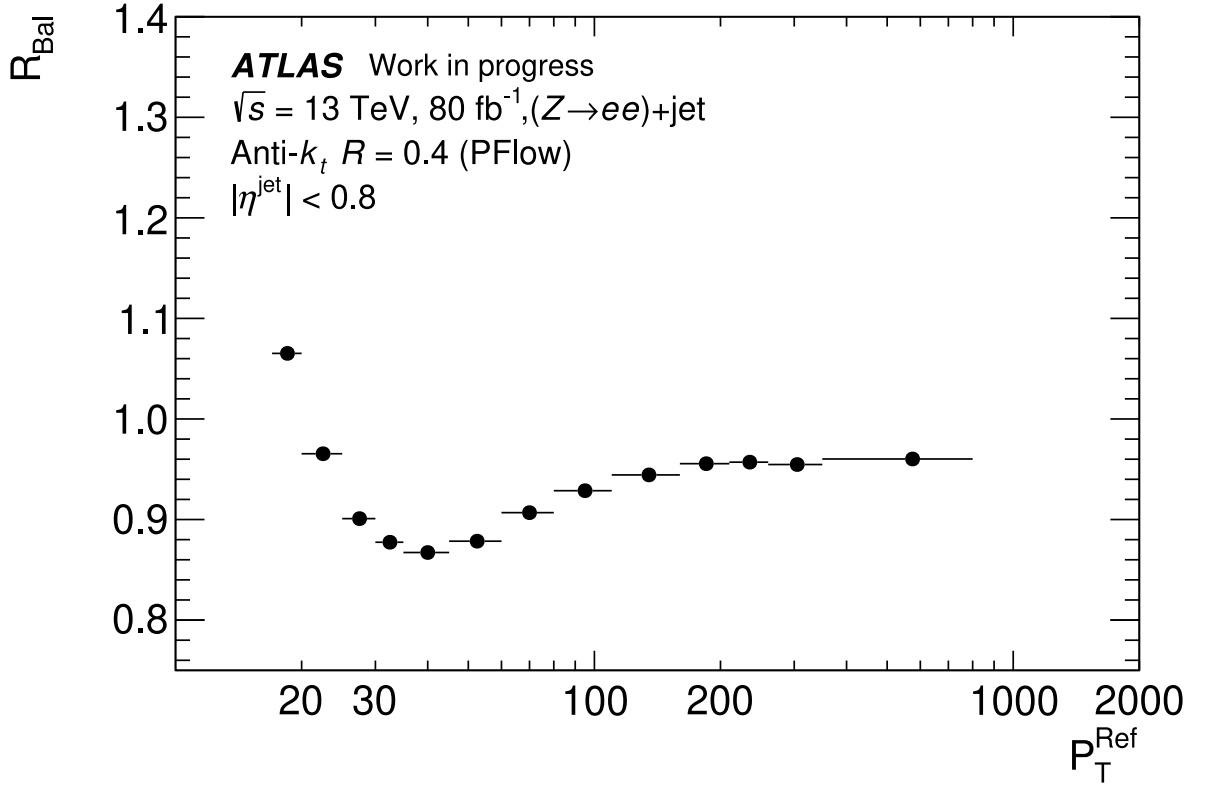


Figure 4.12. The combination of all the insitu measurements and the final insitu correction factor to the JES, with corresponding statistical and systematic uncertainties. The Z +jets and γ +jets results are in very good agreement. These results are derived completely independently using different software packages. The last data point from the $Z(\rightarrow \mu\mu)$ +jets calibration is omitted due to poor statistical precision in this bin. The Z +jets and γ +jets calibrations cover the 150-900 GeV range, and these calibrations typically have $< 1\%$ total uncertainty. From around 150-200 GeV the insitu correction is covered solely by Z +jets and γ +jets measurements, and superior precision is seen in the γ +jets channel. The 150-750 GeV range is covered by all insitu measurements. From around 200-500 GeV, the Z +jets channels have the superior precision, and from 500-900 GeV the γ +jets channel provides the superior measurement. Above 900 GeV, the calibration is solely covered by the MJB measurement. The final uncertainties on the combined calibration are typically below 0.5%. Figure taken from [147].



(a)



(b)

Figure 4.13. Comparison of the R_{DB} response between the InSituBalance software framework (a), and the MPF software framework (b) for 2018 data in the electron channel. The slight differences seen when comparing the first low p_T bins can be attributed to slightly different fit functions and fit range in the fits to determine the average response. The MPF framework response plot (b) was produced by Sahil Singh [153].

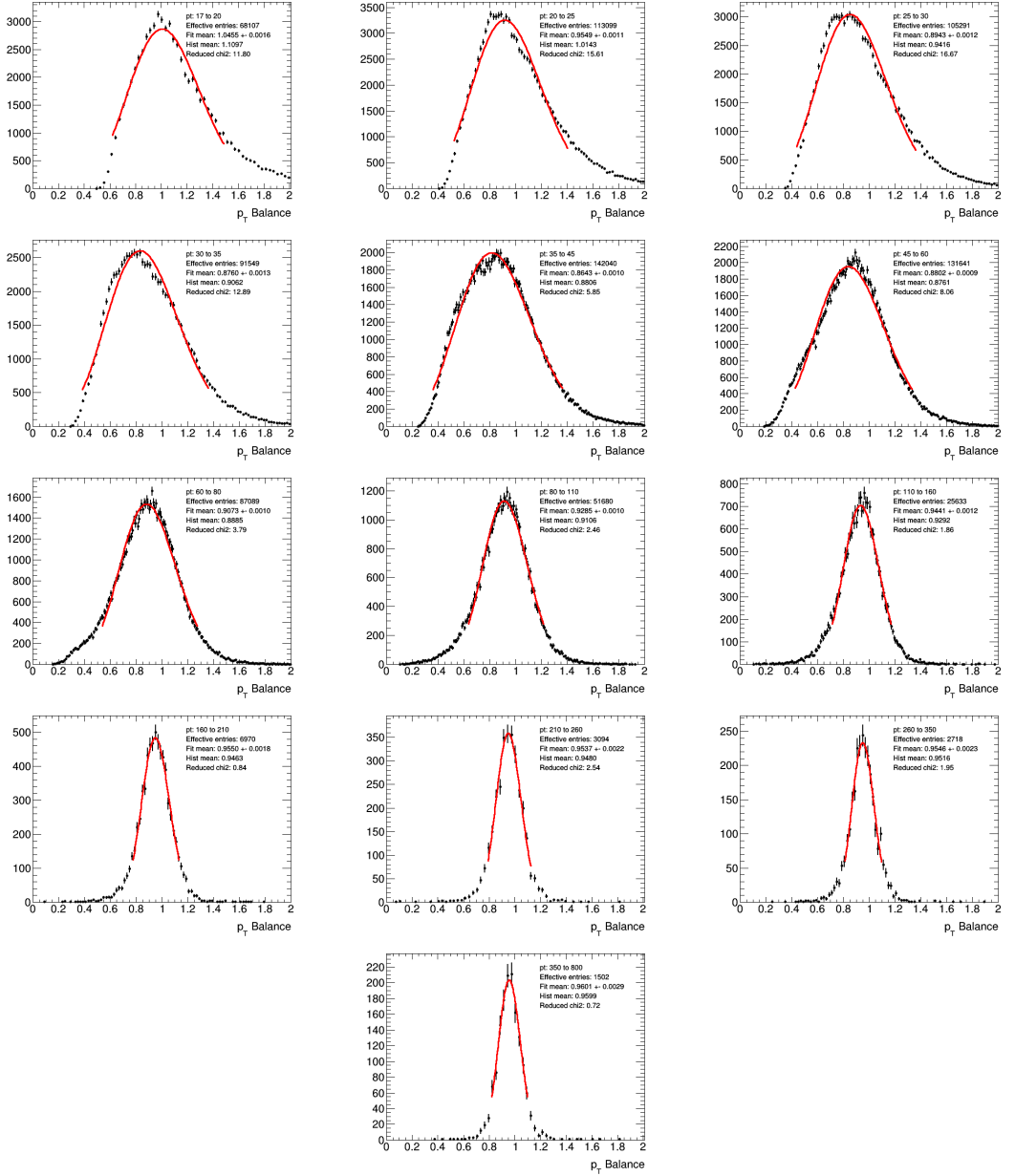


Figure 4.14. p_T^{Bal} distributions in small-R $Z(\rightarrow e^+e^-)$ +jets in the InsituBalance software framework. The increase of R_{DB} at low p_T^{Ref} can be attributed to the non-Gaussian nature of the low p_T^{Ref} bins. This behaviour can be attributed to the 10 GeV p_T^j cut.

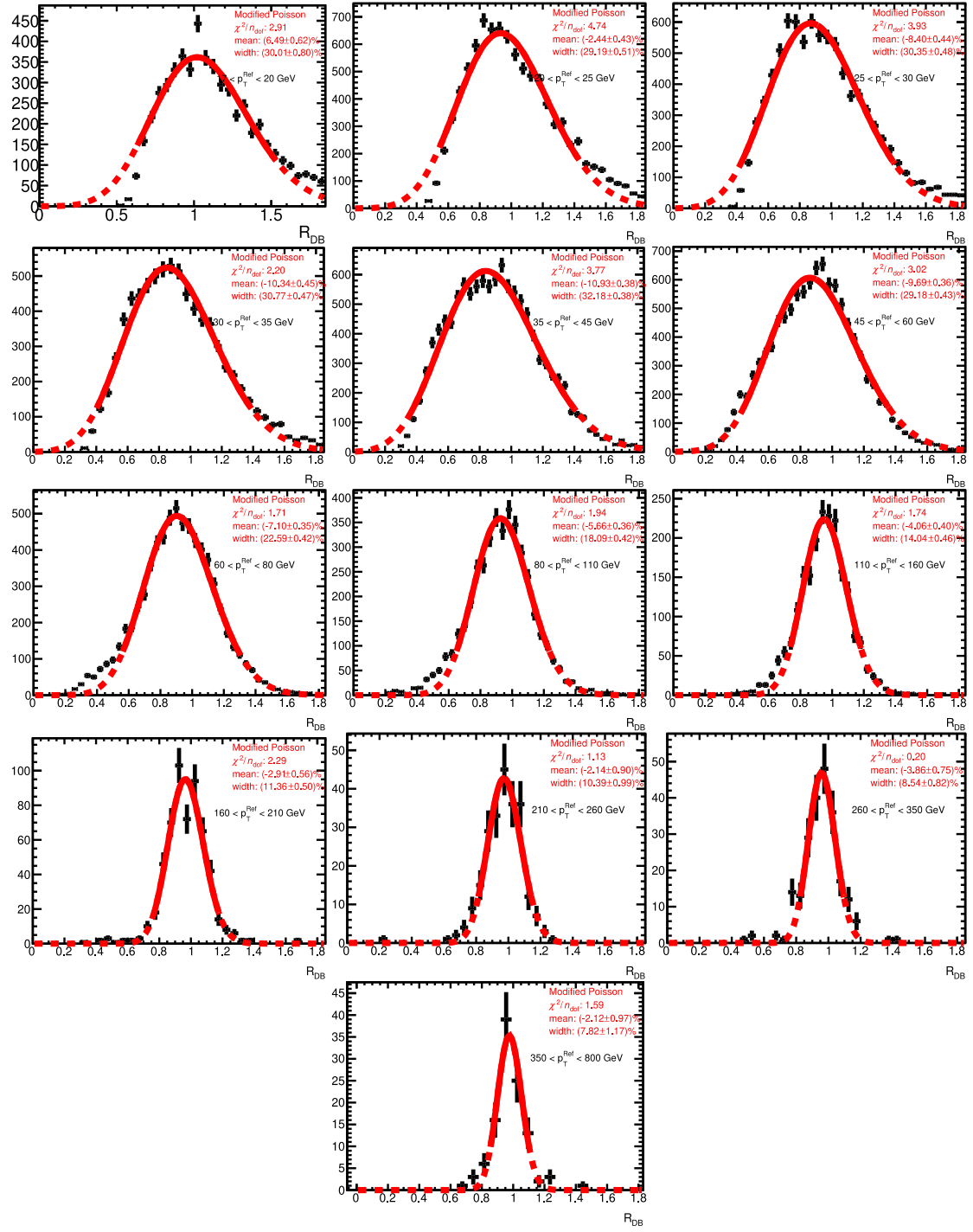


Figure 4.15. p_T^{Bal} distributions in small- R $Z(\rightarrow e^+e^-)+\text{jets}$ in the MPF software framework. A modified Poisson distribution with a dynamic asymmetric fit range is used here.

Chapter 5

Differential Cross-section Measurement of $W\gamma jj$ EW Production at $\sqrt{s} = 13 \text{ TeV}$

This chapter describes the first differential cross-section measurement at ATLAS of the electroweak production of a W boson and a photon in association with two jets. The research detailed in this chapter is included in a paper submitted to journal and publicly available at [53], where the differential cross-section measurements are used to derive constraints on dimension-8 operators in the context of an effective field theory (EFT). The paper also describes the observation and fiducial cross-section measurements of this process. The CMS collaboration has previously reported the observation [48] and differential cross-section measurements of this process [154]. The ATLAS paper is the first to publish constraints on the f_{T3} and f_{T4} operators¹ and also gives differential cross-section measurements of observables sensitive to CP-violating (CPV) Higgs and weak boson interactions. The work shown in this chapter is the authors own except when explicitly stated otherwise.

Unfolded differential cross-sections for EW- $W\gamma jj$ production are measured for 6 different observables. These are the dijet invariant mass m_{jj} , dijet transverse momentum p_T^{jj} , signed dijet azimuthal angle separation $\Delta\phi_{jj}^{\text{signed}}$, lepton transverse momentum p_T^ℓ , signed azimuthal angle separation of the lepton and the photon $\Delta\phi_{\ell\gamma}^{\text{signed}}$, and the invariant mass of the lepton-photon system $m_{\ell\gamma}$. The signed nature of the angular observables refers to the fact that the objects are rapidity ordered before subtracting the azimuthal angles. i.e.

$$\Delta\phi_{ij} = \phi_f^i - \phi_b^j, \text{ where } y_f^i > y_b^j. \quad (5.1)$$

The dijet invariant mass is one of the most important observables used to discriminate the strong production mode from the EW mode in VBS/VBF processes, in this way m_{jj} characterises the VBS measurement. The dijet transverse momentum probes the kinematics of the forward jet system. Preliminary EFT studies showed that $p_{T,jj}$ is expected to be more sensitive to dim-8 EFT contributions than m_{jj} . The p_T^ℓ and $m_{\ell\gamma}$ observables probe the kinematics of the central diboson system. Finally, the angular observables $\Delta\phi_{jj}^{\text{signed}}$ and $\Delta\phi_{\ell\gamma}^{\text{signed}}$ are expected to be sensitive to CPV gauge couplings contributing to the $WW\gamma\gamma$ and $WW\gamma Z$ vertices. The EW- $W\gamma jj$ differential cross-section paper [53] does not publish limits on these couplings as

¹The dimension-8 T operators are given by the different ways of contracting the SU(2) and U(1) field strength tensors, and represent anomalous quartic gauge interactions involving a γ and a W , without trilinear interactions. The T3 and T4 operators were only added to dimension-8 EFT models in March 2021, and have therefore remained unconstrained by measurements prior to this analysis [155].

they still need to be included in EFT models in MC event generators, but the published results may help future analyses looking to derive these limits.

5.1 Signal and Background Processes

5.1.1 Signal

The nominal sample for the EW production mode of $l\nu\gamma jj$ (referred to as $\text{EW-}W\gamma jj$ in this chapter) is generated using **SHERPA** 2.2.12 [37, 38], with LO matrix element accuracy, where the NNPDF3.0NNLO PDF set [131] is used, and the tuned parameter set used in the parton shower (PS), underlying event (UE), and hadronisation is the default one developed by the **SHERPA** authors. The ME calculation is performed for up to three partons in the final state using the internal ME generator **COMIX** [30], and the ME is merged with the PS for events using the **MEPS@LO** prescription [130]. All partons are treated as massless in the ME calculation, and massive in the PS, and diagrams involving initial state b -quarks are explicitly excluded in the ME calculation, as these diagrams are covered by separate single-top MC samples². The PS is conducted by **CSShower** [127], which is based on Catani-Seymour dipole factorisation [128].

An additional $\text{EW-}W\gamma jj$ sample is generated using **MADGRAPH5_AMC@NLO** (v.2.6.5) [39], with LO matrix-element (ME) accuracy in perturbative QCD, where the NNPDF2.3LO [131] PDF set is used in the calculation of the ME. The ME calculation is performed for two partons in the final state. The ME-level final state is interfaced with **PYTHIA8** (v8.240) [36] with dipole recoil turned on for generating the PS and UE, using the A14 [156] tuned parameter set for the modelling of non-perturbative effects. **EVTGEN** (v1.6.0) [126] is used for the properties of b - and c -hadron decays. The **SHERPA** sample has 4783000 total events, whereas the **MADGRAPH5_AMC@NLO** sample has 5013000 total events. The **SHERPA** sample is used as the nominal MC sample since the ME calculation is performed for up to three partons, compared to 2 partons (i.e. no extra emissions) in the **MADGRAPH5_AMC@NLO** sample.

It is worth commenting on the fact that LO samples are used for the simulations of the signal process. The current state-of-the-art for the MCnet MC generators are LO-merged samples, such as the **SHERPA** $\text{EW-}W\gamma jj$ sample used in this analysis. The NLO calculation for $V\gamma jj$ processes is extremely challenging because of the interference with the strong $V\gamma jj$ process and the presence of infrared singularities from NLO correction to both the electroweak and strong diagrams [157, 158].

²With this setup, diagrams involving the t-channel exchange of a Z -boson via a b -quark are excluded from the analysis. Separate studies have shown that this has a negligible impact.

5.1.2 Backgrounds

Strong $W\gamma jj$

The nominal irreducible background sample for the strong production mode of $l\nu\gamma jj$ (referred to as strong- $W\gamma jj$ in this chapter) is generated using **SHERPA** 2.2.11 [37, 38]. The sample is produced with NLO accurate MEs for up to one parton in the final state, LO accuracy MEs for up to 3 partons in the final state are calculated with **AMEGIC** [29] and **COMIX** [30]. Partons are treated as massless in the ME calculation, and massive in the PS. The PS is conducted with **CSShower** [127]. The matrix elements are matched to the PS, and different jet multiplicities are merged using the CKKW matching procedure [40, 41], which is extended to NLO accuracy using the **MEPS@NLO** [130] prescription. The **NNPDF3.0NNLO** [131] PDF set is used and the dedicated set of tuned parameters for the PS is developed by the **SHERPA** authors.

An alternate strong- $W\gamma jj$ background sample is generated using **MADGRAPH5_AMC@NLO** (v2.8.1) [39] with NLO ME accuracy up to one parton in the final state. The **NNPDF3.0NNLO** PDF set is used in the calculation. The partonic final state is interfaced with **PYTHIA8** (v8.244) [36], and the A14 [156] set of tuned parameters is used for PS, hadronisation and UE activity. **EvtGEN** (v1.7.0) [126] is used for the properties of b - and c -hadron decays.

118997000 events were generated for the **MADGRAPH5_AMC@NLO** sample, and 116239203 for the **SHERPA** sample. The **SHERPA** sample is chosen as the nominal MC sample. This choice is made because of the superior statistical precision of the expected number of events after the event selection described in Section 5.3.3. By comparing the statistical uncertainties on the total expected yields calculated using $\sqrt{\sum_i w_i^2}$, where w_i are the MC event weights, the statistical precision of the **SHERPA** sample was found to be 2.3 times better. The improved statistical precision arises due to a larger number of negative weights in **MADGRAPH5_AMC@NLO**.

Interference Between Strong and EW $W\gamma jj$

In the calculation of the inclusive cross-section of $W\gamma jj$ production, the electroweak and the strong scattering amplitudes can interfere. This interference is quantified in the matrix-element squared at LO as

$$|\mathcal{M}|^2 = |\mathcal{M}_{EW} + \mathcal{M}_{QCD}|^2 = |\mathcal{M}_{EW}|^2 + |\mathcal{M}_{QCD}|^2 + 2Re(\mathcal{M}_{EW}^* \mathcal{M}_{QCD}), \quad (5.2)$$

where \mathcal{M}_{EW} and \mathcal{M}_{QCD} represent the matrix elements for EW- $W\gamma jj$ and strong- $W\gamma jj$ production, and the last term corresponds to the interference contribution. The interference must be modelled to understand its impact relative to the EW- $W\gamma jj$ differential cross-section as a function of the measurement observables.

The interference sample was modelled at LO ME accuracy using **MADGRAPH 5**, which was interfaced with **PYTHIA8** (v8.244) for PS, hadronisation, and UE activity. **EvtGEN** (v1.7.0)

was used for the properties of b - and c -hadron decays. This sample was generated by the author. More details about the generation of the sample and truth-level validations studies are shown in Section 5.2.

Prompt Backgrounds

Backgrounds where the final state comprises at least two jets, a prompt lepton, and a prompt photon are referred to as prompt backgrounds. These include the production of top quarks in association with a prompt photon, as well as $Z\gamma jj$ production.

The simulations of top backgrounds consist of:

- $t\bar{t}\gamma$ production. This sample is produced at LO ME accuracy. The all-hadronic $t\bar{t}$ decays are not included in this sample.
- $tq\gamma$, which is the t-channel production of a single top quark in association with a prompt photon, a b -jet, and one additional jet. This sample is produced at NLO accuracy. The s-channel diagrams have a negligible contribution since they produce two b -jets in the final state, and a b -jet veto is applied in the analysis.
- $tW\gamma$ production, where the W decays either hadronically or leptonically, and the photon comes from radiation off a t , W or from their decay products. The sample is produced at LO accuracy. Diagrams where the photon is radiated from the initial state are highly suppressed as these involve additional heavy fermion internal lines.

All of the top background samples are simulated with the same event generation, showering, and hadronisation setup. They are generated with **MADGRAPH5_AMC@NLO** for the ME calculation, where the NNPDF2.3LO PDF set is used. The ME-level final state is interfaced with **PYTHIA8** for hadronisation, showering and UE activity, and the A14 set of tuned parameters is used. **EvtGEN** is used for the properties of b - and c -hadron decays.

The $Z\gamma$ backgrounds consist of:

- Strong- $Z\gamma jj$ production, which include separate samples for e, μ, τ, ν channels. MEs are calculated with **SHERPA 2.2.11** at NLO QCD accuracy for up to one additional parton, and LO accuracy for up to three additional partons.
- EW- $Z\gamma jj$ production with a t-channel requirement to suppress triboson final states. The ME is calculated with **SHERPA 2.2.12** at LO accuracy for up to one additional parton. Diagrams with initial state b -quarks are explicitly excluded.

The treatment of parton shower, hadronisation and underlying event is the same as the $W\gamma jj$ samples. The NNPDF3.0NNLO PDF sets are used.

Non-prompt backgrounds

Background events can arise from non-prompt leptons or photons in association with jets. Additionally, electrons can be mis-reconstructed as photons (referred to as $e \rightarrow \gamma$ backgrounds), and jets can be mis-reconstructed as photons ($j \rightarrow \gamma$) or leptons ($j \rightarrow e, j \rightarrow \mu$). The contributions from these backgrounds are estimated using data-driven methods as described in Section 5.4.

The GEANT4 toolkit [89] is used for detailed modelling of the ATLAS detector response. These simulations are compared to a dataset of pp collisions during the 2015-2018 data-taking period.

5.2 Interference Sample Generation and Validation Studies

The goal of studying the interference contribution was to derive an initial truth-level estimate of the ratio of the number of interference events to signal events. In addition a detector-level MC sample was produced based on this study and used in assigning a systematic uncertainty due to the interference contribution. Understanding the expected interference contribution is an important task, since performing the measurement in a phase space with a large interference fraction ($\gtrsim 20 - 30\%$) would result in a systematic uncertainty that would surpass the dominant uncertainty, potentially rendering the signal process as unmeasurable. A truth-level interference sample comprising of 400,000 events was generated using MADGRAPH to perform these studies.

At the stage of the analysis where these studies were performed, the final selection criteria had not yet been finalised. As a first pass for a VBS-enriched kinematic region, the analysis cuts from the CMS 8 TeV EW- $W\gamma jj$ paper [48] were used to study the expected interference contribution. These selection criteria are outlined in Table 5.1. These selection criteria are quite loose, with relatively soft m_{jj} and $p_{T,j}$ cuts, and no $\Delta y(j, j)$ cut. This allows the interference contribution to be studied as a function of m_{jj} and $\Delta y(j, j)$ spectra.

To investigate the impact of individual cuts on the signal-to-interference fraction (EW/int), the cuts in the bottom row of Table 5.1 were applied sequentially, and the EW/int ratio was plotted for each combination of cuts. This is shown in Figure 5.1 for m_{jj} and $\Delta y(j, j)$.

From Figure 5.1 it can be seen that the interference fraction is very dependent on m_{jj} and $\Delta y(j, j)$. Furthermore, it is evident that applying the cuts in Table 5.1 increases the interference fraction significantly below $\Delta y(j, j) = 2$ and $m_{jj} = 1$ TeV. Above $\Delta y(j, j) = 2$, the interference fraction is about 10% at low $\Delta y(j, j)$ and drops down to 0% at high $\Delta y(j, j)$. Without any $\Delta y(j, j)$ cuts, the interference fraction at $m_{jj} = 1$ TeV is about 10%, and this decreases at higher m_{jj} values. From these results it is clear that a $\Delta y(j, j)$ cut is necessary purely from the context of removing interference events. An m_{jj} cut of 500 – 1000 GeV would also improve the interference fraction. With these cuts, the interference fraction at truth-level is of the order of 5% or less. This was deemed to be an acceptable interference contribution.

Table 5.1. Selection criteria used to analyse the interference/EW ratio. The top part of the table forms the base selection criteria. The bottom half contains the event selection criteria which are sequentially applied in Figure 5.1. These are applied on top of the base selection criteria. The selection criteria are taken from [48], with the ΔR cuts changed to match the ATLAS small-R jet definition.

| Variable | Selection |
|--|------------------------------------|
| $p_T^{e(\mu)}, \eta^{e(\mu)} $ | $> 30(25) \text{ GeV}, < 2.4(2.1)$ |
| $p_T^\gamma, \eta^\gamma $ | $> 22 \text{ GeV}, < 1.44$ |
| Number of electrons/muons; jets; photons | $=1, \geq 2, \geq 1$ |
| E_T^{miss} | $> 35 \text{ GeV}$ |
| $M_T^W \equiv \sqrt{2p_T^l E_T^{\text{miss}}[1 - \cos(\Delta\phi(l, p_T^{\text{miss}}))]}$ | $> 30 \text{ GeV}$ |
| $p_T^{j_1}(p_T^{j_2})$ | $> 40(30) \text{ GeV}$ |
| m_{jj} | $> 200 \text{ GeV}$ |
| $ m_{e,\gamma} - m_Z $ | $< 10 \text{ GeV}$ |
| $\Delta\phi(j, p_T^{\text{miss}})$ | > 0.4 |
| Overlap Removal (OR) (object/against) | j/e, γ/j , $\gamma/e(\mu)$ |
| j_1, j_2 bjet veto | |
| $\Delta R(j_0, j_1), \Delta R(j, \gamma), \Delta R(j, e(\mu)), \Delta R(e(\mu), \gamma)$ | > 0.4 |

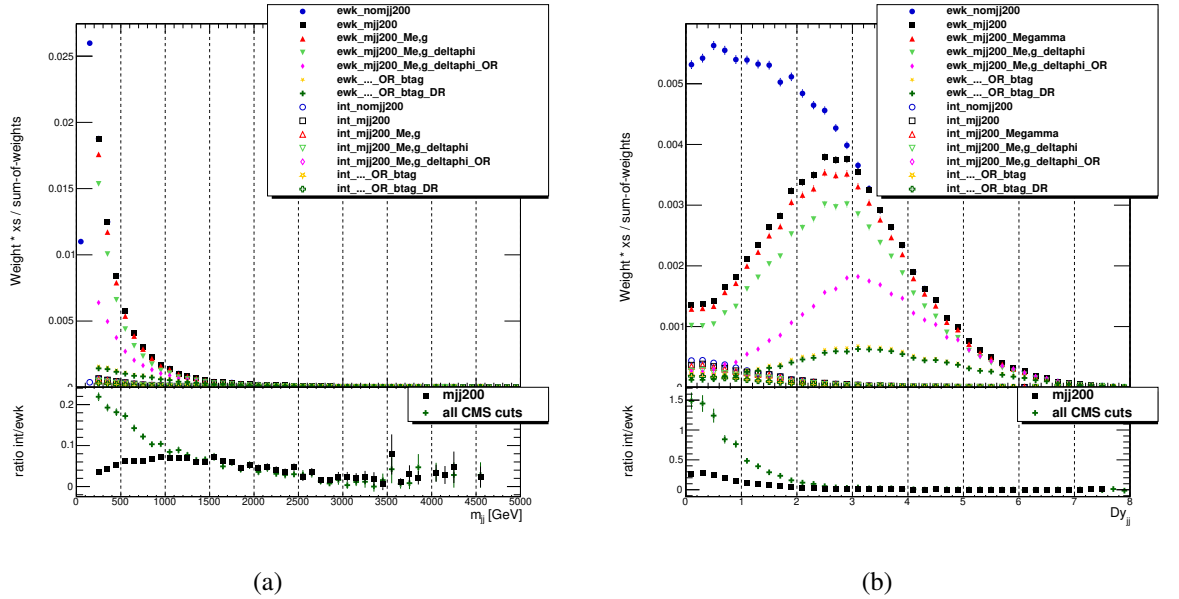


Figure 5.1. Truth level event yields (without a luminosity factor) generated using MADGRAPH 5 for the EW-W γjj signal, and the interference for m_{jj} in (a), and $\Delta y(j, j)$ in (b). The solid markers represent the EW-W γjj signal, and the hollow points represent the interference. The points labelled “_nomjj200” have all the cuts applied above the two horizontal lines in Table 5.1, and subsequent markers listed in the top panel legend have the additional cuts applied in Table 5.1. In the ratio panel, the “mjj200” points have the baseline selections and the $m_{jj} > 200$ GeV cut applied, and the “all CMS cuts” points have all the baseline and additional cuts applied. There is a clear phase space dependence on the interference fraction most notably with m_{jj} and $\Delta y(j, j)$ selection requirements.

The generation of a detector-level interference sample has to be requested centrally, and significant computational resources are required to produce such a sample. Therefore, it is important that an appropriate number of simulated events are requested such as not to unnecessarily waste computational resources.

To calculate the number of simulated events required to reach a similar statistical precision as the nominal EW-W γjj signal sample, the number of negative weights has to be taken into account. Since the signal sample MEs are calculated at LO, the event weights are all positive and there is no penalty to the effective statistical precision due to the presence of negative weights cancelling positive weights. For the interference sample, however, there will be a

significant contribution from negative event weights.

To calculate the statistical penalty due to negative event weights, we use the fact that the LO event weights are given by $\pm c$, i.e. event weights only differ by a change in sign, therefore the event weight just factorises out when calculating the statistical uncertainty:

$$\begin{aligned}\delta_{\text{abs}}^{\text{stat}} &= \sqrt{\sum_{n_+} (+c)^2 + \sum_{n_-} (-c)^2} = c\sqrt{n_+ + n_-} \\ \delta_{\text{rel}}^{\text{stat}} &= \frac{\delta_{\text{abs}}^{\text{stat}}}{(n_+ - n_-)c} = \frac{\sqrt{n_+ + n_-}}{n_+ - n_-} = \frac{1}{\sqrt{N_{\text{gen}}}} \frac{1}{1 - 2f_-},\end{aligned}\quad (5.3)$$

where n_+ and n_- are the number of positive and negative weights, respectively; $N_{\text{gen}} \equiv n_+ + n_-$ is the total number of generated events; $\delta_{\text{abs}}^{\text{stat}}$ and $\delta_{\text{rel}}^{\text{stat}}$ are the absolute and relative MC statistical uncertainties; and $f_- \equiv n_- / N_{\text{gen}}$ is the fraction of negative weights. If $f_- = 0$, the statistical precision is given by $1/\sqrt{N_{\text{gen}}}$. Therefore the effective number of events with a non-zero fraction of negative weights is given by:

$$N_{\text{eff}} = (1 - 2f_-)^2 N_{\text{gen}}, \quad (5.4)$$

i.e. the penalty to the statistical precision due to negative weights is given by $(1 - 2f_-)^2$.

In Figure 5.2, the fraction of negative weights is plotted with m_{jj} and $\Delta y(j, j)$ with cuts at $m_{jj} > 200 \text{ GeV}$; $m_{jj} > 200 \text{ GeV}, \Delta y(j, j) > 1$; and $m_{jj} > 500 \text{ GeV}, \Delta y(j, j) > 2$ in order to investigate the required number of events in different regions of phase space. The fraction of negative weights is relatively flat with m_{jj} and $\Delta y(j, j)$ in the three different regions. Therefore the integrated fraction of negative weights is used as the metric to determine the required statistical precision of the sample. The average integrated fraction of negative weights is $f_- = 0.37$, which gives a statistical penalty of about 12, which means that the interference sample would need about 12 times the number of events to equal the statistical precision of the MADGRAPH EW-W γjj signal sample. However, since the interference fraction is likely to be $< 5\%$, the decision was made to request $5 \times$ the number of events.

5.3 Object and Event Selections

5.3.1 Derivations and Triggers

The analysis uses derivations which are skimmed using the preselections of passing a single-lepton trigger, and the presence of at least one lepton with $p_T \geq 20 \text{ GeV}$ within the $|\eta| < 2.6$ acceptance. The data are required to pass un-prescaled single lepton triggers. These triggers are listed in Table 5.2. The data are required to pass data-quality criteria to ensure the data were taken during periods where the detector subsystems were fully functioning. This is achieved via “GoodRunsLists (GRLs)”, which are provided by the ATLAS Data Quality group.

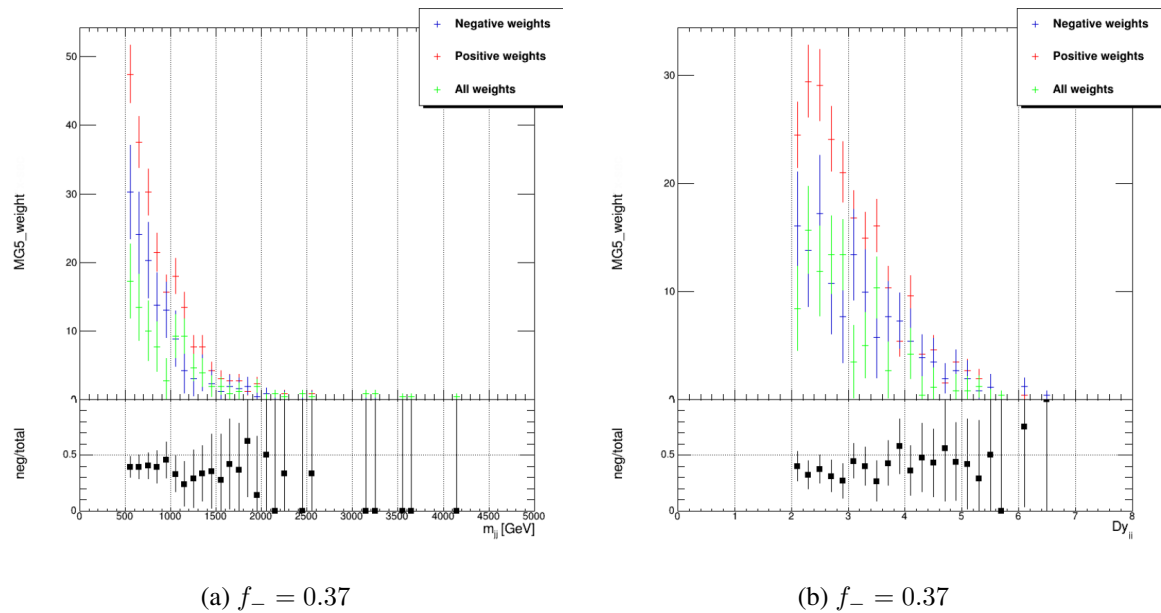


Figure 5.2. MC weights in bins of m_{jj} (a), and $\Delta y(j,j)$ (b) with the $m_{jj} > 500$ GeV, $\Delta y(j,j) > 2$ cuts applied. The integrated fraction of negative weights is shown in the subfigure captions. The sign of the negative weights is not shown. The ratio panel shows the fraction of negative weights for a given m_{jj} or $\Delta y(j,j)$ bin.

5.3.2 Object Selections

Photons

Photons are reconstructed from calorimeter deposits in the second layer of the EM calorimeter as described in Section 3.2.6. Photons are calibrated using the ‘‘EgammaCalibrationAndSmearingTool’’ with the ESModel ‘‘es2018_R21_v0’’ configuration using the decorrelation model setting ‘‘1NP_v1’’, corresponding to only one scale and resolution systematic variation. The ‘‘ElectronPhotonShowerShapeFudgeTool’’ is used to correct for imperfectly modelled shower shape variables. After calibration, photons are required to pass object quality, cleaning, disambiguation, and high-voltage cell removal using the corresponding tools in the ATLAS software framework. The kinematic requirement for photons is $p_T > 22$ GeV. Photons are required to pass *Tight ID* and *FixedCutTightCaloOnly* isolation defined as $E_T^{\text{cone}40} < 0.22p_T + 2.45$ GeV. Scale factors are applied to simulation to correct for the disagreement in the photon selection efficiencies between data and simulation (refer to Section 3.2.6 for a description of scale factors).

Electrons

Electrons are reconstructed from ID tracks and calorimeter information as described in Section 3.2.6. Electrons are calibrated using the ‘‘EgammaCalibrationAndSmearingTool’’ with the ESModel ‘‘es2018_R21_v0’’ configuration and using the decorrelation model setting ‘‘1NP_v1’’, such that there is only one non-zero scale and resolution systematic variation. Electrons are required to satisfy a kinematic requirement of $p_T > 30$ GeV, and are constrained to originate from the primary hard-scatter vertex through the impact parameter requirements

| | Year | Level1 | HLT |
|--------------------------------|----------------|---|---|
| Single electron trigger | 2016/2017/2018 | $E_T > 22 \text{ GeV}(*);$ Hadronic activity veto; Isolated | $E_T > 26 \text{ GeV};$ tight ID, d_0 unused; loose isolation |
| | 2016/2017/2018 | $E_T > 24 \text{ GeV}(*);$ Hadronic activity veto; Isolated | $E_T > 60 \text{ GeV};$ medium ID, d_0 unused |
| | 2016/2017/2018 | $E_T > 24 \text{ GeV}(*);$ Hadronic activity veto; Isolated | $E_T > 140 \text{ GeV};$ loose ID, d_0 unused |
| | 2015 | $E_T > 20 \text{ GeV}(*);$ Hadronic activity veto | $E_T > 24 \text{ GeV};$ medium ID |
| | 2015 | $E_T > 22 \text{ GeV}(*);$ Hadronic activity veto; Isolated | $E_T > 60 \text{ GeV};$ medium ID |
| | 2015 | $E_T > 22 \text{ GeV}(*);$ Hadronic activity veto; Isolated | $E_T > 120 \text{ GeV};$ loose ID |
| Single muon trigger | 2016/2017/2018 | $E_T > 20 \text{ GeV}$ | $E_T > 26 \text{ GeV};$ medium isolation |
| | 2016/2017/2018 | $E_T > 20 \text{ GeV}$ | $E_T > 50 \text{ GeV}$ |
| | 2015 | $E_T > 15 \text{ GeV}$ | $E_T > 20 \text{ GeV};$ loose isolation |

Table 5.2. Triggers used in the differential cross-section measurement. Multiple triggers for the same running period are combined such that an event is accepted when it passes any one of the individual triggers. An η -dependence of the L1 trigger threshold is denoted by (*).

$|d_0|/|\sigma_{d_0}| < 5$ and $|z_0 \sin \theta| < 0.5\text{mm}$. The geometrical acceptance requirements are that electrons satisfy $|\eta| < 2.47$, but excluding the gap region between the barrel and endcap EM calorimeters at $1.36 < |\eta| < 1.52$. Electrons satisfy *Tight* isolation, and *Tight* ID requirements. Scale factors are applied to simulation to correct for the disagreement in the electron selection efficiencies between data and simulation.

Muons

Muons are reconstructed from MS tracks matched to ID tracks as described in Section 3.2.6. Scale factors are applied to simulation to correct for disagreement in the muon selection efficiencies between data and simulation. Muons are calibrated using the “MuonCalibrationAndSmearingTool” with the “correctData_IDMS” scheme which gives muon track resolution and momentum scale systematic variations on the separate ID and MS components of the combined muon. Muons are required to satisfy *Tight* ID and *PflowTight_VarRad* isolation requirements, where the “VarRad” suffix refers to a shrinking isolation cone radius as high p_T . Reconstructed muons have a kinematic requirement of $p_T > 30 \text{ GeV}$, and are constrained to originate from the primary hard-scatter vertex through the impact parameter requirements $|d_0|/|\sigma_{d_0}| < 3$ and $|z_0 \sin \theta| < 0.5\text{mm}$. The geometrical acceptance requirements are that muons satisfy $|\eta| < 2.5$. To get the muon reconstruction and selection, isolation, and track-to-vertex association efficiency scale factors, the “MuonEfficiencyScaleFactors” tool with the “210222_Precision_r21” calibration release is used. This tool is also used to get the individual scale factor systematic variations.

Jets

Jets are reconstructed from EMPFlow input objects using the anti- k_t algorithm with radius parameter $R = 0.4$. Jets are calibrated using the “JetCalibrator” tool in Athena using the “JES_MC16Recommendation_Consolidated_PFlow_Apr2019_Rel21.config” config file. Jets have a kinematic requirement of $p_T > 25 \text{ GeV}$, and are required to satisfy $|\eta| < 4.5$. Jets with $p_T > 60 \text{ GeV}$ and $|\eta| < 2.4$ are required to pass the *Tight Jet Vertex Tagger* [140] working point. Scale factors are applied to simulation to correct for the disagreement in JVT efficiency between simulation and data. For b -jet tagging, the 85% efficiency working point is used in the “BTaggingSelectionTool” which uses the DL1r [114] algorithm. The 85% working point was found to optimise background rejection from single-top backgrounds. Disagreements in b -tagging efficiencies between data and simulation are corrected for with b -tagging scale factors. Jet Energy Scale (JES) and Jet Energy Resolution (JER) systematic uncertainties are evaluated using the “rel21/Summer2022/R4_CategoryReduction_FullJER.config” configuration of the JetCalibrator tool. This configuration is designed for analyses which have large JES and JER uncertainties and contains roughly 30 JES uncertainty components, and 13 JER uncertainty components.

Overlap Removal

To prevent detector signals from one object being used in the reconstruction of a different object, an object overlap removal procedure is applied according to the ATLAS standard overlap removal tool [141] in the following order:

- If two electrons share the same track in the ID, the electron with the lowest p_T is rejected.
- Calorimeter muons are rejected against electrons if they share the same track in the ID.
- Electrons are rejected against muons if they share the same track in the ID.
- Photons are rejected against electrons if $\Delta R < 0.4$.
- Photons are rejected against muons if $\Delta R < 0.4$.
- Jets are rejected against electrons if $\Delta R < 0.2$.
- Electrons are rejected against jets if $\Delta R < 0.4$.
- Jets are rejected against electrons if $\Delta R < 0.2$.
- Jets are rejected against muons if there are < 3 tracks and either the jet and the muon are ghost-associated³ or $\Delta R < 0.2$.
- Muons are rejected against jets if $\Delta R < 0.4$.
- Photons are rejected against jets if $\Delta R < 0.4$.

³With “ghost-association” particles can be associated to jets by treating them as particles with negligible p_T and clustering them within the jet [142].

| Variable | Selection | Description |
|---|--------------------------|---|
| N_{PV} | ≥ 1 | At least one primary vertex |
| $N_{\ell}; N_j; N_\gamma$ | $\geq 1, \geq 2, \geq 1$ | At least one lepton, 2 jets, and one photon |
| Second lepton veto | <i>Loose ID</i> | Veto events with loose second lepton |
| $E_{\text{T}}^{\text{miss}}$ | $> 30 \text{ GeV}$ | Missing transverse energy |
| $\Delta\phi(j, p_{\text{T}}^{\text{miss}})$ | > 0.4 | Azimuthal separation |
| $M_{\text{T}}^W \equiv \sqrt{2p_{\text{T}}^{\ell}E_{\text{T}}^{\text{miss}}[1 - \cos(\Delta\phi(\ell, p_{\text{T}}^{\text{miss}}))]}$ | $> 30 \text{ GeV}$ | Reconstructed transverse W mass |
| $ M_Z - M_{\ell\gamma} $ | $> 10 \text{ GeV}$ | Z -veto in 10 GeV window around Z mass |
| $p_{\text{T}}^{j_1}$ | $> 50 \text{ GeV}$ | Hard leading jet |
| $p_{\text{T}}^{j_2}$ | $> 50 \text{ GeV}$ | Hard subleading jet |
| b -jet veto | 85% WP | Veto events with b -jets |
| m_{jj} | $> 1 \text{ TeV}$ | Dijet mass |
| $\Delta y(j, j)$ | > 2 | Dijet rapidity separation |

Table 5.3. Selection criteria defining the analysis phase space for the differential cross-section measurement.

Missing Tranverse Energy

The $E_{\text{T}}^{\text{miss}}$ is rebuilt per event using the “METMaker” tool, using the Track-based Soft Term which is built up of tracks that are matched the primary hard scatter vertex but not matched to physics objects in the hard-terms. EMPFlow jets with $R = 0.4$ are used for the jet hard term. The preselection criteria on the calibrated physics objects defining the $E_{\text{T}}^{\text{miss}}$ hard terms are:

- $p_{\text{T}}^{\gamma} > 12 \text{ GeV}$,
- $p_{\text{T}}^{e(\mu)} > 7 \text{ GeV}$,
- $p_{\text{T}}^{\text{jet}} > 25 \text{ GeV}$.

The *Tight* jet selection working point is used which requires that forward jets satisfy $p_{\text{T}} > 30 \text{ GeV}$.

In event topologies with zero true $E_{\text{T}}^{\text{miss}}$, the TST would be perfectly balanced against the hard terms. Detector resolution effects alter this p_{T} balance. These resolution effects are quantified as the RMS of parallel and perpendicular projections of the TST against the hard terms, resulting in *parallel* and *perpendicular* resolution systematic variations. There are also two $E_{\text{T}}^{\text{miss}}$ scale variations, where the parallel projection of the TST is smeared by a Gaussian of width equal to the hard term value [159].

5.3.3 Event Selections

The event selections for the differential cross-section measurement are given in Table 5.3.

In order to select for events rich in the EW- $W\gamma jj$ signal, one lepton, one photon, and two jets. Additionally, minimum requirements on the $E_{\text{T}}^{\text{miss}}$ and transverse W mass are applied to reject $j \rightarrow e$ and $j \rightarrow \mu$ background. To minimise contamination from leptonic Z decays, events with a second lepton which satisfies the *Loose ID* requirement are vetoed. To reject events where mismeasurements of jet energies generate large $E_{\text{T}}^{\text{miss}}$, a minimum azimuthal separation between the tag jets (the hardest two jets) and the $p_{\text{T}}^{\text{miss}}$ is required. To reduce

| Variable | $j \rightarrow \mu$ Selection | $j \rightarrow e$ Selection |
|--------------------------|-------------------------------|-----------------------------|
| triggers | single- μ triggers | single- e triggers |
| $N_{e/\mu}$ | = 1 | = 1 |
| $p_T^{e/\mu}$ | > 20 GeV | > 20 GeV |
| N_{jet} | ≥ 1 | ≥ 1 |
| $p_T^{j_0}$ | > 30 GeV | > 30 GeV |
| — | b -jet veto | b -jet veto |
| E_T^{miss} | < 20 GeV | < 20 GeV |
| m_T^W | < 20 GeV | < 20 GeV |
| $ \Delta R(\mu, j_0) $ | > 2.8 | > 3.8 |
| $ \Delta\phi(\mu, j_0) $ | > 2.8 | > 2.5 |

Table 5.4. Selection criteria for the $j \rightarrow \mu$ and $j \rightarrow e$ dijet control region.

contamination from leptons faking photons ($\ell \rightarrow \gamma$), events are vetoed if the invariant mass of the lepton-photon system is within 10 GeV of the Z mass. A b -jet veto is implemented to reduce contamination from single-top production events. The p_T of the tag jets are required to be at least 50 GeV to improve the purity of the signal, and to remove background events with soft jets. Finally, m_{jj} and $\Delta y(j, j)$ cuts select for events with a VBS topology. These cuts greatly improve the EW- $W\gamma jj$ signal purity overall, and remove large contributions from interference events, particularly at low $\Delta y(j, j)$.

5.4 Data-driven Background Estimates

The data-driven background estimates described here are not derived by the author. They are discussed as they have a direct impact on the signal extraction method used by the author in Section 5.6.

5.4.1 Jets Faking Leptons

Estimates for $j \rightarrow e$ and $j \rightarrow \mu$ backgrounds are derived independently using a data-driven method called the “fake factor” method [160]. Data driven methods are used for the non-prompt background estimates since contributions from mis-reconstructed objects are typically not well modelled in simulation.

In the fake factor method, a control region is defined which is enriched with dijet events. In this control region, leptons are partitioned into *tight* and *anti-tight* subsets, where the tight leptons pass tight isolation and ID. Anti-tight muons have the isolation, and d_0 significance cuts inverted, whereas anti-tight electrons have the isolation and ID requirements inverted. The dijet enriched control region is defined by the selection criteria in Table 5.4.

The *fake factor* is derived in the dijet control region using

$$F_{e/\mu} = \frac{N_{e/\mu}^{\text{tight}}}{N_{e/\mu}^{\text{anti-tight}}}, \quad (5.5)$$

where $N_{e/\mu}^{\text{tight}}$ is the number of events with one tight lepton, and $N_{e/\mu}^{\text{anti-tight}}$ is the number of

events with one anti-tight lepton. This factor is used to calculate the $j \rightarrow \ell$ background in the analysis region by

$$N_{\text{non-prompt, tight } e/\mu} = F_{e/\mu} \times N_{\text{non-prompt, anti-tight } e/\mu}, \quad (5.6)$$

where $N_{\text{non-prompt, anti-tight } e/\mu}$ is given by ⁴

$$N_{\text{non-prompt, anti-tight } e/\mu} = N_{\text{anti-tight } e/\mu}^{\text{Data}} - N_{\text{prompt, anti-tight } e/\mu}^{\text{MC}}. \quad (5.7)$$

Here, $N_{\text{anti-tight } e/\mu}^{\text{Data}}$ is the number of events in data with one anti-tight lepton, and $N_{\text{prompt, anti-tight } e/\mu}^{\text{MC}}$ is the number of events in simulation with one prompt, anti-tight lepton. The assumption in the method is that the fake factor calculated in the dijet control region is the same as that in the analysis region. The fake factor is derived as a function of lepton p_T and η .

The $j \rightarrow e$ and $j \rightarrow \mu$ estimates are validated by comparisons with data in a region close to the analysis phase space such as not to compare with unblinded data. These regions are defined by inverting the m_T^W and E_T^{miss} cuts.

Systematic uncertainties are defined for the $j \rightarrow \ell$ estimates and correspond to the choice of using a dijet sample (rather than γ +jets, W +jets, or Z +jets), generator choice of for prompt MC estimates, variations in selection criteria in defining the dijet control region, and the choice of p_T and η binning. Nominal and systematic yields for the $j \rightarrow e$ and $j \rightarrow \mu$ backgrounds as a function of m_{jj} are shown in Figure 5.3.

5.4.2 Jets Faking Photons

The largest background from mis-reconstructed objects comes from jets which are misidentified as photons. This background is estimated using a template fit method, and validated independently using the ABCD method [161]. In the template fit method, the fact that the photon isolation energy distribution is different between prompt and non-prompt photons is exploited. First, the photon isolation energy distribution of tight and truth-matched photons in $W\gamma jj$ MC samples is used to extract the shape for prompt photons. Next, in a control region populated with mis-reconstructed jets, events in data are used to extract a non-prompt photon isolation energy shape. The control region is defined by one of the non-tight *LoosePrime* photon ID working points described in Section 3.2.6.

For the prompt photon shape, a double-sided crystal ball function⁵ was found to best describe the photon isolation energy distribution. The fit is performed through maximising the un-binned likelihood over the parameter space given by the free parameters of the function. Similarly, the non-prompt shape is derived through maximising an unbinned likelihood,

⁴Naively, it would be tempting to calculate the number of fake leptons as $N_{\text{non-prompt, tight } e/\mu} = N_{\text{tight } e/\mu}^{\text{Data}} - N_{\text{prompt, tight } e/\mu}^{\text{MC}}$. However, this would not be correct since the prompt lepton region contains non-negligible contributions from $\text{EW-}W\gamma jj$, strong- $W\gamma jj$, and other non-prompt backgrounds. Therefore the (incorrect) assumption here would be that the signal and background normalisations are correct in MC, and that there were no other non-prompt backgrounds. Reversing the tight lepton selection criteria removes most of these other backgrounds.

⁵A crystal ball function [162, 163] is a Gaussian convoluted with a power-law tail. A double-sided crystal ball is the sum of two crystal ball functions sharing the same mean and width.

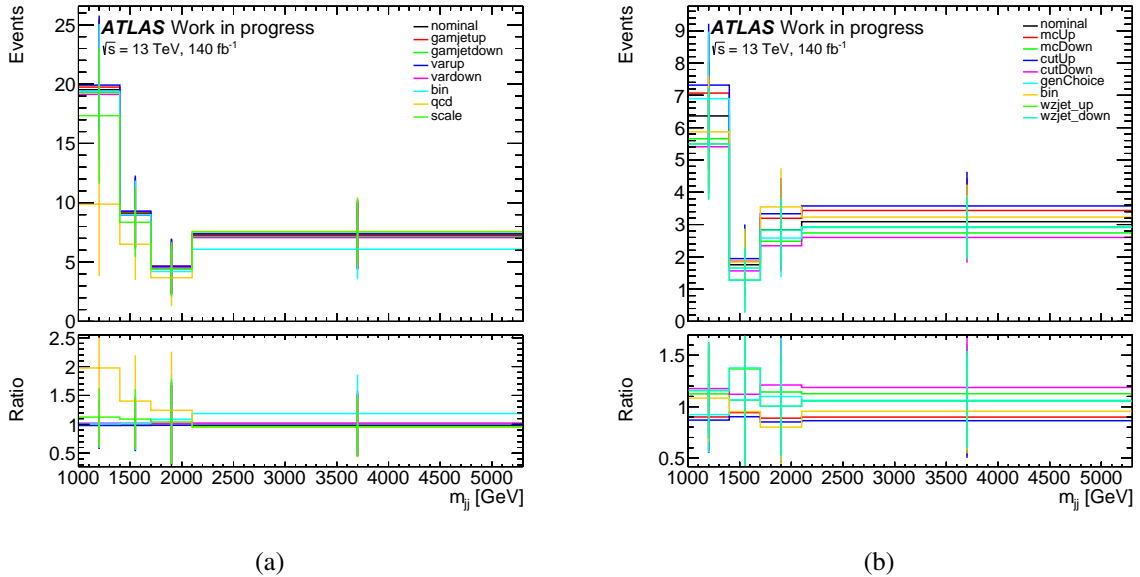


Figure 5.3. Estimates for fake estimate yields with m_{jj} for $j \rightarrow e$ (a) and $j \rightarrow \mu$ (b) in the analysis phase space (no control region cuts). The ratio panel shows the ratio of the systematic variations to the nominal yield. The largest uncertainty comes from variations in the strong- $W\gamma jj$ generator choice for $j \rightarrow e$, and the choice of the dijet sample for $j \rightarrow \mu$. These are shown as ‘‘qcd’’ and ‘‘wzjet’’ in the legend, respectively. The error bars correspond to statistical uncertainty. Plots made by author from fakes estimates provided by another member of the analysis team.

which is defined by Novosibirsk functions.

To derive the $j \rightarrow \gamma$ estimate, events in data containing a reconstructed tight ID photon are partitioned into bins of the observable for which the estimate is to be derived. For each bin, the prompt and non-prompt functions are combined, and the normalisations of the two functions are derived through maximising a likelihood defined by the products of Novosibirsk and double-sided crystal ball functions. Gaussian constraints defined through the mean and width of the tight and non-tight fits are included in the likelihood to ensure the normalisations do not have unreasonably large deviations from the previously derived values. By integrating the post-fit non-prompt photon isolation energy distribution, the expected number of fake photons is derived.

Systematic uncertainties in the $j \rightarrow \gamma$ estimate arise from statistical uncertainties on the $j \rightarrow \gamma$ yield; from real photon leakage into the LoosePrime control region; from the exact LoosePrime working point; and from MC modelling uncertainties. The nominal and systemic $j \rightarrow \gamma$ yields are shown for m_{jj} and p_T^ℓ in Figure 5.4.

5.4.3 Electrons Faking Photons

Prompt electrons and photons leave very similar deposits in the EM calorimeter, i.e. narrow EM showers almost entirely contained in the EM calorimeter. Electrons are distinguished from photons through the presence of a track matched to the primary hard-scatter vertex and the calorimeter deposit. Photons which are converted in the ID can also have an associated track. Electrons can be misidentified as photons primarily due to tracking inefficiencies and bad track-cluster matching.

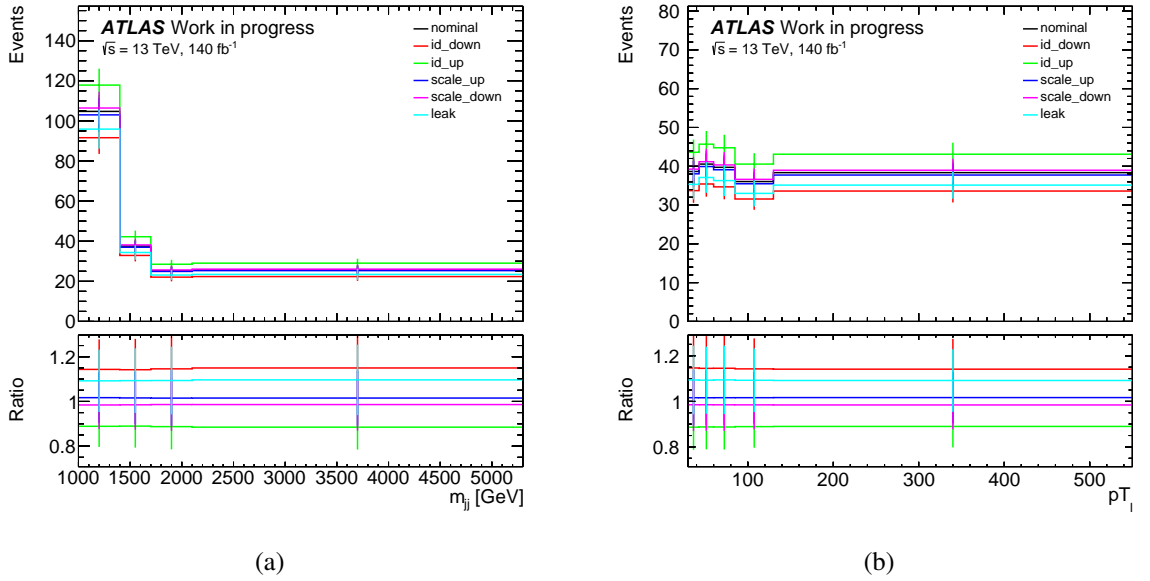


Figure 5.4. Estimates for $j \rightarrow \gamma$ yields with m_{jj} (a) and p_T^ℓ (b) in the analysis phase space (no control region cuts). The ratio panel shows the ratio of the systematic variations to the nominal yield. The largest uncertainty comes from variations in the LoosePrime definition. These are shown as “id_{up}” and “id_{down}” in the legend. The error bars correspond to statistical uncertainty. Plots made by author from fakes estimates provided by another member of the analysis team.

The $e \rightarrow \gamma$ fake rate is measured using the “tag and probe” method [164]. The electron-to-photon fake rate is determined in a control region enriched with $Z \rightarrow ee$ events. A well identified electron is defined as the tag object, and a probe candidate is either a second electron or a photon, where the invariant mass of the tag-probe system corresponds to the Z -boson invariant mass. The fake rate is then determined in a similar way to the fake factor method in this $Z \rightarrow ee$ control region. The fake rate is applied in a similar way to equation 5.6 to obtain the final $e \rightarrow \gamma$ yield. The $e \rightarrow \gamma$ yield for m_{jj} and p_T^ℓ in the analysis phase space is shown in Figure 5.5. The $e \rightarrow \gamma$ background is validated in the analysis phase space inside of the Z-veto region.

5.5 Expected Yields and Events in Data

After applying the selection cuts discussed in Section 5.3.3, the expected event yields from simulation compared with observed numbers of events in data are shown in Figure 5.6. Non-prompt backgrounds are estimated using the methods discussed in the previous section. The agreement between data and prediction is reasonable as a function of m_{jj} and $\Delta\phi_{jj}^{\text{signed}}$. However, the data overshoots the prediction at high $m_{\ell\gamma}$ and low $p_{T,jj}$.

5.6 Signal Extraction Methodology

This section describes the extraction of the EW- $W\gamma jj$ differential event yields. The differential cross-section of a given observable x for EW- $W\gamma jj$ production is defined in a given bin i

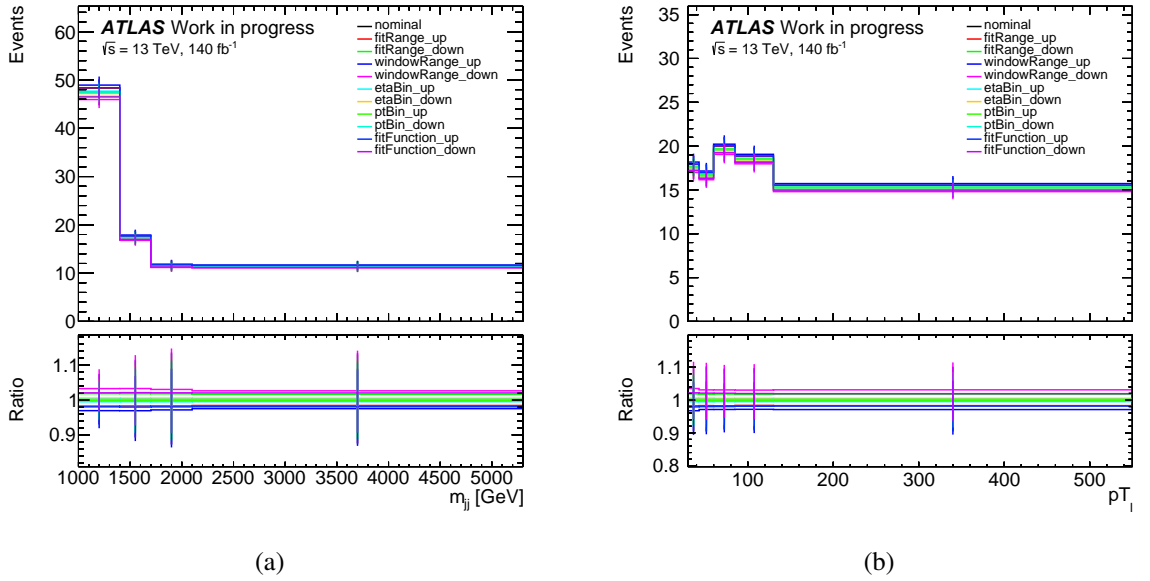


Figure 5.5. Estimates for $e \rightarrow \gamma$ yields with $m_{\gamma\gamma}$ (a) and p_T^ℓ (b) in the analysis phase space (no control region cuts). The ratio panel shows the ratio of the systematic variations to the nominal yield. The largest uncertainties come from variations in the function for fitting the signal and background, and the Z -mass window range. These are shown as the “fitFunction” and “windowRange” systematics in the legend. The error bars correspond to statistical uncertainty. Plots made by author from fakes estimates provided by another member of the analysis team.

of a signal region (SR) (defined in Table 5.5) by

$$\frac{d\sigma_i^{\text{EW}}}{dx} = \frac{\mathcal{U} \hat{N}_{\text{SR},i}^{\text{EW}}}{\Delta x_i \mathcal{L}}, \quad (5.8)$$

where \mathcal{L} is the integrated luminosity of the dataset, \mathcal{U} represents the detector unfolding corrections described in Section 5.16, and $\hat{N}_{\text{SR},i}^{\text{EW}}$ is the estimated number of EW- $W\gamma\gamma$ events contributing to the observed data. This value is estimated using a binned log-likelihood fit which is performed simultaneously in a EW- $W\gamma\gamma$ enriched signal region and three EW- $W\gamma\gamma$ deficient control regions. These regions are defined through imposing criteria on the lepton-photon system centrality, $\xi_{l\gamma}$, and the number of jets in the rapidity interval of the two tag jets, $N_{\text{jets}}^{\text{gap}}$. The centrality is defined as

$$\xi_{l\gamma} \equiv \frac{|(y_{l\gamma} - (y_{j1} + y_{j2})/2)|}{|(y_{j1} - y_{j2})|}, \quad (5.9)$$

where $y_{l\gamma}$ is the rapidity of the lepton-photon system, y_{j1} is the rapidity of the leading jet, and y_{j2} is the rapidity of the sub-leading jet. The $N_{\text{jets}}^{\text{gap}}$ and $\xi_{l\gamma}$ variables are uncorrelated for the strong- $W\gamma\gamma$ and EW- $W\gamma\gamma$ processes, as can be seen in Figure 5.7, making this a good choice for an ABCD-like method. The definitions of the four regions are shown in Table 5.5.

This fit is used to constrain the shape and normalization of the strong- $W\gamma\gamma$ background in addition to constraining the shape and normalisation of the EW- $W\gamma\gamma$ event yield. The fit is performed in the combined electron and muon channels, since it was not possible to derive separate lepton channel distributions due to statistical limitations. The signal region was blinded during the stage where analysis decisions and optimisations were being made.

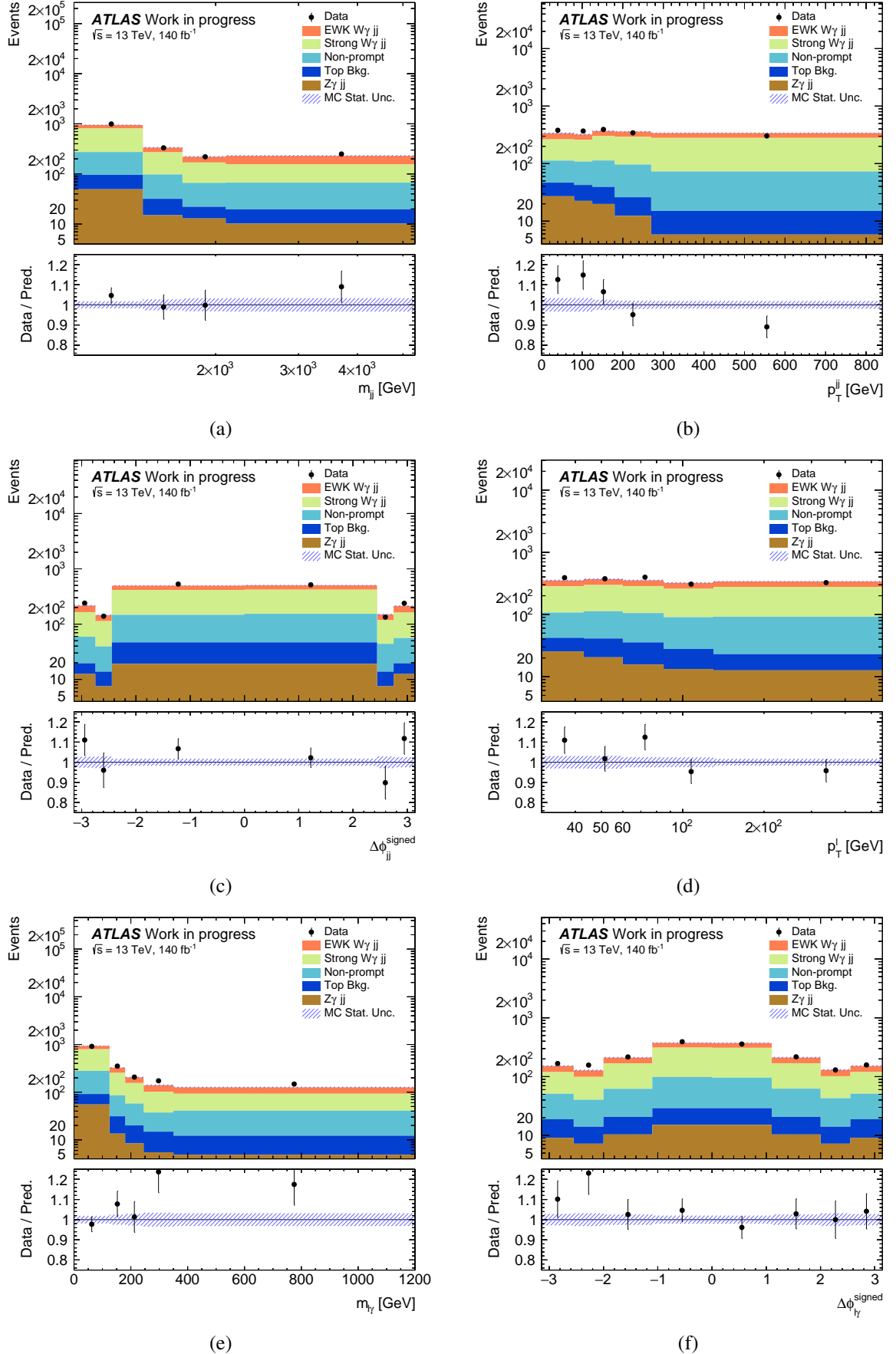


Figure 5.6. Event yields in the analysis phase space without any control region cuts. The angular observable distributions have been symmetrised. For details on the symmetrisation procedure see Section 5.10.

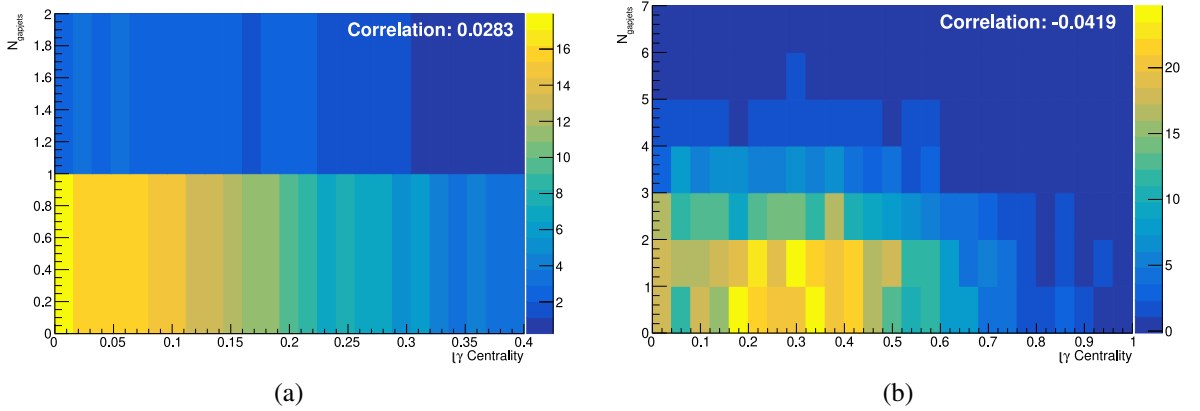


Figure 5.7. 2D Histograms and correlation coefficients for EW- $W\gamma jj$ (a) and strong- $W\gamma jj$ (b) of $\xi_{l\gamma}$ centrality against $N_{\text{jets}}^{\text{gap}}$. Note the scales are different for the two plots. Also note that the bins are not normalised. Because the cross-sections are larger at lower centrality and $N_{\text{jets}}^{\text{gap}}$ values, these bins have a higher occupancy. This does not imply a correlation between the two observables. The correlation coefficients are shown in the top right of the plots.

| Region | Selection | Abbreviation |
|------------------|--|--------------|
| Signal Region | $N_{\text{jets}}^{\text{gap}} = 0, \xi_{l\gamma} < 0.35$ | SR |
| Control Region A | $N_{\text{jets}}^{\text{gap}} = 0, 0.35 \leq \xi_{l\gamma} < 1$ | CRa |
| Control Region B | $N_{\text{jets}}^{\text{gap}} \geq 1, 0.35 \leq \xi_{l\gamma} < 1$ | CRb |
| Control Region C | $N_{\text{jets}}^{\text{gap}} \geq 1, \xi_{l\gamma} < 0.35$ | CRc |

Table 5.5. The definitions of the signal and control regions used in the extraction of the EW- $W\gamma jj$ signal.

The Signal Region has the requirements that there must be little hadronic activity in the rapidity interval between the tagging jets and that the reconstructed $\ell\gamma$ system is produced centrally relative to the tagging jets.

The control regions are defined through inverting one or both of these cuts.

The likelihood function is defined as (with indices r, i running over regions and bins respectively)

$$L = \prod_{r,i} \text{Pois}(N_{ri}^{\text{data}} | \gamma_{ri} \nu_{ri}(\boldsymbol{\alpha})) \text{Pois}\left(\left(\frac{\nu_{ri}(\mathbf{1})}{\delta_{ri}}\right)^2 \middle| \gamma_{ri} \left(\frac{\nu_{ri}(\mathbf{1})}{\delta_{ri}}\right)^2\right), \quad (5.10)$$

where ν_{ri} is the total MC estimate given by

$$\nu_{ri} = \mu_i \nu_{ri}^{\text{EW,MC}} + \nu_{ri}^{\text{strong}} + \nu_{ri}^{\text{other}}, \quad (5.11)$$

and the $\nu_{ri}^{\text{EW,MC}}$ is the MC prediction for the EW- $W\gamma jj$ event yield. ν_{ri}^{other} is the prediction for the non-strong- $W\gamma jj$ background processes ($Z\gamma jj$, top, and non-prompt). μ_i is a free parameter in the fit, and represents the EW signal strength. The term ν_{ri}^{strong} is the prediction for the strong- $W\gamma jj$ event yield, and is defined by

$$\nu_{\text{CRa},i}^{\text{strong}} = b_{\text{L},i} \nu_{\text{CRa},i}^{\text{strong,MC}}, \quad \nu_{\text{CRb},i}^{\text{strong}} = b_{\text{H},i} \nu_{\text{CRb},i}^{\text{strong,MC}}, \quad (5.12)$$

$$\nu_{\text{SR},i}^{\text{strong}} = b_{\text{L},i} c \nu_{\text{SR},i}^{\text{strong,MC}}, \quad \nu_{\text{CRc},i}^{\text{strong}} = b_{\text{H},i} c \nu_{\text{CRc},i}^{\text{strong,MC}}, \quad (5.13)$$

where $\nu_{ri}^{\text{EW,MC}}$ are the MC predictions for the strong- $W\gamma jj$ backgrounds. The parameters

$b_{L,i}, b_{H,i}$ are responsible for constraining the strong- $W\gamma jj$ background in regions of low and high centrality, respectively. The c parameter is a constant and acts as a residual correction which accounts for non-closure when transferring the b factors to the signal region.

The term $\text{Pois}(N|\lambda)$ in Equation 5.10 is the Poisson probability mass function for N events given the parameter λ . The vector α contains all free parameters except γ_{ri} , i.e.

$$\alpha \equiv (\mu_1, \dots, \mu_n, b_{L,1}, \dots, b_{L,n}, b_{H,1}, \dots, b_{H,n}, c). \quad (5.14)$$

The number of bins is given by n , and γ_{ri} is a nuisance parameter which accounts for the finite MC statistical precision. The inclusion of the Poisson constraint parameters γ_{ri} gives the MC templates additional freedom to float within their statistical uncertainties. The γ_{ri} are themselves constrained by the terms $\text{Pois}((\frac{\nu_{ri}}{\delta_{ri}})^2 | \gamma_{ri}(\frac{\nu_{ri}}{\delta_{ri}})^2)$, where the δ_{ri} denote the statistical uncertainty on the MC estimate. These constraint terms come about by treating the MC estimate as an auxiliary measurement with the relative stat uncertainty given by $\frac{\nu_{ri}(1)}{\delta_{ri}}$ [165]. The “Beeston-Barlow” [166] treatment to MC stat uncertainties is used where the Poisson constraint parameter γ_{ri} is shared between the MC samples that enter the likelihood. This has the implication that $\nu_{ri}(1)$ is implicitly a sum over all MC samples and the MC error δ_{ri} is the quadrature sum of all the MC statistical errors of all the samples.

Note that there is no Gaussian constraint term for systematic uncertainty nuisance parameters in the likelihood. This is because each systematic variation of MC simulations is fit separately and the difference in event yield between the nominal and systematic variation post-fit is taken to be the systematic uncertainty (before smoothing) in the extracted yield. This is covered in more detail in section 5.13 and is equivalent to the approach where all systematic uncertainties are simultaneously constrained through the inclusion of Gaussian constrained nuisance parameters in the likelihood. The reason for using the former approach is because makes it simpler to propagate each systematic variation through the unfolding procedure.

5.6.1 Choice of Model Parameters

The choice for the set of floating parameters in the likelihood as described in eqs. (5.11) to (5.13) is motivated as follows. The simplest possible configuration would be to constrain the background using one control region where either the $N_{\text{jets}}^{\text{gap}}$ or $\xi_{l\gamma}\text{cut}$ is inverted. The problem with inverting the centrality cut is that there are very few events in CRc, at high centrality. This could be overcome by lowering the centrality threshold, but then the purity of the EW- $W\gamma jj$ signal becomes significantly worse, resulting in larger modelling uncertainties. Inverting the $N_{\text{jets}}^{\text{gap}}$ cut gives a control region with a greater event yield, however, this results in a large non-closure as the jet multiplicity distribution is not well modelled. In this one control region configuration, there are as many floating parameters as there are degrees of freedom, hence it is not possible to introduce another floating parameter to account for the modelling differences across the $N_{\text{jets}}^{\text{gap}}$ boundary.

In the nominal three control region method described by Equations (5.10) to (5.12), two

signal-like regions are defined, namely SR and CRc, alongside their corresponding control regions CRa, and CRb. The two constraint factors $b_{L,i}$ and $b_{H,i}$ are applied to the strong- $W\gamma jj$ background in SR and CRc respectively, where L and H denote “Low” and “High” centrality. These factors are primarily constrained in CRa and CRb, respectively. This is because CRa and CRb have high event yields and higher background purity. Hence, changes to the signal strength will have little to no effect on the post-fit event yields, and conversely, changes to the b_i factors will have a large effect.

With fewer free parameters than the available DoF, one has the freedom to define an additional floating parameter c , which is shared between the signal-like regions SR and CRc. This parameter acts to correct any non-closure in applying deriving $b_{L,i}$ and $b_{H,i}$ at large $N_{\text{jets}}^{\text{gap}}$ and then applying them at low $N_{\text{jets}}^{\text{gap}}$. The number of parameters in the fit is given by $3N_{\text{bins}} + 1$. The residual correction c is chosen to be a constant rather than a polynomial. This choice is discussed in further detail in Section 5.12.2. This method to constrain the dominant background was first developed for the ATLAS EW Zjj measurement [167].

The default method is to use CRa to derive the bin-dependent factors b_i with the signal region (this is called the *CRa method*). This is not the only reasonable choice. CRc could be chosen to derive the b_i parameters (the *CRc method*). These two configurations are equivalent, ignoring statistical effects [167]. Ultimately, the CRa method is chosen as the nominal method because CRa has larger event yields compared to CRc. The effects of smaller statistics in CRc will be discussed in Section 5.15. The CRc method serves as a cross-check.

5.7 Shape Dependence of $N_{\text{jets}}^{\text{gap}}$ and $\xi_{l\gamma}$

A large shape difference between the observed data and the MC predictions of the $\xi_{l\gamma}$ and $N_{\text{jets}}^{\text{gap}}$ distributions would not be desirable, as this would imply that the strong constraint derived in a control region would not do well to constrain the same background in the SR. Figure 5.8 shows the normalised number of events as a function of $N_{\text{jets}}^{\text{gap}}$ and $\xi_{l\gamma}$ for data with all predictions subtracted except for the strong- $W\gamma jj$ MC prediction. These are shown separately at high $N_{\text{jets}}^{\text{gap}}$ (CRa + CRb) and at high $\xi_{l\gamma}$ (CRb + CRc). The reason for not showing the $N_{\text{jets}}^{\text{gap}}$ shape at low $\xi_{l\gamma}$ and the $\xi_{l\gamma}$ shape at low $N_{\text{jets}}^{\text{gap}}$ is that this would correspond to unblinding the data. Figures 5.8a and 5.8c show that the shape of the $N_{\text{jets}}^{\text{gap}}$ distribution in data agrees with the prediction from simulation within strong- $W\gamma jj$ generator choice uncertainties. Figures 5.8b and 5.8d show that the shape of the $\xi_{l\gamma}$ distribution is consistent with simulation, after accounting for strong- $W\gamma jj$ and EW- $W\gamma jj$ generator choice uncertainties and statistical uncertainties in the data and simulation.

5.8 Construction of the Asimov Dataset

To prevent any unintended bias, e.g. tuning of parameters so that the data match the simulation, the data were blinded in the signal region until the analysis was formally approved.

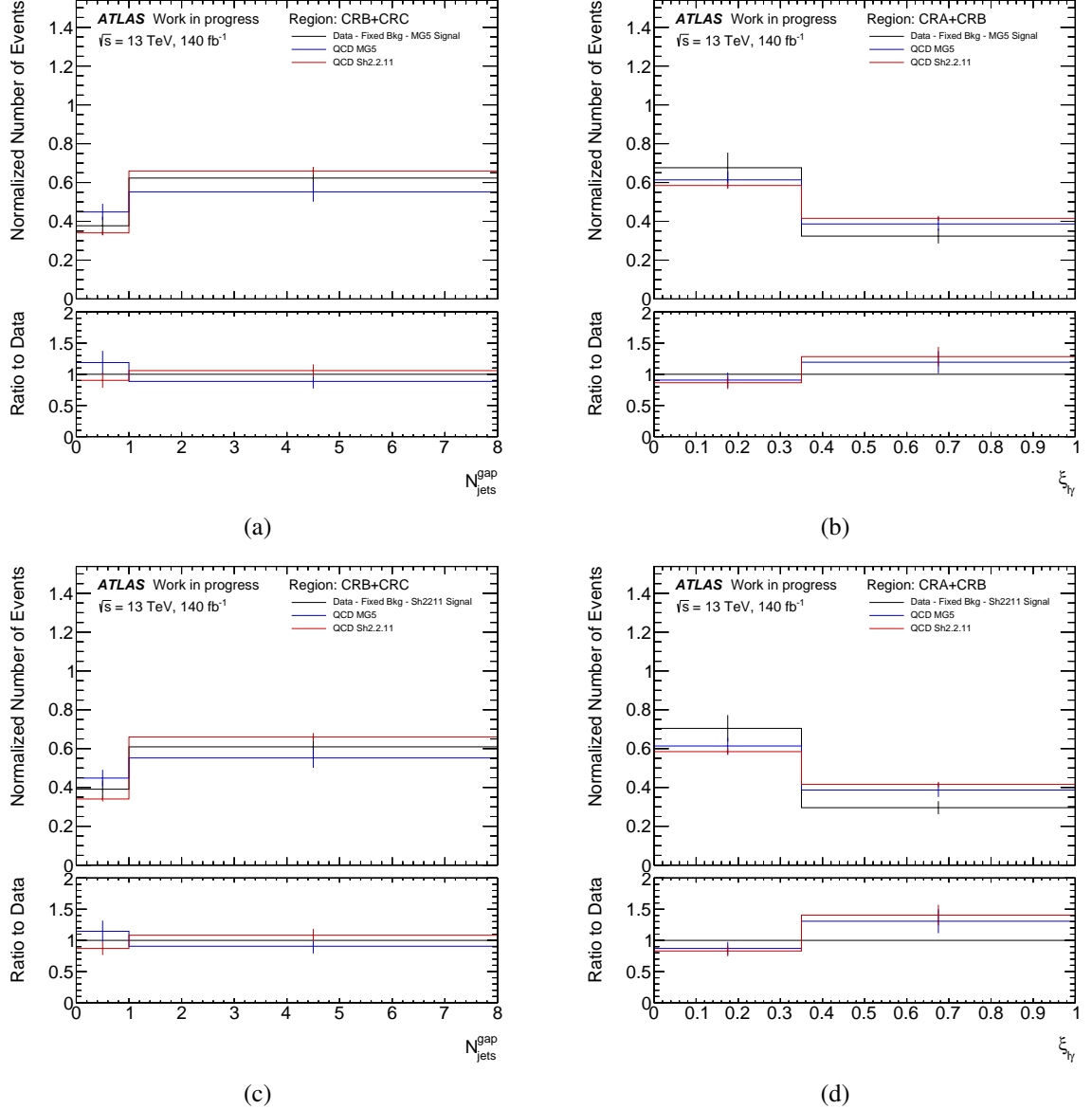


Figure 5.8. The $N_{\text{jets}}^{\text{gap}}$ distribution is shown in (a,c), and the $\xi_{l\gamma}$ in (b,d). The top two plots (a,b) show the results where the SHERPA-2.2.11 EW- $W\gamma jj$ MC sample is used, and the bottom two plots (c,d) show the results where the MADGRAPH 5 EW- $W\gamma jj$ MC sample is used. The shape differences between data - [fixed background + signal] (black line) and the strong- $W\gamma jj$ MC predictions (red and blue lines) are shown in the top canvas. The bottom canvas shows the ratio between the purely MC and data-MC predictions. The error bars on the black lines in the ratio plot are the data statistical uncertainty combined with the MC statistical uncertainty in the ratio. The error bars on the red and blue lines correspond to the MC statistical uncertainty.

The analysis was optimised using a dataset which acts as a proxy for real data, called an Asimov dataset. The number of events in the Asimov sample is given by $N_{ri}^{\text{Asimov}} = \sum_s \nu_{ri}^{s,\text{MC}}$, where the index s runs over the EW- $W\gamma jj$, strong- $W\gamma jj$, non-prompt, top, and $Z\gamma jj$ samples. The indices r and i run over the regions, and the observable bins, respectively. The strong- $W\gamma jj$ background used in the Asimov is the nominal SHERPA 2.2.11 sample. However, for certain tests an alternative Asimov dataset is constructed using the MADGRAPH strong- $W\gamma jj$ sample. It is explicitly stated whenever this alternative Asimov dataset is used. The Asimov statistical uncertainties are given by $\sqrt{N_{ri}^{\text{Asimov}}}$.

5.9 Binning Determination

The binning is determined for each observable using the following criteria:

- The relative statistical precision of the extracted $\text{EW-}W\gamma\text{jj}$ yield must be similar across the bins.
- The bin width must be at least as large as twice the detector resolution in that bin.

For the angular observables, $\Delta\phi_{jj}^{\text{signed}}$ and $\Delta\phi_{\ell\gamma}^{\text{signed}}$, the range is designed by geometry to be $[-\pi, \pi]$. For the kinematic observables, the upper bound k is chosen to be at a value in which there is at most one expected event in the interval $[k, \infty]$.

Since the analysis optimisations were performed blinded, the binning was determined using the Asimov dataset. The binning was initially optimised to target statistical uncertainty in each bin of about 30-35%, they were then adjusted to account ensure adequate detector resolution.

5.9.1 Detector Resolution with Bin Width

If the detector resolution is large relative to the bin width, the unfolding will have to correct for a larger amount of bin migrations. This step relies on the MC simulation of the signal. Therefore, by requiring the resolution to be small relative to the bin width, the model dependence of the measurement is reduced.

The $\text{EW-}W\gamma\text{jj}$ predictions in the signal region are used to estimate the measurement variable resolution in each bin. The set of events which pass the reco-level selections in Table 5.3 are stored in a 2-dimensional histogram of truth-variable vs reco-variable. Within each reco bin, a fine truth bin splitting is chosen such that a Gaussian can be fit over the truth predictions. The width of this Gaussian is taken to be the resolution. Comparisons of these resolution values to the width of the bins are shown in Figure 5.9. A bin is sufficiently wide if the bin width is at least twice the averaged resolution.

The fits which lead to the resolution values shown in this plot can be seen in Figure 5.10 for m_{jj} . For very large ranges such as the last bin of m_{jj} , p_T^ℓ , and $m_{\ell\gamma}$, the truth distribution is not well described by a Gaussian. This is simply an artifact of the bin range, and these bins therefore implicitly pass the 2σ requirement.

5.10 Symmetrising of the $\Delta\phi_{\ell\gamma}^{\text{signed}}$ and $\Delta\phi_{jj}^{\text{signed}}$ Templates

Under the assumption of the standard model, the azimuthal separation of two objects is independent of the rapidity ordering, and any asymmetry would be an indication of CP violation. Furthermore, the ATLAS detector is symmetric in ϕ , and therefore there is no a-priori reason for the fit templates to be asymmetric. In light of this, the possibility of symmetrising the fit templates of the angular observables around $\Delta\phi = 0$ is explored.

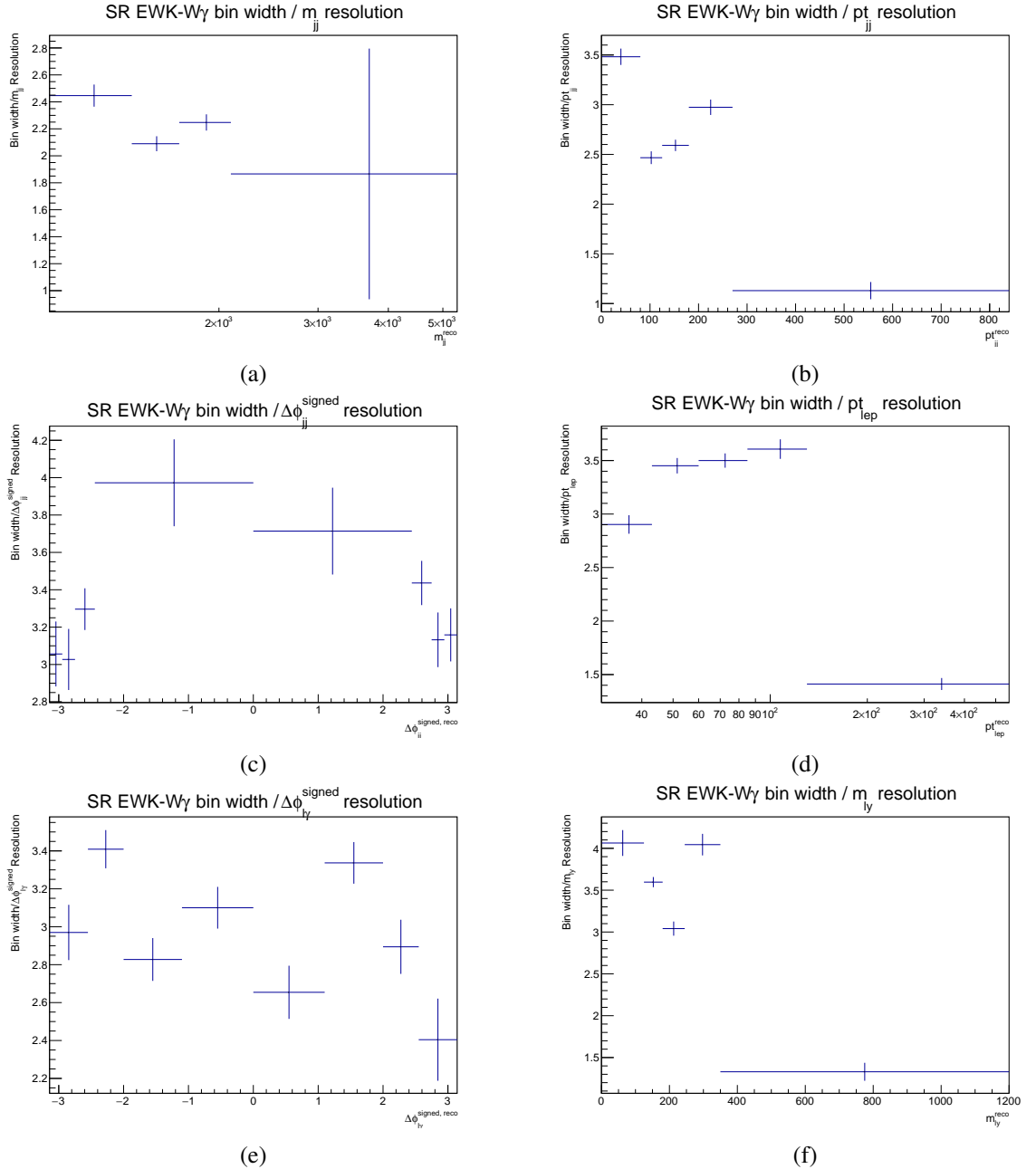


Figure 5.9. Reco bin width / resolution for each measured observable in the signal region for the $\text{EW}-W\gamma jj$ prediction. For all observables, the bin widths are consistent with passing the 2σ threshold after ignoring the last bins of the kinematic observables.

To test whether it is valid to symmetrise the $\Delta\phi_{\ell\gamma}^{\text{signed}}$ and $\Delta\phi_{jj}^{\text{signed}}$ templates, the data are plotted for these observables in the control regions, this is shown in Figure 5.11. From this figure it is evident that the data are consistent with a symmetric distribution within statistical uncertainties. Therefore the Asimov dataset, data-driven fakes estimates and MC templates are all symmetrised for $\Delta\phi_{\ell\gamma}^{\text{signed}}$ and $\Delta\phi_{jj}^{\text{signed}}$ prior to performing the likelihood fit. The observed data are left un-symmetrised. The benefits of this prescription are that the statistical precision each bin is then improved by a factor of $\sqrt{2}$ and that simulated events with large event weights are less likely to skew the likelihood fit results.

The symmetrisation is performed by taking the weighted arithmetic mean of paired bins given by

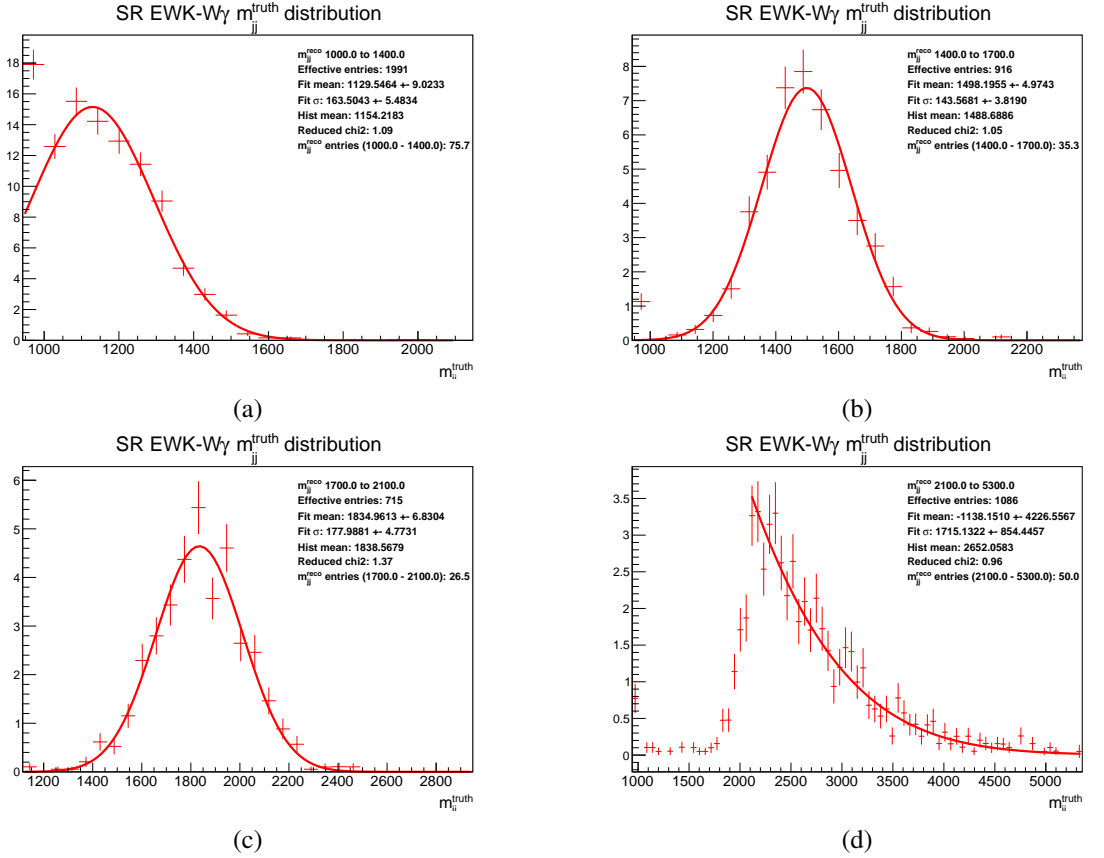


Figure 5.10. Resolution fits for m_{jj} . The first three bins are well described by a Gaussian distribution as the truth distribution is relatively uniform in these bins. The non-Gaussian shape in the last bin is an artifact of the large reco-variable range, therefore the last bin implicitly passes the 2σ requirement. The error on the fit parameters are defined as the change in the parameter value required to change the chi-squared value by 1 [168].

$$x_{ij} = \frac{w_i x_i + w_j x_j}{w_i + w_j}, \quad (5.15)$$

where x_{ij} is the averaged value of the observable x in paired bins i and j , and the weights w_i are given by $w_i = \frac{1}{\epsilon_i^2}$, where ϵ_i is the error in bin i .

5.11 Testing of the Binned Likelihood Fit

A number of tests of the likelihood fit were performed using the Asimov dataset to ensure that it performed as expected. The most basic test is that perfect closure is achieved when fitting the nominal Asimov dataset constructed using the SHERPA strong- $W\gamma jj$ sample against the nominal MC templates, which are also defined using the SHERPA strong- $W\gamma jj$ sample. Perfect closure is observed for all observables.

As another test of the fit, the QCD template was halved in the low $N_{\text{jets}}^{\text{gap}}$ regions to test that the residual correction, c , would yield exactly $c = 2$. The QCD template was also halved simultaneously in the SR and CRa to test that $b_{L,i}$ would yield a value of 2, and in CRb and CRc to test that $b_{H,i}$ would yield a value of 2. In this test, the fit parameters were seen to correspond exactly to the expected values.

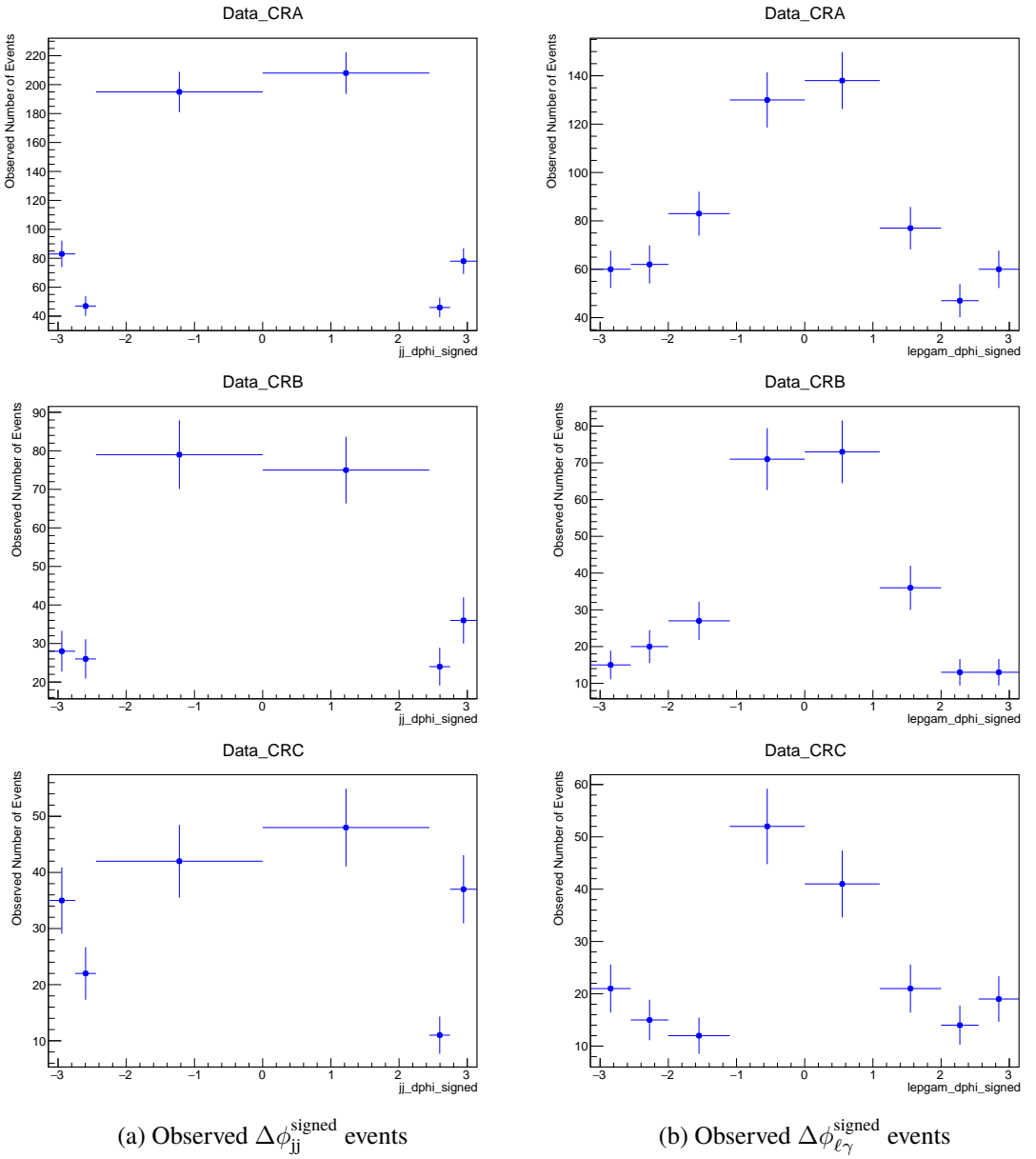


Figure 5.11. The observed numbers of events for $\Delta\phi_{jj}^{\text{signed}}$ and $\Delta\phi_{\ell\gamma}^{\text{signed}}$ in the CRs. These distributions are consistent with being symmetric.

As a third test of the signal extraction, an Asimov dataset is constructed using the alternate **MADGRAPH** strong- $W\gamma jj$ MC sample (rather than the nominal **SHERPA** sample). Figure 5.12 shows the m_{jj} prefit yields for this configuration. From this it is clear that the **MADGRAPH** strong- $W\gamma jj$ prediction is higher than the **SHERPA** prediction in the SR for all bins. In CRA, the agreement is relatively good in all bins. The **MADGRAPH** prediction undershoot in bins 2 and 4 in CRb, and overshoots in all but the last bin in CRC. The modelling of the dominant background is therefore very dependent on the kinematic region, which highlights the importance of deriving bin depending corrections in addition to a residual correction factor.

The likelihood fit is then performed with this configuration, and the postfit results of the fit parameters $\mu_{\text{EW},i}$, $b_{\text{L},i}$, $b_{\text{H},i}$, and c , are compared with expectations derived from logical arguments. This test is performed for all observables, however, only m_{jj} is shown here for brevity. Figure 5.13 shows the postfit yields, and Figure 5.14 shows the constrained values of the parameters after the fit. The postfit agreement is good in the SR and CRA, where the

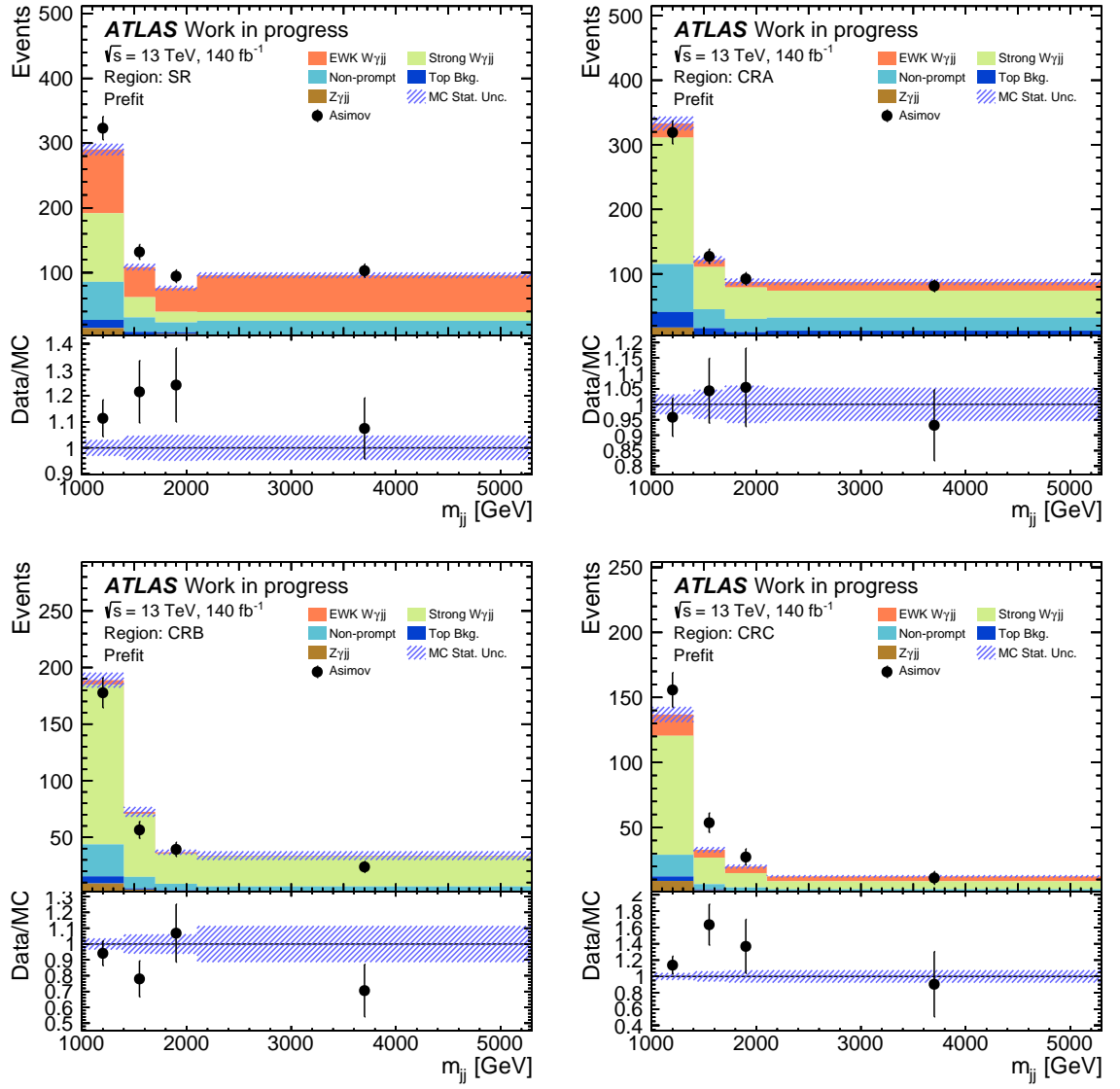


Figure 5.12. Prefit differential event yields with the Asimov dataset constructed using the `MADGRAPH` strong- $W\gamma jj$ sample.

statistical precision of the data and fit templates is superior, and conversely, the agreement is slightly worse in CRb and CRC.

Since $b_{L,i}$ is applied in CRA, this parameter is primarily constrained in CRA. Therefore, the expectation from Figure 5.12 is that $b_{L,i}$ takes values ($<1, >1, >1, <1$). Similarly, $b_{H,i}$ is applied in CRb and CRC, but the strong- $W\gamma jj$ background in CRC is constrained by an additional parameter, c . Therefore, $b_{H,i}$ is primarily constrained in CRb. From Figure 5.12, $b_{H,i}$ should take the values ($<1, <1, >1, <1$). Finally, since c is applied in CRC, c is constrained primarily by CRC. Furthermore, $b_{H,i}$ should have an average correction of about 0.85 (taking the average of the Asimov/MC values in CRb), which after applying to CRC results in an Asimov/MC disagreement in CRC of about 1.5 on average. Therefore c is expected to be about 1.5. $\mu_{EW,i}$ is then determined in the SR after applying $b_{L,i}$ and c to the strong- $W\gamma jj$ background. The postfit fit parameters shown in Figure 5.14 broadly confirm the expectation of this simple consideration.

The values of the constrained fit parameters align well with the expectations described above.

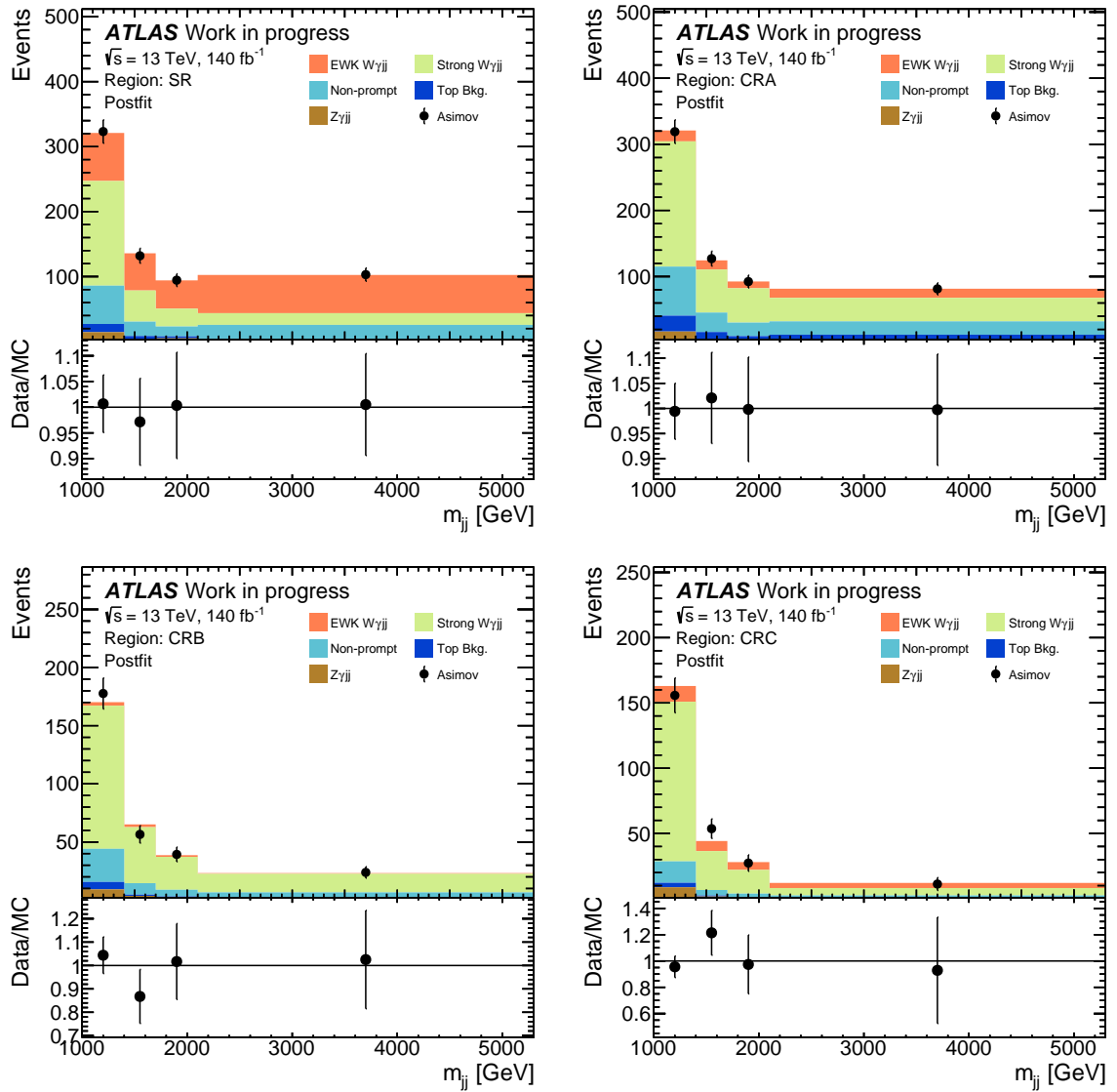


Figure 5.13. Postfit event yields for the fit with the Asimov dataset constructed from the `MADGRAPH` strong- $W\gamma\gamma$ sample.

The only deviation from the expectation is in the second bin for the $b_{L,i}$ parameter, where the value is just below 1, whereas the expectation was that this would be greater than 1. This is explained by the fact that there is some signal leakage into the control regions, and background leakage into the signal region. Therefore the assumptions made above do not hold perfectly.

5.12 Choice of Function for the Residual Correction

In equation 5.13 the choice is made for the residual correction to take the form of a constant factor c . However, without this factor, there are N_{bins} degrees of freedom remaining. Therefore, this residual correction factor can in principle take the form of a polynomial, or any other function with up to N_{bins} free parameters. For the discussion in this chapter, the residual correction function is denoted by $f(x_i)$, where i runs over the number of bins of the observable x . The following choices of function are investigated:

- $f(x_i) = 1$,

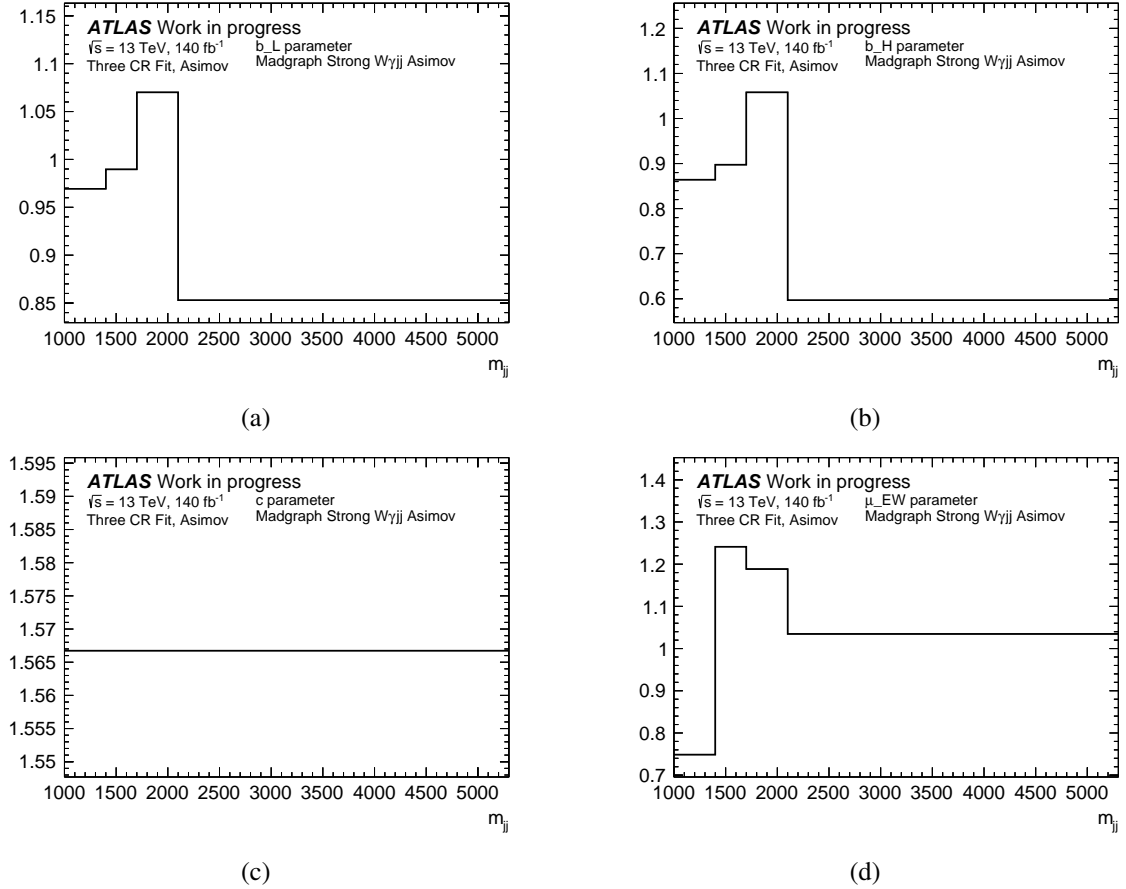


Figure 5.14. The constrained fit parameters for the fit with the Asimov dataset constructed from the MADGRAPH strong- $W\gamma jj$ sample. (a) corresponds to the parameter $b_{L,i}$, (b) to $b_{H,i}$, (c) to c , and (d) to $\mu_{EW,i}$. These are seen to be consistent with expectations from logical arguments. The fact that $\mu_{EW,i}$ does not equal 1 is a reflection of the uncertainty on the extracted EW- $W\gamma jj$ yield due to the choice of MC generator in the strong- $W\gamma jj$ sample.

- $f(x_i) = c$,
- $f(x_i) = mx_i + c$.

5.12.1 $f(x_i) = 1$

With $f(x_i) = 1$, the signal extraction method is equivalent to a fit with one control region, i.e. there is no residual correction applied. It can be seen from Figure 5.12 that this would not adequately constrain the dominant background. With this configuration the only strong- $W\gamma jj$ constraint is derived in CRa, and the difference between the strong- $W\gamma jj$ SHERPA and MADGRAPH predictions in this region are only of the order of 5 – 10%. Therefore the data-to-MC disagreement in the SR is resolved primarily through shifts in $\mu_{EW,i}$. It is clear that there are large modelling differences between the low and high centrality regions which are not captured by a single constraint to the strong- $W\gamma jj$ background. A residual correction factor is therefore absolutely necessary to prevent the measurement from being limited by background modelling uncertainties. This configuration also results in larger systematic uncertainties, which can be seen in Section 5.13.

5.12.2 $f(x_i) = mx_i + c$ or $f(x_i) = c$

It is possible that the data-to-MC non-closure is not uniform after applying the $b_{L,i}$ constraint in the SR. In fact, this was seen in [167]. Allowing $f(x_i)$ to depend on an extra parameter, means the signal extraction is sensitive to this non-uniformity. However, the addition of an extra parameter results in the procedure being less robust to statistical fluctuations. This is true particularly of m_{jj} , where all but the first bin in CRc have fewer than 30 expected events. This puts into question whether probing the shape of the non-closure is valid, and if it will lead to robust results. To test this, the signal is extracted for 1000 pseudo-experiments, where for each pseudo-experiment the strong- $W\gamma jj$ fit template in a given region is fluctuated in accordance with the statistical uncertainties⁶. For each fluctuation, the extracted signal is recorded, and the result is plotted on a 2D histogram of strong- $W\gamma jj$ template fluctuation vs post-fit EW- $W\gamma jj$ yield. This is repeated for each region, separately. The goal of this test is to understand how a given statistical fluctuation is able to affect the extracted EW- $W\gamma jj$ yield. If the likelihood fit is robust, then small statistical fluctuations in the templates should lead to small changes in the extracted EW- $W\gamma jj$ yield. The results of this test are shown in Figure 5.15 for the fourth bin of m_{jj} , where the **MADGRAPH** strong- $W\gamma jj$ template is used, and the **MADGRAPH** strong- $W\gamma jj$ sample is used in the construction of the Asimov dataset⁷.

The CRc subfigure in Figure 5.15 shows that the likelihood fit is not robust when $f(x_i) = mx_i + c$ is used. Shifts of $< 20\%$ in the strong- $W\gamma jj$ template result in $50 - 100\%$ shifts in the extracted EW- $W\gamma jj$ yield. Moreover, there are only around 5 MC events in this bin in CRc which lead to the $50 - 100\%$ shifts in the extracted yield. Therefore, because $f(x_i)$ is allowed too much freedom to float, the statistical precision of $\mu_{EW,i}$ is compromised by a small prediction for the background. If the likelihood fit is robust, a small background prediction should lead to a more precise prediction on $\mu_{EW,i}$, and not the other way round.

Figure 5.16 shows the same thing as Figure 5.15, except now $f(x_i)$ is defined to be a constant factor, i.e. $f(x_i) = c$. With this configuration, a 20% shift in the strong- $W\gamma jj$ template in CRc leads to a shift in $\mu_{EW,i}$ of about $10 - 20\%$. Removing a degree of freedom in the definition of $f(x_i)$ has resolved the problems seen in Figure 5.15. With $f(x_i) = c$, the high-occupancy first bin of m_{jj} now primarily constrains this factor, and the final result is much more robust to statistical fluctuations. To summarise, restricting the residual correction to a constant factor leads to significantly more robust predictions of $\mu_{EW,i}$.

The 2D plots shown above were constructed for all possible configurations, and for all bins of all observables to check the robustness of the likelihood fit. The different configurations explore the effects of fluctuating the Asimov dataset, rather than the strong- $W\gamma jj$ template; and using the **SHERPA** sample or the **MADGRAPH** sample in either constructing the strong- $W\gamma jj$ template or the Asimov dataset. With $f(x_i) = mx_i + c$, many similar plots to Figure 5.15 with unstable behaviour are observed. In contrast, all of the 2D plots for the

⁶This is done by multiplying each event weight by a list of 1000 random numbers sampled from a Poisson distribution of unit mean.

⁷For this test, the Asimov dataset is constructed using the **MADGRAPH** strong- $W\gamma jj$ template because this particular configuration does a good job at highlighting the unstable behaviour of the fit. The fit ought to be stable regardless of how the Asimov dataset is defined, hence any undesirable behaviour observed for this configuration should be treated with equal importance as the nominal configuration (where the Sherpa-2.2.11 strong- $W\gamma jj$ template is used to construct the Asimov dataset).

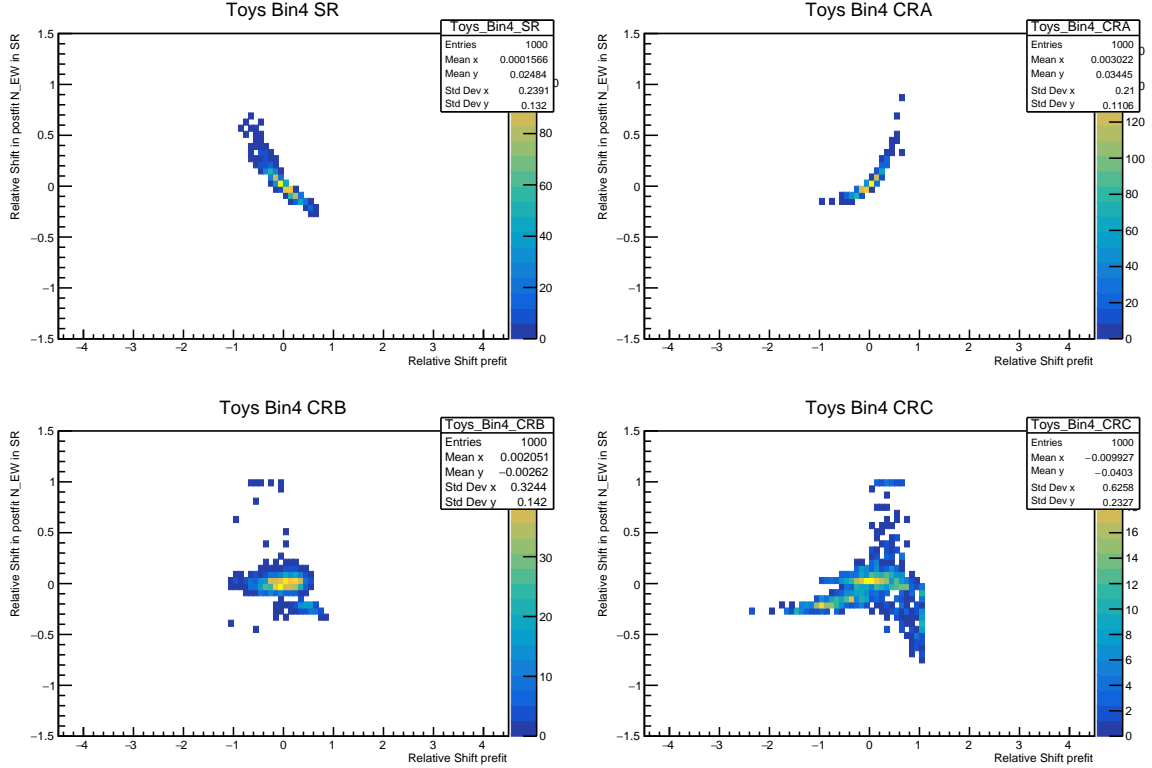


Figure 5.15. The relative shift in the extracted electroweak yield in bin-4 of m_{jj} for the linear $f(x)$ definition when fitting using the MADGRAPH strong- $W\gamma jj$ template, and MADGRAPH strong- $W\gamma jj$ Asimov definition.

The x -axis is the shift in the strong- $W\gamma jj$ template from the nominal, and the y -axis is the shift in the extracted EW yield. Particularly in CRC, small fluctuations in the QCD template result in very large fluctuations in the extracted EW yield result.

$f(x_i) = c$ definition are consistent with robust fit behaviour. These plots are shown in Appendix B.1 for other bins of m_{jj} (the other observables are omitted for brevity).

It is also worth commenting on the shapes of the 2D distributions in Figures 5.15 and 5.16. For $f(x_i) = c$, The shapes are roughly ellipsoidal in nature, suggesting that μ_{EW} is roughly Gaussian distributed. This is not the case for the $f(x_i) = mx_i + c$ definition. The Gaussian shape is potentially more desirable as a more symmetrical distribution of pseudo-experiments corresponds to a smaller statistical bias, which makes the results easier to interpret. The results are not completely free of bias, and this is clear in the upward turning shape in CRA. This happens because there is an inherent asymmetry associated with fluctuating the strong- $W\gamma jj$ template statistics, in that the purity of the signal increases with shifts to lower values, and decreases with shifts to higher values of the strong- $W\gamma jj$ yield.

The choice of $f(x_i) = c$ is made for this analysis since it resolves the robustness issues mentioned for $f(x_i) = mx_i + c$. Appendix B.1.1 shows the $f(x_i) = c$ stability plots for m_{jj} . All results shown outside of this Section and Appendix B.1.2 are for the $f(x_i) = c$ definition. It is worth noting that with this definition, there will be a relatively large range of integrated yields between observables. This is because it is likely that $f(x_i)$ does in fact have a non-uniform shape, which results in the overall normalisation of the strong- $W\gamma jj$ background being constrained to variable values depending on the observable. To resolve this issue, the option of adding an additional Gaussian constraint to the likelihood was explored. This term would then act to constrain the overall normalisation of the strong- $W\gamma jj$ background such

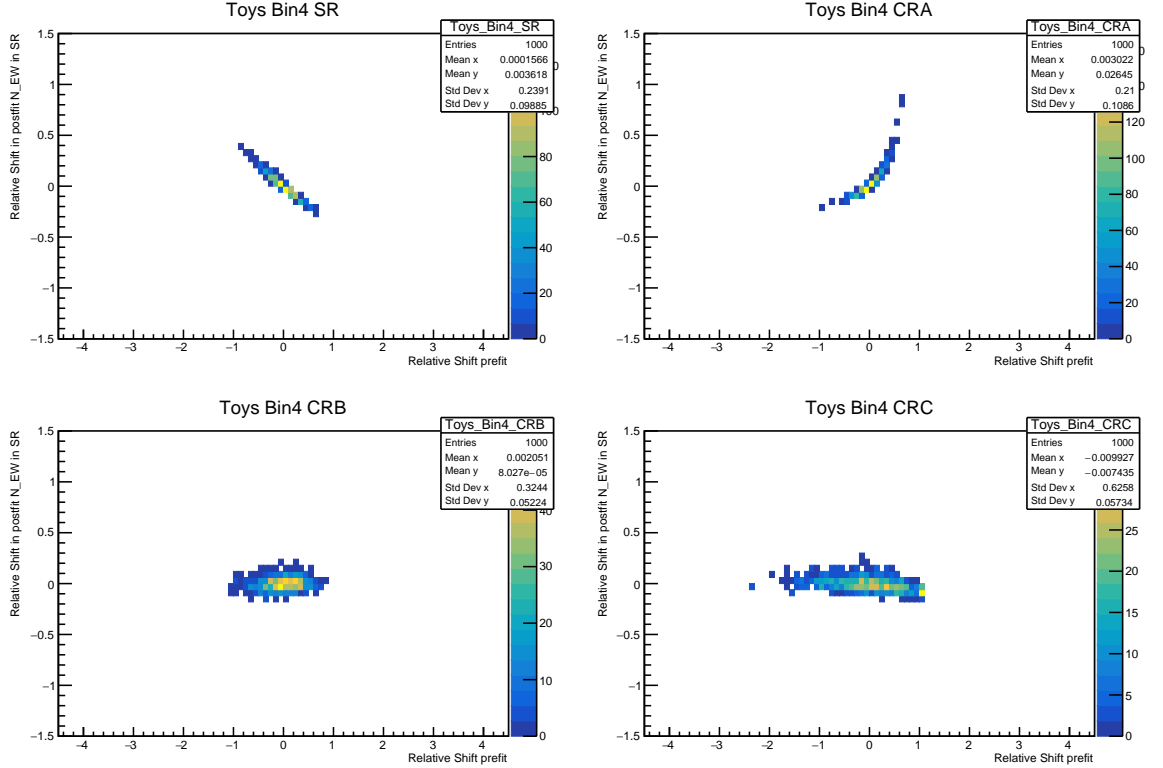


Figure 5.16. Relative yield results in the fourth bin of m_{jj} for the $f(x_i) = c$ fit. From the CRC plot it can be seen that the poor QCD statistics here no longer have an impact on the stability of the fit. Additionally, the statistical precision on the extracted yield due to fluctuations in CRC has improved by a factor of 4 by switching to $f(x_i) = c$ from $f(x_i) = mx_i + c$.

that there are only very small fluctuations between observables. In adding this term, the final systematic uncertainties were seen to be biased significantly. Therefore, no such constraint is added in the final signal extraction method. Moreover, the integrated yields are seen to be statistically consistent between observables, therefore there are no actual inconsistencies between the results of different observables.

5.13 Uncertainties

The uncertainties on the extracted EW- $W\gamma jj$ yield are split into systematic and statistical uncertainties. The systematic uncertainties are divided into theoretical uncertainties, which affect the shape and normalisation of the MC samples, and experimental uncertainties, which affect the event reconstruction. The systematic uncertainties are broken down into components that are fully correlated between bins and regions. This means that, for every systematic variation, the templates are varied simultaneously in the signal and control regions before constructing the likelihood.

A complete list of experimental uncertainties is given in Section 5.13.4, the dominant experimental uncertainties are Jet Energy Scale (JES) and Jet Energy Resolution (JER) uncertainties. The theoretical uncertainties on the measurement are described in Section 5.13.6. The dominant theoretical uncertainty is from strong- $W\gamma jj$ generator choice.

5.13.1 Data Statistical Uncertainties

To determine the statistical uncertainty on the extracted EW- $W\gamma jj$ yield due to the statistical precision of the data (referred to as data stat uncertainty), 10,000 pseudo-experiments are created from the data sample, where for each pseudo-experiment, the bin contents are sampled from a Poisson distribution of mean equal to the original bin yields. In generating the pseudo-experiments, each region and bin is sampled independently using different a different random number seed. The extracted EW- $W\gamma jj$ yield is recorded for each of the 10,000 pseudo-experiments. The RMS of the extracted EW- $W\gamma jj$ yields of the pseudo-experiments is taken as the data statistical uncertainty. Figures 5.17 and 5.18 show the pseudo-experiments for each of the observables for two example bins in m_{jj} and p_T^ℓ , respectively. In each case they are consistent with a Gaussian distribution. For the first bin on m_{jj} , there is small spike at zero caused by the large width of the Gaussian in this bin. The width is large in the first bin because there is a large background contamination at low m_{jj} which results in larger uncertainties in the extracted EW- $W\gamma jj$ yield. In the case of p_T^ℓ , the background contamination is not so large in the first bin which results in a more narrow Gaussian, and therefore there is no spike around 0.

5.13.2 MC Statistical Uncertainties

The statistical uncertainty on the extracted EW- $W\gamma jj$ yield due to the combined statistical precision of the MC samples (referred to as MC stat uncertainty) is evaluated similarly to the data stat uncertainty, by creating 10,000 pseudo-templates in the signal region and the control regions, and propagating each combination of pseudo-experiments through the likelihood fit. The only difference with the MC stat uncertainty calculation is in the preparation of the pseudo-experiments. Instead of sampling from a Poisson distribution of mean equal to the bin content, each MC weight is multiplied by an integer sampled from a unit Poisson distribution.

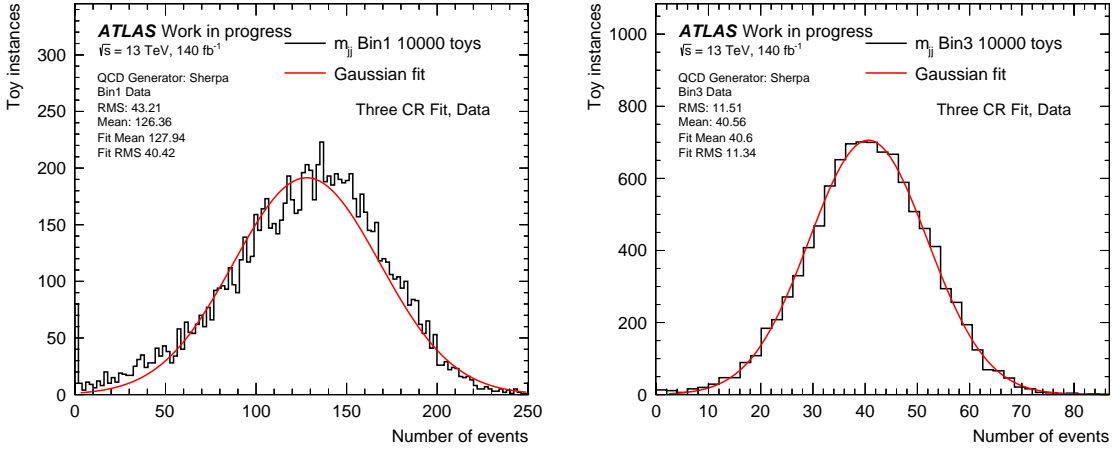


Figure 5.17. The pseudo-experiment extracted yields for m_{jj} for the first and third bins. Each pseudo-experiment represents represents a statistical fluctuation in the data. The RMS' of these distributions form the data stat uncertainty, R^{stat} . Note that the mean values in each of these plots do not correspond exactly to the central value of the extracted yield (the prescription is to average over all data and MC pseudo-experiments, rather than only pseudo-experiments in data). For display purposes, the shapes of the pseudo-experiments are fit with a Gaussian omitting the bin at zero.

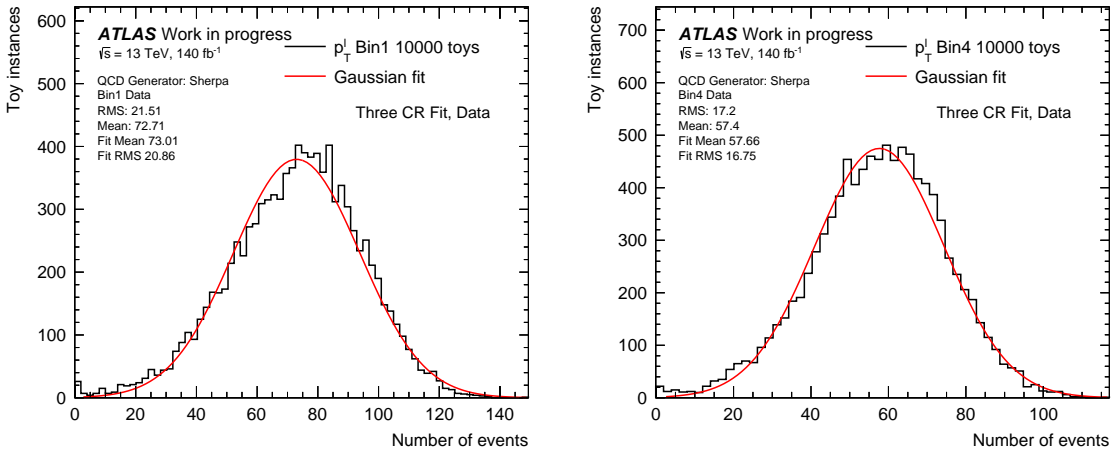


Figure 5.18. The extracted yields of the pseudo-experiments for p_T^l for the first and fourth bins. Each pseudo-experiment represents represents a statistical fluctuation in the data.

The reason for the difference in the pseudo-experiment preparation methods is that when it comes to keeping track of correlations between nominal and systematic MC templates, the latter approach must be used. This is explained in more detail in Section 5.13.4.

The relative data and MC stat uncertainties are shown in Figure 5.19 for the signal extraction in data. The relative statistical uncertainties are calculated with respect to the nominal extracted yield given by

$$N_{EW}^{\text{Nom}} \equiv \langle N_{EW,i} \rangle, \quad (5.16)$$

where $N_{EW,i}$ is the postfit EW- $W\gamma jj$ yield in the signal region, and the index i runs over 10,000 pseudo-experiment, where for each pseudo-experiment, the data and all MC templates are fluctuated in all CRs and the SR before performing the signal extraction. The angled brackets denote taking the mean value. The reason for taking the mean of the pseudo-experiments is because there is a slight bias in the toy distributions which results in the mean lying away

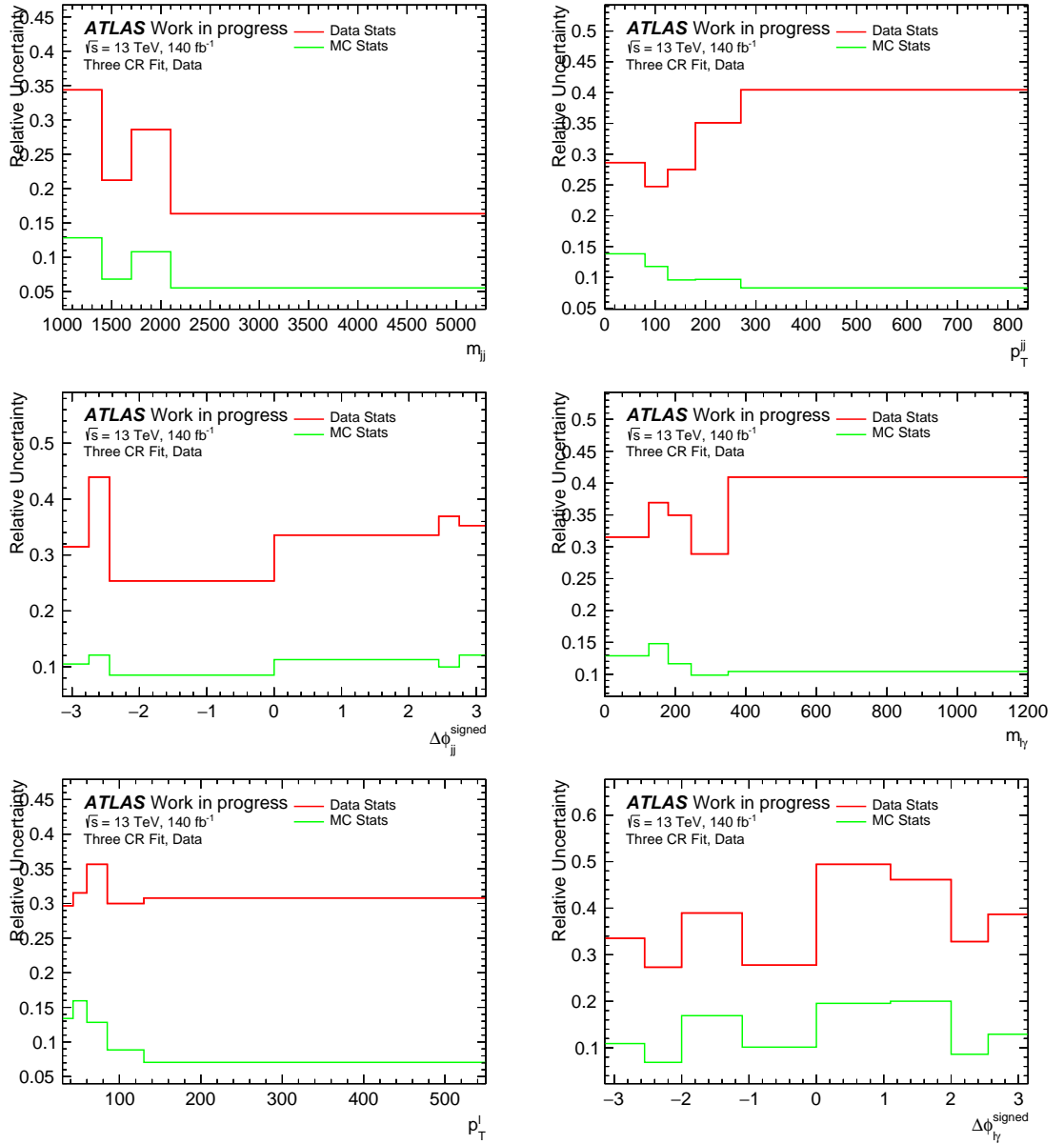


Figure 5.19. Statistical uncertainty on the central value $N_{\text{EW,Nominal}}$ for m_{jj} , $p_{T,jj}$, $\Delta\phi_{jj}^{\text{signed}}$, $m_{\ell\gamma}$, p_T^ℓ , $\Delta\phi_{\ell\gamma}^{\text{signed}}$, where data is used.

from the nominal value. Not doing this would result in asymmetric uncertainties.

5.13.3 Treatment of Systematic Uncertainties

Before going on to describe the different sources of systematic uncertainties, it is useful to outline the processing of the systematic uncertainties.

Bootstrapping and statistical significance

In order to understand how systematic uncertainties are treated in this analysis, it is necessary to introduce the *bootstrapping* procedure. This procedure allows for the statistical uncertainty on each systematic uncertainty to be determined. Consider one set of MC events where, for example, the Jet Energy Scale (JES) is fixed at its nominal value and the same set of events

where the JES is fixed at a slightly different value. The events remain entirely correlated, one just has a different scaling for the jet energies and p_T . One of the implications of this correlation is that in order to determine the statistical uncertainty on the JES (from taking the difference in extracted yields derived using nominal and varied templates), the standard error propagation formalism cannot be used, since this assumes uncorrelated uncertainties. One way to approach this problem is through the *bootstrapping* procedure, where $N_{\text{bootstraps}}$ pseudo-experiments are constructed for the nominal case and for each systematic variation. These bootstraps are created by multiplying each MC event weight by a random number sampled from a unit (discrete) Poisson distribution. The bootstraps are created in such a way as to preserve the correlations between the nominal pseudo-experiment numbered i , and systematic one corresponding to the same number. The correlations are preserved by choosing the random number for a given event when creating the nominal and systematic MC templates. 1000 pseudo-experiments is determined to be sufficient for calculating the statistical uncertainty in the systematic uncertainties.

Note that the random number seeds for the bootstrapping procedure are chosen according to the run number and event number. The statistical uncertainties are calculated by constructing each pseudo-experiment and constructing a new likelihood.

The statistical uncertainty of each systematic is important because this provides information about the statistical significance of the systematic uncertainty, i.e. how likely it is that the difference between the nominal and systematic extracted yields is not due to statistical fluctuations. To decide whether an uncertainty is statistically insignificant, the significance threshold, σ_{thresh} , is defined, where if the systematic uncertainty is greater than σ_{thresh} times its statistical uncertainty, it is deemed to be statistically significant. In this analysis, a systematic uncertainty is deemed to be statistically significant if the significance in at least one of the observable bins is greater than σ_{thresh} . If the systematic uncertainty is statistically insignificant, it is set to zero in all bins. Three values of σ_{thresh} and their corresponding impact to the systematic uncertainties were investigated. These are $\sigma_{\text{thresh}} = 1.6$, $\sigma_{\text{thresh}} = 1.0$, and $\sigma_{\text{thresh}} = 0$. In the end, it was decided to quote the systematic uncertainties at the level of $\sigma_{\text{thresh}} = 0$, i.e. to keep all systematic uncertainties since the difference in overall systematic uncertainty on the extracted yield is very small between the choices by virtue of the fact that the most statistically insignificant systematic uncertainties are also those which have the smallest impact. See Appendix B.2 for the final uncertainties on the extracted yield with each choice of significance threshold.

Smoothing procedure

All systematic uncertainties except for the uncertainties from the non-prompt background estimates are smoothed. Those which have their statistical significance evaluated using bootstrapping are smoothed through a Linear Gaussian Kernel smoothing algorithm [169], which uses the statistical errors on the systematic uncertainties as inputs to the smoothing algorithm. Using Gaussian Kernel smoothing reduces the likelihood of over-smoothing, i.e. where the

smoothed value is far away from what would be expected from statistical fluctuations.

The theory uncertainties on the $Z\gamma$ and top backgrounds do not have their statistical significance evaluated using bootstrapping. This is because these uncertainties are very small, and deriving the bootstrapping is computationally expensive. These uncertainties are smoothed using the Root TH1::Smooth(3) function. This completes three iterations of the “353QH, twice” algorithm outlined in the 1974 Cern School of Computing proceedings [170]. This is a running median smoothing algorithm that uses a combination of operations given by its name, where the integers refer to the window size, “Q” refers to quadratic interpolation, “H” refers to the use of the Hann function, and “twice” refers to doubling the sequence.

The smoothing is always performed on the relative uncertainties. The smoothed relative uncertainties are applied to $N_{\text{EW}}^{\text{Nom}}$ to get the final absolute uncertainties.

Symmetrising

All experimental uncertainties, and some data-driven background uncertainties have “up” and “down” variations, where for example the JES is increased (up) and decreased (down) with respect to the nominal JES. These variations are propagated separately through the likelihood before symmetrising, and the sign of the shift is kept during the symmetrisation. The symmetrised uncertainties are unfolded using the response matrices corresponding to the “up” variation.

5.13.4 Experimental Systematic Uncertainties

The following experimental uncertainties are included:

- Jet uncertainties [121]:
 - The EffectiveNP JES nuisance parameters which capture the uncertainties from the in-situ calibrations ($\gamma/Z+\text{jet}$ and multi-jet balance).
 - Other JES uncertainties coming from the eta-intercalibration, pileup, flavour-related, and punch-through uncertainty sources.
 - The EffectiveNP JER nuisance parameters which capture uncertainties from the noise term and di-jet in-situ sources.
 - Differences between the MC and data in the JER.
 - Flavour tagging uncertainties
 - Precision flavour uncertainties
 - Vertex tagging
 - b -tagging uncertainties

- Electron and muon uncertainties including uncertainties [93, 99, 106]:
 - Identification efficiency scale factors
 - Isolation efficiency scale factors
 - Reconstruction efficiency scale factors
 - Trigger efficiency scale factors
 - Energy scale and resolution
 - Track-to-vertex-association (TTVA) – muons only
- Photon uncertainties including uncertainties from [93, 99]:
 - Photon energy resolution
 - Photon energy scale
- E_T^{miss} uncertainties including uncertainties [115]:
 - Soft track resolution
 - Soft track scale
- Pileup reweighting (PRW) uncertainties⁸
- Uncertainty in the integrated luminosity ($\pm 0.83\%$) [70]

The dominant sources of experimental uncertainties come from JER and JES sources. This is because VBS events are primarily characterised by kinematic parameters relating to jets (see the VBS cuts in table 5.3). Therefore scale and resolution effects relating to jets can have a large impact on the number of selected events in the analysis phasespace.

The signal is extracted using the nominal templates for 1000 bootstraps, and separately using the templates corresponding to the experimental systematic nuisance parameters. For any given nuisance parameter (e.g. “JER_EffectiveNP_1up”), the strong- $W\gamma jj$, EW- $W\gamma jj$ and prompt background yields are all varied simultaneously according to this nuisance parameter – i.e. the experimental uncertainties are treated as correlated between samples. The nominal systematic uncertainty for a given systematic variation is calculated by determining the average deviation from the nominal for each bootstrap, divided by the average of all the nominal bootstraps. The relative experimental uncertainty on the central value for the extracted EW yield is denoted as $R_{\text{exp}}^{\text{sys}}$

$$R_{\text{exp}}^{\text{sys}} = \frac{\langle N_{\text{EW},i}^{\text{Nom}} - N_{\text{EW},i}^{\text{exp}} \rangle}{\langle N_{\text{EW},i}^{\text{Nom}} \rangle}, \quad \Delta R_{\text{exp}}^{\text{sys}} = \frac{\text{RMS}(N_{\text{EW},i}^{\text{Nom}} - N_{\text{EW},i}^{\text{exp}})}{\langle N_{\text{EW},i}^{\text{Nom}} \rangle}, \quad (5.17)$$

⁸PRW refers to the correction of the pileup profile in simulation to that of data using a set of weights.

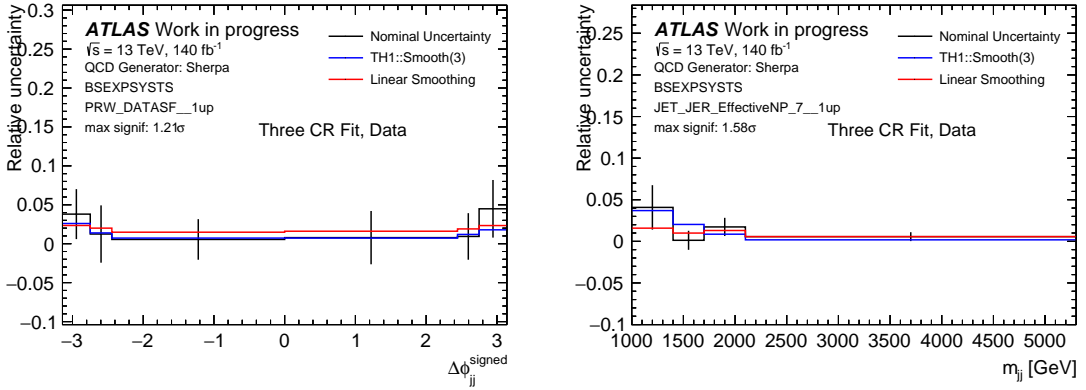


Figure 5.20. Examples of smoothed experimental systematic uncertainties in $\Delta\phi_{jj}^{\text{signed}}$ and m_{jj} . Error bars on the relative systematic uncertainties are statistical uncertainties derived using bootstrapping. The statistical uncertainties are used in the smoothing algorithms, the results of which are shown by the blue and red lines.

The red line is used as the final systematic uncertainty for all bootstrapped systematic uncertainties.

where the extracted EW yield in the SR, for bootstrap i , corresponding to a systematic variation is denoted $N_{\text{EW},i}^{\text{exp}}$. And the extracted EW yield for bootstrap i , corresponding to the nominal is denoted as $N_{\text{EW},i}^{\text{Nom}}$.

The statistical uncertainties on $R_{\text{exp}}^{\text{sys}}$, denoted here as $\Delta R_{\text{exp}}^{\text{sys}}$ are evaluated by subtracting each systematic bootstrap from the nominal bootstrap, and taking the RMS of the resulting distributions.⁹ Figure 5.20 shows an example selection of individual systematic uncertainties (before symmetrising up and down variations) and the smoothing of these uncertainties using their statistical errors. The results of smoothing and symmetrising the up and down variations for a selection of jet uncertainty sources and a selection of other experimental sources are shown for m_{jj} in Figures 5.21 and 5.22, respectively. These show the individual variations in the central value due to experimental uncertainty sources for the extracted EW yield and the relative uncertainties.

5.13.5 Non-prompt Background Uncertainties

The uncertainties on the non-prompt background estimates as described in Section 5.4 are propagated to the extracted EW yield by simply shifting the data-driven background template in the fit corresponding to the uncertainty, where this is correlated between regions. Statistical uncertainties on the templates are treated in the same was as MC stat uncertainties in the likelihood – i.e. they are included in the construction of the Poisson constraints. Additionally, statistical uncertainties are explicitly included as up and down variations when shifting the templates. There is no bootstrapping performed for uncertainties on the data-driven backgrounds, and there is also no smoothing performed on the final uncertainties on the extracted EW yield. The reason for not smoothing is because, without bootstrapping to determine their statistical significance, these uncertainties could easily be oversmoothed.

⁹There is small technicality in the calculation of the relative uncertainties prior to smoothing, in that the pseudo-experiments in the denominator are always the same pseudo-experiments as those in the numerator. Therefore $\langle N_{\text{EW},i}^{\text{Nom}} \rangle$ is not exactly the same as the nominal yield $N_{\text{EW}}^{\text{Nom}}$ in equation 5.16, since this is calculated from MC+data stat pseudo-experiments. It's also worth pointing out that when there is no bootstrapping performed, the value in the denominator for the relative uncertainty calculation is always the nominal yield without any average over pseudo-experiments.

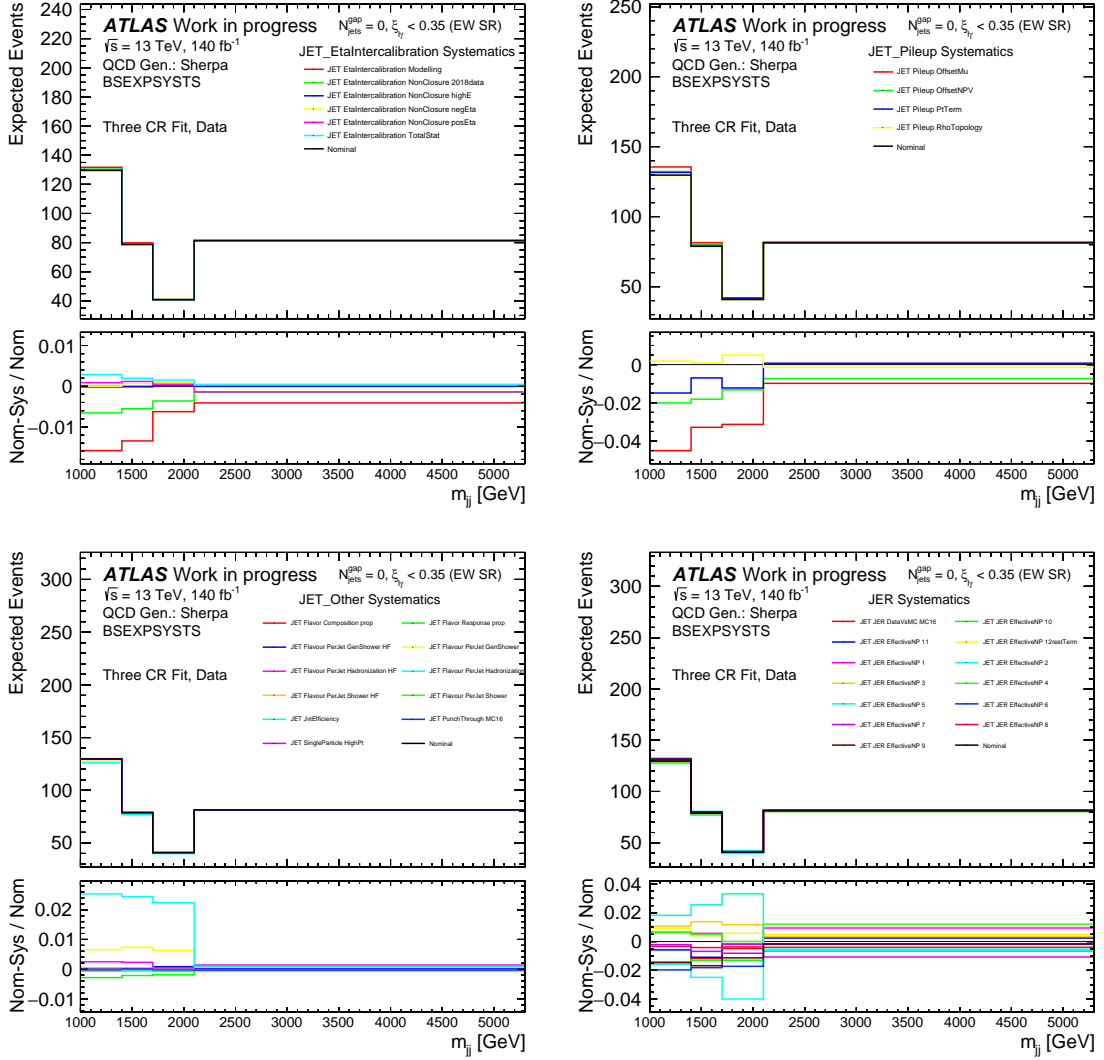


Figure 5.21. Example of relative uncertainties due to the different JES and JER variations propagated to the final extracted EW yield with m_{jj} .

The uncertainties on the extracted $EW-W\gamma jj$ yield from the non-prompt backgrounds are shown for the m_{jj} distribution in Figure 5.24. The other observables are omitted for brevity.

5.13.6 Theoretical Uncertainties

Theoretical uncertainties affect the shape and normalisation of the individual MC backgrounds. These effects are not correlated between the backgrounds, therefore theoretical uncertainties are calculated for each background separately and are all added in quadrature in the calculation of the total theoretical uncertainty on the extracted $EW-W\gamma jj$ yield.

The theoretical uncertainties considered are (i) scale uncertainties, which characterise missing high order corrections in perturbative QCD calculations; (ii) uncertainties in the strong coupling constant α_s ; (iii) PDF uncertainties; (iv) generator choice uncertainties; and (v) the effect of the interference between the strong- $W\gamma jj$ and $EW-W\gamma jj$ processes.

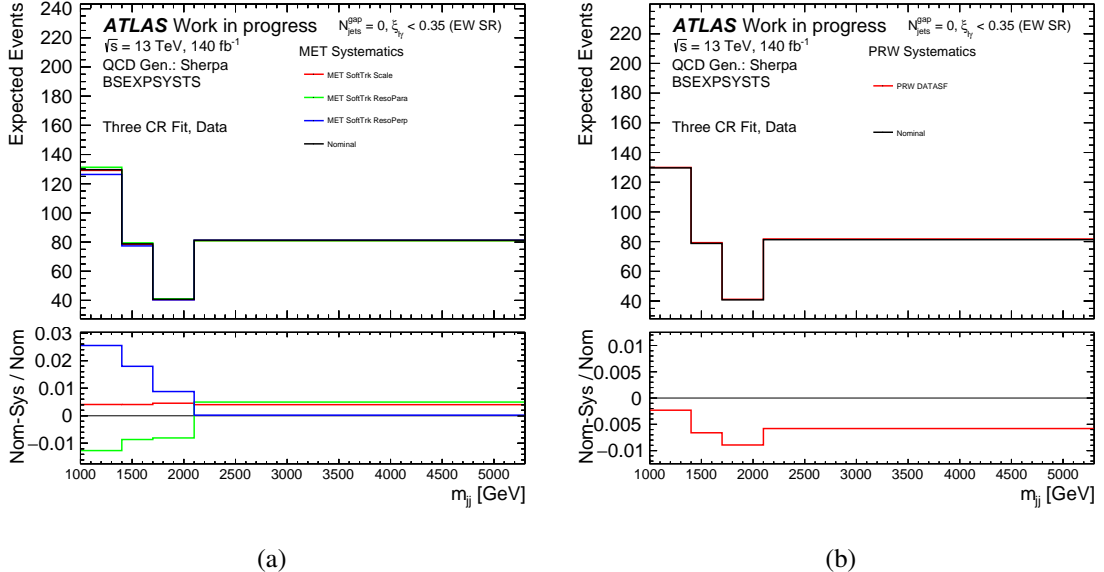


Figure 5.22. Relative uncertainties due to E_T^{miss} (a) and PRW (b) systematic variations propagated to the final extracted EW yield with m_{jj} .

Strong- $W\gamma jj$ Generator Choice

There is a significant difference in the modelling of the strong- $W\gamma jj$ background between the **SHERPA** and **MADGRAPH** MC generators. In order probe the degree to which the measurement depends on the of background model, it an uncertainty is assigned to this choice.

The strong- $W\gamma jj$ generator choice uncertainty before smoothing, $R_{\text{gen}}^{\text{sys}}$, is calculated by extracting an EW yield in the SR for both strong- $W\gamma jj$ templates for 10,000 bootstraps over the strong- $W\gamma jj$ templates. The difference in extracted yield is computed for every pair of bootstraps, and the mean over all bootstraps is taken. This is turned into a relative uncertainty by dividing by the central value; i.e.

$$R_{\text{gen}}^{\text{sys}} = \frac{\langle N_{\text{EW},i}^{\text{Nom, Sherpa}} - N_{\text{EW},i}^{\text{Nom, MG5}} \rangle}{\langle N_{\text{EW},i}^{\text{Nom, Sherpa}} \rangle}, \quad \Delta R_{\text{gen}}^{\text{sys}} = \frac{\text{RMS}(N_{\text{EW},i}^{\text{Nom, Sherpa}} - N_{\text{EW},i}^{\text{Nom, MG5}})}{\langle N_{\text{EW},i}^{\text{Nom, Sherpa}} \rangle}, \quad (5.18)$$

where the index i runs over bootstraps (note that even though the index i is the same for **SHERPA** and **MADGRAPH**, these bootstraps are uncorrelated). The statistical uncertainty on $R_{\text{gen}}^{\text{sys}}$ is denoted by $\Delta R_{\text{gen}}^{\text{sys}}$, and is evaluated by taking the standard deviation (denoted RMS) for each pair of bootstraps. The strong- $W\gamma jj$ generator choice uncertainties are shown in Figure 5.25.

The statistical uncertainty of the generator choice uncertainties is relatively high, this is evident in the around 20-30% statistical uncertainties on the $R_{\text{gen}}^{\text{sys}}$ values. The reason for this is that, since the **SHERPA** and **MADGRAPH** predictions are statistically independent, the statistical uncertainties on the generator choice is the quadrature sum of the individual statistical uncertainties. Furthermore, the statistical precision of the **MADGRAPH** sample is around 2.3 times worse than the **SHERPA** sample, hence the statistical resolution of the combined uncer-

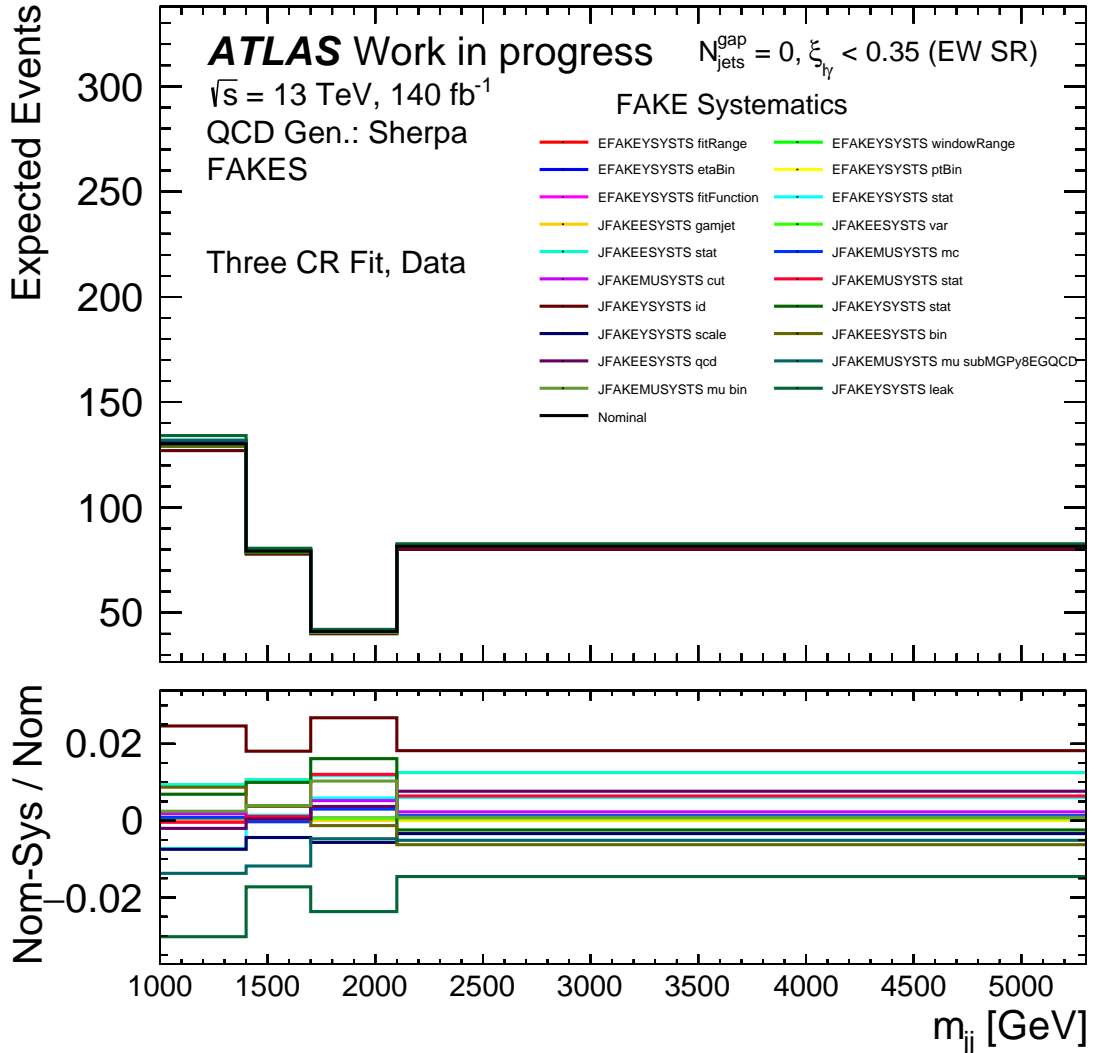


Figure 5.23

Figure 5.24. Relative uncertainties on the extracted EW- $W\gamma jj$ yield from the non-prompt background estimates with m_{jj} .

tainty is limited by the precision of the MADGRAPH sample.¹⁰ The fact that it is difficult to statistically resolve these uncertainties is one of the main motivating factors behind choosing the Gaussian kernel smoothing algorithm over the root TH1 smoothing. It is evident from the last bin of the p_T^ℓ plot in Figure 5.25, that choosing the TH1 smoothing would have resulted in an over-smoothed uncertainty – i.e. the smoothed value is $> 2\sigma$ above the nominal value in the last bin. It is important to note that this choice – as with any analysis optimisation decision – was made based on blinded Asimov results.

The generator choice uncertainties are consistent with zero. This is somewhat expected as the three control region fit is designed to be robust against modelling uncertainties due to the additional residual correction, $f(x_i) = c$. Without this residual correction, the generator choice uncertainties are significantly larger, as shown in Figure 5.26 where $f(x_i) = 1$. Even though $R_{\text{gen}}^{\text{sys}}$ is consistent with zero, the conservative approach is taken to still include these

¹⁰Ideally, a new MADGRAPH sample would have been generated with a similar statistical precision to the nominal SHERPA sample. However, this was not done because of time limitations, and because these samples already contain over 100 million events each.

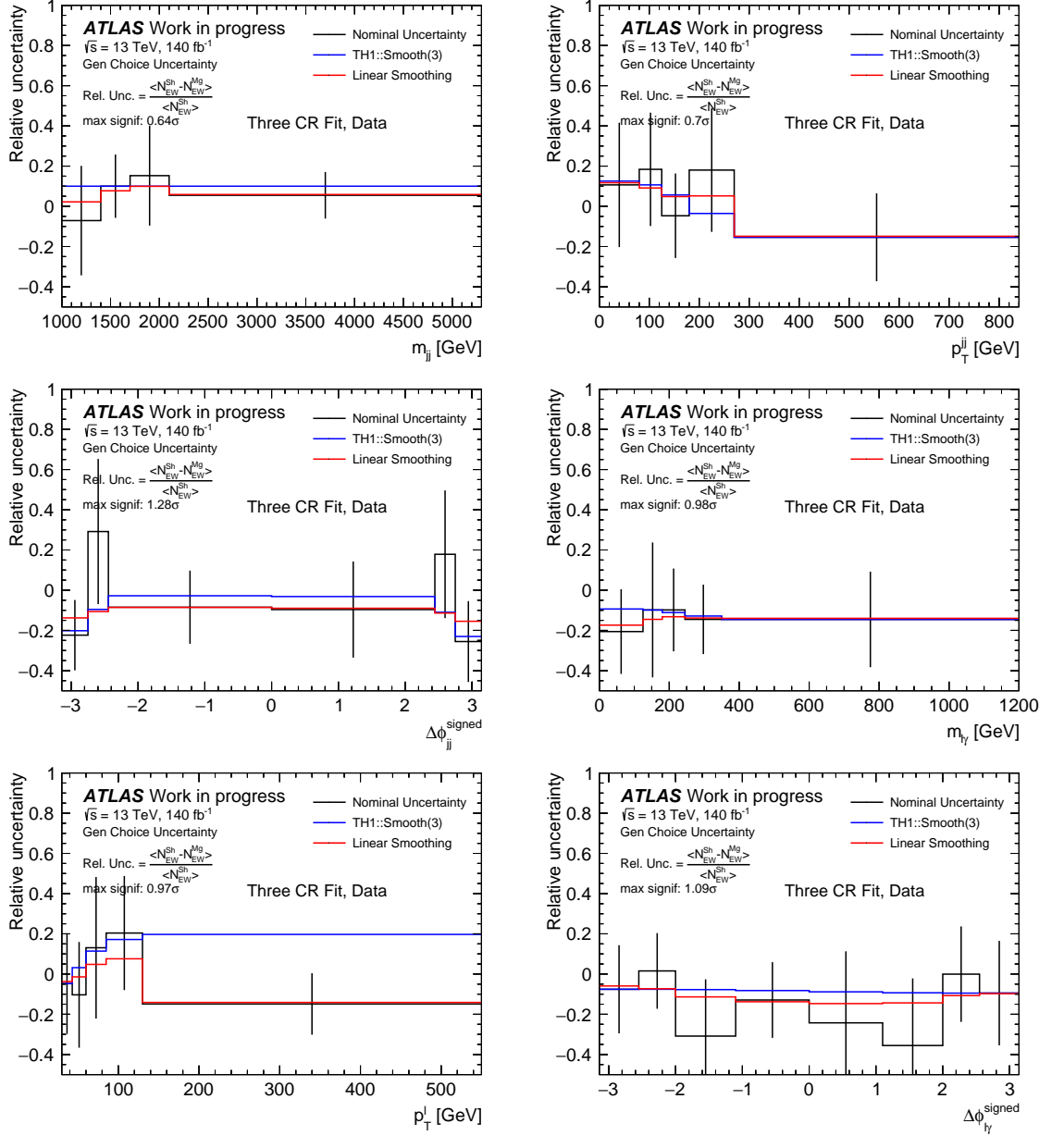


Figure 5.25. Data QCD generator choice uncertainties with m_{jj} , $p_{T,jj}$, $\Delta\phi_{jj}^{\text{signed}}$, $m_{\ell\gamma}$, p_T^ℓ , and $\Delta\phi_{\ell\gamma}^{\text{signed}}$ before and after smoothing. Note that because $f(x_i) = c$ introduces correlations between the bins, the statistical error bars are correlated between bins.

uncertainties after smoothing.

EW-W γ jj Generator Choice

The uncertainty due to the choice of MC generator in the EW-W γ jj sample is evaluated in almost the same way as the strong-W γ jj generator choice, where now the **MADGRAPH** EW-W γ jj sample is used as the alternate sample. The only difference is that the EW-W γ jj generator choice uncertainties are not smoothed. The reason for not smoothing these uncertainties is that in order to evaluate the final uncertainty after unfolding, the extracted yield using **MADGRAPH** has to be unfolded using the response matrix from the same sample. This is called the ‘‘hidden variables test’’, and aims to probe the effect of MC shape differences in the unfolding procedure which are not covered by detector simulation uncertainties. There-

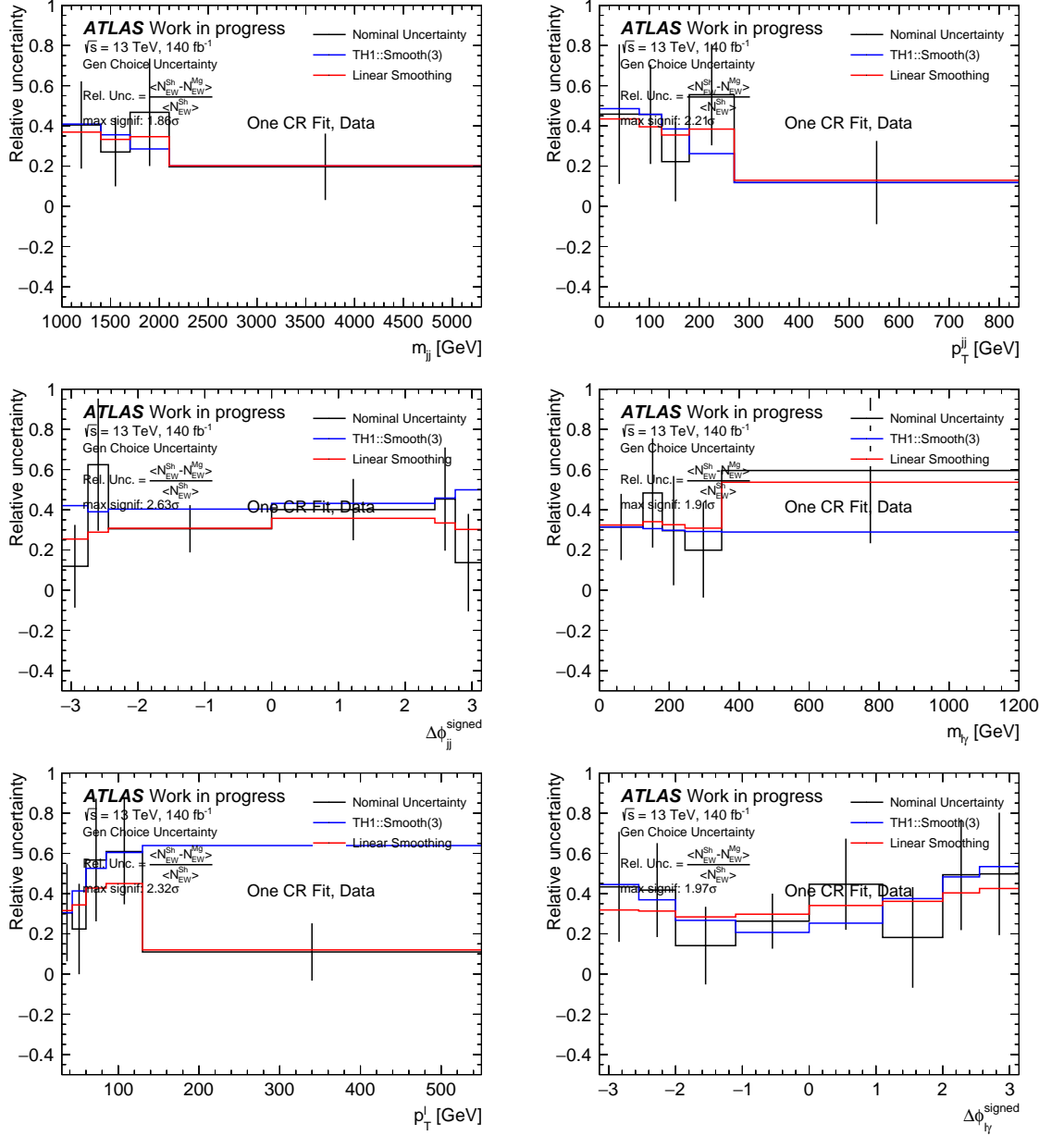


Figure 5.26. Data QCD generator choice uncertainties for the $f(x_i) = 1$ (equivalently one control region) configuration with m_{jj} , $p_{T,jj}$, $\Delta\phi_{jj}^{signed}$, $m_{\ell\gamma}$, p_T^ℓ , and $\Delta\phi_{\ell\gamma}^{signed}$ before and after smoothing. It is clear that the generator choice uncertainty on the measurement is no longer consistent with zero, but fluctuates around 30-40% instead.

fore, the smoothing is not implemented in order to prevent smoothing over valid effects from hidden variables. The data EW-W γjj generator choice uncertainty results is shown for m_{jj} in Figure 5.27, where the other observables are omitted for brevity. The uncertainty is below 5% in all bins of m_{jj} , and therefore represents a relatively unimportant contribution. The differences between the SHERPA and MADGRAPH EW-W γjj simulations are primarily in the overall normalisation, therefore the choice of generator in the simulation of the signal corresponds to only a small uncertainty on the extracted EW-W γjj yield.

Scale Uncertainties

The theoretical calculation of the pp collision cross-section for a particular process depends on μ_F , μ_R , and α_s . These symbols denote the factorisation scale, renormalisation scale,

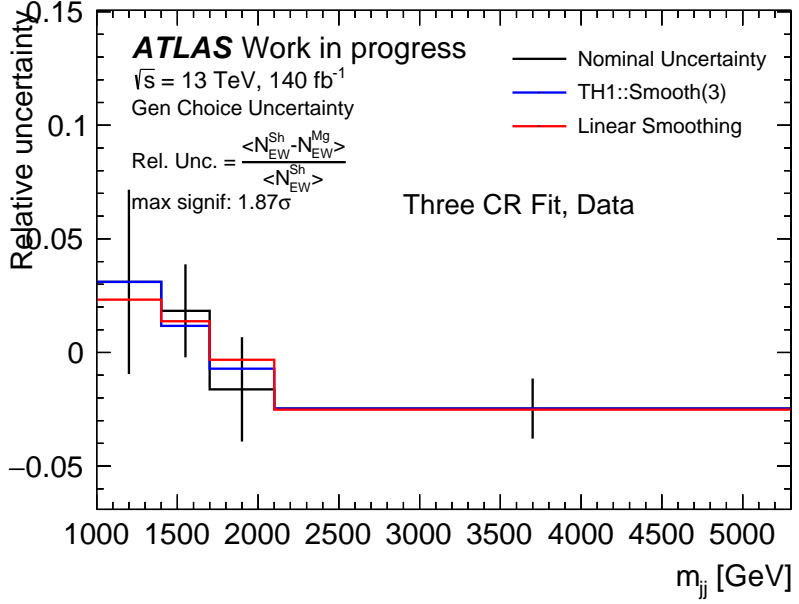


Figure 5.27. Data EW generator choice uncertainties with m_{jj} before and after smoothing. The smoothing has a small effect on the final uncertainty.

and the strong coupling constant. The factorisation scale represents the momentum scale at which particles couple to each other. The renormalisation scale describes the running of the strong coupling constant, α_s . The factorisation and renormalisation scale are associated with collinear and ultraviolet divergences in higher-order contributions to the hard scatter, respectively, and can be chosen independently in the perturbative calculation of the collision cross-section. Since the hard scatter depends on μ_F and μ_R , varying these scales is a way of estimating contributions from missing higher orders [171].

For each sample, the (μ_F, μ_R) combination is altered by multiplicative factors of (1.0, 1.0), (1.5, 1.0), (1.0, 1.5), (0.5, 1.0), (1.0, 1.5), (2.0, 1.0), and (1.0, 2.0) to evaluate these uncertainties. For every (μ_F, μ_R) combination the EW- $W\gamma jj$ yield is extracted, and the systematic uncertainty is calculated from:

$$R_{(\mu_F, \mu_R)}^{\text{sys}} = \frac{\langle N_{\text{EW},i}^{\text{Nom}} - N_{\text{EW},i}^{(\mu_F, \mu_R)} \rangle}{\langle N_{\text{EW},i}^{\text{Nom}} \rangle}, \quad (5.19)$$

where $R_{(\mu_F, \mu_R)}^{\text{sys}}$ is the uncertainty from a given (μ_F, μ_R) combination, $N_{\text{EW},i}^{(\mu_F, \mu_R)}$ is the corresponding extracted EW- $W\gamma jj$ yield, and i represents the bootstrap pseudo-experiments. No average over bootstraps is taken for the $Z\gamma jj$ and top scale uncertainties as no bootstrapping is performed for these samples. The final uncertainty due to scale variations is given by the envelope of all the $R_{(\mu_F, \mu_R)}^{\text{sys}}$ values, where the envelope is defined by:

$$R_{\text{scale}}^{\text{sys}} = \max_{(\mu_F, \mu_R)} (R_{(\mu_F, \mu_R)}^{\text{sys}}), \quad (5.20)$$

where the maximum is taken over the different (μ_F, μ_R) values. For the calculation of the unfolded uncertainties, the individual variations corresponding to $R_{(\mu_F, \mu_R)}^{\text{sys}}$ are unfolded prior

to taking the envelope.

The scale uncertainties for data are shown for the m_{jj} distribution in 5.28, where the other observables are omitted for brevity. Changes in the renormalisation and factorisation scale primarily result in shifts in the normalisation, where these can be as high as 45% in the SHERPA strong- $W\gamma jj$ sample. However, because the likelihood fit is robust to changes in normalisation, these get constrained in the fit and only result in a small systematic effect on the extracted EW- $W\gamma jj$ yield. The largest uncertainty comes from scale variations the $Z\gamma jj$ sample. This is because the normalisation of this template is not constrained in the fit. However, these uncertainties are below 4%, and so are still considered small.

α_s uncertainties

The theoretical MC predictions depend on Standard Model parameters such as the strong coupling constant α_s . This parameter is determined from experimental measurements, and therefore comes with statistical and systematic uncertainties. At LO α_s only effects the parton shower calculation, therefore only the SHERPA strong- $W\gamma jj$ and $Z\gamma jj$ samples come with α_s uncertainties, since the other MC generators are interfaced with PYTHIA8 for the parton shower calculation. Up and down variations in the value of α_s are propagated to the extracted EW- $W\gamma jj$ yield. The uncertainty from an α_s variation is calculated in the same way as Equation 5.20. The symmetrised uncertainty is shown in Figure 5.29 for the m_{jj} distribution, where the other observables are omitted for brevity.

PDF Uncertainties

Uncertainties in the underlying PDF in the MC simulations are another source of theoretical uncertainties. These uncertainties stem from experimental uncertainties in the PDF fits and the functional form used in the fits. The uncertainties on the measurements from these effects are estimated by performing the signal extraction with 100 different PDFs for each MC sample, where the NNPDF30 [131] PDF set is used. The uncertainty from a single PDF variation is calculated in the same way as equation 5.20. After calculating the uncertainties from the individual variations, the standard deviation of the 100 different individual PDF uncertainties is taken as the final uncertainty on the extracted EW- $W\gamma jj$ yield due to PDF variations. As an example, the 100 PDF variations are shown for the strong- $W\gamma jj$ sample in m_{jj} in Figure 5.30. The other observables are omitted for brevity.

Uncertainty Due to EW- $W\gamma jj$ and strong- $W\gamma jj$ Interference

To evaluate the uncertainty from the interference between the EW- $W\gamma jj$ and strong- $W\gamma jj$ processes, the signal is extracted with the nominal SHERPA signal sample, and with the sum of the SHERPA and the interference sample (from Section 5.2). The difference between the two extracted yields gives the uncertainty prior to smoothing. Since the interference uncertainty

is of the order of 0-3%, these uncertainties are not bootstrapped, and the TH1 smoothing procedure is used to get the final smoothed uncertainties. These are shown for the m_{jj} distribution in Figure 5.31, where the other observables are omitted for brevity.

5.13.7 Summary of the Systematic Uncertainties

Figures 5.32 show the relative systematic uncertainties on N_{EW}^{Nom} for all distributions, in different categories of experimental and theoretical sources. For all observables, the MC statistical uncertainty and the strong- $W\gamma jj$ generator choice uncertainties dominate, where these are around 10-15% for most bins. Subsequently, the JES and JER uncertainties contribute at around the 5-10% level. For some the $p_{T,jj}$ and $\Delta\phi_{\ell\gamma}^{\text{signed}}$ observables there is a contribution from the EW- $W\gamma jj$ generator choice uncertainty at the level of 10%. This is because there for certain observables there are some non-negligible shape differences between the **MADGRAPH** and **SHERPA** EW- $W\gamma jj$ simulations, particularly in extreme regions of phase-space, such as high $p_{T,jj}$ and low $\Delta\phi_{\ell\gamma}^{\text{signed}}$. Comparing the systematic uncertainties to the data statistical uncertainties in Figure 5.19, it is clear that the differential cross-section measurement will be dominated by the statistical precision of the data.

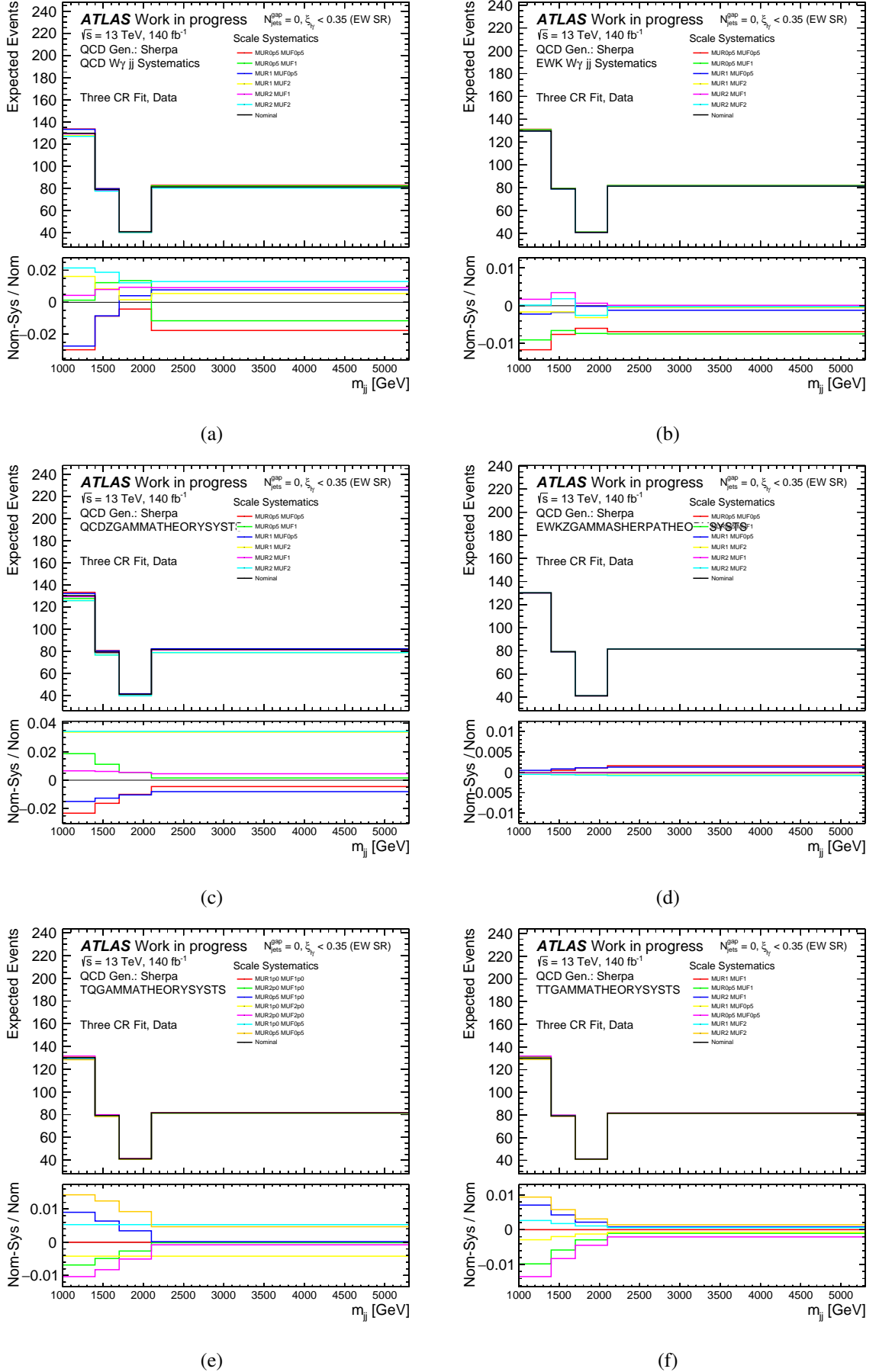


Figure 5.28. Scale uncertainties on the strong- $W\gamma jj$ background (a), EW- $W\gamma jj$ signal (b), strong $Z\gamma jj$ background (c), EW strong $Z\gamma jj$ background (d), non-negligible top backgrounds (e,f) propagated to the extracted EW- $W\gamma jj$ yield with m_{jj} .

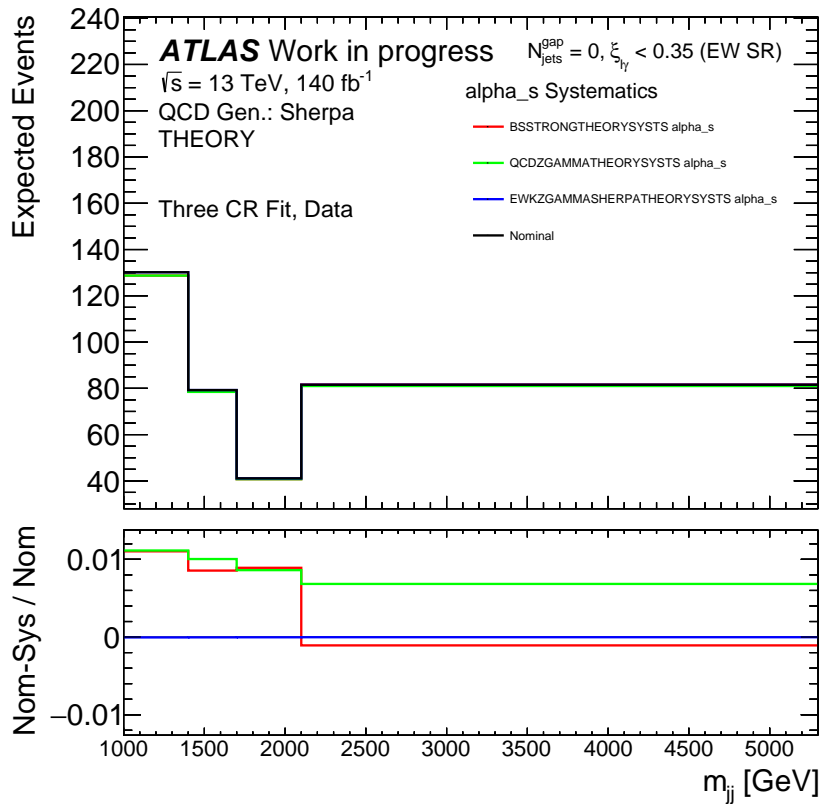
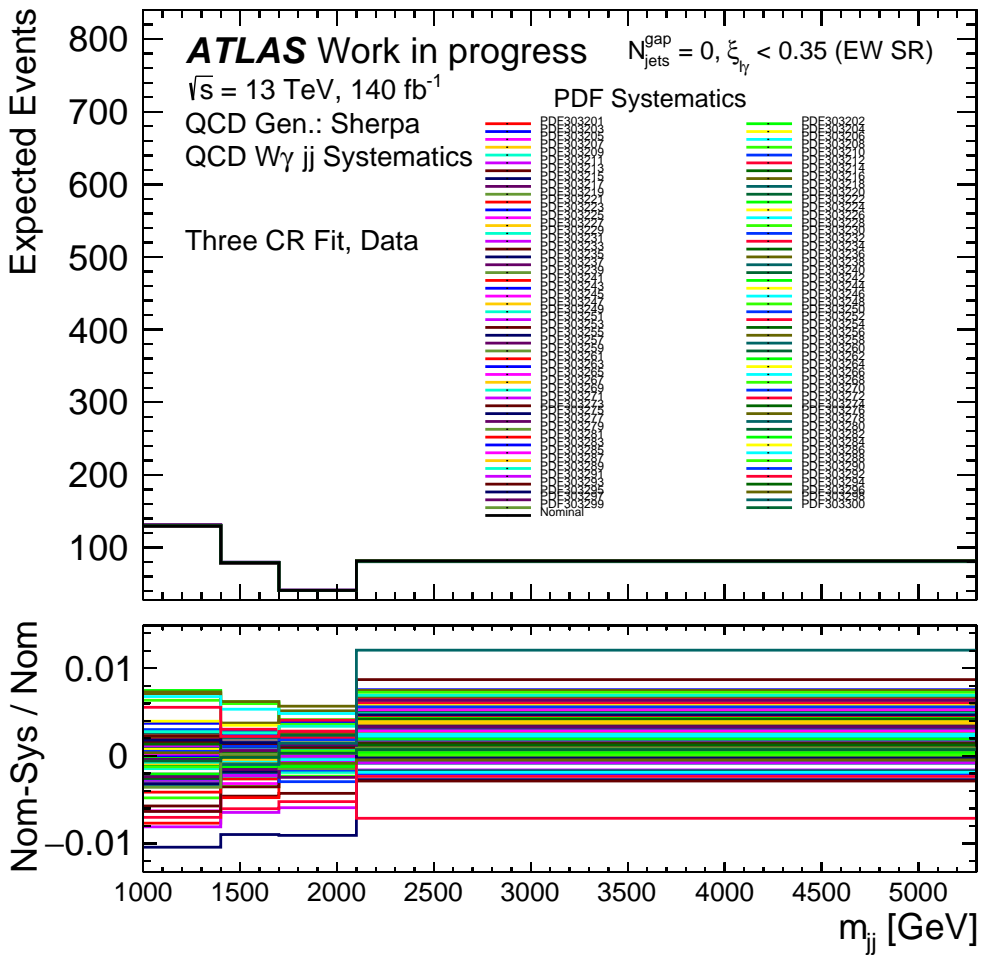
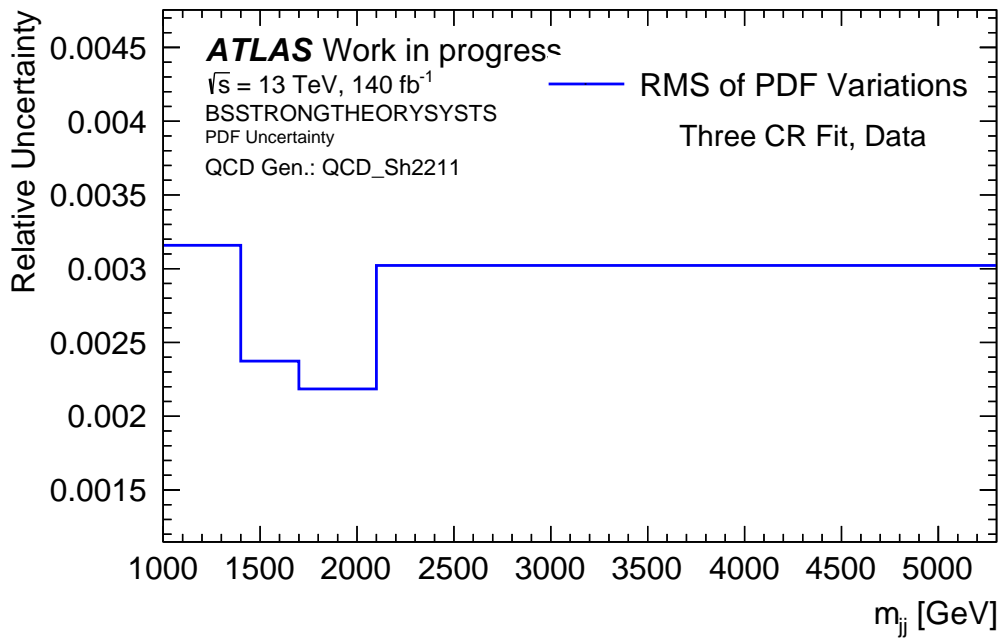


Figure 5.29. Data α_s uncertainties propagated to the extracted EW- $W\gamma jj$ yield with m_{jj} , $p_{T,jj}$, $\Delta\phi_{jj}^{\text{signed}}$, $m_{\ell\gamma}$, p_T^ℓ , and $\Delta\phi_{\ell\gamma}^{\text{signed}}$.



(a)



(b)

Figure 5.30. (a) shows all 100 PDF variations on the strong- $W\gamma\text{jj}$ background propagated to the extracted EW- $W\gamma\text{jj}$ yield for m_{jj} . The RMS of these values in each bin is shown in (b), and determines the final uncertainty due to PDF variations.

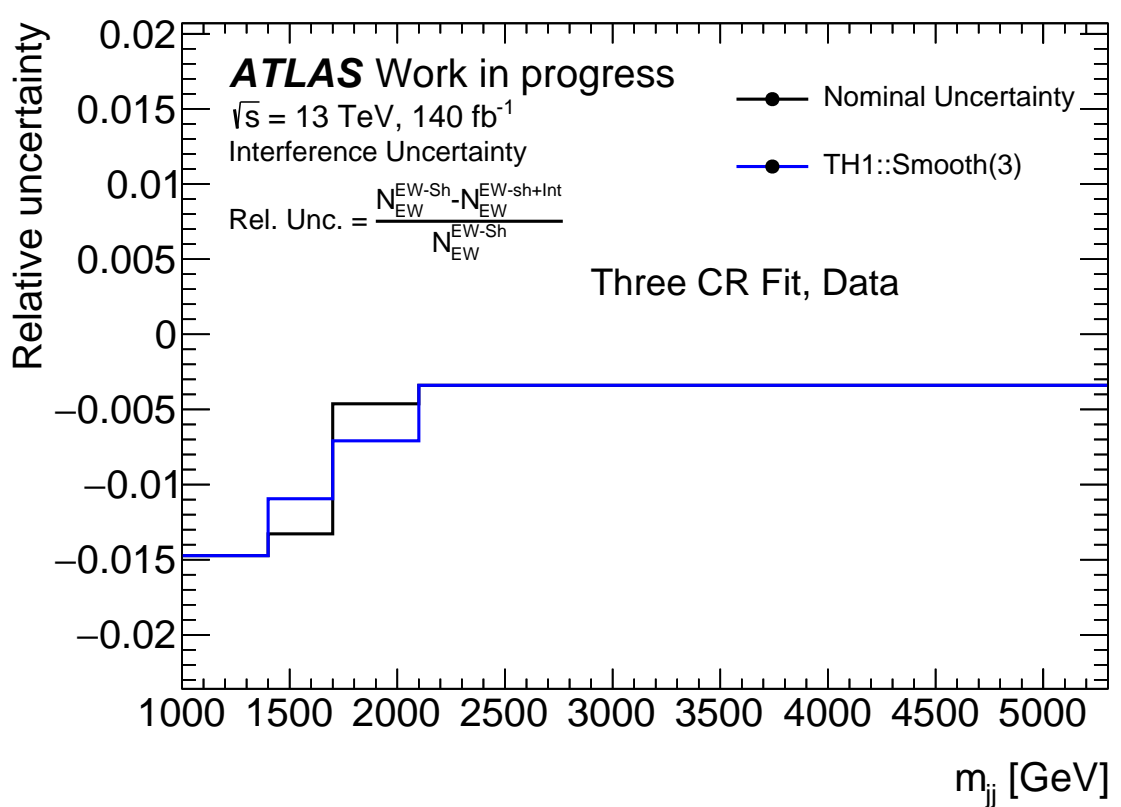


Figure 5.31. Data interference uncertainties with m_{jj} .

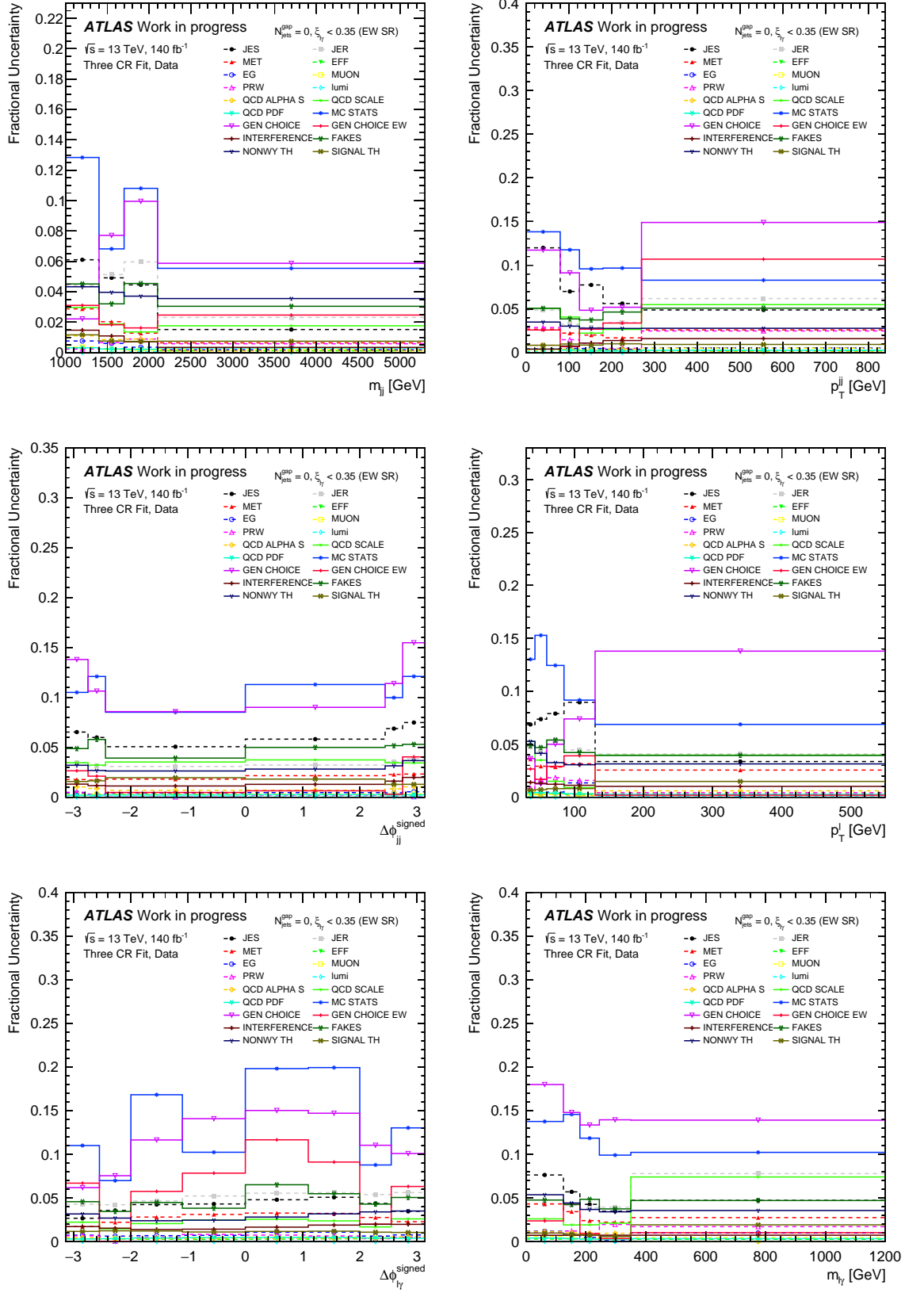


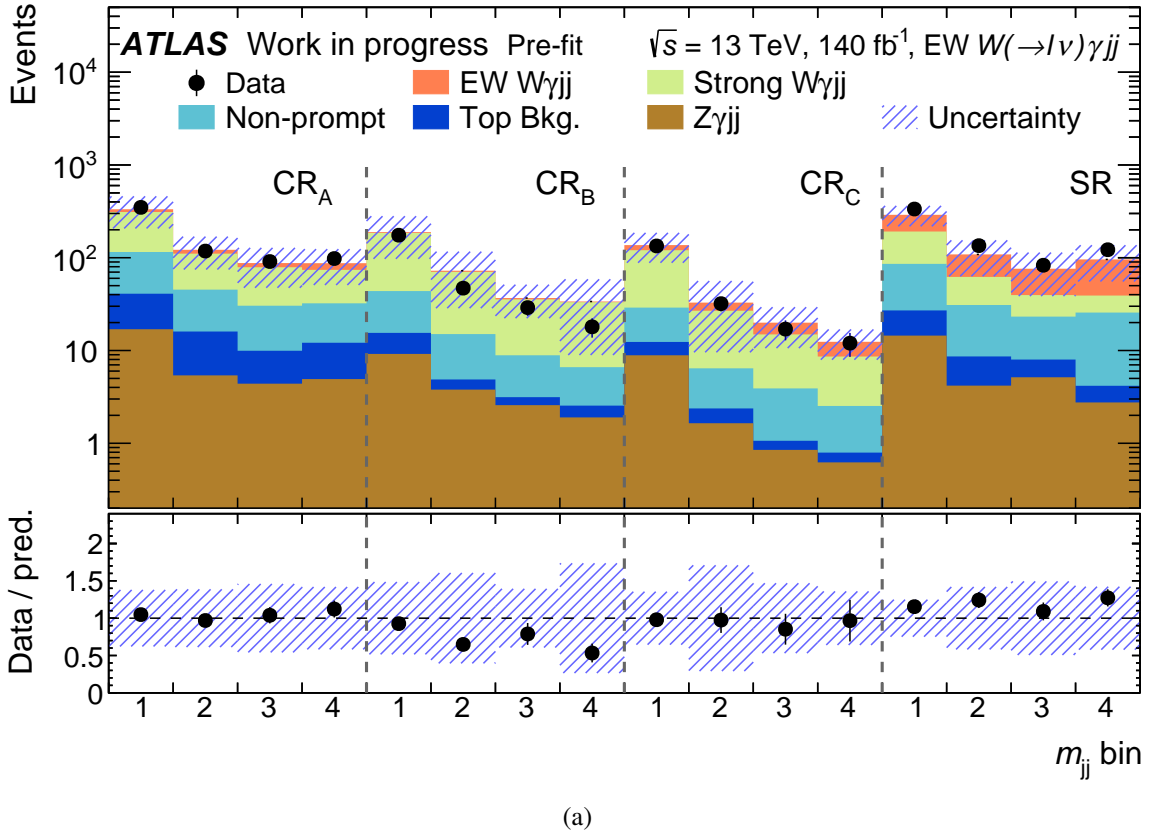
Figure 5.32. Relative systematic uncertainties on $N_{\text{EW}}^{\text{Nom}}$ for the data results.

5.14 Prefit and Postfit Distributions

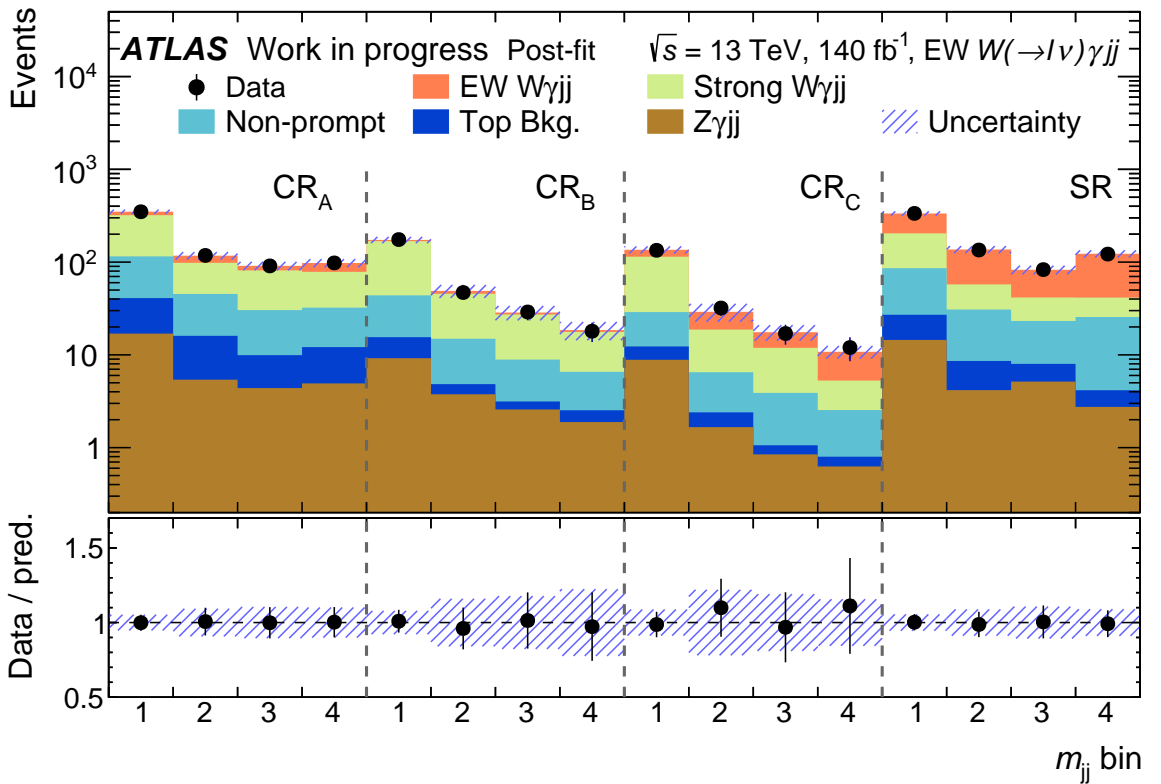
The fit templates before and after the likelihood fit with unblinded data are shown in figs. 5.33 to 5.38. The SHERPA EW- $W\gamma jj$ sample and the SHERPA strong- $W\gamma jj$ sample are used in these plots. The uncertainty bands (see Section 5.13.7 for a summary of the systematic uncertainties) shown in these plots are calculated from combined statistical and systematic uncertainties and show the uncertainty on the entire stack before and after the fit. Before the fit, the uncertainty is dominated by the QCD scale uncertainties. After the fit, the normalisation of the scale uncertainties gets constrained, and the uncertainty is dominated by the statistical precision of the data. The precise treatment of the statistical and systematic uncertainties is outlined in Section 5.13.

The post-fit data-to-prediction agreement is very good in CRa for all observables. This is because the purity of the background is very high in this region, so the $b_{L,i}$ factors are able to effectively constrain the background to agree with the data. The post-fit agreement in the SR is also very good for all observables, which shows that strong- $W\gamma jj$ constraints derived in the control regions are effective in constraining this background in the SR, and that any signal leakage into the control regions does not have a large impact on the signal strength $\mu_{EW,i}$. The statistical precision of the data and predictions in CRb and CRc is worse than in CRa and the SR, which results in generally worse agreement between data and predictions after the fit in these regions.

For the angular observables, the choice is made to symmetrise the MC templates. The reasoning behind and validity of this choice is explained in Section 5.10. Additionally, the assumption is made that the strong- $W\gamma jj$ yields are symmetric in ϕ , hence the $b_{H,i}$ and $b_{L,i}$ parameters are shared between symmetric bins. The $\mu_{EW,i}$ parameter is not treated as symmetric since the goal of measuring the angular observables is to probe the CP structure of the signal, which would be highlighted by any significant asymmetries in the extracted EW- $W\gamma jj$ yields. The increase in the statistical precision of the MC predictions obtained from symmetrising the angular observable templates allows for a finer binning than the kinematic observables. The optimisation of the binning of the observables is outlined in Section 5.9.

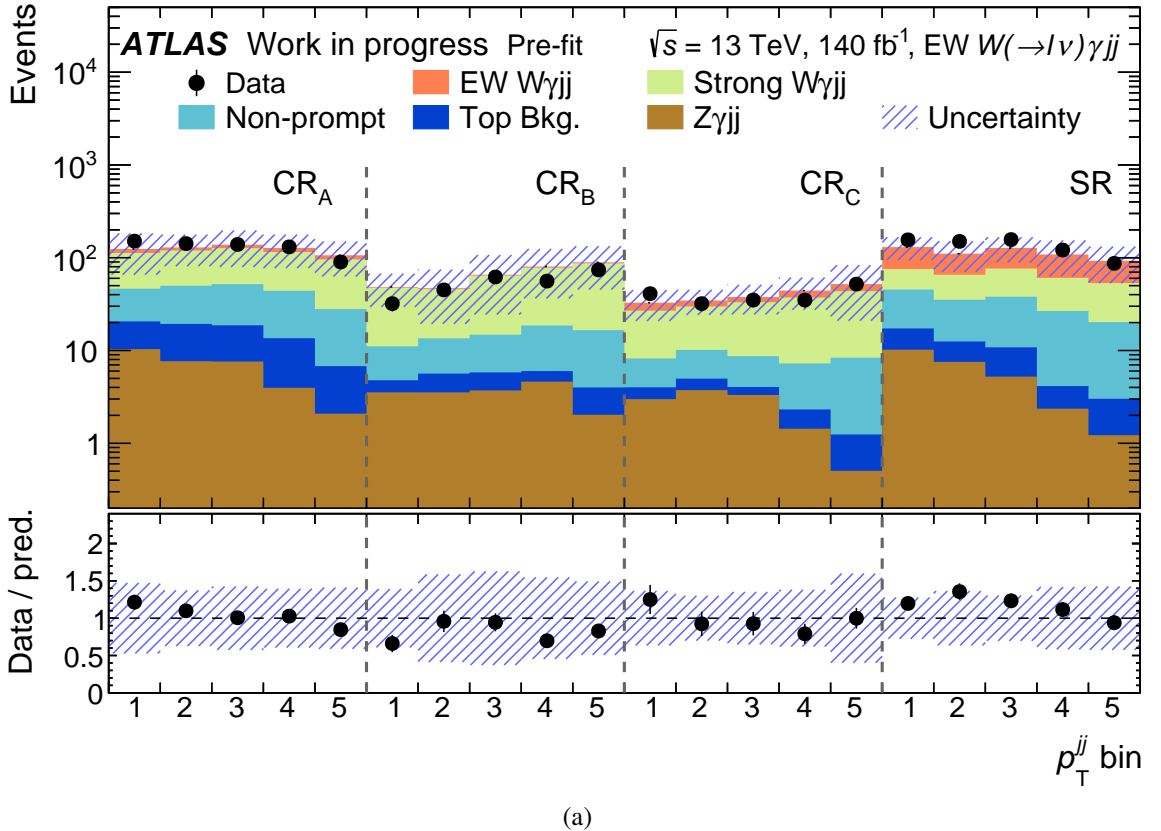


(a)

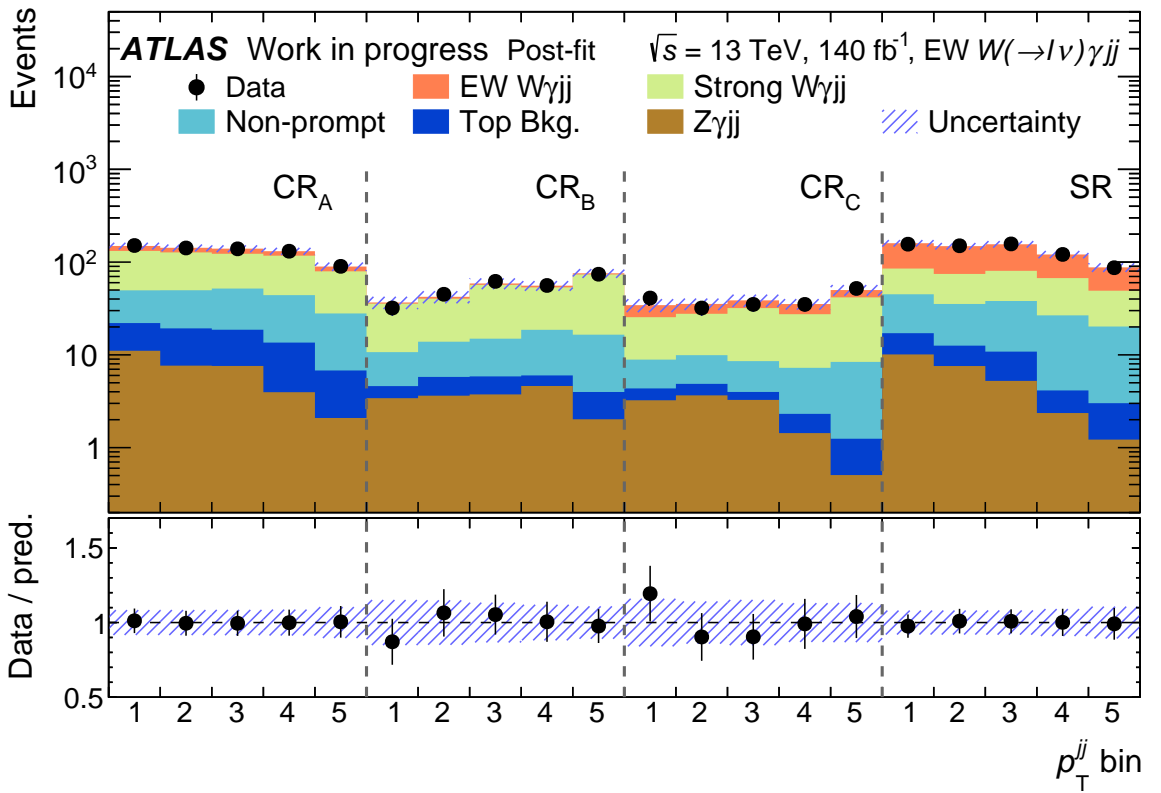


(b)

Figure 5.33. Prefit and postfit MC templates and unblinded data in the SR and three CRs for m_{jj} .

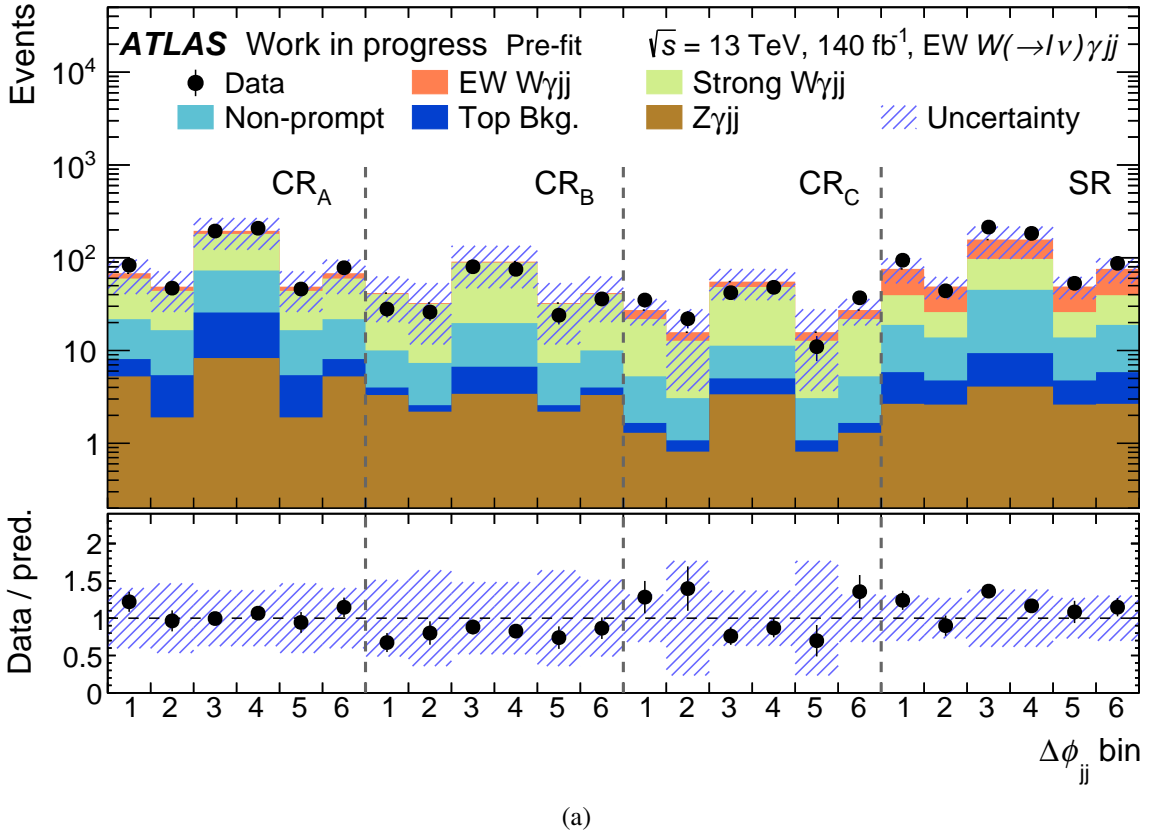


(a)

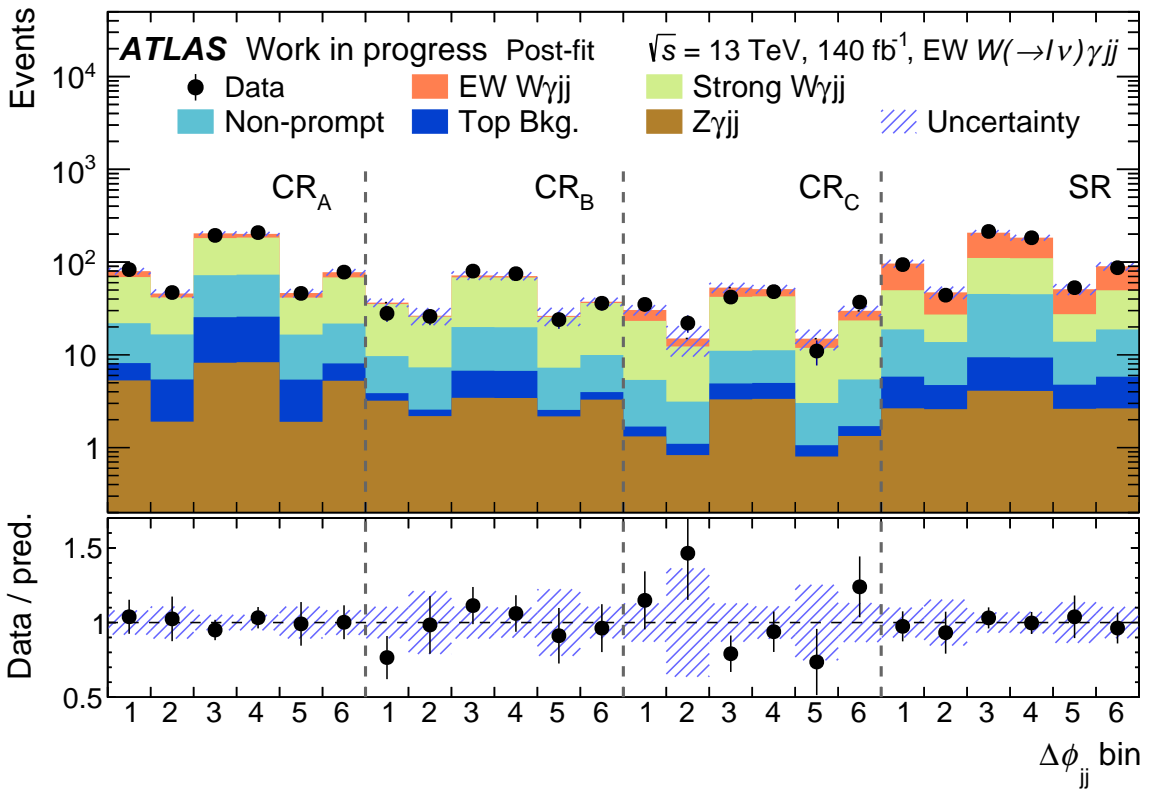


(b)

Figure 5.34. Prefit and postfit MC templates and unblinded data in the SR and three CRs for p_T^{jj} .

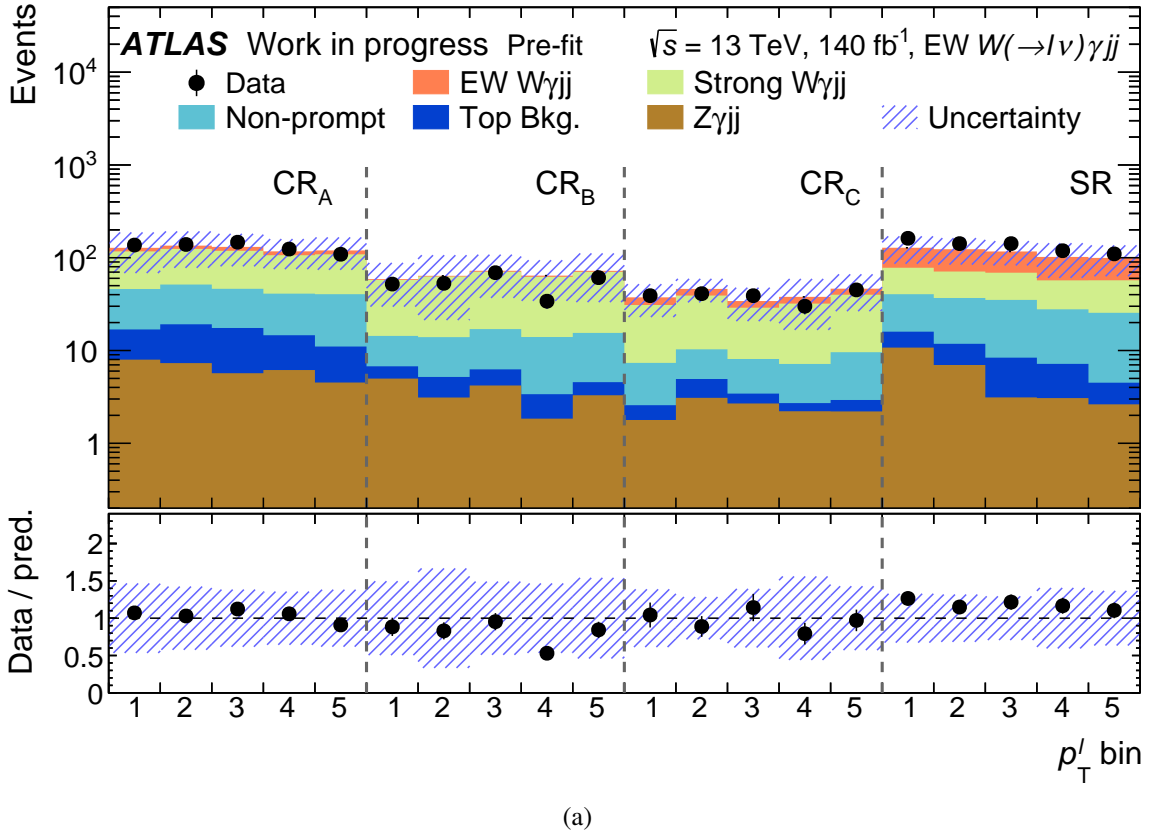


(a)

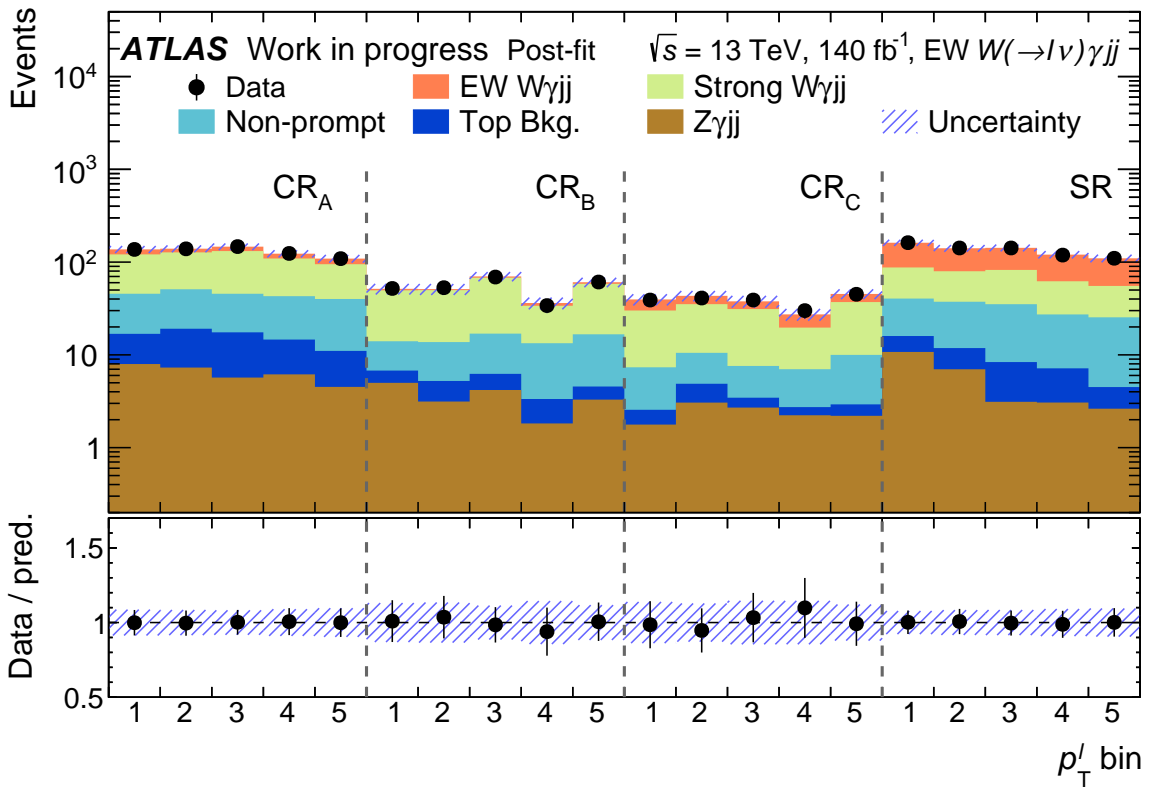


(b)

Figure 5.35. Prefit and postfit MC templates and unblinded data in the SR and three CRs for $\Delta\phi_{jj}^{\text{signed}}$.

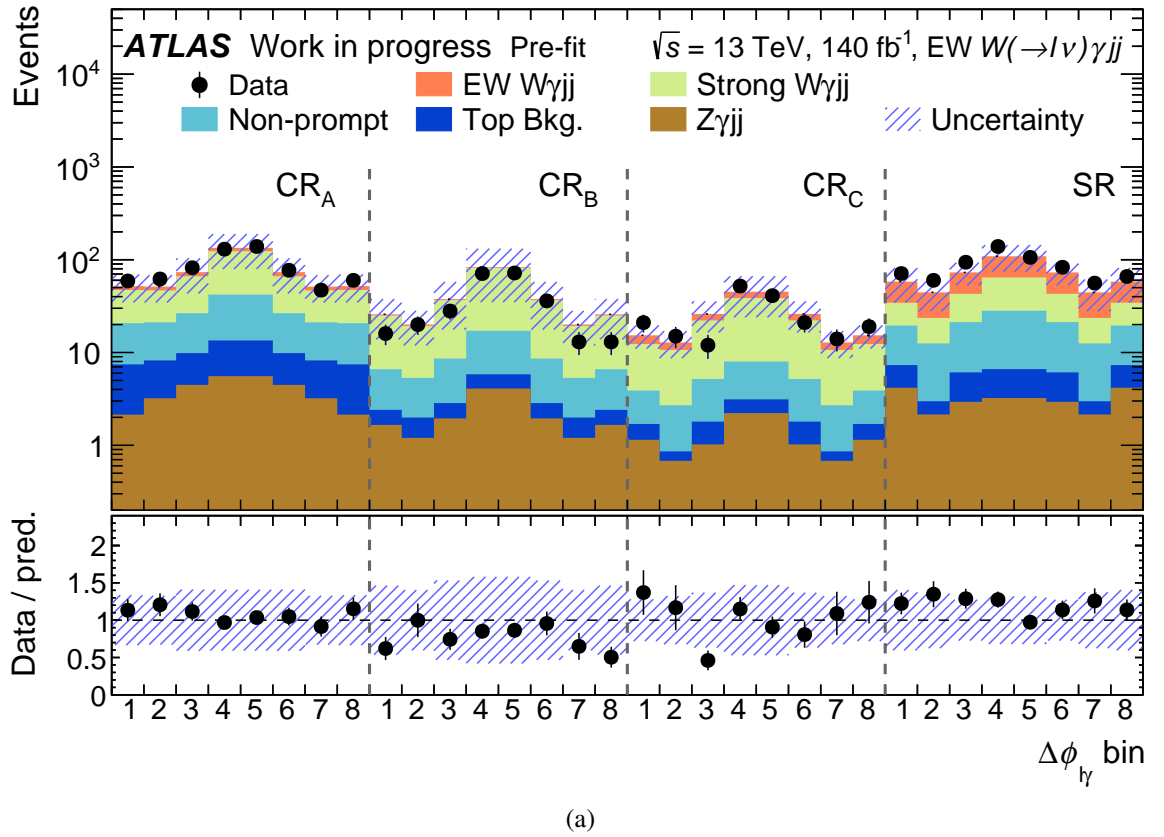


(a)

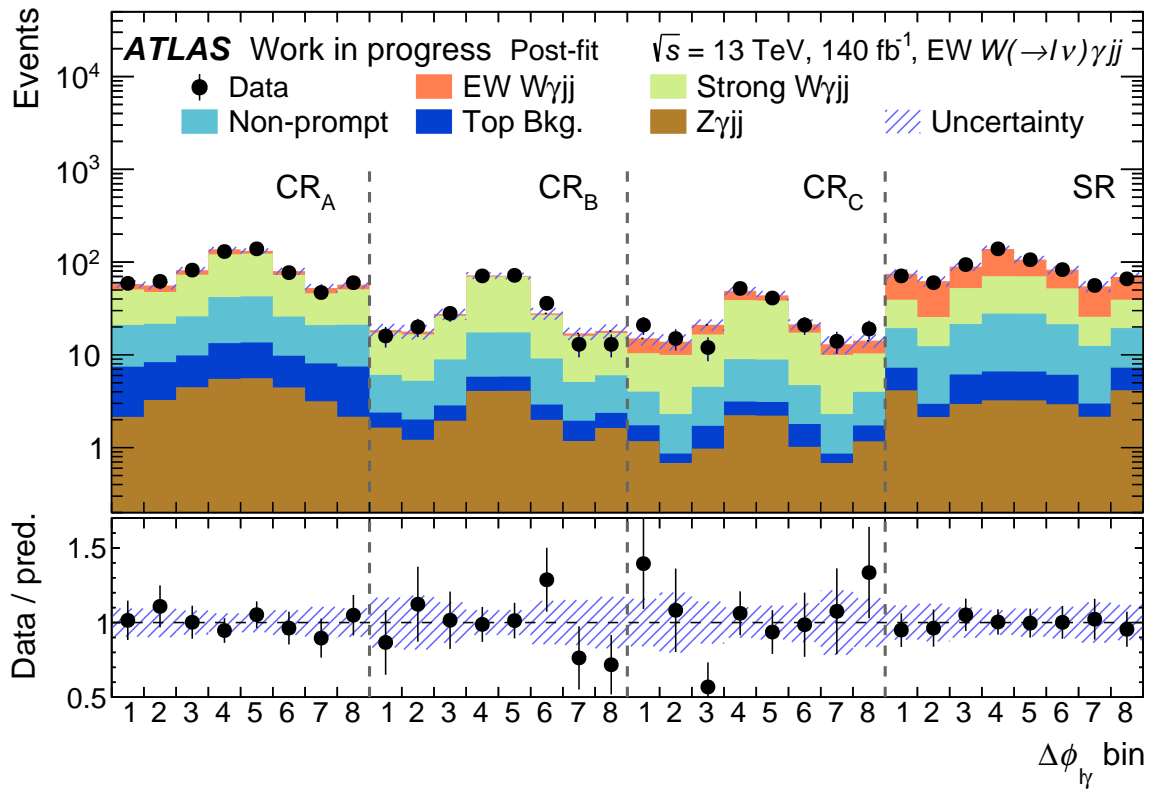


(b)

Figure 5.36. Prefit and postfit MC templates and unblinded data in the SR and three CRs for p_T^ℓ .

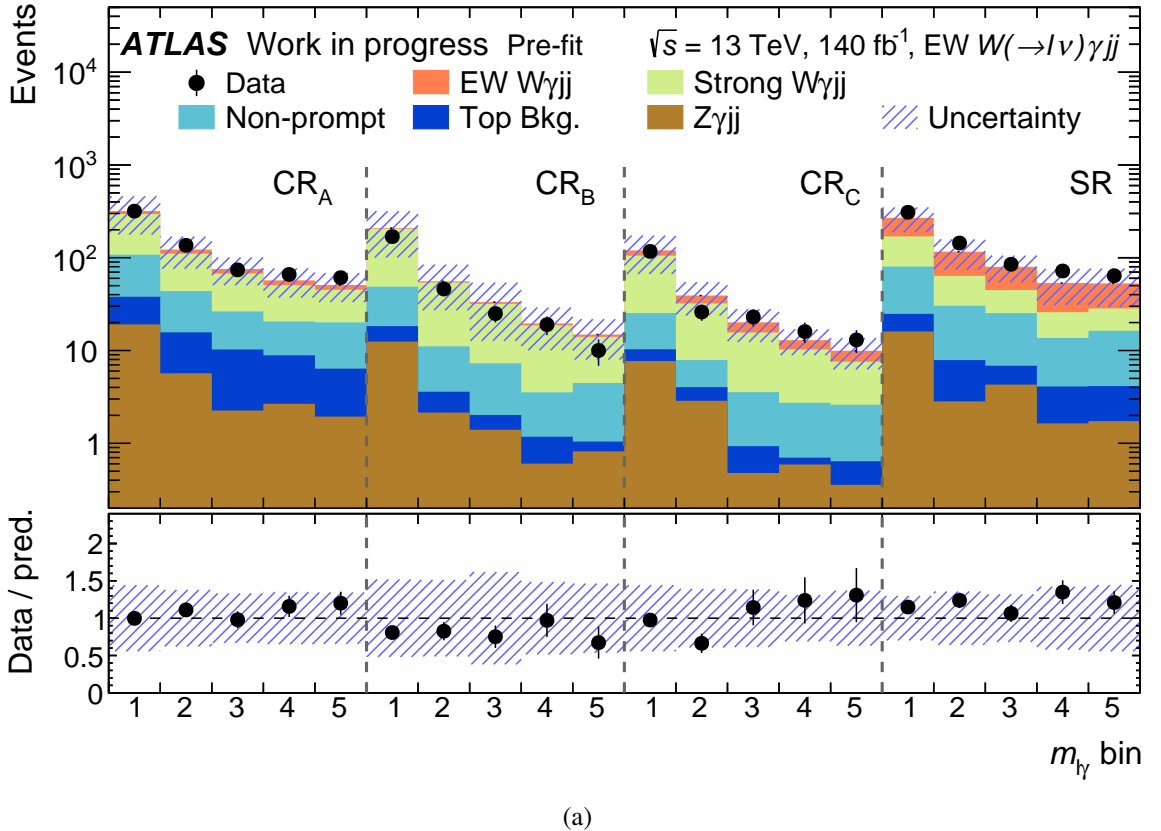


(a)

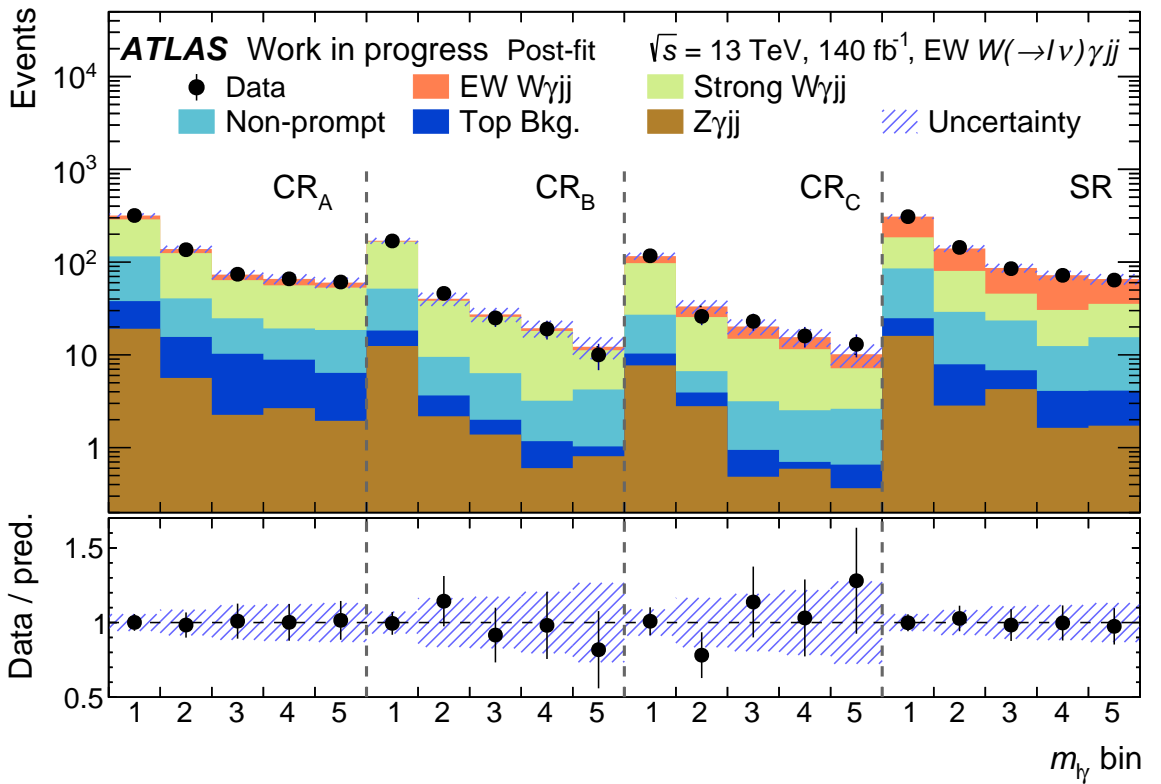


(b)

Figure 5.37. Prefit and postfit MC templates and unblinded data in the SR and three CRs for $\Delta\phi_{\ell\gamma}^{\text{signed}}$.



(a)



(b)

Figure 5.38. Prefit and postfit MC templates and unblinded data in the SR and three CRs for $m_{\ell\gamma}$.

5.15 Cross-checks

5.15.1 Changes to the Likelihood Fit

The systematic uncertainties for the $f(x_i) = 1$ (i.e. One CR) fit, and for the fit where the CRc method is used as described in Section 5.6.1. Similar yields and similar systematic uncertainties should be derived using the two alternative methods. The expectation from using $f(x_i) = 1$ in the fit is that the experimental uncertainties should be similar, but that the modelling uncertainties are significantly larger. The CRc method results are expected to have similar systematic uncertainties, and the values of $N_{\text{EW}}^{\text{Nom}}$ should be consistent within uncertainties. The extracted yields with systematic uncertainties are shown in Figure 5.39 for the nominal cra method for all observables. The corresponding plots for the $f(x_i) = c$, and the CRc method are shown in Figures 5.40 and 5.41, respectively, where only m_{jj} and p_T^{jj} are shown for brevity.

The comparisons of the extracted yields in Figures 5.39 and 5.41 show that the total systematic uncertainties are similar between the nominal CRa method and the CRc method. Comparison of Figures 5.39 and 5.40 show that the systematic uncertainties derived used the $f(x_i) = 1$ fit are significantly larger. When comparing the yields, the $f(x_i) = 1$ results agree with the CRa method results within 10%, and the CRa method results agree with the CRc method results within uncertainties.

The relative systematic uncertainty breakdown of the $f(x_i) = 1$ fit and the CRc method are shown in Figures 5.42 and 5.43. Only m_{jj} and p_T^{jj} are shown for brevity.

The comparison of the uncertainties in Figures 5.42 and 5.43 and Figure 5.32 shows that the $f(x_i) = 1$ results have similar systematic uncertainties apart from the inflated generator choice uncertainty. The systematic uncertainties derived using the CRc method are not as well resolved statistically as the CRa method, the result of this can be seen the jumps in primarily the generator choice and MC stat uncertainties. This happens because CRc is now being used to derive the main constraint on the QCD background $b_{L,i}$ ($b_{L,i}$ is solely responsible for the shape corrections to strong- $W\gamma jj$ in the SR), and CRc has a small amount of strong- $W\gamma jj$ events, resulting in large fluctuations in $b_{L,i}$. In the case where CRc is mainly used to derive $f(x_i)$ (i.e. the nominal case), the fact that $f(x_i)$ is defined to be a constant means that a control region which has a large number of events is not required to derive the residual correction since a shape is not being extracted.

The crosschecks of the nominal (CRa) method with the $f(x_i) = 1$ and CRc methods show that the results of the nominal yields and uncertainties agree with expectations, and that the CRa method is the most optimal as it leads to the smallest uncertainties, whilst these still being well resolved statistically.

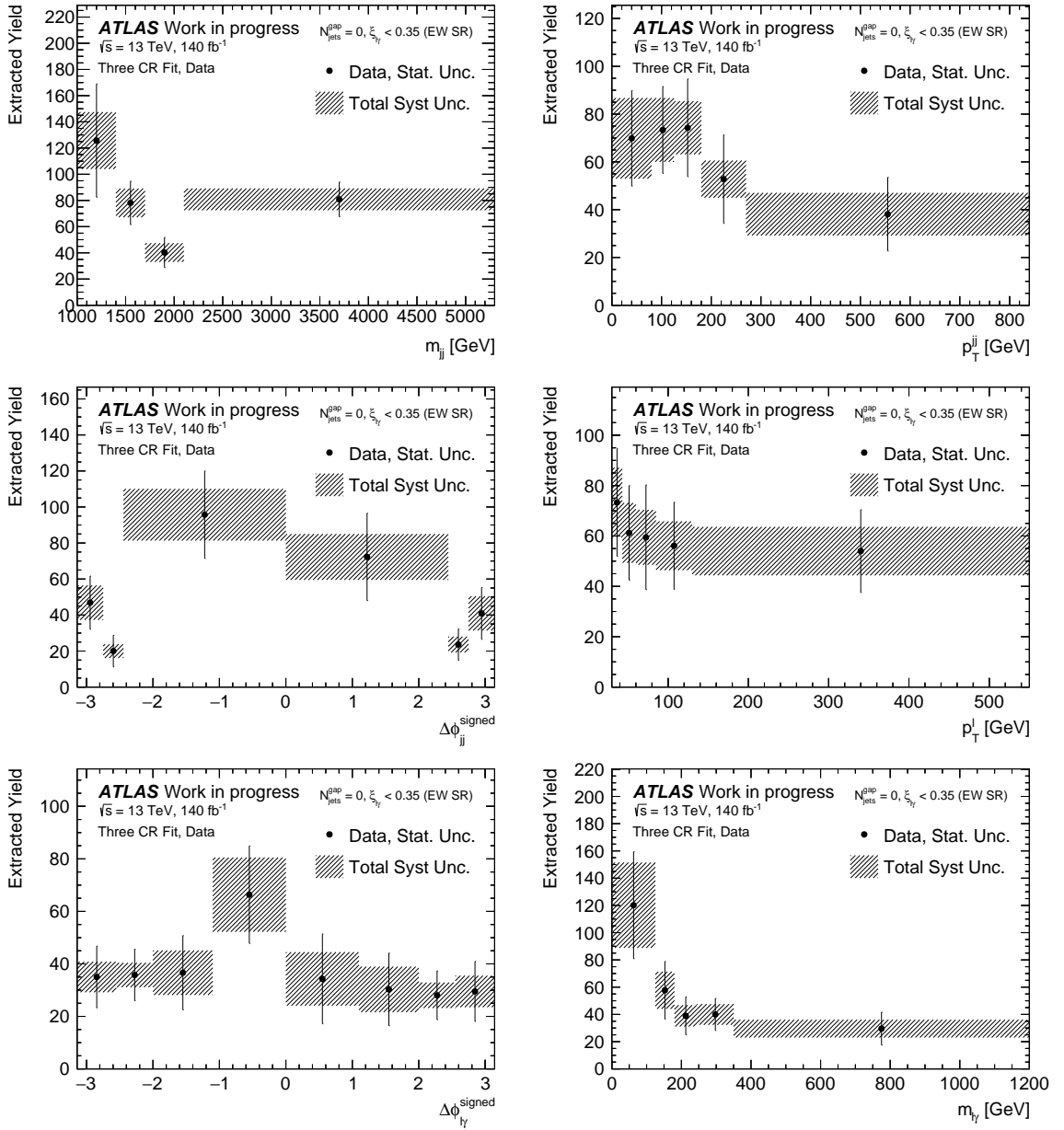


Figure 5.39. The $N_{\text{EW}}^{\text{Nom}}$ results with systematic uncertainties for the data using the nominal CRa method.

5.15.2 Signal Injection Test

The unfolded differential cross-section measurements are used to set limits on aQGCs using an EFT parametrisation (this is not described in this thesis as it is not the work of the author). The limit setting includes a test where an Asimov dataset is constructed using the nominal MC templates in addition to an injected detector-level EFT contribution. The signal extraction and the detector unfolding (Section 5.16) should recover the truth-level prediction of the EFT contribution. It is expected that the two results should not close completely as there will be a small amount of leakage of the EFT contribution into the control regions resulting in strong- $W\gamma jj$ constraints which deviate from unity. However, in setting the EFT limits, the assumption is made that there is little contribution in the control regions, therefore the non-closure should be small. The result of this test is shown for the most sensitive observable, p_T^{jj} , in Figure 5.44. It is clear that the closure is excellent, therefore giving confidence in the efficacy of the signal extraction procedure.

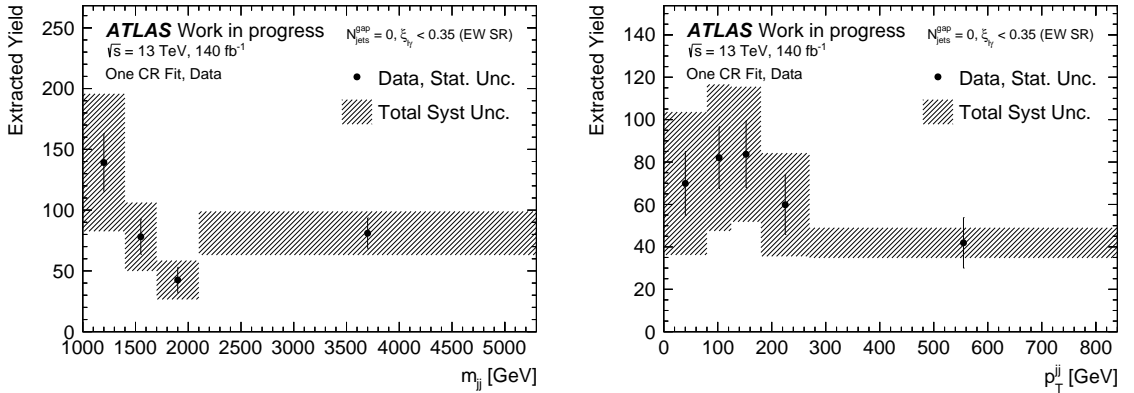


Figure 5.40. The $N_{\text{EW}}^{\text{Nom}}$ results with systematic uncertainties for the data derived using the $f(x_i) = 1$ (i.e. One CR) fit.

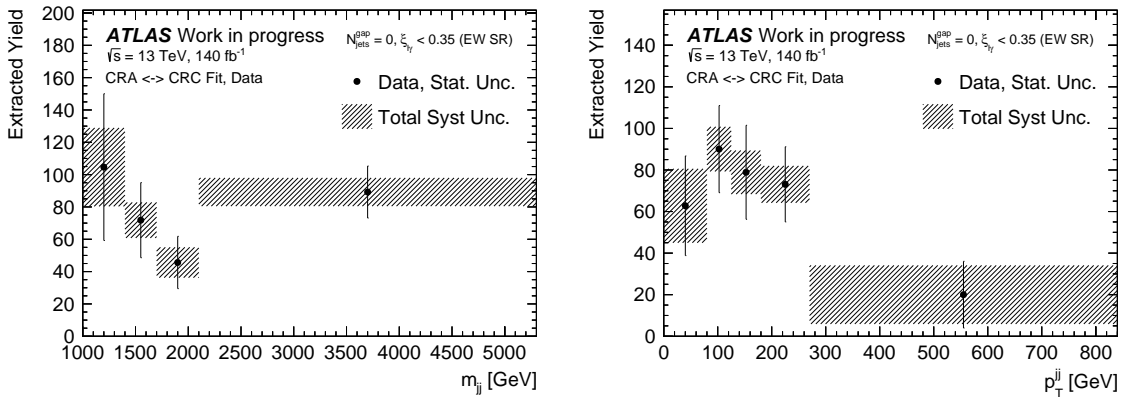


Figure 5.41. The $N_{\text{EW}}^{\text{Nom}}$ results with systematic uncertainties for the data derived using the CRc method, where the $b_{L,i}$ parameters are assigned to CRc instead of CRA.

5.16 Correction for Detector Effects

The correction for detector effects (i.e. unfolding) of the extracted $\text{EW-W}\gamma\text{jj}$ yields and uncertainties was not performed by the author. However, all plots shown in this section were derived by the author, and the derivation of the RMS of the PDF uncertainties and the envelopes of the scale uncertainties were performed by the author. Additionally, the truth-level yields and theoretical uncertainties in Figure 5.45 were derived by the author.

The goal of the analysis is to derive differential cross-section results which are not detector-specific. The process of “unfolding” is to correct for the detector effects of inefficiency and resolution by deriving a mapping from the detector specific differential results to a set of detector-independent, particle-level, results. Particle level is defined by stable particles with mean lifetime $c\tau > 10\text{mm}$. To avoid large extrapolations across phase-space, a particle-level fiducial volume is designed to mimic the detector-level selection criteria in 5.3.3.

The map from the detector-level data space to the particle-level data space is described through the *response matrix* \mathcal{R}_{ij} :

$$r_i = \sum_j \mathcal{R}_{ij} t_j, \quad (5.21)$$

where r_i and t_j are detector-level and particle-level observable bin values. The response

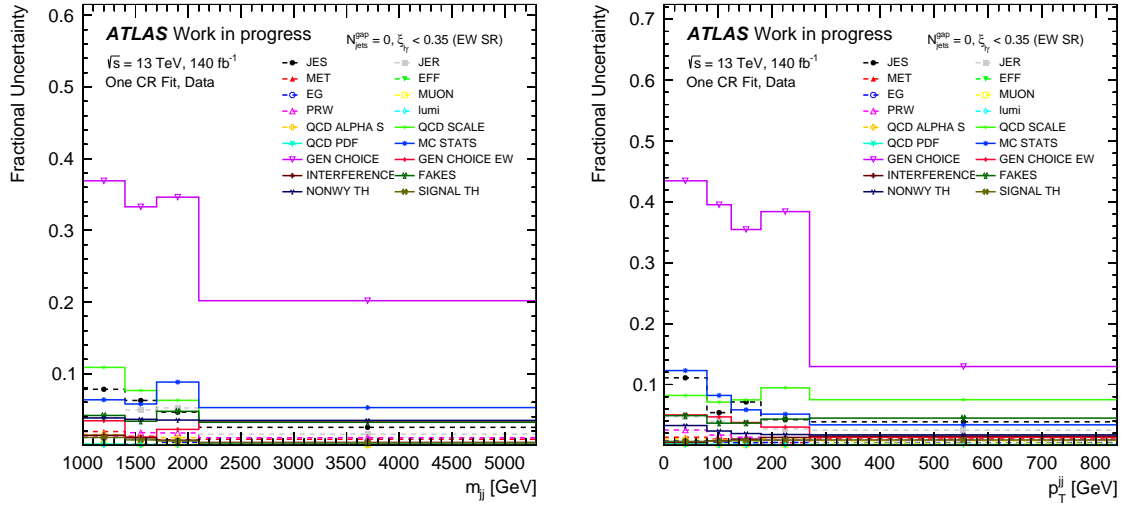


Figure 5.42. Relative systematic uncertainties for data derived using the $f(x_i) = 1$ method.

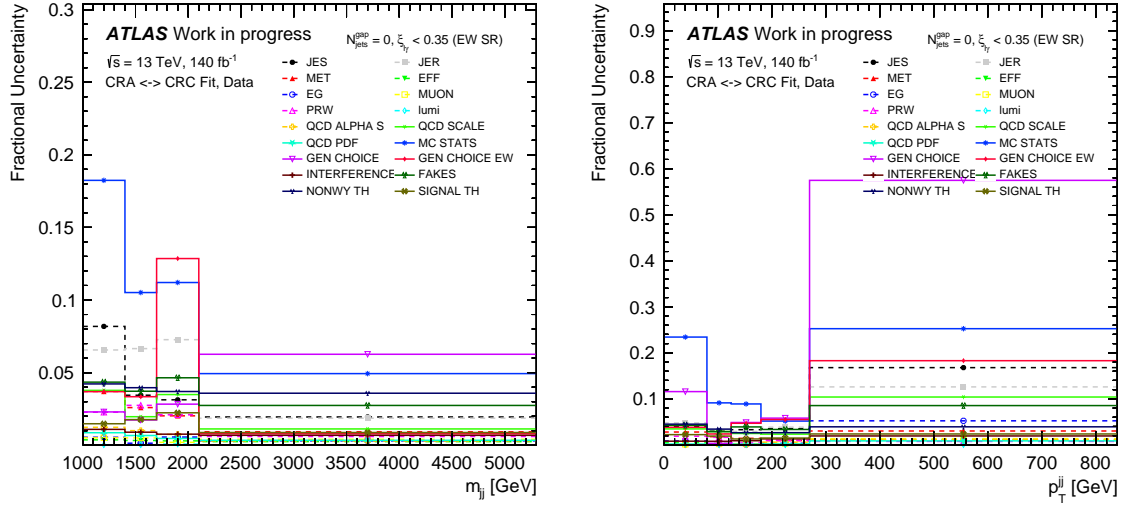


Figure 5.43. Relative systematic uncertainties for data derived using the CRc method.

matrix encodes the bin migrations between detector and particle-level observables. To unfold r_i is to attempt an inversion of \mathcal{R}_{ij} . Numerically inverting \mathcal{R}_{ij} is numerically fragile, and multiple unfolding strategies exist to deal with this. In this analysis the Iterative Bayesian Unfolding (IBU) approach with two iterations is used [172]. Corrections are derived using the MC simulations for events passing the detector-level simulation, without passing the particle-level simulation. Subsequently, bin-migrations in the differential differential distributions are corrected for, and finally, a correction is derived to account for events passing the particle-level simulation without passing the detector-level simulation.

Increasing the number of iterations of IBU increases the bias from the prior probability distribution, whilst increasing the statistical uncertainty on the measurement. The number of iterations is therefore determined through the optimisation of this tradeoff. The bias is estimated through comparisons of the unfolded differential distributions and the truth EW-W γjj differential distributions. The statistical uncertainty after unfolding is derived by unfolding each of the 10,000 pseudo-experiments mentioned in section 5.13.2, and taking the standard de-

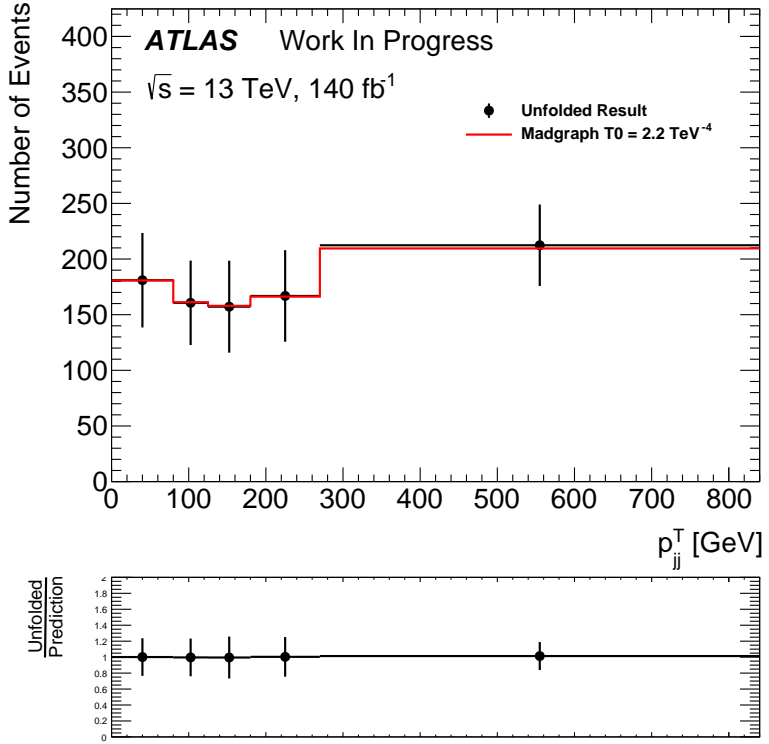


Figure 5.44. Unfolded results from the signal injection test where an Asimov dataset is constructed with the injection of an EFT sample, where the coupling of the T_0 operator is set to 2.2TeV^{-4} . The closure demonstrates that the signal extraction and unfolding correctly recover the injected EFT contribution. Figure made by other member of the analysis team.

viation of the unfolded yields. The systematic uncertainties after unfolding are determined through propagating the extracted $\text{EW}-W\gamma jj$ yields of each systematic variation through the unfolding. For the evaluation of the $\text{EW}-W\gamma jj$ generator choice uncertainty, the same MADGRAPH EW- $W\gamma jj$ sample is used for both the signal extraction and the unfolding.

5.16.1 Unfolded Differential Cross-section Results

The final unfolded differential cross-section measurements are shown in Figure 5.45. This Figure also shows the truth-level SHERPA and MADGRAPH EW- $W\gamma jj$ predictions. The truth-level uncertainties include the MC statistical uncertainties, PDF uncertainties, and scale scale uncertainties. The breakdown of the systematic uncertainties on the differential cross-section measurements are shown in Figure 5.46.

The final results show that for m_{jj} and $p_{T,jj}$, the MADGRAPH prediction is more consistent with the data at low values, and the SHERPA prediction is more consistent at larger values. Some disagreements between the predicted MADGRAPH results and the data can be seen in the angular distributions in some bins. In the leptonic observables, the SHERPA predictions are generally more consistent with the data. Note that the predictions display large differences in total cross-section, however this can be attributed to the SHERPA 2.2.12 prediction having the third parton included in the matrix element calculation [173].

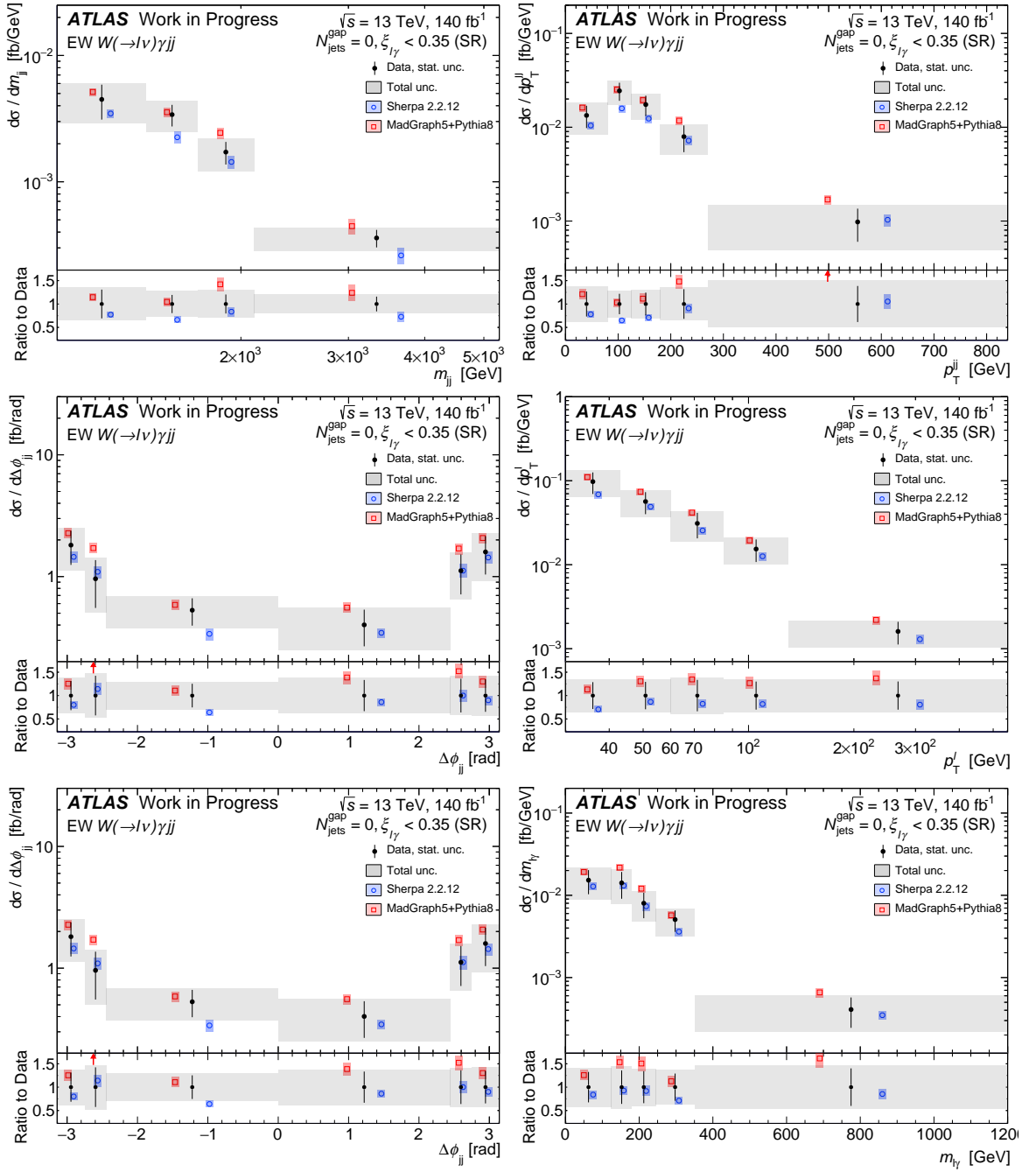


Figure 5.45. The black circles show the unfolded differential cross-section results obtained by extracting the $\text{EW-}W\gamma\gamma$ yield in data and unfolding the result. The black error bars are the statistical uncertainty on the data propagated to the unfolded result. The grey boxes show the combined systematic uncertainty on the data. The blue and red points represent the theoretical $\text{EW-}W\gamma\gamma$ predictions obtained using SHERPA and MADGRAPH, respectively, where the uncertainties on these predictions are shown as the coloured transparent boxes. The x-axis displacement of the theoretical results relative to the observed is only present for ease of comparison.

5.16.2 Validation of the Unfolding Procedure

The relative systematic uncertainties before and after the unfolding were compared to check that there were no unreasonably large changes. These comparisons are shown in Figures 5.47 and 5.48. Some changes in the uncertainties are expected because of bin migrations. Additionally, the $\text{EW-}W\gamma\gamma$ generator choice uncertainty after unfolding includes the difference in using the SHERPA and MADGRAPH MC samples for the determination of the response matrices. Therefore, this uncertainty is expected to change substantially.

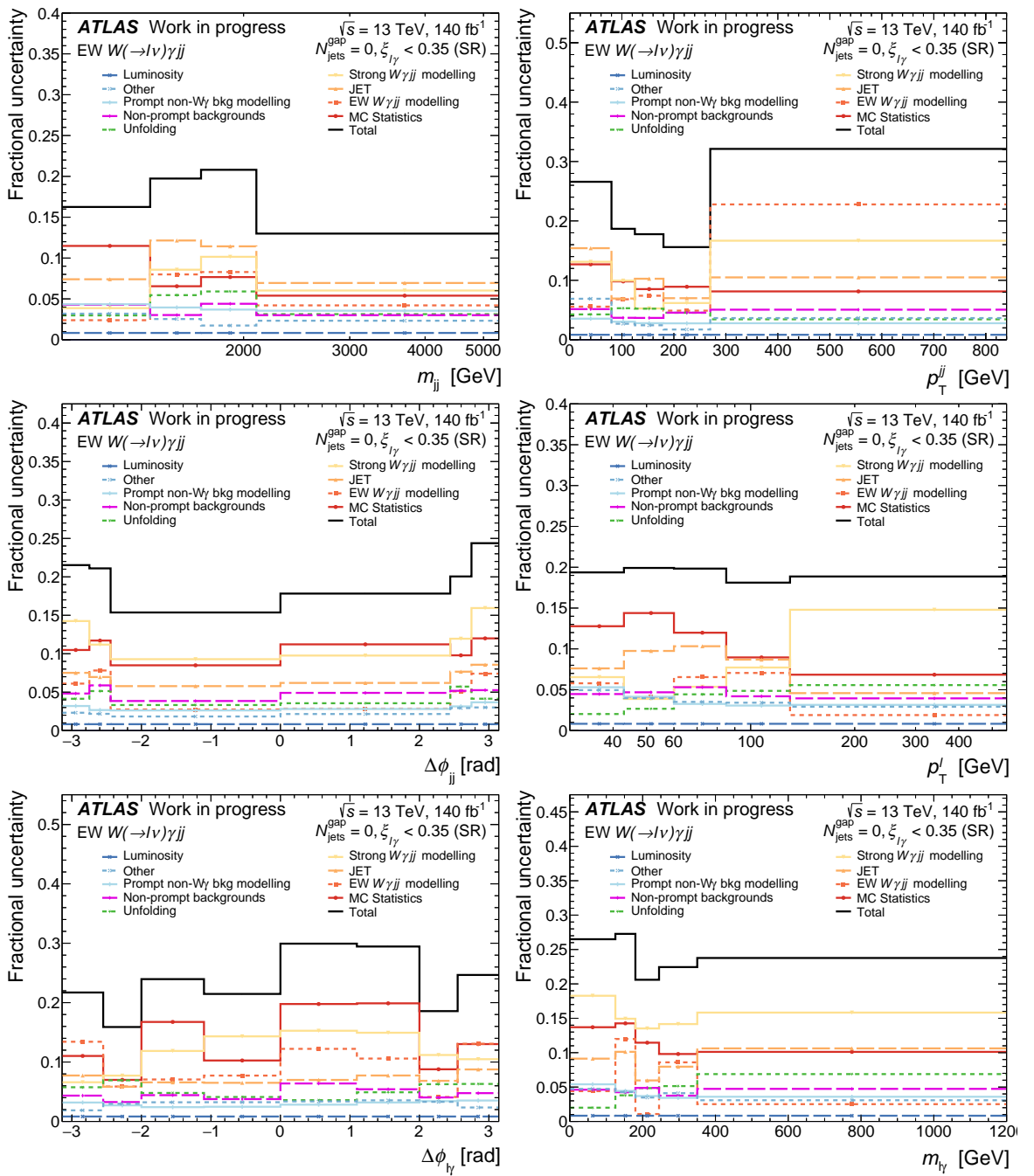


Figure 5.46. Breakdown of the relative systematic uncertainties on the unfolded differential cross-sections.

The comparisons show that in most cases the uncertainties only change by a few percent after unfolding, save the EW-W γ jj generator choice. The unfolding procedure itself was validated (this was not performed by the author) using using a set of closure tests.

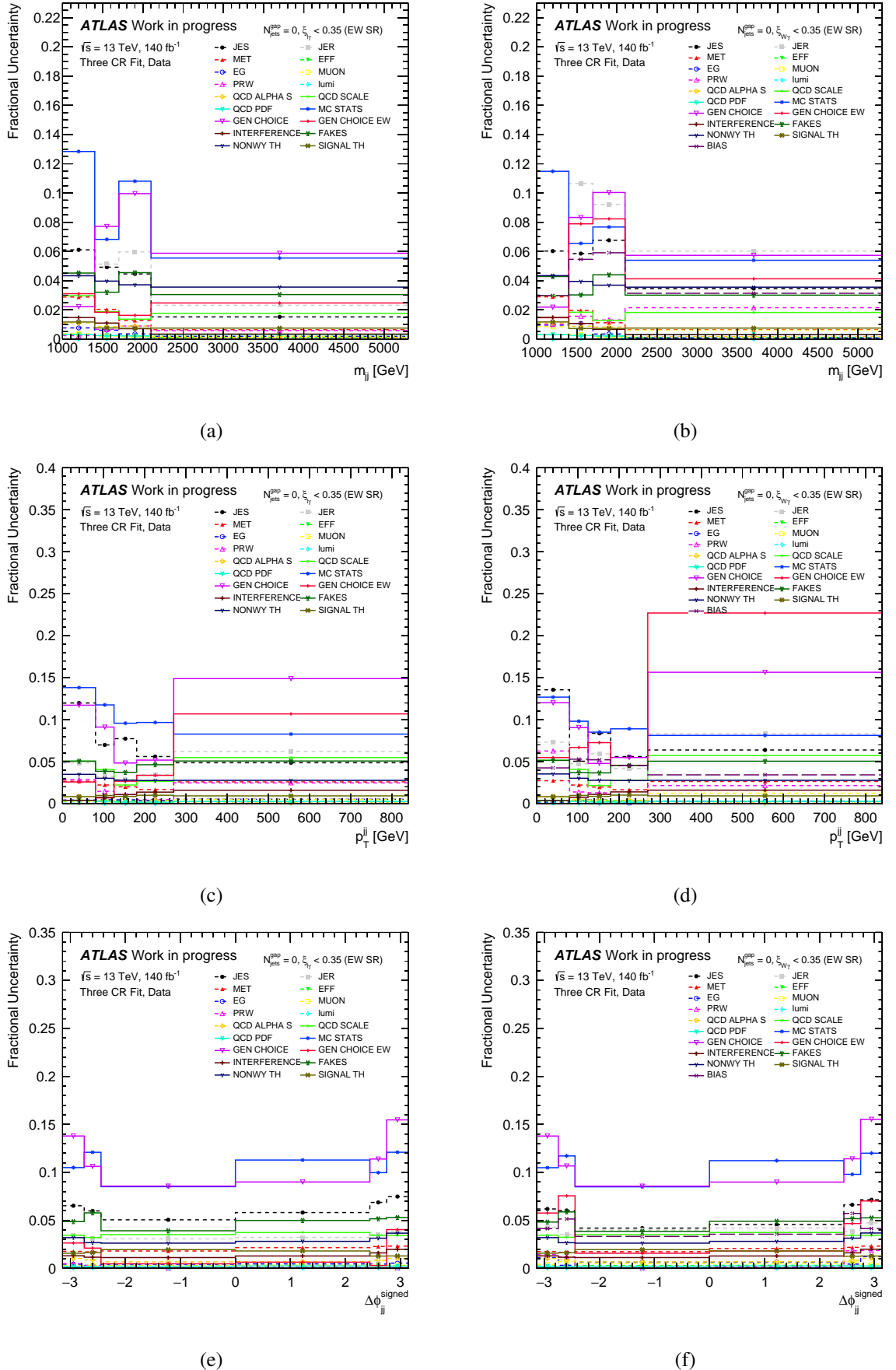


Figure 5.47. Comparison of relative uncertainties on the extracted $\text{EW-W}\gamma\gamma$ yield before (a,c,e) and after (b,d,f) unfolding for $m_{\gamma\gamma}$, $p_T^{\gamma\gamma}$, and $\Delta\phi_{\gamma\gamma}^{\text{signed}}$.

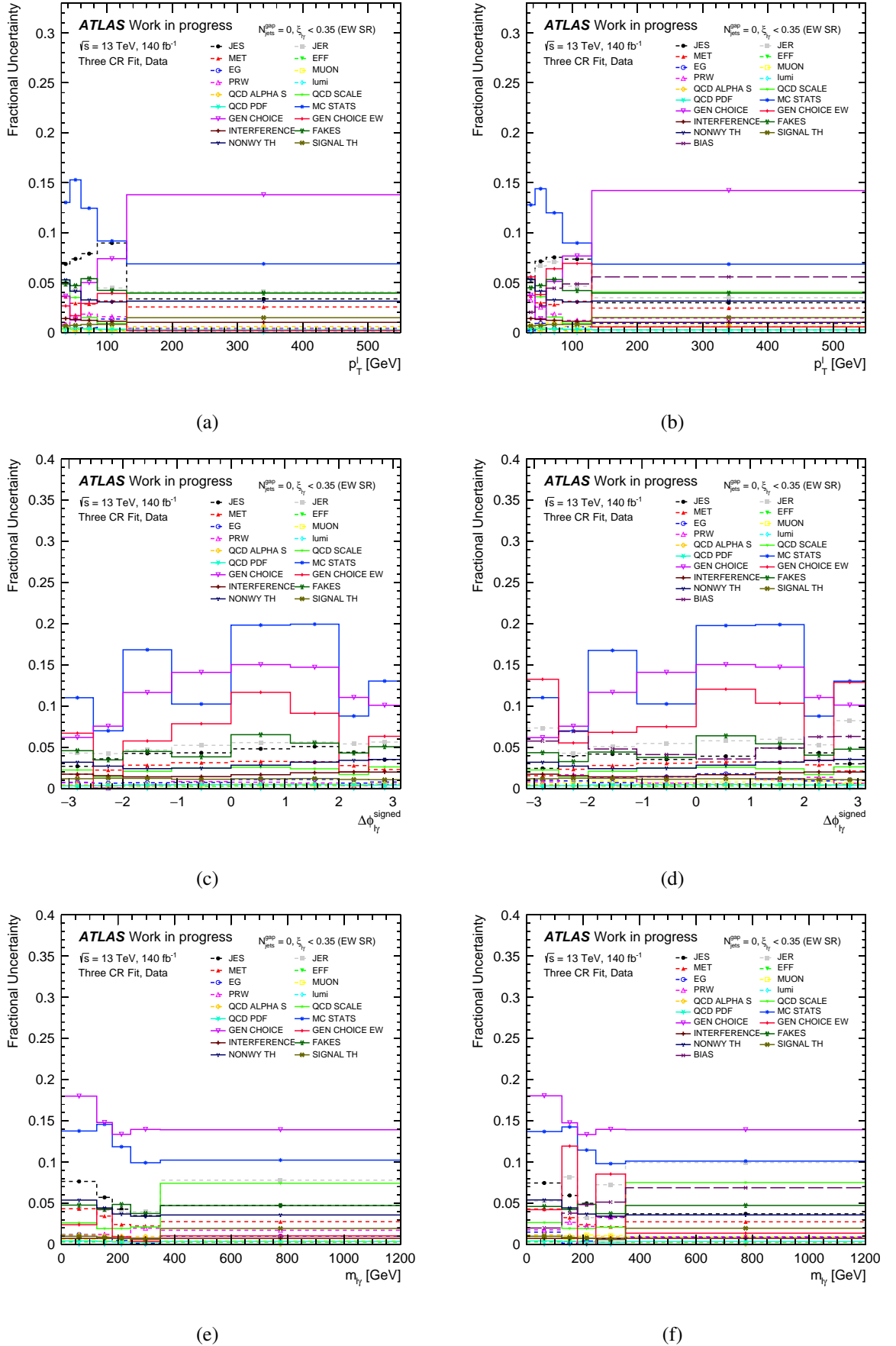


Figure 5.48. Comparison of relative uncertainties on the extracted $\text{EW-W}\gamma\text{jj}$ yield before (a,c,e) and after (b,d,f) unfolding for p_T^ℓ , $\Delta\phi_{\ell\gamma}^{\text{signed}}$, and $m_{\ell\gamma}$.

Chapter 6

Conclusions

The first differential cross-section measurements of the electroweak production of $W(\rightarrow \ell\nu)\gamma$ in association with two jets at ATLAS are derived in a VBS enriched phase-space as a function of six different observables sensitive to quartic electroweak gauge couplings.

The differential cross-section measurements are performed by extracting the EW- $W\gamma jj$ signal and constraining the dominant strong- $W\gamma jj$ background simultaneously in a binned log-likelihood fit. Constraints to the background are determined using three signal deficient control regions defined by inverting the $\xi_{l\gamma}$ and $N_{\text{jets}}^{\text{gap}}$ cuts defining the signal region. The main background constraint is primarily derived in the high $N_{\text{jets}}^{\text{gap}}$ control region, and a residual correction is derived primarily in the high $\xi_{l\gamma}$ control region. The optimum shape of the residual correction factor is determined to be a constant based on arguments related to the stability of the likelihood fit. The final constraint to the strong- $W\gamma jj$ background in the signal region ($c \cdot b_{L,i}$) ranges from 1.07 to 1.39, and the value of c ranges from 1.06 to 1.22, where these values differ depending on the bin and observable. After extracting the signal, detector unfolding corrections are applied to derive the final differential cross-section measurements.

A cross-check of the nominal signal extraction method is performed by repeating the signal extraction for a different configuration of the parameters in the likelihood. In this alternative configuration, the primary constraint to the strong background is derived in the high $\xi_{l\gamma}$ region, and the residual correction factor is derived in the high $N_{\text{jets}}^{\text{gap}}$ region. The results from this cross-check agree with the expectations that the nominal extracted yields should be similar. In the end, this configuration is not used to derive the final results because the lower yields in the high $\xi_{l\gamma}$ region results in worse statistical resolution of the systematic uncertainties. An additional cross-check of only using one control region to derive the backgrounds constraints confirms that the addition of the residual constraint drastically reduces the modelling uncertainties on the measurement.

Because of the small fiducial cross-section of the signal process, the measurement uncertainties are dominated by the statistical precision of the data. The total data statistical uncertainty on the differential cross-section ranges from 16-50% depending on the bin of the observable. The systematic uncertainties are dominated by the modelling uncertainties on the strong- $W\gamma jj$ background and the statistical precision of the MC simulations, where these range from 15-33% depending of the bin of the observable.

The differential cross-section measurements are compared to predictions from simulations

of EW- $W\gamma jj$ production using the **SHERPA** 2.2.12 and **MADGRAPH** 5 event generators at LO accuracy. The results show better agreement with **MADGRAPH** 5 at low m_{jj} and $p_{T,jj}$, but better agreement with **SHERPA** 2.2.12 at high m_{jj} and $p_{T,jj}$. For the angular observables, the results are seen to agree better with the **SHERPA** 2.2.12 predictions. The measured $m_{\ell\gamma}$ and p_T^ℓ differential cross-sections display better agreement with the **SHERPA** 2.2.12 predictions.

The differential cross-sections shown in this thesis are included in the publication [53], and contribute to the derivation of constraints on aQGCs derived through an EFT parametrisation. These results include the first LHC constraints of the f_{T3} and f_{T4} operator couplings, and the measurements of the angular observables $\Delta\phi_{jj}^{\text{signed}}$ and $\Delta\phi_{\ell\gamma}^{\text{signed}}$ may help future EFT efforts in deriving constraints to CP violating gauge couplings.

In addition to the differential cross-section measurements, the Z -jets insitu calibration is performed for large-R UFO jets. This calibration is derived as part of a series of calibrations, which differ in the reference system used to balance the transverse momentum of the probe jet. The Z -jets calibration has the superior precision over the other insitu calibrations in kinematic range of around $200 \text{ GeV} < p_T^{\text{jet}} < 500 \text{ GeV}$. The total uncertainty on the insitu calibration factor is around $0.5 - 1.5\%$ depending on the Z decay channel and the transverse momentum of the large-R jet.

The calibrations derived in this thesis are of direct importance to any future ATLAS physics analysis working on large-radius jets using Run-2 or Run-3 data, and the differential cross-section measurements are likely to be used in future global EFT fit efforts to constrain our knowledge of anomalous quadratic gauge interactions. Furthermore, measurements sensitive to vector boson scattering are of growing importance as future experiments begin to probe larger centre-of-mass energies. The state-of-the-art measurements documented in this thesis therefore form part of an increasingly important body of research surrounding some of the rarest and kinematically extreme electroweak processes in the standard model.

References

- [1] K. Tomio, “Experimental verification of the standard model of particle physics.,” *Proc Jpn Acad Ser B Phys Biol Sci.*, no. 2021;97(5):211-235, (cited on p. 9).
- [2] S. Raby and R. Slansky, “Neutrino masses: How to add them to the standard model,” *Los Alamos Sci.*, vol. 25, pp. 64–71, 1997 (cited on p. 9).
- [3] M. Goldhaber, “A Closer look at the elementary fermions,” *Proc. Nat. Acad. Sci.*, vol. 99, p. 33, 2002. doi: [10.1073/pnas.221582298](https://doi.org/10.1073/pnas.221582298). arXiv: [hep-ph/0201208](https://arxiv.org/abs/hep-ph/0201208) (cited on p. 9).
- [4] R. Foot and T. A. Tuan, *Explicit electroweak symmetry breaking?* 1994. arXiv: [hep-ph/9402239 \[hep-ph\]](https://arxiv.org/abs/hep-ph/9402239) (cited on p. 9).
- [5] S. Biondini, D. Boer, and R. Peeters, “Hierarchy problem and fine-tuning in a decoupling approach to multiscale effective potentials,” *Physical Review D*, vol. 104, no. 3, Aug. 2021, issn: 2470-0029. doi: [10.1103/physrevd.104.036013](https://doi.org/10.1103/physrevd.104.036013). [Online]. Available: <http://dx.doi.org/10.1103/PhysRevD.104.036013> (cited on p. 9).
- [6] B. Alessandro *et al.*, “Vector boson scattering: Recent experimental and theory developments,” *Reviews in Physics*, vol. 3, pp. 44–63, 2018, issn: 2405-4283. doi: <https://doi.org/10.1016/j.revip.2018.11.001>. [Online]. Available: <https://www.sciencedirect.com/science/article/pii/S2405428318300789> (cited on p. 9).
- [7] B. W. Lee, C. Quigg, and H. B. Thacker, “Strength of weak interactions at very high energies and the higgs boson mass,” *Phys. Rev. Lett.*, vol. 38, pp. 883–885, 16 Apr. 1977. doi: [10.1103/PhysRevLett.38.883](https://doi.org/10.1103/PhysRevLett.38.883). [Online]. Available: <https://link.aps.org/doi/10.1103/PhysRevLett.38.883> (cited on p. 9).
- [8] B. W. Lee, C. Quigg, and H. B. Thacker, “Weak interactions at very high energies: The role of the higgs-boson mass,” *Phys. Rev. D*, vol. 16, pp. 1519–1531, 5 Sep. 1977. doi: [10.1103/PhysRevD.16.1519](https://doi.org/10.1103/PhysRevD.16.1519). [Online]. Available: <https://link.aps.org/doi/10.1103/PhysRevD.16.1519> (cited on p. 9).
- [9] “Standard Model Summary Plots October 2023,” CERN, Geneva, Tech. Rep., 2023. [Online]. Available: <https://cds.cern.ch/record/2882448> (cited on pp. 9, 35, 36).

- [10] “In situ calibration of large- R jet energy and mass in 13 TeV proton-proton collisions with the ATLAS detector,” *Eur. Phys. J. C*, vol. 79, no. 2, p. 135, 2019, Submitted to Eur.Phys.J. doi: [10.1140/epjc/s10052-019-6632-8](https://doi.org/10.1140/epjc/s10052-019-6632-8). arXiv: [1807.09477](https://arxiv.org/abs/1807.09477). [Online]. Available: <https://cds.cern.ch/record/2632341> (cited on pp. 10, 66, 67, 69–71, 74, 76, 80).
- [11] S. Schramm, “ATLAS Jet Reconstruction, Calibration, and Tagging of Lorentz-boosted Objects,” *EPJ Web Conf.*, vol. 182, p. 02113, 2018. doi: [10.1051/epjconf/201818202113](https://doi.org/10.1051/epjconf/201818202113) (cited on pp. 10, 67).
- [12] “Jet reconstruction and performance using particle flow with the ATLAS Detector. Jet reconstruction and performance using particle flow with the ATLAS Detector,” *Eur. Phys. J. C*, vol. 77, no. CERN-EP-2017-024. 7, 466. 67 p, Mar. 2017. doi: [10.1140/epjc/s10052-017-5031-2](https://doi.org/10.1140/epjc/s10052-017-5031-2). [Online]. Available: <https://cds.cern.ch/record/2257597> (cited on pp. 10, 59–62, 71).
- [13] “Improving jet substructure performance in ATLAS using Track-Calorimeters,” CERN, Geneva, Tech. Rep. ATL-PHYS-PUB-2017-015, 2017. [Online]. Available: <https://cds.cern.ch/record/2275636> (cited on pp. 10, 61, 62).
- [14] “Optimisation of large-radius jet reconstruction for the ATLAS detector in 13 TeV proton–proton collisions,” Tech. Rep. 4, 2021, p. 334. doi: [10.1140/epjc/s10052-021-09054-3](https://doi.org/10.1140/epjc/s10052-021-09054-3). arXiv: [2009.04986](https://arxiv.org/abs/2009.04986). [Online]. Available: <https://cds.cern.ch/record/2730141> (cited on pp. 10, 71).
- [15] Tim Evans, *Quantum Field Theory Course 2015*. [Online]. Available: <https://plato.tp.ph.ic.ac.uk/~time/qft/index.html> (cited on pp. 11, 22).
- [16] David Tong, *Lectures on Quantum Field Theory*. [Online]. Available: <https://www.damtp.cam.ac.uk/user/tong/qft.html> (cited on p. 11).
- [17] M. E. Peskin and D. V. Schroeder, *An Introduction to quantum field theory*. Reading, USA: Addison-Wesley, 1995, ISBN: 978-0-201-50397-5 (cited on pp. 12, 15, 24).
- [18] C. S. Wu, E. Ambler, R. W. Hayward, D. D. Hoppes, and R. P. Hudson, “Experimental test of parity conservation in beta decay,” *Phys. Rev.*, vol. 105, pp. 1413–1415, 4 Feb. 1957. doi: [10.1103/PhysRev.105.1413](https://doi.org/10.1103/PhysRev.105.1413). [Online]. Available: <https://link.aps.org/doi/10.1103/PhysRev.105.1413> (cited on p. 15).
- [19] A. Buckley, C. White, and M. White, *Practical Collider Physics*. IOP, Dec. 2021, ISBN: 978-0-7503-2444-1, 978-0-7503-2443-4, 978-0-7503-2442-7. doi: [10.1088/978-0-7503-2444-1](https://doi.org/10.1088/978-0-7503-2444-1) (cited on pp. 22, 26, 28, 40, 45, 48, 49, 52, 58, 63–65).

- [20] A. Buckley *et al.*, “General-purpose event generators for lhc physics,” *Physics Reports*, vol. 504, no. 5, pp. 145–233, 2011, issn: 0370-1573. doi: <https://doi.org/10.1016/j.physrep.2011.03.005>. [Online]. Available: <https://www.sciencedirect.com/science/article/pii/S0370157311000846> (cited on pp. 22, 31, 32).
- [21] C. Bierlich *et al.*, *A comprehensive guide to the physics and usage of pythia 8.3*, 2022. arXiv: [2203.11601 \[hep-ph\]](https://arxiv.org/abs/2203.11601) (cited on pp. 30, 32).
- [22] G. P. Salam, “Towards Jetography,” *Eur. Phys. J. C*, vol. 67, pp. 637–686, 2010. doi: [10.1140/epjc/s10052-010-1314-6](https://doi.org/10.1140/epjc/s10052-010-1314-6). arXiv: [0906.1833 \[hep-ph\]](https://arxiv.org/abs/0906.1833) (cited on p. 31).
- [23] M. Cacciari, G. P. Salam, and G. Soyez, “The anti-kt jet clustering algorithm,” *Journal of High Energy Physics*, vol. 2008, no. 04, p. 063, Apr. 2008. doi: [10.1088/1126-6708/2008/04/063](https://doi.org/10.1088/1126-6708/2008/04/063). [Online]. Available: <https://dx.doi.org/10.1088/1126-6708/2008/04/063> (cited on pp. 31, 71).
- [24] J. S. Lee, “Multi-jet correlations and colour coherence phenomena,” *EPJ Web Conf.*, vol. 141, I.-K. Yoo, Ed., p. 04003, 2017. doi: [10.1051/epjconf/201714104003](https://doi.org/10.1051/epjconf/201714104003) (cited on p. 31).
- [25] Y. L. Dokshitzer, V. S. Fadin, and V. A. Khoze, “On the Sensitivity of the Inclusive Distributions in Parton Jets to the Coherence Effects in QCD Gluon Cascades,” *Z. Phys. C*, vol. 18, p. 37, 1983. doi: [10.1007/BF01571703](https://doi.org/10.1007/BF01571703) (cited on p. 31).
- [26] S. Catani, Y. L. Dokshitzer, M. Olsson, G. Turnock, and B. Webber, “New clustering algorithm for multi - jet cross-sections in e+ e- annihilation,” *Phys. Lett. B*, vol. 269, pp. 432–438, 1991. doi: [10.1016/0370-2693\(91\)90196-W](https://doi.org/10.1016/0370-2693(91)90196-W) (cited on p. 31).
- [27] M. Cacciari, G. P. Salam, and G. Soyez, “The anti- k_t jet clustering algorithm,” *JHEP*, vol. 04, p. 063, 2008. doi: [10.1088/1126-6708/2008/04/063](https://doi.org/10.1088/1126-6708/2008/04/063). arXiv: [0802.1189 \[hep-ph\]](https://arxiv.org/abs/0802.1189) (cited on p. 31).
- [28] M. L. Mangano, F. Piccinini, A. D. Polosa, M. Moretti, and R. Pittau, “Alpgen, a generator for hard multiparton processes in hadronic collisions,” *Journal of High Energy Physics*, vol. 2003, no. 07, pp. 001–001, Jul. 2003, issn: 1029-8479. doi: [10.1088/1126-6708/2003/07/001](https://doi.org/10.1088/1126-6708/2003/07/001). [Online]. Available: <http://dx.doi.org/10.1088/1126-6708/2003/07/001> (cited on p. 32).
- [29] F. Krauss, R. Kuhn, and G. Soff, “AMEGIC++ 1.0: A Matrix element generator in C++,” *JHEP*, vol. 02, p. 044, 2002. doi: [10.1088/1126-6708/2002/02/044](https://doi.org/10.1088/1126-6708/2002/02/044). arXiv: [hep-ph/0109036](https://arxiv.org/abs/hep-ph/0109036) (cited on pp. 32, 91).

- [30] T. Gleisberg and S. Höche, “Comix, a new matrix element generator,” *Journal of High Energy Physics*, vol. 2008, no. 12, p. 039, Dec. 2008. doi: [10.1088/1126-6708/2008/12/039](https://doi.org/10.1088/1126-6708/2008/12/039). [Online]. Available: <https://dx.doi.org/10.1088/1126-6708/2008/12/039> (cited on pp. 32, 71, 90, 91).
- [31] E. Byckling and K. Kajantie, “N-particle phase space in terms of invariant momentum transfers,” *Nucl. Phys. B*, vol. 9, pp. 568–576, 1969. doi: [10.1016/0550-3213\(69\)90271-5](https://doi.org/10.1016/0550-3213(69)90271-5) (cited on p. 32).
- [32] R. Kleiss and R. Pittau, “Weight optimization in multichannel monte carlo,” *Computer Physics Communications*, vol. 83, no. 2–3, pp. 141–146, Dec. 1994, issn: 0010-4655. doi: [10.1016/0010-4655\(94\)90043-4](https://doi.org/10.1016/0010-4655(94)90043-4). [Online]. Available: [http://dx.doi.org/10.1016/0010-4655\(94\)90043-4](http://dx.doi.org/10.1016/0010-4655(94)90043-4) (cited on p. 32).
- [33] S. Alioli, P. Nason, C. Oleari, and E. Re, “A general framework for implementing NLO calculations in shower monte carlo programs: The POWHEG BOX,” *Journal of High Energy Physics*, vol. 2010, no. 6, Jun. 2010. doi: [10.1007/jhep06\(2010\)043](https://doi.org/10.1007/jhep06(2010)043). [Online]. Available: <https://doi.org/10.1007%2Fjhep06%282010%29043> (cited on pp. 32, 70).
- [34] S. Frixione, P. Nason, and C. Oleari, “Matching NLO QCD computations with parton shower simulations: The POWHEG method,” *Journal of High Energy Physics*, vol. 2007, no. 11, pp. 070–070, Nov. 2007. doi: [10.1088/1126-6708/2007/11/070](https://doi.org/10.1088/1126-6708/2007/11/070). [Online]. Available: <https://doi.org/10.1088%2F1126-6708%2F2007%2F11%2F070> (cited on pp. 32, 70).
- [35] P. Nason, “A new method for combining NLO QCD with shower monte carlo algorithms,” *Journal of High Energy Physics*, vol. 2004, no. 11, pp. 040–040, Nov. 2004. doi: [10.1088/1126-6708/2004/11/040](https://doi.org/10.1088/1126-6708/2004/11/040). [Online]. Available: <https://doi.org/10.1088%2F1126-6708%2F2004%2F11%2F040> (cited on pp. 32, 70).
- [36] T. Sjöstrand *et al.*, “An introduction to pythia 8.2,” *Computer Physics Communications*, vol. 191, pp. 159–177, 2015, issn: 0010-4655. doi: <https://doi.org/10.1016/j.cpc.2015.01.024>. [Online]. Available: <https://www.sciencedirect.com/science/article/pii/S0010465515000442> (cited on pp. 32, 71, 90, 91).
- [37] T. Gleisberg *et al.*, “Event generation with sherpa 1.1,” *Journal of High Energy Physics*, vol. 2009, no. 02, p. 007, Feb. 2009. doi: [10.1088/1126-6708/2009/02/007](https://doi.org/10.1088/1126-6708/2009/02/007). [Online]. Available: <https://dx.doi.org/10.1088/1126-6708/2009/02/007> (cited on pp. 32, 71, 90, 91).

- [38] E. Bothmann *et al.*, “Event Generation with Sherpa 2.2,” *SciPost Phys.*, vol. 7, no. 3, p. 034, 2019. doi: [10.21468/SciPostPhys.7.3.034](https://doi.org/10.21468/SciPostPhys.7.3.034). arXiv: [1905.09127](https://arxiv.org/abs/1905.09127) [hep-ph] (cited on pp. 32, 71, 90, 91).
- [39] J. Alwall *et al.*, “The automated computation of tree-level and next-to-leading order differential cross sections, and their matching to parton shower simulations,” *JHEP*, vol. 07, p. 079, 2014, Comments: 158 pages, 27 figures; a few references have been added. doi: [10.1007/JHEP07\(2014\)079](https://doi.org/10.1007/JHEP07(2014)079). arXiv: [1405.0301](https://arxiv.org/abs/1405.0301). [Online]. Available: <https://cds.cern.ch/record/1699128> (cited on pp. 32, 90, 91).
- [40] S. Catani, F. Krauss, B. R. Webber, and R. Kuhn, “Qcd matrix elements + parton showers,” *Journal of High Energy Physics*, vol. 2001, no. 11, p. 063, Jan. 2002. doi: [10.1088/1126-6708/2001/11/063](https://doi.org/10.1088/1126-6708/2001/11/063). [Online]. Available: <https://dx.doi.org/10.1088/1126-6708/2001/11/063> (cited on pp. 32, 71, 91).
- [41] S. Höche, F. Krauss, S. Schumann, and F. Siegert, “Qcd matrix elements and truncated showers,” *Journal of High Energy Physics*, vol. 2009, no. 05, p. 053, May 2009. doi: [10.1088/1126-6708/2009/05/053](https://doi.org/10.1088/1126-6708/2009/05/053). [Online]. Available: <https://dx.doi.org/10.1088/1126-6708/2009/05/053> (cited on pp. 32, 71, 91).
- [42] M. L. Mangano, M. Moretti, F. Piccinini, and M. Treccani, “Matching matrix elements and shower evolution for top-pair production in hadronic collisions,” *Journal of High Energy Physics*, vol. 2007, no. 01, pp. 013–013, Jan. 2007, issn: 1029-8479. doi: [10.1088/1126-6708/2007/01/013](https://doi.org/10.1088/1126-6708/2007/01/013). [Online]. Available: [http://dx.doi.org/10.1088/1126-6708/2007/01/013](https://dx.doi.org/10.1088/1126-6708/2007/01/013) (cited on p. 32).
- [43] R. Frederix and S. Frixione, “Merging meets matching in mc@nlo,” *Journal of High Energy Physics*, vol. 2012, no. 12, Dec. 2012, issn: 1029-8479. doi: [10.1007/jhep12\(2012\)061](https://doi.org/10.1007/jhep12(2012)061). [Online]. Available: [http://dx.doi.org/10.1007/JHEP12\(2012\)061](https://dx.doi.org/10.1007/JHEP12(2012)061) (cited on p. 32).
- [44] S. Höche, F. Krauss, M. Schönherr, and F. Siegert, “A critical appraisal of nlo+ps matching methods,” *Journal of High Energy Physics*, vol. 2012, no. 9, Sep. 2012, issn: 1029-8479. doi: [10.1007/jhep09\(2012\)049](https://doi.org/10.1007/jhep09(2012)049). [Online]. Available: [http://dx.doi.org/10.1007/JHEP09\(2012\)049](https://dx.doi.org/10.1007/JHEP09(2012)049) (cited on p. 32).
- [45] V. Khachatryan *et al.*, “Study of vector boson scattering and search for new physics in events with two same-sign leptons and two jets,” *Phys. Rev. Lett.*, vol. 114, no. 5, p. 051801, 2015. doi: [10.1103/PhysRevLett.114.051801](https://doi.org/10.1103/PhysRevLett.114.051801). arXiv: [1410.6315](https://arxiv.org/abs/1410.6315) [hep-ex] (cited on p. 32).

- [46] “Evidence of $W\gamma\gamma$ production in pp collisions at $\sqrt{s} = 8$ TeV and limits on anomalous quartic gauge couplings with the ATLAS detector. Evidence of $W\gamma\gamma$ production in pp collisions at $\sqrt{s} = 8$ TeV and limits on anomalous quartic gauge couplings with the ATLAS detector,” *Phys. Rev. Lett.*, vol. 115, p. 031802, 2015. doi: [10.1103/PhysRevLett.115.031802](https://doi.org/10.1103/PhysRevLett.115.031802). arXiv: [1503.03243](https://arxiv.org/abs/1503.03243). [Online]. Available: <https://cds.cern.ch/record/2000307> (cited on p. 32).
- [47] “Search for anomalous electroweak production of WW/WZ in association with a high-mass dijet system in pp collisions at $\sqrt{s} = 8$ TeV with the ATLAS detector. Search for anomalous electroweak production of WW/WZ in association with a high-mass dijet system in pp collisions at $\sqrt{s} = 8$ TeV with the ATLAS detector,” *Phys. Rev. D*, vol. 95, p. 032001, 2017. doi: [10.1103/PhysRevD.95.032001](https://doi.org/10.1103/PhysRevD.95.032001). arXiv: [1609.05122](https://arxiv.org/abs/1609.05122). [Online]. Available: <https://cds.cern.ch/record/2216191> (cited on p. 32).
- [48] V. Khachatryan *et al.*, “Measurement of electroweak-induced production of $w\gamma$ with two jets in pp collisions at $\sqrt{s}=8$ tev and constraints on anomalous quartic gauge couplings,” *Journal of High Energy Physics*, vol. 2017, Jun. 2017 (cited on pp. 32, 89, 93, 94).
- [49] “Measurement of $W^\pm W^\pm$ vector-boson scattering and limits on anomalous quartic gauge couplings with the atlas detector,” *Phys. Rev. D*, vol. 96, p. 012007, 1 Jul. 2017. doi: [10.1103/PhysRevD.96.012007](https://doi.org/10.1103/PhysRevD.96.012007). [Online]. Available: <https://link.aps.org/doi/10.1103/PhysRevD.96.012007> (cited on p. 32).
- [50] V. Khachatryan *et al.*, “Measurement of the cross section for electroweak production of $Z\gamma$ in association with two jets and constraints on anomalous quartic gauge couplings in proton–proton collisions at $\sqrt{s} = 8$ TeV,” *Phys. Lett. B*, vol. 770, pp. 380–402, 2017. doi: [10.1016/j.physletb.2017.04.071](https://doi.org/10.1016/j.physletb.2017.04.071). arXiv: [1702.03025 \[hep-ex\]](https://arxiv.org/abs/1702.03025) (cited on p. 32).
- [51] “Studies of $z\gamma$ production in association with a high-mass dijet system in pp collisions at $\sqrt{s} = 8$ tev with the atlas detector,” *Journal of High Energy Physics*, vol. 2017, p. 107, Jul. 2017. doi: [10.1007/jhep07\(2017\)107](https://doi.org/10.1007/jhep07(2017)107) (cited on p. 32).
- [52] T. Plehn, “Lectures on LHC Physics,” *Lect. Notes Phys.*, vol. 844, pp. 1–193, 2012. doi: [10.1007/978-3-642-24040-9](https://doi.org/10.1007/978-3-642-24040-9). arXiv: [0910.4182 \[hep-ph\]](https://arxiv.org/abs/0910.4182) (cited on p. 33).
- [53] *Fiducial and differential cross-section measurements of electroweak $W\gamma jj$ production in pp collisions at $\sqrt{s} = 13$ tev with the atlas detector*, 2024. arXiv: [2403.02809 \[hep-ex\]](https://arxiv.org/abs/2403.02809). [Online]. Available: <https://arxiv.org/abs/2403.02809> (cited on pp. 34, 89, 157).

- [54] “Observation of electroweak production of W^+W^- in association with jets using the ATLAS Detector,” CERN, Geneva, Tech. Rep., 2023. [Online]. Available: <https://cds.cern.ch/record/2865482> (cited on p. 34).
- [55] T. A. Collaboration, *Measurement and interpretation of same-sign W boson pair production in association with two jets in pp collisions at $\sqrt{s} = 13$ tev with the atlas detector*, 2023. arXiv: [2312.00420 \[hep-ex\]](https://arxiv.org/abs/2312.00420) (cited on p. 34).
- [56] “Differential cross-section measurements of the production of four charged leptons in association with two jets using the ATLAS detector,” *JHEP*, vol. 2401, p. 004, 2024. doi: [10.1007/JHEP01\(2024\)004](https://doi.org/10.1007/JHEP01(2024)004). arXiv: [2308.12324](https://arxiv.org/abs/2308.12324). [Online]. Available: <https://cds.cern.ch/record/2868294> (cited on p. 34).
- [57] L. Evans and P. Bryant, “Lhc machine,” *Journal of Instrumentation*, vol. 3, no. 08, S08001, Aug. 2008. doi: [10.1088/1748-0221/3/08/S08001](https://doi.org/10.1088/1748-0221/3/08/S08001). [Online]. Available: <https://dx.doi.org/10.1088/1748-0221/3/08/S08001> (cited on p. 37).
- [58] The ATLAS Collaboration, “Observation of a new particle in the search for the standard model higgs boson with the atlas detector at the lhc,” *Physics Letters B*, vol. 716, no. 1, pp. 1–29, 2012, ISSN: 0370-2693. doi: <https://doi.org/10.1016/j.physletb.2012.08.020>. [Online]. Available: <https://www.sciencedirect.com/science/article/pii/S037026931200857X> (cited on p. 37).
- [59] The ATLAS Collaboration, “The atlas experiment at the cern large hadron collider,” *Journal of Instrumentation*, vol. 3, no. 08, S08003, Aug. 2008. doi: [10.1088/1748-0221/3/08/S08003](https://doi.org/10.1088/1748-0221/3/08/S08003). [Online]. Available: <https://dx.doi.org/10.1088/1748-0221/3/08/S08003> (cited on pp. 37, 45–48).
- [60] “The cms experiment at the cern lhc,” *Journal of Instrumentation*, vol. 3, no. 08, S08004, Aug. 2008. doi: [10.1088/1748-0221/3/08/S08004](https://doi.org/10.1088/1748-0221/3/08/S08004). [Online]. Available: <https://dx.doi.org/10.1088/1748-0221/3/08/S08004> (cited on p. 37).
- [61] “The totem experiment at the cern large hadron collider,” *Journal of Instrumentation*, vol. 3, no. 08, S08007, Aug. 2008. doi: [10.1088/1748-0221/3/08/S08007](https://doi.org/10.1088/1748-0221/3/08/S08007). [Online]. Available: <https://dx.doi.org/10.1088/1748-0221/3/08/S08007> (cited on p. 37).
- [62] “The lhcb detector at the lhc,” *Journal of Instrumentation*, vol. 3, no. 08, S08005, Aug. 2008. doi: [10.1088/1748-0221/3/08/S08005](https://doi.org/10.1088/1748-0221/3/08/S08005). [Online]. Available: <https://dx.doi.org/10.1088/1748-0221/3/08/S08005> (cited on p. 37).
- [63] “The alice experiment at the cern lhc,” *Journal of Instrumentation*, vol. 3, no. 08, S08002, Aug. 2008. doi: [10.1088/1748-0221/3/08/S08002](https://doi.org/10.1088/1748-0221/3/08/S08002). [Online]. Available: <https://dx.doi.org/10.1088/1748-0221/3/08/S08002> (cited on p. 37).

- [64] O. S. Brüning *et al.*, *LHC Design Report* (CERN Yellow Reports: Monographs). Geneva: CERN, 2004. doi: [10.5170/CERN-2004-003-V-1](https://doi.org/10.5170/CERN-2004-003-V-1). [Online]. Available: <https://cds.cern.ch/record/782076> (cited on pp. 37–39).
- [65] S. Baird, “Accelerators for pedestrians,” CERN, Geneva, Tech. Rep., 2007 (cited on p. 37).
- [66] “Buckets and bunches.” (), [Online]. Available: https://www.lhc-closer.es/taking_a_closer_look_at_lhc/0.buckets_and_bunches (visited on 10/03/2023) (cited on p. 37).
- [67] E. Lopienska, “The CERN accelerator complex, layout in 2022. Complexe des accélérateurs du CERN en janvier 2022,” 2022, General Photo. [Online]. Available: <https://cds.cern.ch/record/2800984> (cited on p. 38).
- [68] L. Rossi, “The LHC superconducting magnets,” *Conf. Proc. C*, vol. 030512, p. 141, 2003 (cited on p. 38).
- [69] R. Perin and J. Vlogaert, “Magnets for the Large Hadron Collider,” CERN, Geneva, Tech. Rep., 1994. [Online]. Available: <https://cds.cern.ch/record/260440> (cited on p. 38).
- [70] G. Aad *et al.*, “Luminosity determination in pp collisions at $\sqrt{s} = 13$ TeV using the ATLAS detector at the LHC,” *Eur. Phys. J. C*, vol. 83, no. 10, p. 982, 2023. doi: [10.1140/epjc/s10052-023-11747-w](https://doi.org/10.1140/epjc/s10052-023-11747-w). arXiv: [2212.09379 \[hep-ex\]](https://arxiv.org/abs/2212.09379) (cited on pp. 39, 40, 125).
- [71] The ATLAS Collaboration, “ATLAS Public Luminosity Plots,” 2022. [Online]. Available: <https://twiki.cern.ch/twiki/bin/view/AtlasPublic/LuminosityPublicResu...> (cited on p. 40).
- [72] G. Soyez, “Pileup mitigation at the LHC: A theorist’s view,” *Phys. Rept.*, vol. 803, pp. 1–158, 2019. doi: [10.1016/j.physrep.2019.01.007](https://doi.org/10.1016/j.physrep.2019.01.007). arXiv: [1801.09721 \[hep-ph\]](https://arxiv.org/abs/1801.09721) (cited on p. 40).
- [73] J. Pequenao, “Computer generated image of the whole ATLAS detector,” 2008. [Online]. Available: <https://cds.cern.ch/record/1095924> (cited on p. 42).
- [74] I. Neutelings, *The ATLAS coordinate system, including the LHC*, https://tikz.net/axis3d_cms/, Accessed: 07-02-2023 (cited on p. 42).
- [75] R. Beccherle *et al.*, “MCC: the Module Controller Chip for the ATLAS Pixel Detector,” CERN, Geneva, Tech. Rep., 2002. doi: [10.1016/S0168-9002\(02\)01279-2](https://doi.org/10.1016/S0168-9002(02)01279-2). [Online]. Available: <http://cds.cern.ch/record/685344> (cited on p. 43).

- [76] A. A. Carter, R. De Oliveira, and A. Gaudi, *Novel thermal management structures and their applications in new hybrid technologies and feed-through structures* (CERN Yellow Reports: Monographs). Geneva: CERN, 1999. doi: [10.5170/CERN-1999-008](https://doi.org/10.5170/CERN-1999-008). [Online]. Available: <https://cds.cern.ch/record/406549> (cited on p. 43).
- [77] The ATLAS Collaboration, “The ATLAS Transition Radiation Tracker (TRT) proportional drift tube: design and performance,” *JINST*, vol. 3, P02013, 2008. doi: [10.1088/1748-0221/3/02/P02013](https://doi.org/10.1088/1748-0221/3/02/P02013). [Online]. Available: <http://cds.cern.ch/record/1094549> (cited on p. 44).
- [78] *CAS - CERN Accelerator School: Beam Injection, Extraction and Transfer: Erice, Italy 10 - 19 Mar 2017. CAS - CERN Accelerator School: Beam Injection, Extraction and Transfer*, CERN, Geneva: CERN, 2018. doi: [10.23730/CYRSP-2018-005](https://doi.org/10.23730/CYRSP-2018-005). [Online]. Available: <https://cds.cern.ch/record/2646489> (cited on p. 45).
- [79] “Performance of the ATLAS Hadronic Endcap Calorimeter in beam tests: Selected results,” CERN, Geneva, Tech. Rep., 2022. [Online]. Available: <https://cds.cern.ch/record/2811731> (cited on p. 46).
- [80] The ATLAS Collaboration, “Energy Linearity and Resolution of the ATLAS Electromagnetic Barrel Calorimeter in an Electron Test-Beam,” *Nucl. Instrum. Methods Phys. Res., A*, vol. 568, pp. 601–623, 2006. doi: [10.1016/j.nima.2006.07.053](https://doi.org/10.1016/j.nima.2006.07.053). [Online]. Available: <http://cds.cern.ch/record/976098> (cited on p. 47).
- [81] K. S. Suslick, “Encyclopedia of physical science and technology,” *Sonoluminescence and sonochemistry, 3rd edn. Elsevier Science Ltd, Massachusetts*, pp. 1–20, 2001 (cited on p. 48).
- [82] L. Pontecorvo, “The ATLAS Muon Spectrometer,” 2004, revised version number 1 submitted on 2003-07-27 16:31:16. doi: [10.1140/epjcd/s2004-04-013-y](https://doi.org/10.1140/epjcd/s2004-04-013-y). [Online]. Available: <https://cds.cern.ch/record/676896> (cited on p. 48).
- [83] “Operation of the ATLAS trigger system in Run 2,” *JINST*, vol. 15, no. 10, P10004, 2020. doi: [10.1088/1748-0221/15/10/P10004](https://doi.org/10.1088/1748-0221/15/10/P10004). arXiv: [2007.12539](https://arxiv.org/abs/2007.12539). [Online]. Available: <https://cds.cern.ch/record/2725146> (cited on pp. 48, 49).
- [84] W. Buttinger, “The ATLAS Level-1 Trigger System,” CERN, Geneva, Tech. Rep., 2012. doi: [10.1088/1742-6596/396/1/012010](https://doi.org/10.1088/1742-6596/396/1/012010). [Online]. Available: <https://cds.cern.ch/record/1456546> (cited on p. 48).
- [85] “Performance of the ATLAS Trigger System in 2015. Performance of the ATLAS Trigger System in 2015,” *Eur. Phys. J. C*, vol. 77, no. 5, p. 317, 2017. doi: [10.1140/epjc/s10052-017-4852-3](https://doi.org/10.1140/epjc/s10052-017-4852-3). arXiv: [1611.09661](https://arxiv.org/abs/1611.09661). [Online]. Available: <https://cds.cern.ch/record/2235584> (cited on pp. 49, 50).

- [86] W. H. Smith, “Triggering at the lhc,” *Annual Review of Nuclear and Particle Science*, vol. 66, no. 1, pp. 123–141, 2016. doi: [10.1146/annurev-nucl-102115-044713](https://doi.org/10.1146/annurev-nucl-102115-044713). eprint: <https://doi.org/10.1146/annurev-nucl-102115-044713>. [Online]. Available: <https://doi.org/10.1146/annurev-nucl-102115-044713> (cited on p. 50).
- [87] “Trigger menu in 2018,” CERN, Geneva, Tech. Rep., 2019. [Online]. Available: <https://cds.cern.ch/record/2693402> (cited on p. 50).
- [88] “Performance of electron and photon triggers in ATLAS during LHC Run 2,” *Eur. Phys. J. C*, vol. 80, no. 1, p. 47, 2020. doi: [10.1140/epjc/s10052-019-7500-2](https://doi.org/10.1140/epjc/s10052-019-7500-2). arXiv: [1909.00761](https://arxiv.org/abs/1909.00761). [Online]. Available: <https://cds.cern.ch/record/2688248> (cited on pp. 50, 51).
- [89] S. Agostinelli *et al.*, “Geant4—a simulation toolkit,” *Nuclear Instruments and Methods in Physics Research Section A: Accelerators, Spectrometers, Detectors and Associated Equipment*, vol. 506, no. 3, pp. 250–303, 2003, issn: 0168-9002. doi: [https://doi.org/10.1016/S0168-9002\(03\)01368-8](https://doi.org/10.1016/S0168-9002(03)01368-8). [Online]. Available: <https://www.sciencedirect.com/science/article/pii/S0168900203013688> (cited on pp. 51, 71, 93).
- [90] T. G. Cornelissen *et al.*, “Updates of the ATLAS Tracking Event Data Model (Release 13),” CERN, Geneva, Tech. Rep., 2007. [Online]. Available: <https://cds.cern.ch/record/1038095> (cited on p. 52).
- [91] N. Braun, “Combinatorial kalman filter,” in *Combinatorial Kalman Filter and High Level Trigger Reconstruction for the Belle II Experiment*. Cham: Springer International Publishing, 2019, pp. 117–174, isbn: 978-3-030-24997-7. doi: [10.1007/978-3-030-24997-7_6](https://doi.org/10.1007/978-3-030-24997-7_6). [Online]. Available: https://doi.org/10.1007/978-3-030-24997-7_6 (cited on p. 53).
- [92] Makayla Vessella, Adam Edward Barton, *ATLAS Track Reconstruction – General Overview*, <https://atlassoftwaredocs.web.cern.ch/trackingTutorial/idooverview/>, Accessed: 07-03-2024 (cited on p. 53).
- [93] “Electron reconstruction and identification in the ATLAS experiment using the 2015 and 2016 LHC proton-proton collision data at $\sqrt{s} = 13 \text{ TeV}$,” *Eur. Phys. J. C*, vol. 79, no. 8, p. 639, 2019. doi: [10.1140/epjc/s10052-019-7140-6](https://doi.org/10.1140/epjc/s10052-019-7140-6). arXiv: [1902.04655](https://arxiv.org/abs/1902.04655). [Online]. Available: <https://cds.cern.ch/record/2657964> (cited on pp. 53, 125).

- [94] “Software Performance of the ATLAS Track Reconstruction for LHC Run 3,” CERN, Geneva, Tech. Rep., 2021. [Online]. Available: <http://cds.cern.ch/record/2766886> (cited on p. 53).
- [95] The ATLAS Collaboration, *Mean Number of Interactions per Crossing*, 2023. [Online]. Available: https://atlas.web.cern.ch/Atlas/GROUPS/DATAPREPARATION/PublicPlots/2023/DataSummary/figs/mu_run123.png (cited on p. 53).
- [96] B. Acharya and ATLAS Collaboration, “A study of the material in the atlas inner detector using secondary hadronic interactions.,” English, *Journal of Instrumentation*, vol. 7, no. 7, Jan. 2012, issn: 1748-0221. doi: [10.1088/1748-0221/7/01/P01013](https://doi.org/10.1088/1748-0221/7/01/P01013) (cited on p. 53).
- [97] The ATLAS Collaboration, “Reconstruction of primary vertices at the ATLAS experiment in Run 1 proton–proton collisions at the LHC. Reconstruction of primary vertices at the ATLAS experiment in Run 1 proton-proton collisions at the LHC,” *Eur. Phys. J. C*, vol. 77, no. 5, p. 332, 2017. doi: [10.1140/epjc/s10052-017-4887-5](https://doi.org/10.1140/epjc/s10052-017-4887-5). arXiv: [1611.10235](https://arxiv.org/abs/1611.10235). [Online]. Available: <https://cds.cern.ch/record/2235651> (cited on p. 53).
- [98] The ATLAS Collaboration, “Topological cell clustering in the ATLAS calorimeters and its performance in LHC Run 1,” *Eur. Phys. J. C*, vol. 77, p. 490, 2017. doi: [10.1140/epjc/s10052-017-5004-5](https://doi.org/10.1140/epjc/s10052-017-5004-5). arXiv: [1603.02934 \[hep-ex\]](https://arxiv.org/abs/1603.02934) (cited on p. 54).
- [99] The ATLAS Collaboration, “Electron and photon performance measurements with the atlas detector using the 2015–2017 lhc proton-proton collision data,” *Journal of Instrumentation*, vol. 14, no. 12, P12006, Dec. 2019. doi: [10.1088/1748-0221/14/12/P12006](https://doi.org/10.1088/1748-0221/14/12/P12006). [Online]. Available: <https://dx.doi.org/10.1088/1748-0221/14/12/P12006> (cited on pp. 54–56, 125).
- [100] “Electron and photon energy calibration with the ATLAS detector using data collected in 2015 at $\sqrt{s} = 13$ TeV,” CERN, Geneva, Tech. Rep., 2016. [Online]. Available: <https://cds.cern.ch/record/2203514> (cited on pp. 54–56, 76).
- [101] “Electron and photon energy calibration with the ATLAS detector using LHC Run 1 data. Electron and photon energy calibration with the ATLAS detector using LHC Run 1 data,” *Eur. Phys. J. C*, vol. C74, p. 3071, 2014. doi: [10.1140/epjc/s10052-014-3071-4](https://doi.org/10.1140/epjc/s10052-014-3071-4). arXiv: [1407.5063](https://arxiv.org/abs/1407.5063). [Online]. Available: <https://cds.cern.ch/record/1744017> (cited on p. 54).
- [102] “Electron and photon energy calibration with the ATLAS detector using LHC Run 2 data,” CERN, Geneva, Tech. Rep., 2023. arXiv: [2309.05471](https://arxiv.org/abs/2309.05471). [Online]. Available: <https://cds.cern.ch/record/2870086> (cited on pp. 54, 55, 76).

- [103] “Proposal for particle-level object and observable definitions for use in physics measurements at the LHC,” CERN, Geneva, Tech. Rep., 2015. [Online]. Available: <https://cds.cern.ch/record/2022743> (cited on p. 55).
- [104] John Butterworth, *Underlying Events*, 2006. [Online]. Available: <https://hep.ucl.ac.uk/~jmb/Talks/dresden2005.pdf> (cited on p. 56).
- [105] The ATLAS Collaboration, “Measurement of the photon identification efficiencies with the ATLAS detector using LHC Run 2 data collected in 2015 and 2016,” *Eur. Phys. J. C*, vol. 79, no. 3, p. 205, 2019. doi: [10.1140/epjc/s10052-019-6650-6](https://doi.org/10.1140/epjc/s10052-019-6650-6). arXiv: [1810.05087](https://arxiv.org/abs/1810.05087). [Online]. Available: <https://cds.cern.ch/record/2643391> (cited on p. 56).
- [106] ATLAS, “Muon reconstruction and identification efficiency in ATLAS using the full Run 2 pp collision data set at $\sqrt{s} = 13$ TeV,” *Eur. Phys. J. C*, vol. 81, p. 578, 2021. doi: [10.1140/epjc/s10052-021-09233-2](https://doi.org/10.1140/epjc/s10052-021-09233-2). arXiv: [2012.00578](https://arxiv.org/abs/2012.00578). [Online]. Available: <https://cds.cern.ch/record/2746302> (cited on pp. 57, 58, 125).
- [107] “Impact of Alternative Inputs and Jet Grooming on Large-R Jet Performance,” CERN, Geneva, Tech. Rep., 2019. [Online]. Available: <https://cds.cern.ch/record/2683619> (cited on p. 58).
- [108] F. A. Di Bello *et al.*, “Towards a Computer Vision Particle Flow,” *Eur. Phys. J. C*, vol. 81, no. 2, p. 107, 2021. doi: [10.1140/epjc/s10052-021-08897-0](https://doi.org/10.1140/epjc/s10052-021-08897-0). arXiv: [2003.08863](https://arxiv.org/abs/2003.08863). [Online]. Available: <https://cds.cern.ch/record/2715739> (cited on pp. 59, 61).
- [109] I. G. Knowles and G. D. Lafferty, “Hadronization in $z0$ decay,” *J. Phys. G: Nucl. Part. Phys.* **23** 731, 1997 (cited on p. 59).
- [110] P. R. M. Green S. Lloyd and D. Ward, “Electron-positron physics at the z ,” *Studies in high energy physics, cosmology, and gravitation*, IOP Pub., 1998 (cited on p. 59).
- [111] “Jet energy scale and resolution measured in proton–proton collisions at $\sqrt{s} = 13$ TeV with the ATLAS detector,” *Eur. Phys. J. C*, vol. 81, no. 8, p. 689, 2021. doi: [10.1140/epjc/s10052-021-09402-3](https://doi.org/10.1140/epjc/s10052-021-09402-3). arXiv: [2007.02645](https://arxiv.org/abs/2007.02645). [Online]. Available: <https://cds.cern.ch/record/2722869> (cited on pp. 62, 71).
- [112] “Measurements of WH and ZH production in the $H \rightarrow b\bar{b}$ decay channel in pp collisions at 13 TeV with the ATLAS detector,” *Eur. Phys. J. C*, vol. 81, no. 2, p. 178, 2021. doi: [10.1140/epjc/s10052-020-08677-2](https://doi.org/10.1140/epjc/s10052-020-08677-2). arXiv: [2007.02873](https://arxiv.org/abs/2007.02873). [Online]. Available: <https://cds.cern.ch/record/2723187> (cited on p. 62).

- [113] “Direct constraint on the Higgs-charm coupling from a search for Higgs boson decays to charm quarks with the ATLAS detector,” CERN, Geneva, Tech. Rep., 2021. [Online]. Available: <https://cds.cern.ch/record/2771724> (cited on p. 62).
- [114] “Optimisation and performance studies of the ATLAS b -tagging algorithms for the 2017-18 LHC run,” CERN, Geneva, Tech. Rep., 2017. [Online]. Available: <https://cds.cern.ch/record/2273281> (cited on pp. 62, 98).
- [115] “Performance of missing transverse momentum reconstruction with the ATLAS detector using proton-proton collisions at $\sqrt{s} = 13$ TeV,” *Eur. Phys. J. C*, vol. 78, no. 11, p. 903, 2018. doi: [10.1140/epjc/s10052-018-6288-9](https://doi.org/10.1140/epjc/s10052-018-6288-9). arXiv: [1802.08168](https://arxiv.org/abs/1802.08168). [Online]. Available: <https://cds.cern.ch/record/2305380> (cited on pp. 64, 125).
- [116] “Measurement of the charged-particle multiplicity inside jets from $\sqrt{s} = 8$ TeV pp collisions with the ATLAS detector. Measurement of the charged-particle multiplicity inside jets from $\sqrt{s} = 8$ TeV pp collisions with the ATLAS detector,” *Eur. Phys. J. C*, vol. 76, p. 322, 2016. doi: [10.1140/epjc/s10052-016-4126-5](https://doi.org/10.1140/epjc/s10052-016-4126-5). arXiv: [1602.00988](https://arxiv.org/abs/1602.00988). [Online]. Available: <https://cds.cern.ch/record/2128767> (cited on p. 64).
- [117] “Measurement of the tau lepton reconstruction and identification performance in the ATLAS experiment using pp collisions at $\sqrt{s} = 13$ TeV,” CERN, Geneva, Tech. Rep., 2017. [Online]. Available: <https://cds.cern.ch/record/2261772> (cited on p. 65).
- [118] “R=0.4 jets input comparison and Monte Carlo calibration with the ATLAS Detector,” CERN, Geneva, Tech. Rep., 2022. [Online]. Available: <https://cds.cern.ch/record/2824558> (cited on p. 67).
- [119] S. Schramm, “ATLAS Jet Reconstruction, Calibration, and Tagging of Lorentz-boosted Objects,” *EPJ Web Conf.*, vol. 182, p. 02113, 2018. doi: [10.1051/epjconf/201818202113](https://doi.org/10.1051/epjconf/201818202113) (cited on p. 67).
- [120] “New techniques for jet calibration with the ATLAS detector,” *Eur. Phys. J. C*, vol. 83, p. 761, 2023. doi: [10.1140/epjc/s10052-023-11837-9](https://doi.org/10.1140/epjc/s10052-023-11837-9). arXiv: [2303.17312](https://arxiv.org/abs/2303.17312). [Online]. Available: <https://cds.cern.ch/record/2854733> (cited on pp. 68, 69).
- [121] “Jet energy scale and resolution measured in proton–proton collisions at $\sqrt{s} = 13$ TeV with the ATLAS detector,” *Eur. Phys. J. C*, vol. 81, no. 8, p. 689, 2021. doi: [10.1140/epjc/s10052-021-09402-3](https://doi.org/10.1140/epjc/s10052-021-09402-3). arXiv: [2007.02645](https://arxiv.org/abs/2007.02645). [Online]. Available: <https://cds.cern.ch/record/2722869> (cited on pp. 69, 124).

- [122] “Luminosity determination in pp collisions at $\sqrt{s} = 13$ TeV using the ATLAS detector at the LHC,” CERN, Geneva, Tech. Rep., 2019. [Online]. Available: <https://cds.cern.ch/record/2677054> (cited on p. 70).
- [123] H.-L. Lai *et al.*, “New parton distributions for collider physics,” *Phys. Rev. D*, vol. 82, p. 074024, 7 Oct. 2010. doi: [10.1103/PhysRevD.82.074024](https://doi.org/10.1103/PhysRevD.82.074024). [Online]. Available: <https://link.aps.org/doi/10.1103/PhysRevD.82.074024> (cited on p. 70).
- [124] “Measurement of the Z/γ^* boson transverse momentum distribution in pp collisions at $\sqrt{s} = 7$ TeV with the ATLAS detector. Measurement of the Z/γ^* boson transverse momentum distribution in pp collisions at $\sqrt{s} = 7$ TeV with the ATLAS detector,” *Journal of High Energy Physics*, vol. 2014, no. 9, Sep. 2014. doi: [10.1007/jhep09\(2014\)145](https://doi.org/10.1007/jhep09(2014)145). [Online]. Available: <https://doi.org/10.1007%2Fjhep09%282014%29145> (cited on p. 71).
- [125] N. Davidson, T. Przedzinski, and Z. Was, *Photos interface in c++; technical and physics documentation*, 2015. arXiv: [1011.0937 \[hep-ph\]](https://arxiv.org/abs/1011.0937) (cited on p. 71).
- [126] D. J. Lange, “The evtgen particle decay simulation package,” *Nuclear Instruments and Methods in Physics Research Section A: Accelerators, Spectrometers, Detectors and Associated Equipment*, vol. 462, no. 1, pp. 152–155, 2001, BEAUTY2000, Proceedings of the 7th Int. Conf. on B-Physics at Hadron Machines, ISSN: 0168-9002. doi: [https://doi.org/10.1016/S0168-9002\(01\)00089-4](https://doi.org/10.1016/S0168-9002(01)00089-4). [Online]. Available: <https://www.sciencedirect.com/science/article/pii/S0168900201000894> (cited on pp. 71, 90, 91).
- [127] S. Schumann and F. Krauss, “A Parton shower algorithm based on Catani-Seymour dipole factorisation,” *JHEP*, vol. 03, p. 038, 2008. doi: [10.1088/1126-6708/2008/03/038](https://doi.org/10.1088/1126-6708/2008/03/038). arXiv: [0709.1027 \[hep-ph\]](https://arxiv.org/abs/0709.1027) (cited on pp. 71, 90, 91).
- [128] S. Catani and M. H. Seymour, “A General algorithm for calculating jet cross-sections in NLO QCD,” *Nucl. Phys. B*, vol. 485, pp. 291–419, 1997, [Erratum: Nucl.Phys.B 510, 503–504 (1998)]. doi: [10.1016/S0550-3213\(96\)00589-5](https://doi.org/10.1016/S0550-3213(96)00589-5). arXiv: [hep-ph/9605323](https://arxiv.org/abs/hep-ph/9605323) (cited on pp. 71, 90).
- [129] F. Cascioli, P. Maierhöfer, and S. Pozzorini, “Scattering amplitudes with open loops,” *Phys. Rev. Lett.*, vol. 108, p. 111601, 11 Mar. 2012. doi: [10.1103/PhysRevLett.108.111601](https://doi.org/10.1103/PhysRevLett.108.111601). [Online]. Available: <https://link.aps.org/doi/10.1103/PhysRevLett.108.111601> (cited on p. 71).
- [130] S. Hoeche, F. Krauss, M. Schonherr, and F. Siegert, “QCD matrix elements + parton showers: The NLO case,” *JHEP*, vol. 04, p. 027, 2013. doi: [10.1007/JHEP04\(2013\)027](https://doi.org/10.1007/JHEP04(2013)027). arXiv: [1207.5030 \[hep-ph\]](https://arxiv.org/abs/1207.5030) (cited on pp. 71, 90, 91).

- [131] R. D. Ball *et al.*, “Parton distributions for the LHC Run II,” *JHEP*, vol. 04, p. 040, 2015. doi: [10.1007/JHEP04\(2015\)040](https://doi.org/10.1007/JHEP04(2015)040). arXiv: [1410.8849 \[hep-ph\]](https://arxiv.org/abs/1410.8849) (cited on pp. 71, 90, 91, 133).
- [132] “Modelling and computational improvements to the simulation of single vector-boson plus jet processes for the ATLAS experiment,” *JHEP*, vol. 2208, p. 089, 2022. doi: [10.1007/JHEP08\(2022\)089](https://doi.org/10.1007/JHEP08(2022)089). arXiv: [2112.09588](https://arxiv.org/abs/2112.09588). [Online]. Available: <https://cds.cern.ch/record/2798348> (cited on p. 71).
- [133] G. Aad *et al.*, “The ATLAS Simulation Infrastructure,” *Eur. Phys. J. C*, vol. 70, pp. 823–874, 2010. doi: [10.1140/epjc/s10052-010-1429-9](https://doi.org/10.1140/epjc/s10052-010-1429-9). arXiv: [1005.4568 \[physics.ins-det\]](https://arxiv.org/abs/1005.4568) (cited on p. 71).
- [134] P. Berta, M. Spousta, D. W. Miller, and R. Leitner, “Particle-level pileup subtraction for jets and jet shapes,” *Journal of High Energy Physics*, vol. 2014, no. 6, Jun. 2014. doi: [10.1007/jhep06\(2014\)092](https://doi.org/10.1007/jhep06(2014)092). [Online]. Available: <https://doi.org/10.1007%2Fjhep06%282014%29092> (cited on pp. 71, 72).
- [135] M. Cacciari, G. P. Salam, and G. Soyez, “SoftKiller, a particle-level pileup removal method,” *The European Physical Journal C*, vol. 75, no. 2, Feb. 2015. doi: [10.1140/epjc/s10052-015-3267-2](https://doi.org/10.1140/epjc/s10052-015-3267-2). [Online]. Available: <https://doi.org/10.1140/2Fepjc%2Fs10052-015-3267-2> (cited on pp. 71, 72).
- [136] A. J. Larkoski, S. Marzani, G. Soyez, and J. Thaler, “Soft drop,” *Journal of High Energy Physics*, vol. 2014, no. 5, May 2014. doi: [10.1007/jhep05\(2014\)146](https://doi.org/10.1007/jhep05(2014)146). [Online]. Available: <https://doi.org/10.1007%2Fjhep05%282014%29146> (cited on pp. 71, 72).
- [137] “Jet energy scale measurements and their systematic uncertainties in proton-proton collisions at $\sqrt{s} = 13$ TeV with the atlas detector,” *Physical Review D*, vol. 96, no. 7, Oct. 2017. doi: [10.1103/physrevd.96.072002](https://doi.org/10.1103/physrevd.96.072002). [Online]. Available: <https://doi.org/10.1103%2Fphysrevd.96.072002> (cited on p. 71).
- [138] M. Cacciari, G. P. Salam, and G. Soyez, “FastJet user manual,” *The European Physical Journal C*, vol. 72, no. 3, Mar. 2012. doi: [10.1140/epjc/s10052-012-1896-2](https://doi.org/10.1140/epjc/s10052-012-1896-2). [Online]. Available: <https://doi.org/10.1140/2Fepjc%2Fs10052-012-1896-2> (cited on p. 71).
- [139] M. Cacciari and G. P. Salam, “Dispelling the N^3 myth for the k_t jet-finder,” *Phys. Lett. B*, vol. 641, pp. 57–61, 2006. doi: [10.1016/j.physletb.2006.08.037](https://doi.org/10.1016/j.physletb.2006.08.037). arXiv: [hep-ph/0512210](https://arxiv.org/abs/hep-ph/0512210) (cited on p. 71).

- [140] M. Testa, “Performance of pile-up mitigation techniques for jets in pp collisions with the atlas detector,” *Nuclear Instruments and Methods in Physics Research Section A: Accelerators, Spectrometers, Detectors and Associated Equipment*, vol. 824, pp. 367–370, 2016, Frontier Detectors for Frontier Physics: Proceedings of the 13th Pisa Meeting on Advanced Detectors, ISSN: 0168-9002. doi: <https://doi.org/10.1016/j.nima.2015.10.039>. [Online]. Available: <https://www.sciencedirect.com/science/article/pii/S0168900215012516> (cited on pp. 73, 78, 98).
- [141] Steve Farrell, *Overlap Removal Tools*, 2017. [Online]. Available: https://indico.cern.ch/event/631313/contributions/2683959/attachments/1518878/2373377/Farrell_ORTools_ftaghbb.pdf (cited on pp. 73, 98).
- [142] M. Cacciari and G. P. Salam, “Pileup subtraction using jet areas,” *Physics Letters B*, vol. 659, no. 1, pp. 119–126, 2008, ISSN: 0370-2693. doi: <https://doi.org/10.1016/j.physletb.2007.09.077>. [Online]. Available: <https://www.sciencedirect.com/science/article/pii/S0370269307011094> (cited on pp. 73, 98).
- [143] D. W. Scott, “Sturges’ and scott’s rules,” in *International Encyclopedia of Statistical Science*, M. Lovric, Ed. Berlin, Heidelberg: Springer Berlin Heidelberg, 2011, pp. 1563–1566, ISBN: 978-3-642-04898-2. doi: [10.1007/978-3-642-04898-2_578](https://doi.org/10.1007/978-3-642-04898-2_578). [Online]. Available: https://doi.org/10.1007/978-3-642-04898-2_578 (cited on p. 74).
- [144] S. Baker and R. D. Cousins, “Clarification of the use of chi-square and likelihood functions in fits to histograms,” *Nuclear Instruments and Methods in Physics Research*, vol. 221, no. 2, pp. 437–442, 1984, ISSN: 0167-5087. doi: [https://doi.org/10.1016/0167-5087\(84\)90016-4](https://doi.org/10.1016/0167-5087(84)90016-4). [Online]. Available: <https://www.sciencedirect.com/science/article/pii/0167508784900164> (cited on p. 75).
- [145] Matt Relich, *Common Fitting Tool*, 2012. [Online]. Available: https://indico.cern.ch/event/213454/contributions/430232/attachments/337413/470895/FitResults_Nov21_v3.pdf (cited on p. 75).
- [146] “Studies of the muon momentum calibration and performance of the ATLAS detector with pp collisions at $\sqrt{s}=13$ TeV,” *Eur. Phys. J. C*, vol. 83, no. 8, p. 686, 2023. doi: [10.1140/epjc/s10052-023-11584-x](https://doi.org/10.1140/epjc/s10052-023-11584-x). arXiv: [2212.07338](https://arxiv.org/abs/2212.07338). [Online]. Available: <https://cds.cern.ch/record/2844624> (cited on p. 76).
- [147] Mariana Toscani, *Overview of Large R in-situ JES*, 2022. [Online]. Available: <https://indico.cern.ch/event/1207677/contributions/5079756/attachments/>

- 2531419/4355547/Overview%20of%20Large%20R%20in-situ%20JES%20(1).pdf (cited on pp. 80, 85).
- [148] Sundeep Singh, *Determining the Jet Energy Scale for ATLAS in the Z+Jet Channel*, 2016. [Online]. Available: https://summit.sfu.ca/_flysystem/fedora/2022-08/input_data/21142/etd21203.pdf (cited on p. 82).
- [149] Oleksandr (Sasha) Burlayenko, *New Jet Samples Preparation and Their Impact in Jet Calibration Uncertainties*, 2022. [Online]. Available: https://indico.cern.ch/event/1202933/contributions/5058540/attachments/2513258/4320313/QTpart2_Burlayenko21092022MainJetEt.pdf (cited on p. 80).
- [150] Julio Lozano Bahilo and Naseem Bouchhar, *Large-R Calibration for Gamma+Jet Events*, 2022. [Online]. Available: [https://indico.cern.ch/event/1148615/contributions/4915701/attachments/2460233/4217960/Large-R_10_june%20\(1\).pdf](https://indico.cern.ch/event/1148615/contributions/4915701/attachments/2460233/4217960/Large-R_10_june%20(1).pdf) (cited on p. 80).
- [151] Benjamin Honan, *Large-R JES using Z+jet events*, 2020. [Online]. Available: [https://indico.cern.ch/event/971848/contributions/4093651/attachments/2141016/3607874/QT_Report__Large_R_JES_using_Z_jet_events\(3\).pdf](https://indico.cern.ch/event/971848/contributions/4093651/attachments/2141016/3607874/QT_Report__Large_R_JES_using_Z_jet_events(3).pdf) (cited on p. 80).
- [152] Evan Van de Wall, *Multijet Balance Update*, 2022. [Online]. Available: https://indico.cern.ch/event/1084917/contributions/4770656/attachments/2406615/4117073/MJB_update.pdf (cited on p. 80).
- [153] Sahil Singh, *Direct Balance Cross-Check Using the Insitu Framework*, 2021 (cited on p. 86).
- [154] A. Tumasyan *et al.*, “Measurement of the electroweak production of $W\gamma$ in association with two jets in proton-proton collisions at $\sqrt{s} = 13$ TeV,” *Phys. Rev. D*, vol. 108, no. 3, p. 032017, 2023. doi: [10.1103/PhysRevD.108.032017](https://doi.org/10.1103/PhysRevD.108.032017). arXiv: [2212.12592](https://arxiv.org/abs/2212.12592) [hep-ex] (cited on p. 89).
- [155] Ilaria Brivio (Universidad Autonoma de Madrid (ES)), *$W\gamma$ scattering as a probe for quartic gauge couplings*, 2023. [Online]. Available: <https://indico.cern.ch/event/1227204/> (cited on p. 89).
- [156] “ATLAS Pythia 8 tunes to 7 TeV data,” CERN, Geneva, Tech. Rep., 2014. [Online]. Available: <https://cds.cern.ch/record/1966419> (cited on pp. 90, 91).
- [157] Ansgar Denner, *VBS precision predictions*, 2019. [Online]. Available: https://indico.cern.ch/event/799542/contributions/3489882/attachments/1951454/3239733/denner_wien19.pdf (cited on p. 90).

- [158] Jonas M. Lindert, *Aspects of the EW Standard Model II*, 2022. [Online]. Available: https://indico.cern.ch/event/1104027/contributions/4818733/attachments/2467875/4232927/JL_MCnet2022_2.pdf (cited on p. 90).
- [159] “ E_T^{miss} performance in the ATLAS detector using 2015-2016 LHC p-p collisions,” CERN, Geneva, Tech. Rep., 2018. [Online]. Available: <https://cds.cern.ch/record/2625233> (cited on p. 99).
- [160] “Tools for estimating fake/non-prompt lepton backgrounds with the ATLAS detector at the LHC,” *JINST*, vol. 18, no. 11, T11004, 2023. doi: [10.1088/1748-0221/18/11/T11004](https://doi.org/10.1088/1748-0221/18/11/T11004). arXiv: [2211.16178](https://arxiv.org/abs/2211.16178). [Online]. Available: <https://cds.cern.ch/record/2842463> (cited on p. 100).
- [161] G. Kasieczka, B. Nachman, M. D. Schwartz, and D. Shih, “Automating the abcd method with machine learning,” *Phys. Rev. D*, vol. 103, p. 035021, 3 Feb. 2021. doi: [10.1103/PhysRevD.103.035021](https://doi.org/10.1103/PhysRevD.103.035021). [Online]. Available: <https://link.aps.org/doi/10.1103/PhysRevD.103.035021> (cited on p. 101).
- [162] M. Oreglia, “A Study of the Reactions $\psi' \rightarrow \gamma\gamma\psi$,” Other thesis, Dec. 1980 (cited on p. 101).
- [163] M. Oreglia, “A Study of the Reactions $\psi' \rightarrow \gamma\gamma\psi$,” Other thesis, Dec. 1980 (cited on p. 101).
- [164] S. Manzoni, L. Carminati, and G. Marchiori, “Electron-to-photon fake rate measurements - Supporting documentation for the paper Photon identification in 2015+2016 ATLAS data,” CERN, Geneva, Tech. Rep., 2017. [Online]. Available: <https://cds.cern.ch/record/2280801> (cited on p. 103).
- [165] K. Cranmer, “Practical Statistics for the LHC,” in *2011 European School of High-Energy Physics*, 2014, pp. 267–308. doi: [10.5170/CERN-2014-003.267](https://doi.org/10.5170/CERN-2014-003.267). arXiv: [1503.07622 \[physics.data-an\]](https://arxiv.org/abs/1503.07622) (cited on p. 107).
- [166] R. J. Barlow and C. Beeston, “Fitting using finite Monte Carlo samples,” *Comput. Phys. Commun.*, vol. 77, pp. 219–228, 1993. doi: [10.1016/0010-4655\(93\)90005-W](https://doi.org/10.1016/0010-4655(93)90005-W) (cited on p. 107).
- [167] “Differential cross-section measurements for the electroweak production of dijets in association with a Z boson in proton–proton collisions at ATLAS,” *Eur. Phys. J. C*, vol. 81, no. 2, p. 163, 2021. doi: [10.1140/epjc/s10052-020-08734-w](https://doi.org/10.1140/epjc/s10052-020-08734-w). arXiv: [2006.15458](https://arxiv.org/abs/2006.15458). [Online]. Available: <https://cds.cern.ch/record/2722304> (cited on pp. 108, 117).

- [168] F. a. James, “MINUIT: Function Minimization and Error Analysis Reference Manual,” 1998, CERN Program Library Long Writeups. [Online]. Available: <https://cds.cern.ch/record/2296388> (cited on p. 112).
- [169] Dag Gillberg, *Combining measurements with a Gaussian kernel*, 2012. [Online]. Available: <https://twiki.cern.ch/twiki/pub/AtlasProtected/EtaIntercalibration2012/GausKernel.pdf> (cited on p. 123).
- [170] *Proceedings of the 1974 CERN School of Computing: Godøysund, Norway 11 - 24 Aug 1974. 3rd CERN School of Computing*, CERN, Geneva: CERN, 1974. doi: [10.5170/CERN-1974-023](https://doi.org/10.5170/CERN-1974-023). [Online]. Available: <https://cds.cern.ch/record/186223> (cited on p. 124).
- [171] O. Behnke, K. Kröninger, T. Schörner-Sadenius, and G. Schott, Eds., *Data analysis in high energy physics: A practical guide to statistical methods*. Weinheim, Germany: Wiley-VCH, 2013, ISBN: 978-3-527-41058-3, 978-3-527-65344-7, 978-3-527-65343-0 (cited on p. 132).
- [172] G. D’Agostini, “A multidimensional unfolding method based on Bayes’ Theorem,” DESY, Hamburg, Tech. Rep., 1994. [Online]. Available: <https://cds.cern.ch/record/265717> (cited on p. 150).
- [173] A. Ballestrero *et al.*, “Precise predictions for same-sign w-boson scattering at the lhc,” *The European Physical Journal C*, vol. 78, no. 8, Aug. 2018, issn: 1434-6052. doi: [10.1140/epjc/s10052-018-6136-y](https://doi.org/10.1140/epjc/s10052-018-6136-y). [Online]. Available: <http://dx.doi.org/10.1140/epjc/s10052-018-6136-y> (cited on p. 151).

Appendices

Appendix A

Large-R Z +jets Insitu Calibration

A.1 Z +jets response fits

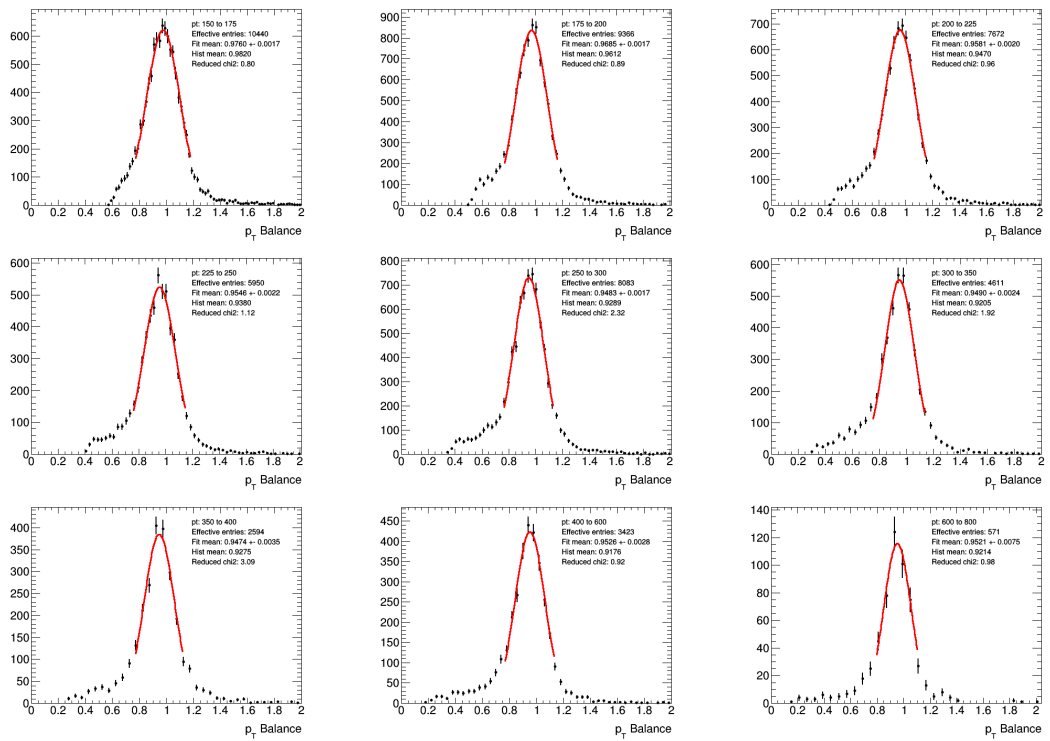


Figure A.1. Data $Z(\rightarrow e^+e^-)$ +jets response distributions

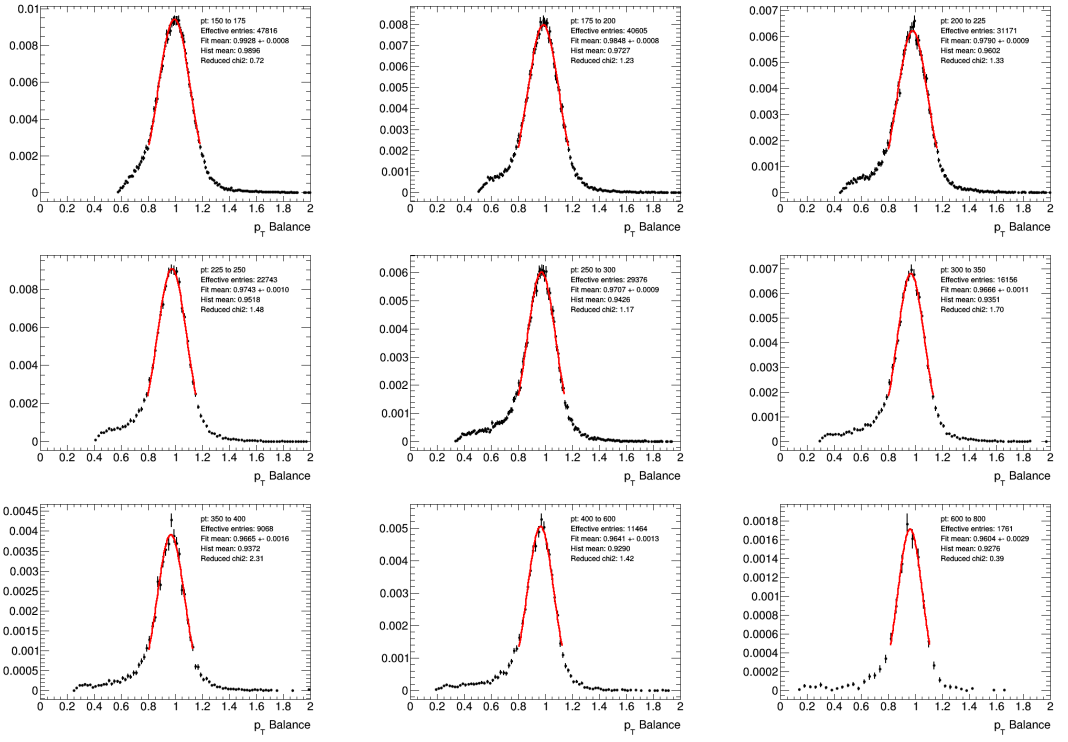


Figure A.2. Pythia MC $Z(\rightarrow e^+e^-)$ +jets response distributions

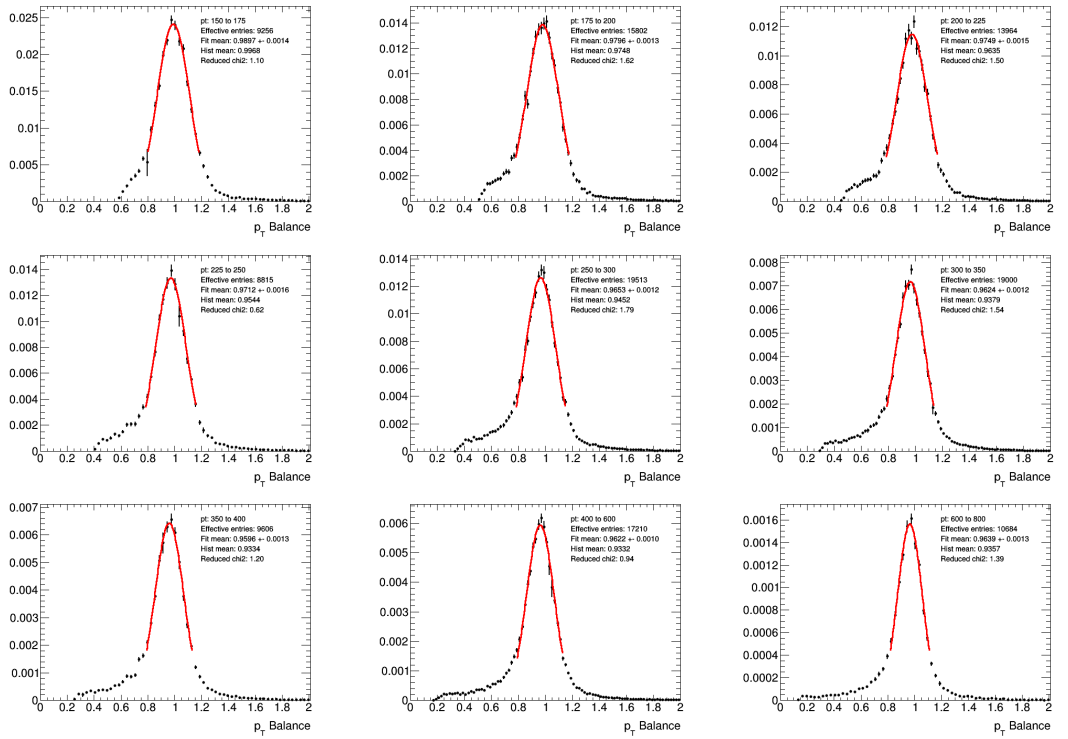


Figure A.3. Sherpa MC $Z(\rightarrow e^+e^-)$ +jets response distributions

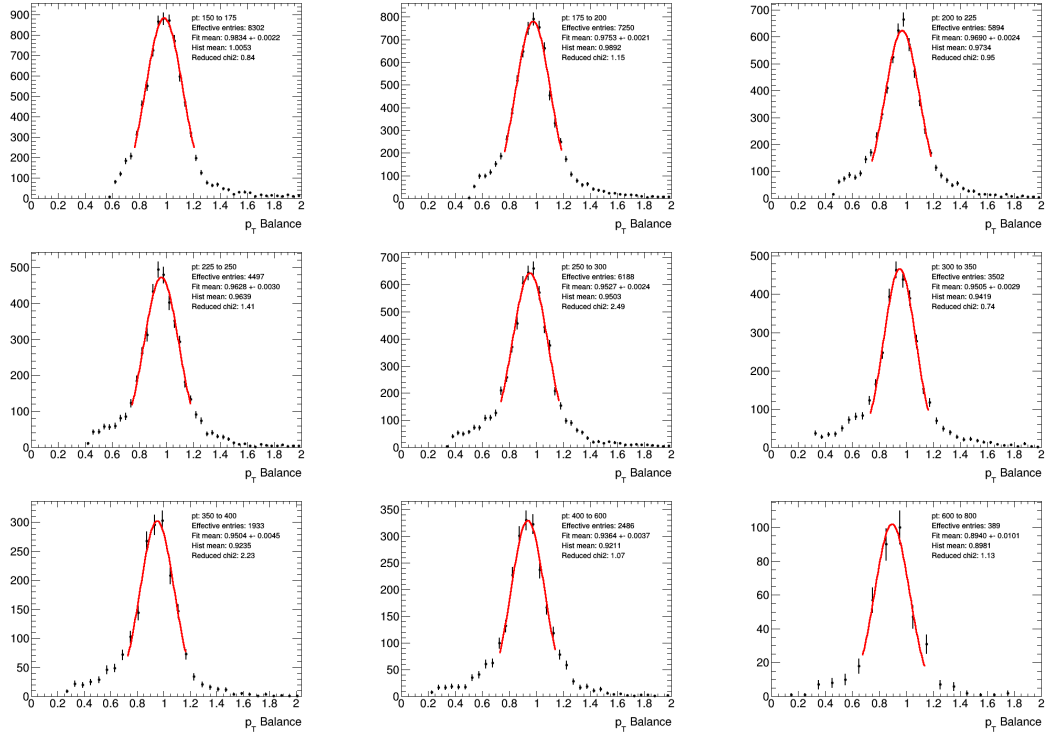


Figure A.4. Data $Z(\rightarrow \mu\mu)$ +jets response distributions

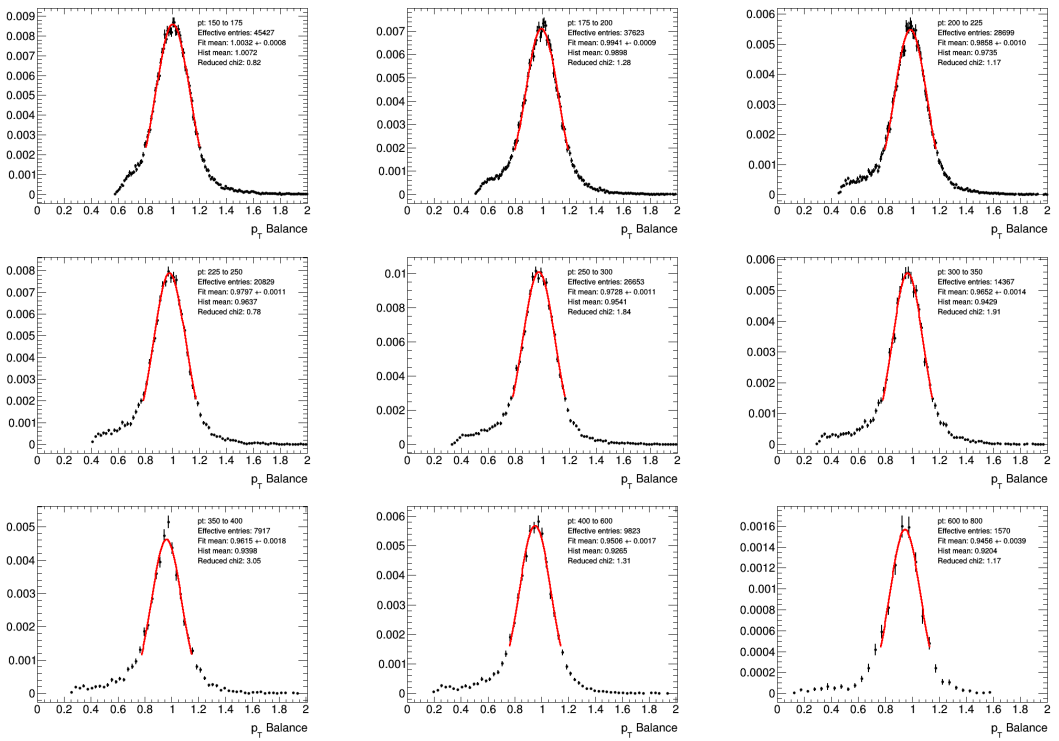


Figure A.5. Pythia MC $Z(\rightarrow \mu\mu)$ +jets response distributions

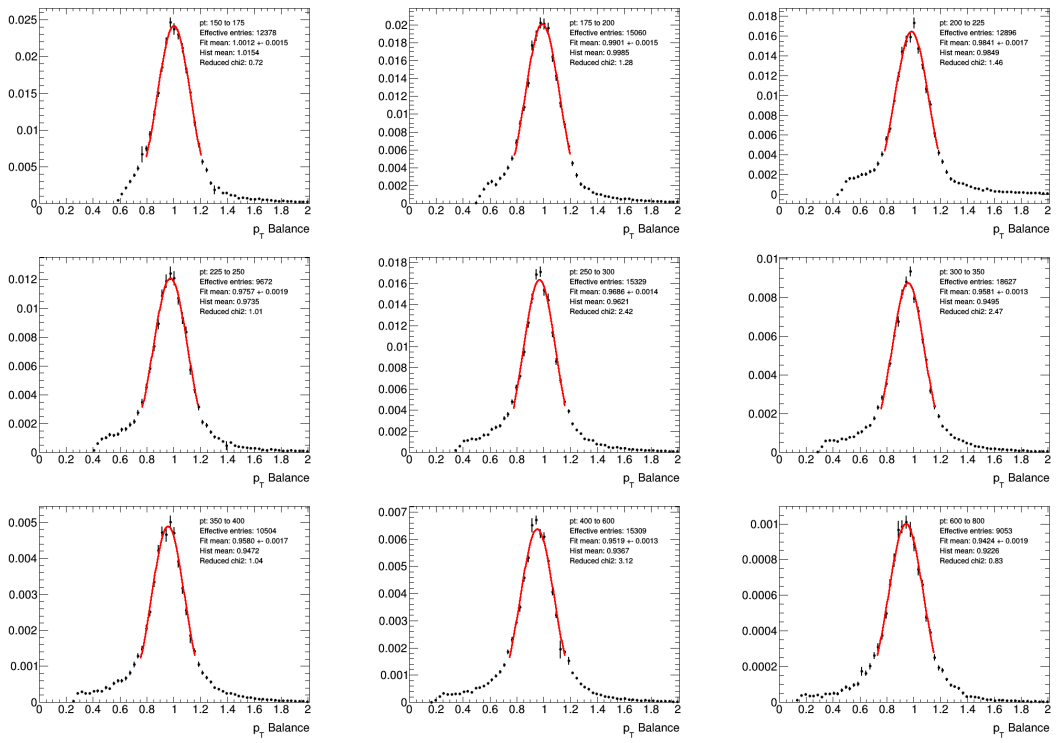


Figure A.6. Sherpa MC $Z(\rightarrow \mu\mu)$ +jets response distributions

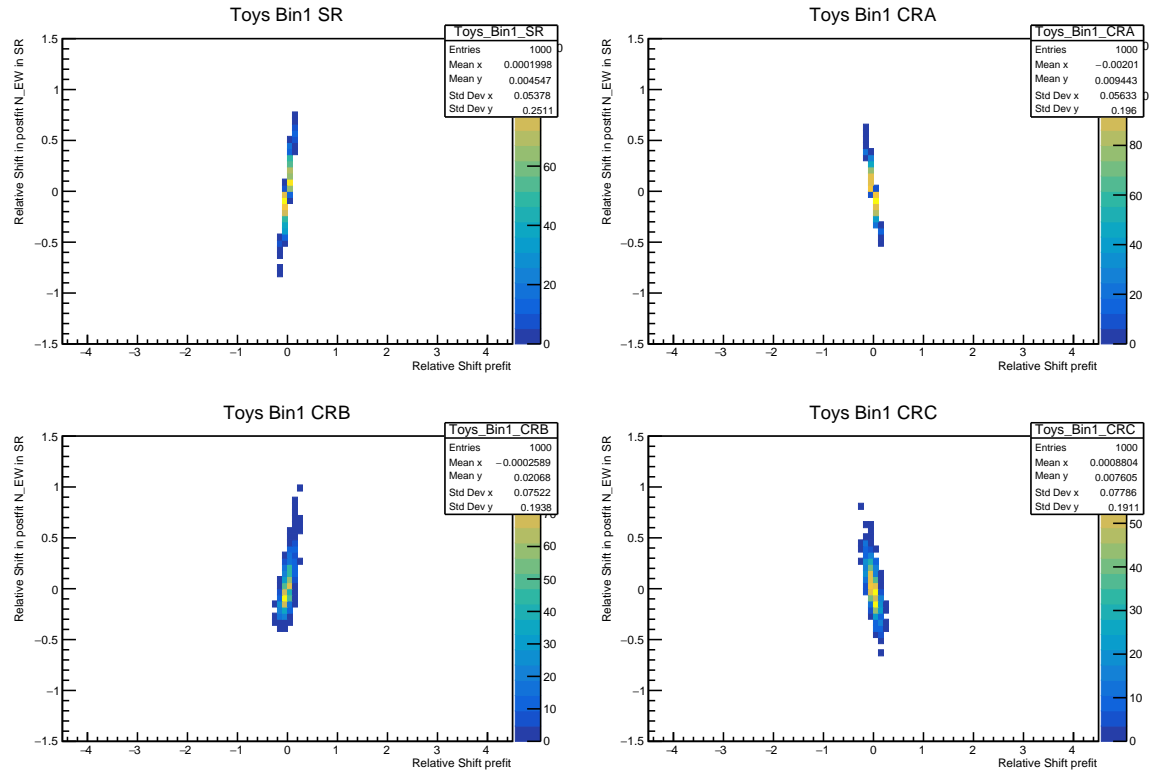
Appendix B

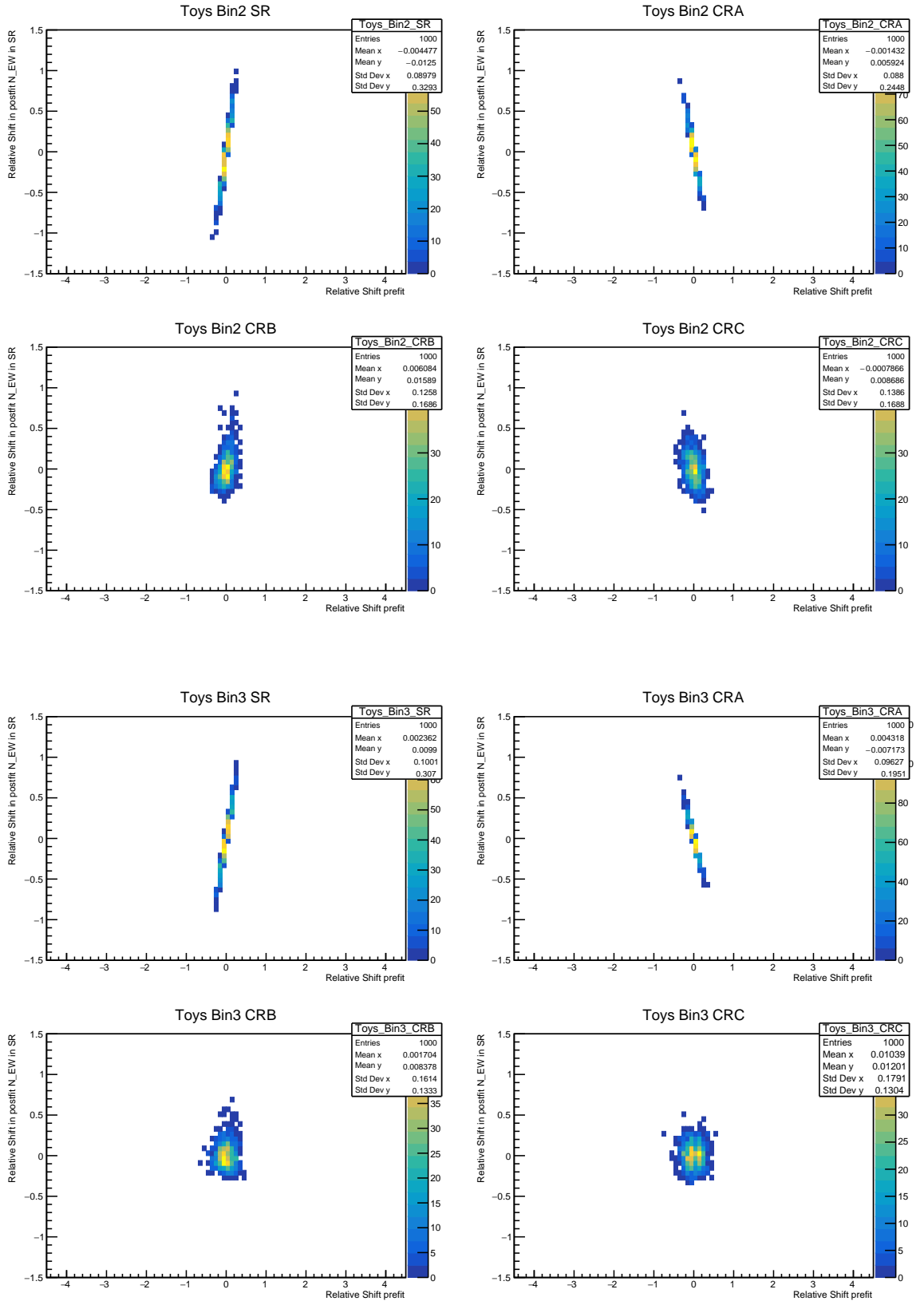
Differential Cross-section Measurement

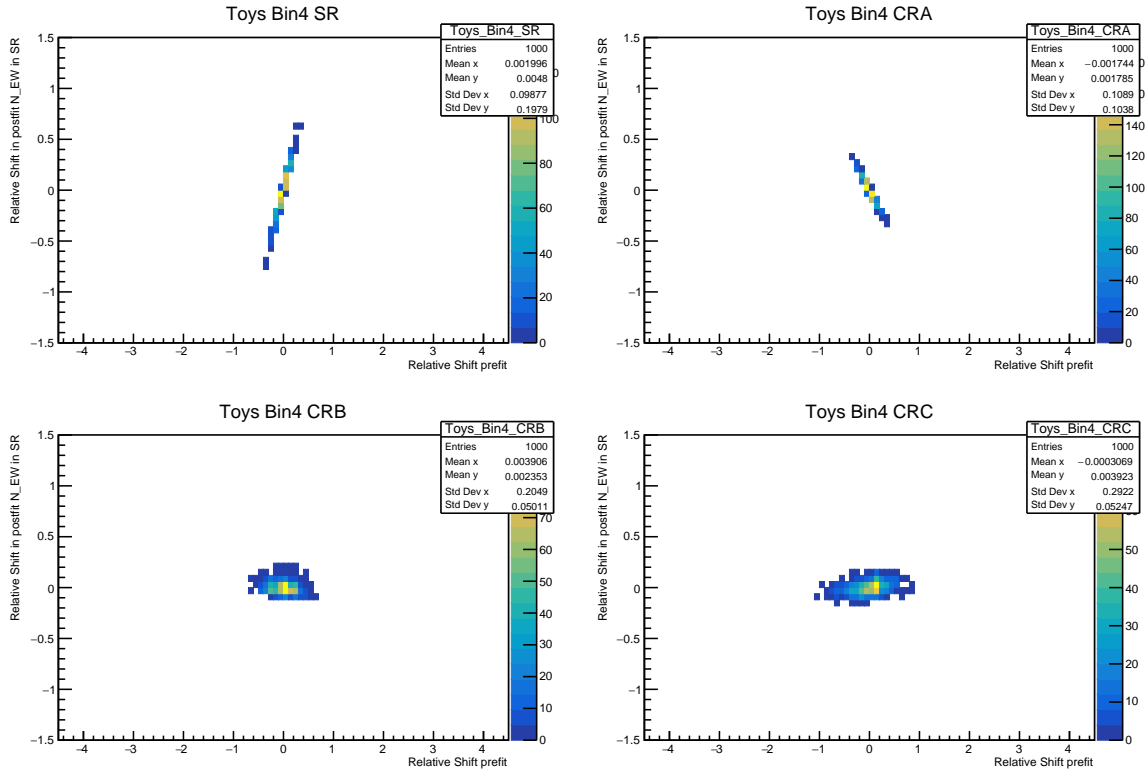
B.1 Stability Plots

B.1.1 $f(x_i) = c$

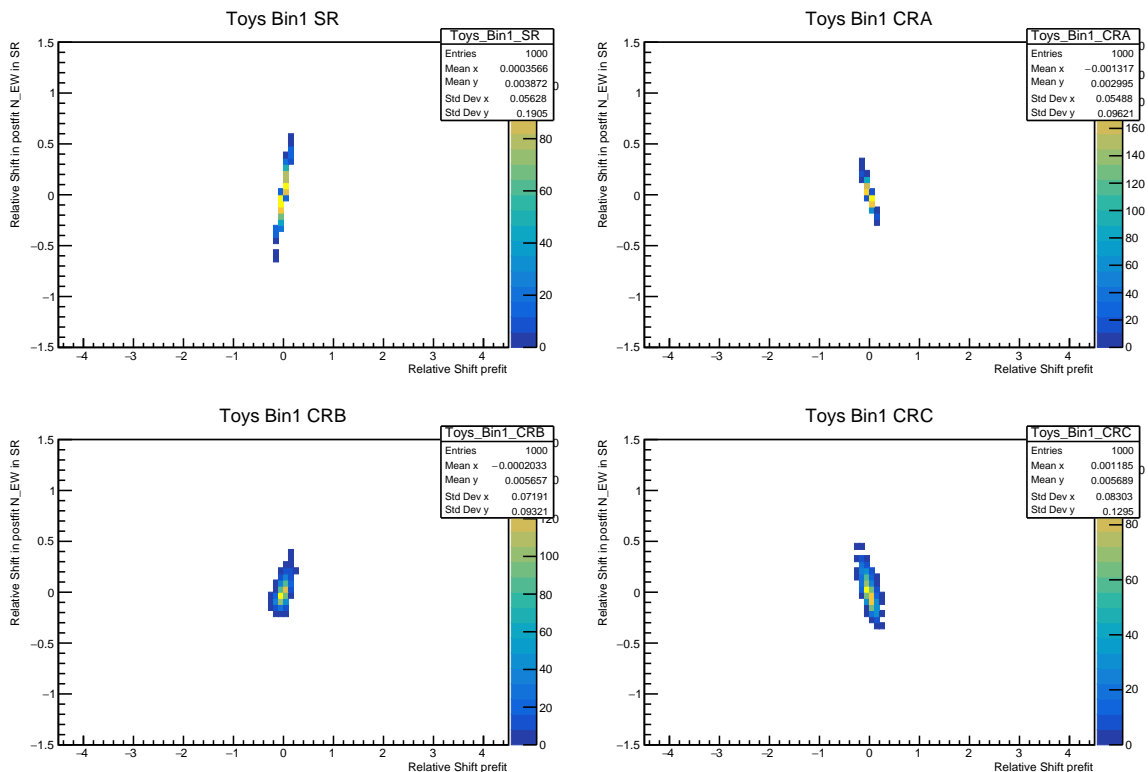
m_{jj} Asimov fluctuations, MG5 QCD in Asimov, MG5 QCD template

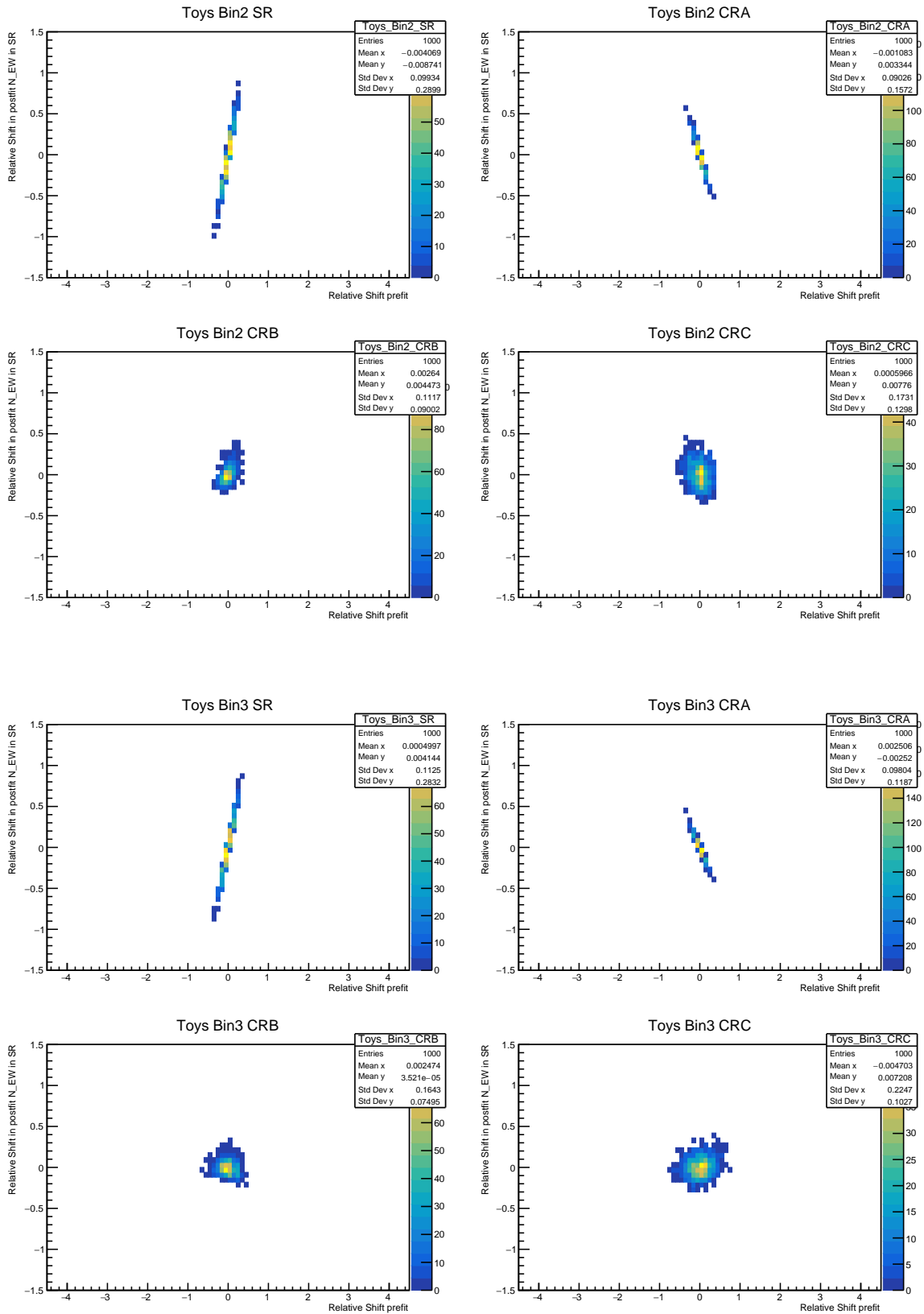


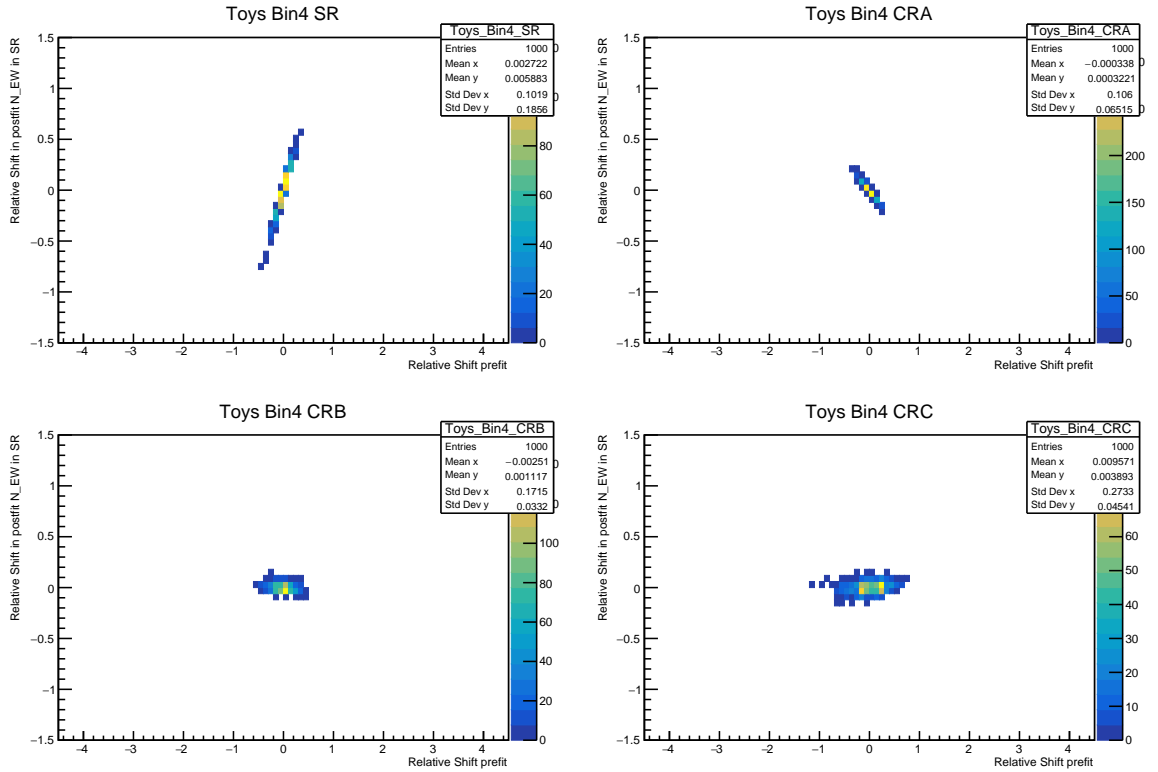




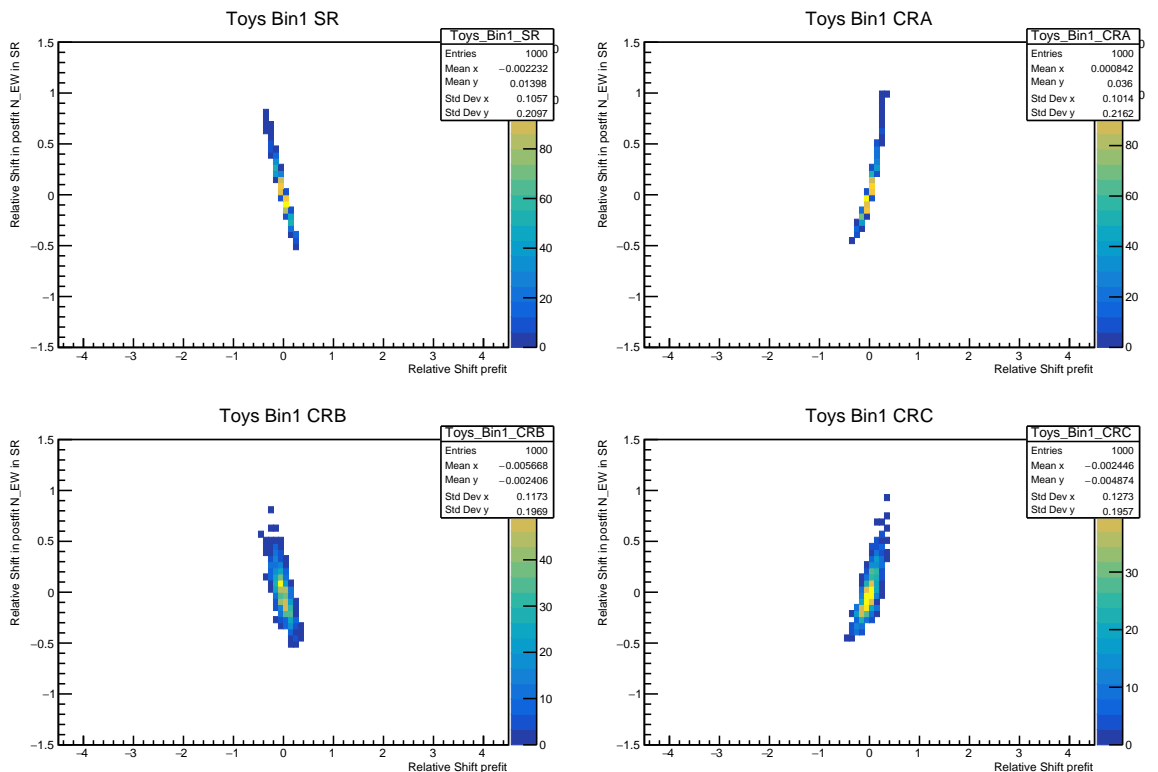
m_{jj} Asimov fluctuations, Sherpa-2.2.11 QCD in Asimov, MG5 QCD template

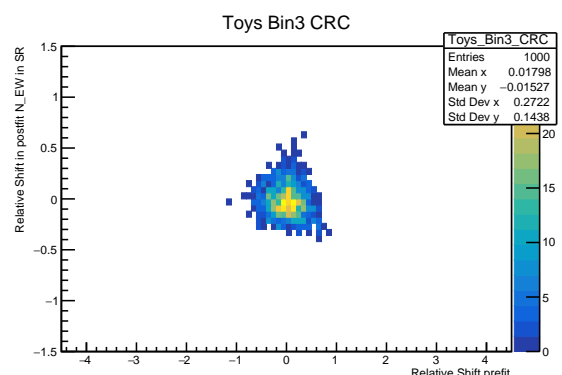
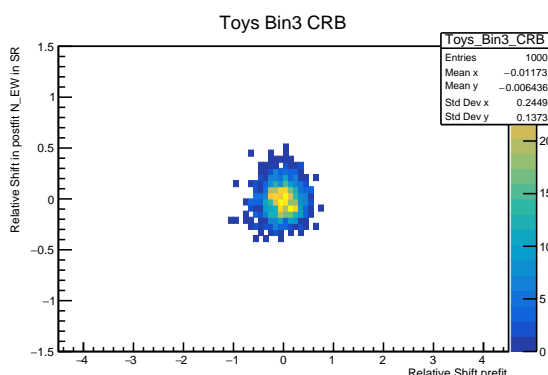
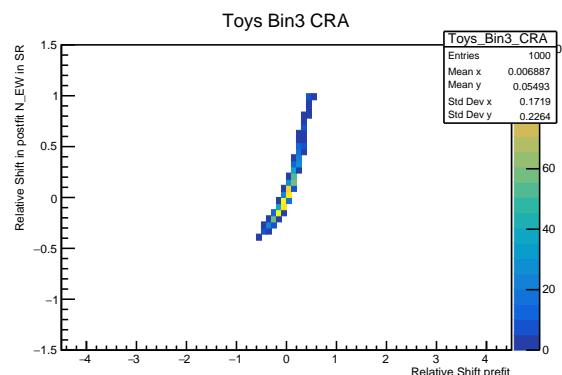
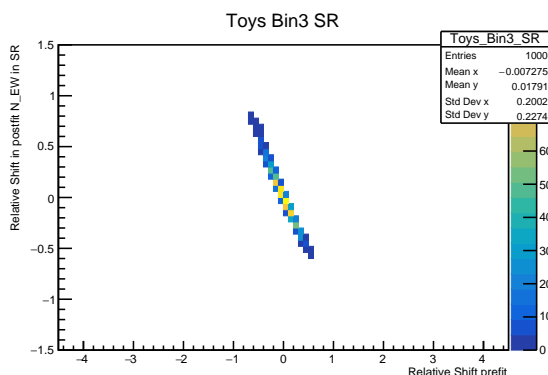
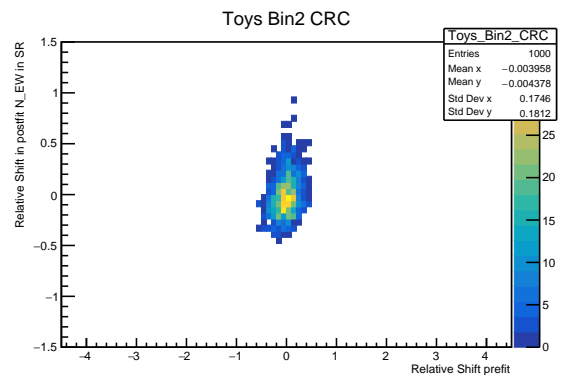
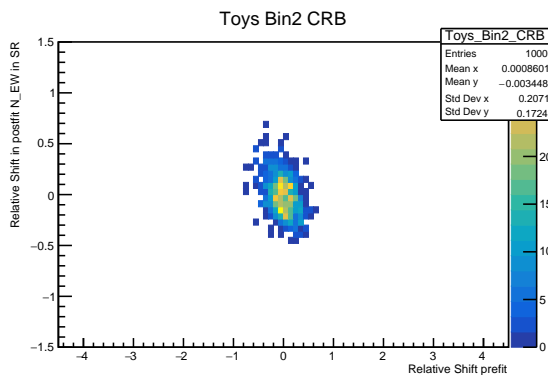
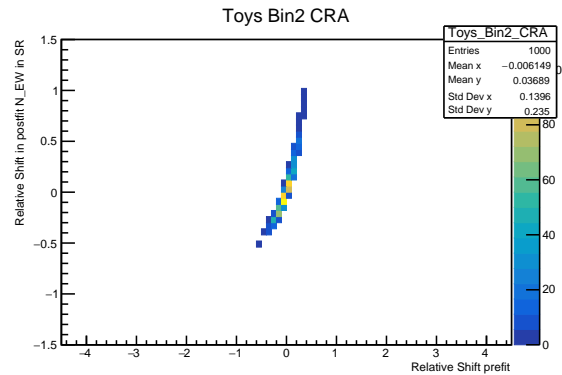
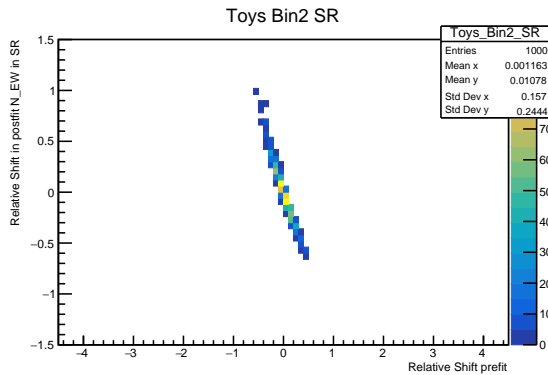


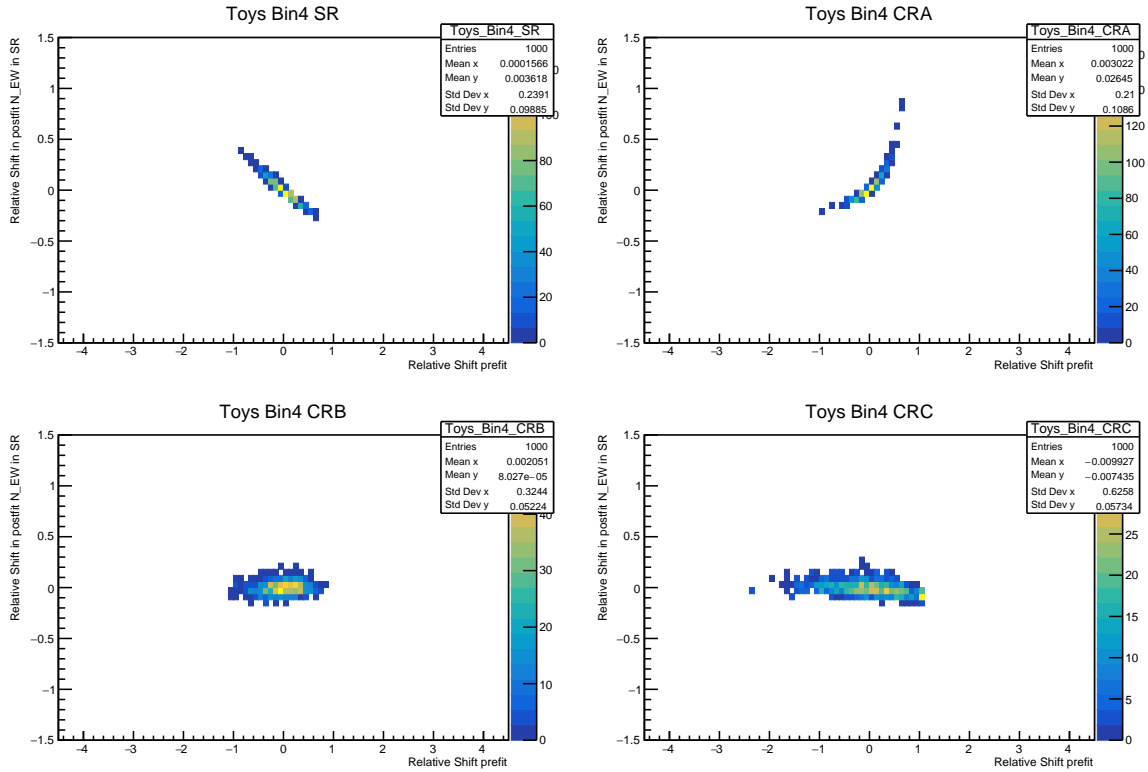




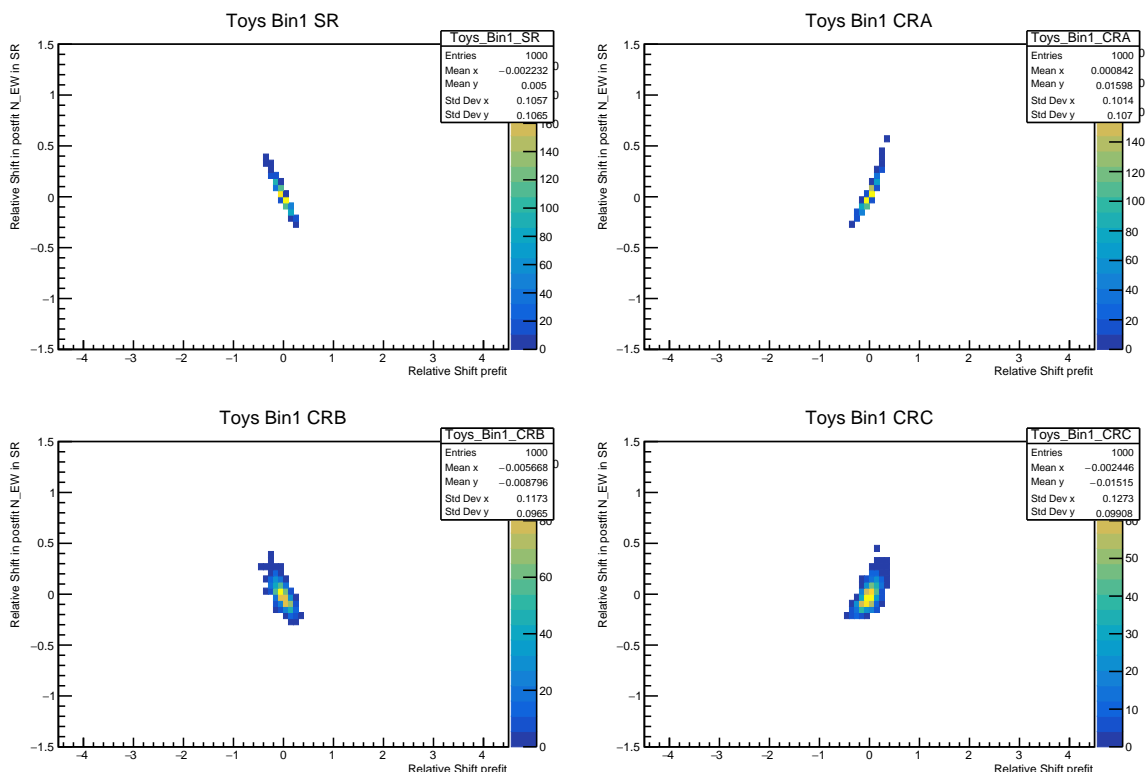
m_{jj} QCD template fluctuations, MG5 QCD in Asimov, MG5 QCD template

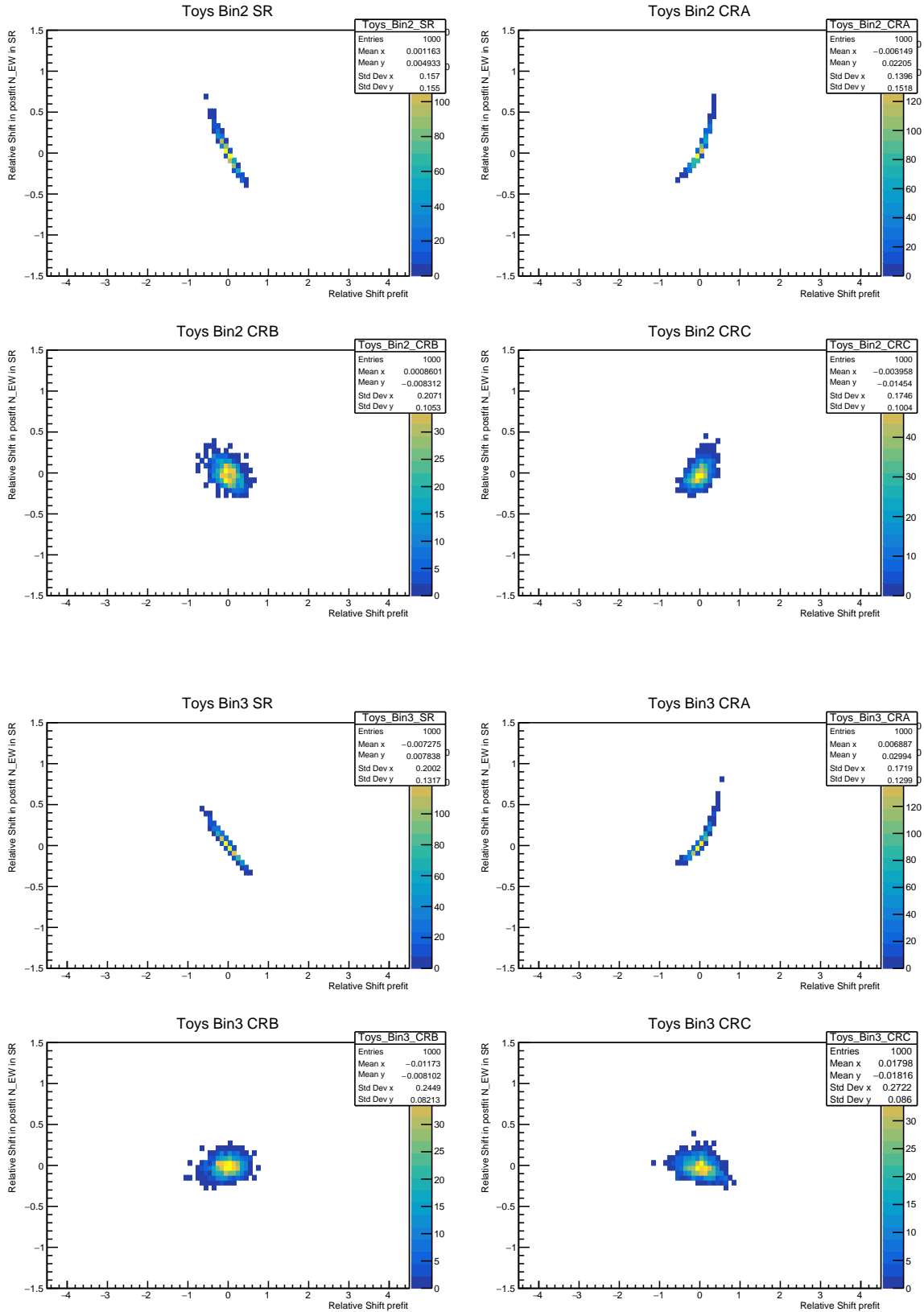


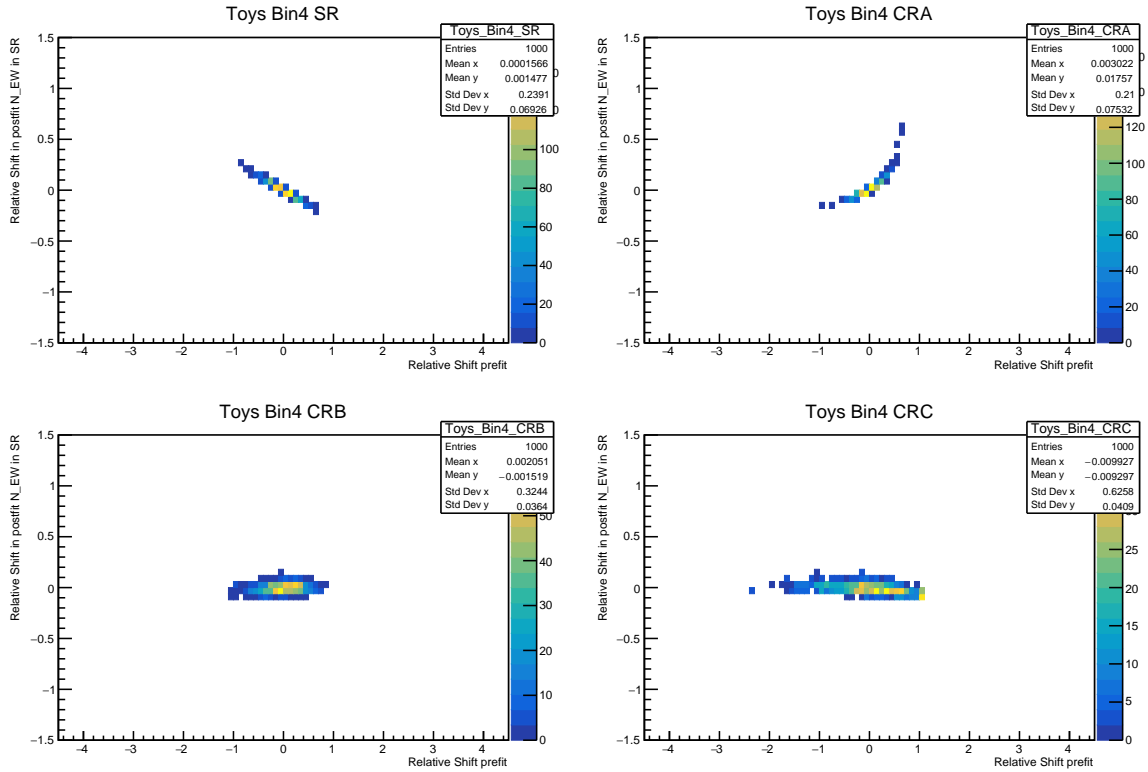




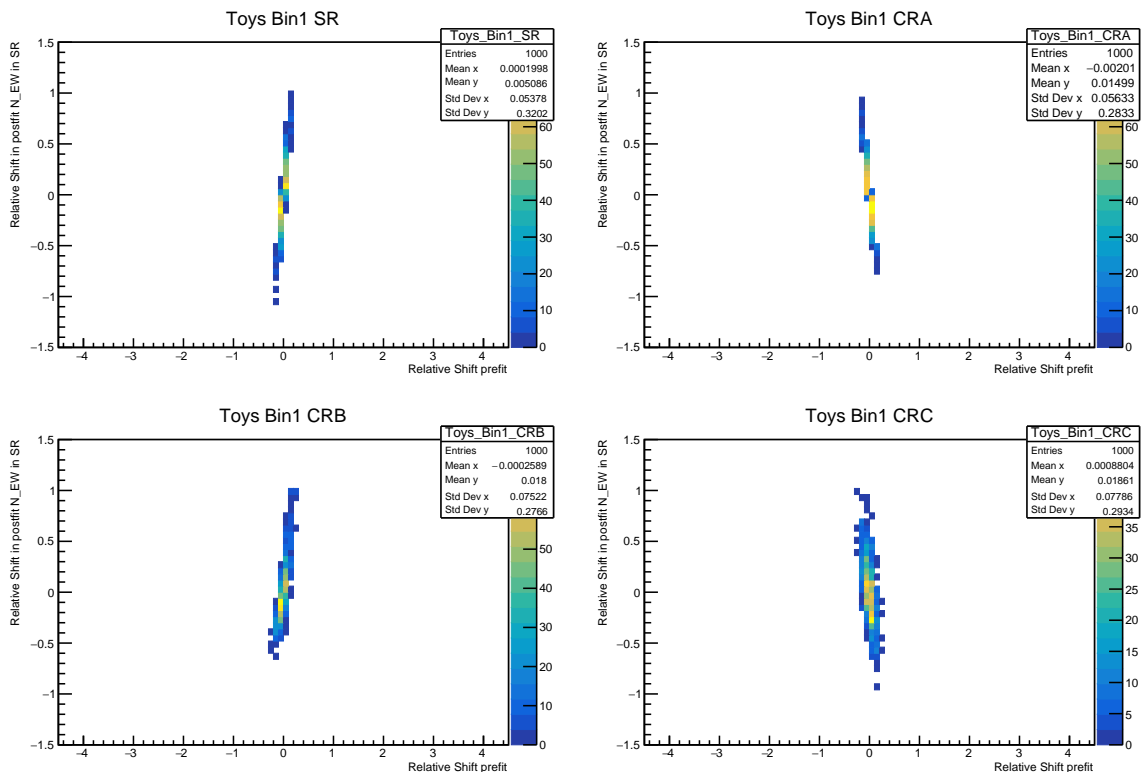
m_{jj} QCD template fluctuations, Sherpa-2.2.11 QCD in Asimov, MG5 QCD template

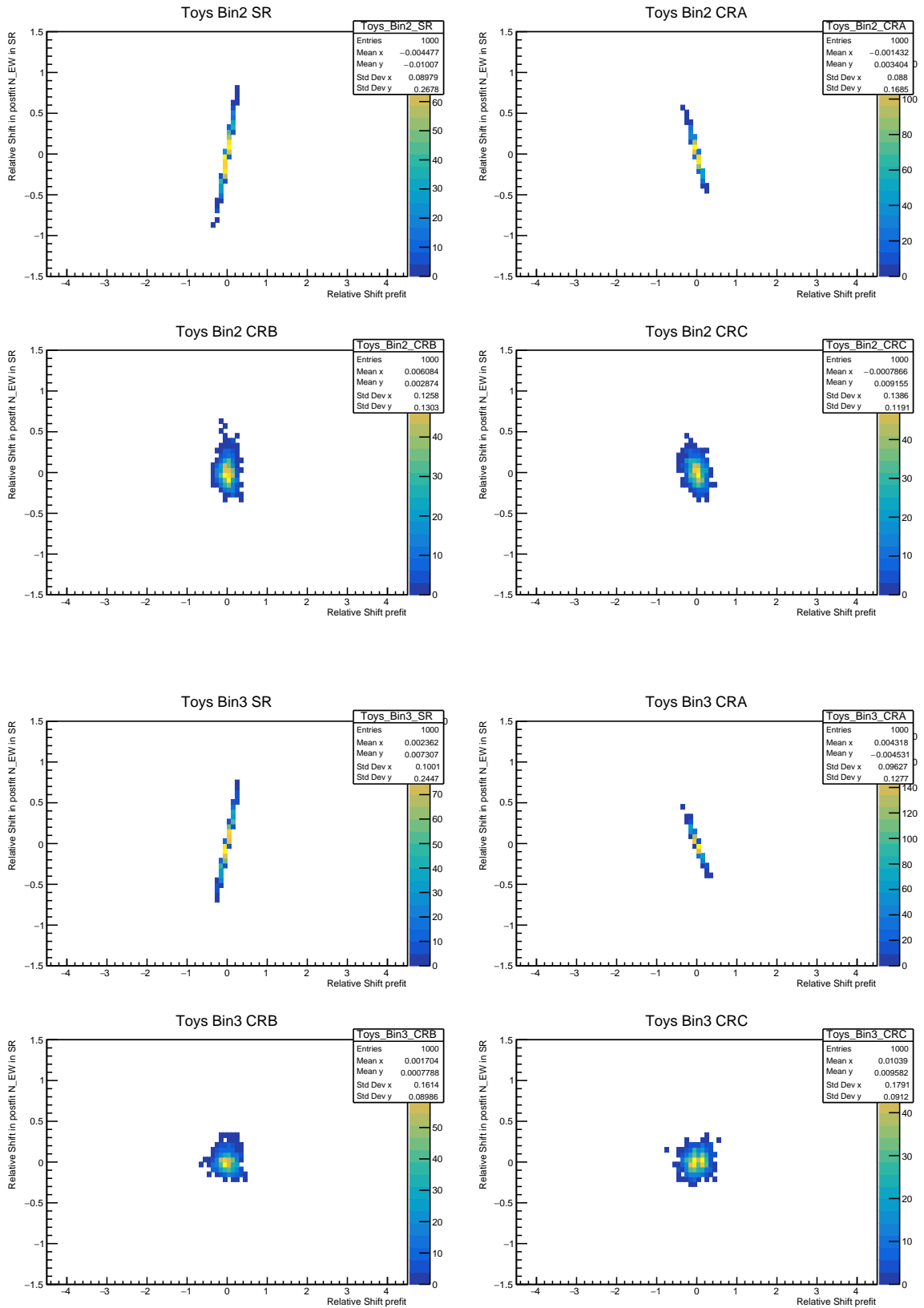


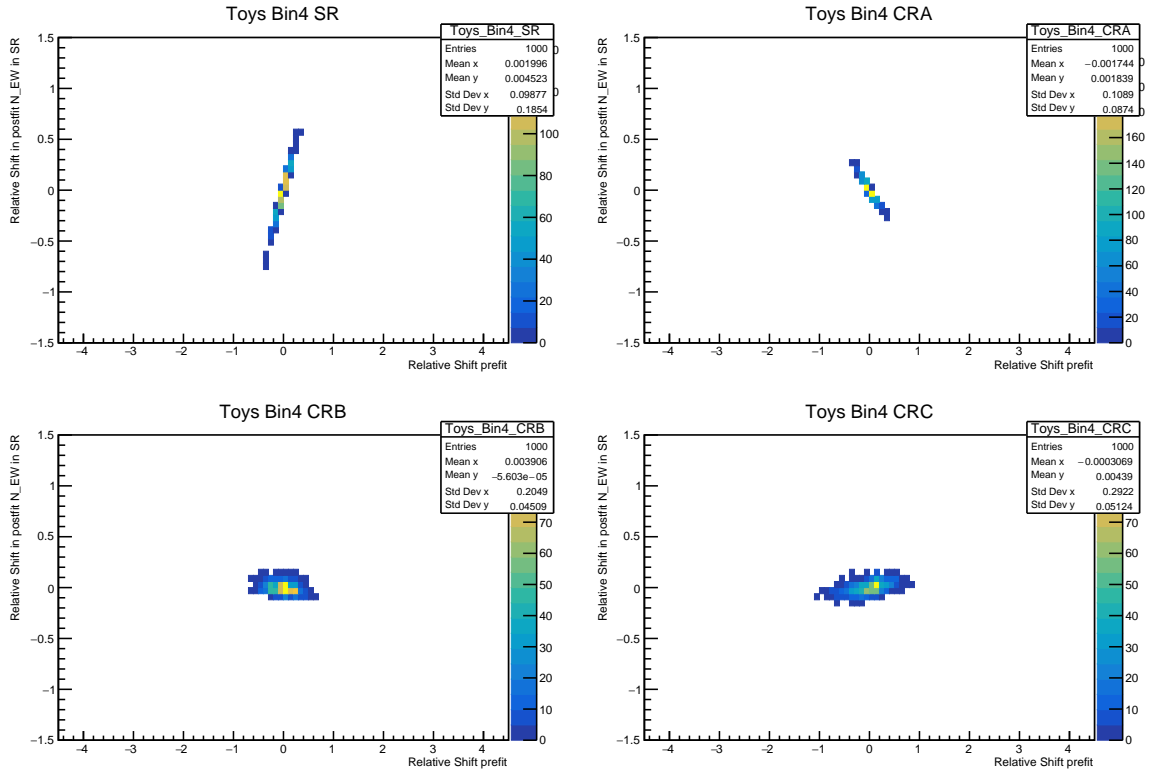




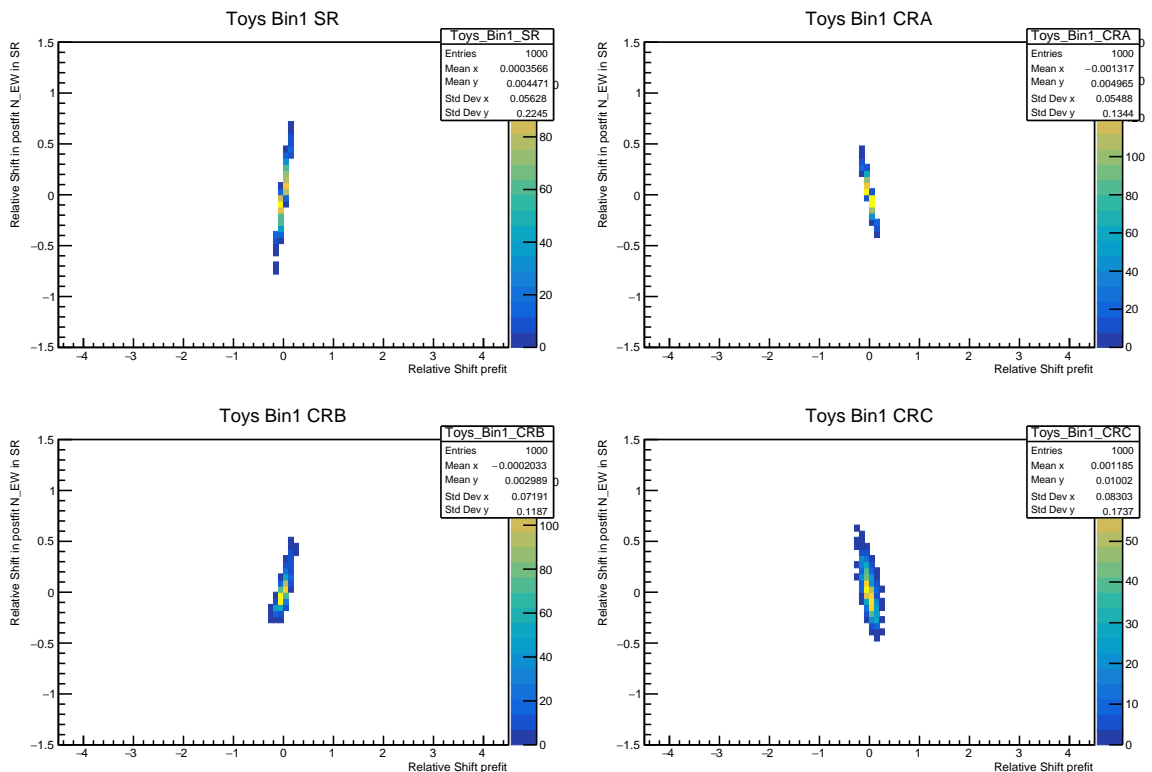
m_{jj} Asimov fluctuations, MG5 QCD in Asimov, Sherpa-2.2.11 QCD template

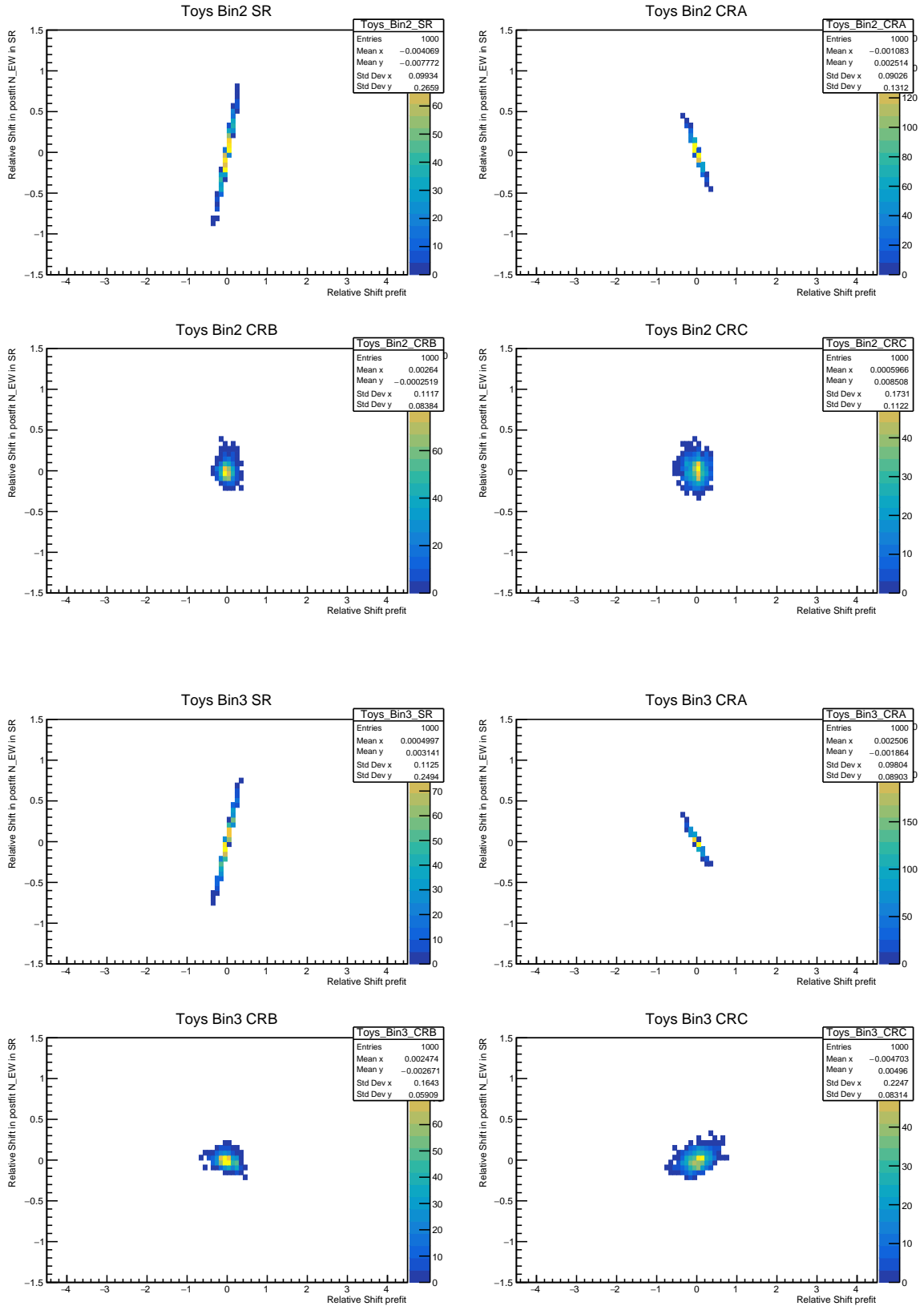


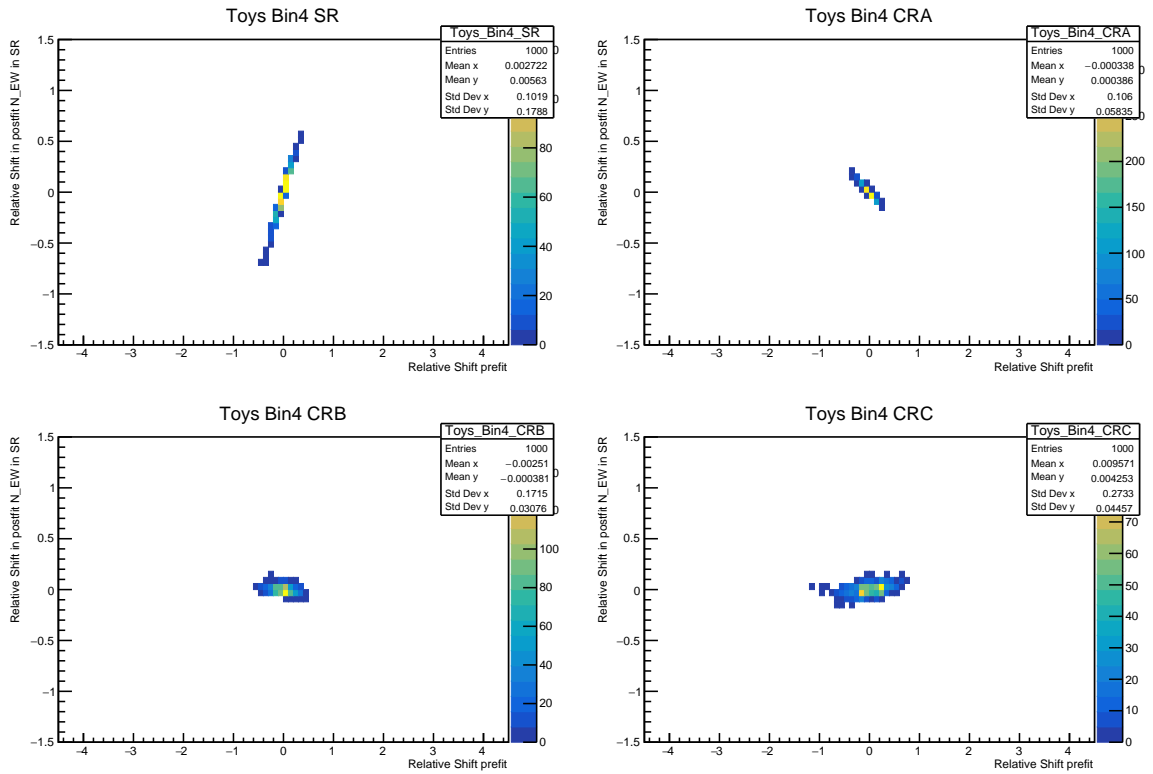




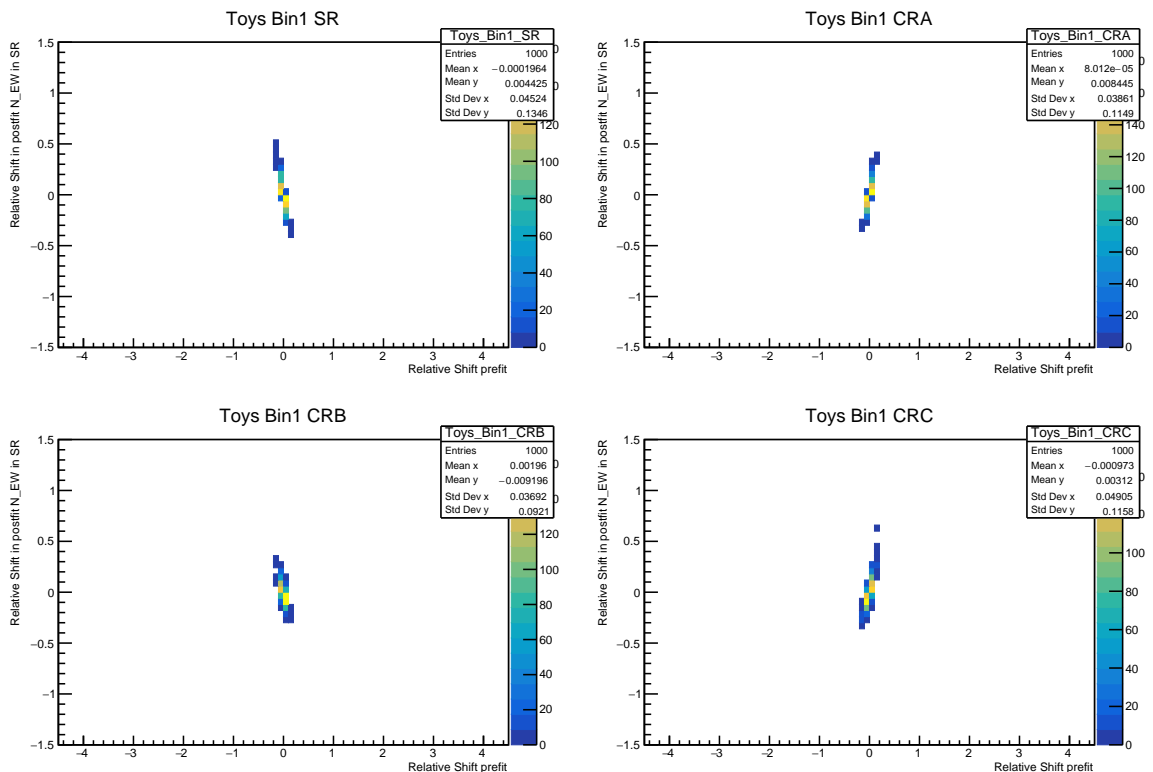
m_{jj} Asimov fluctuations, Sherpa-2.2.11 QCD in Asimov, Sherpa-2.2.11 QCD template

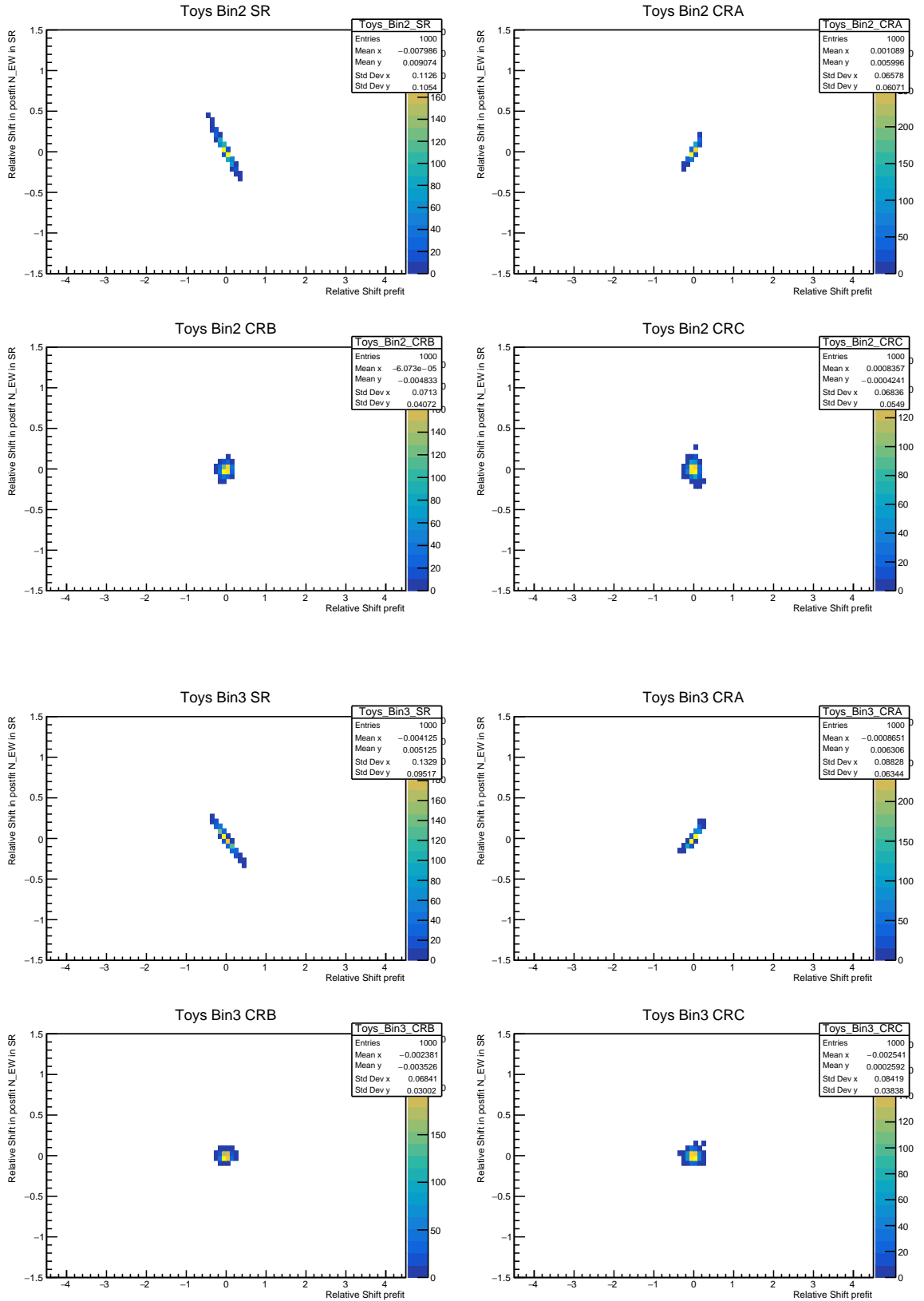


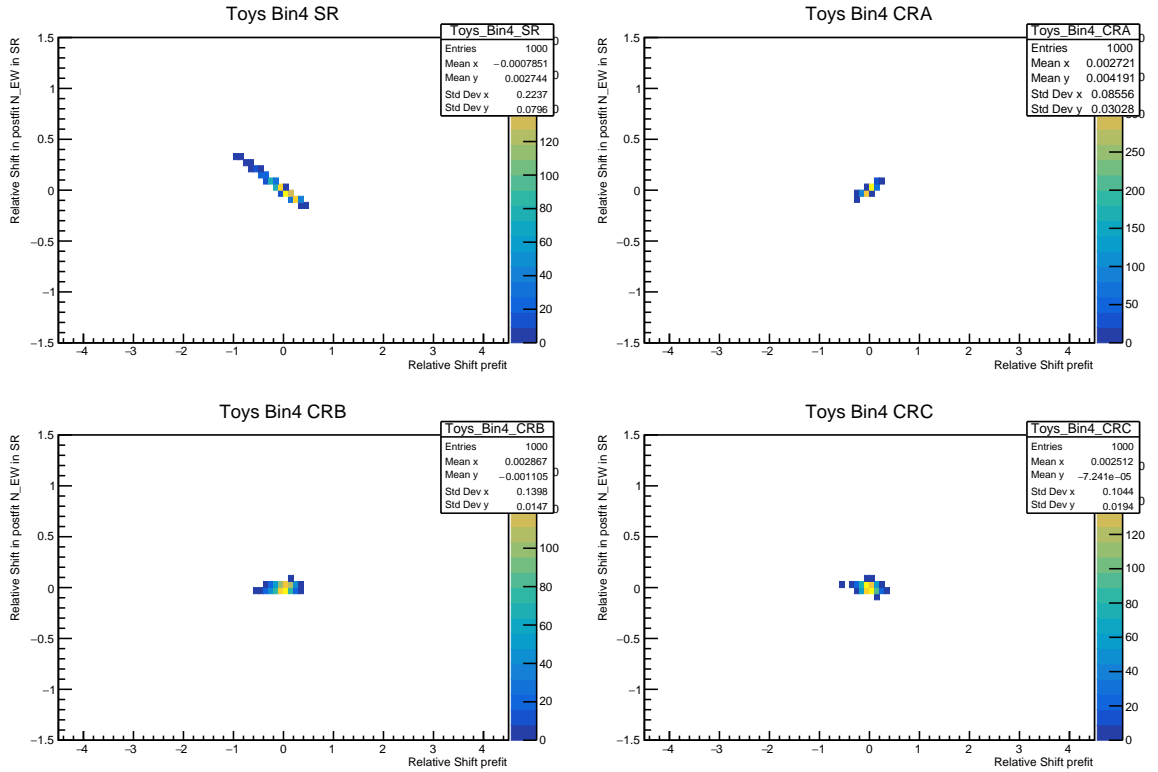




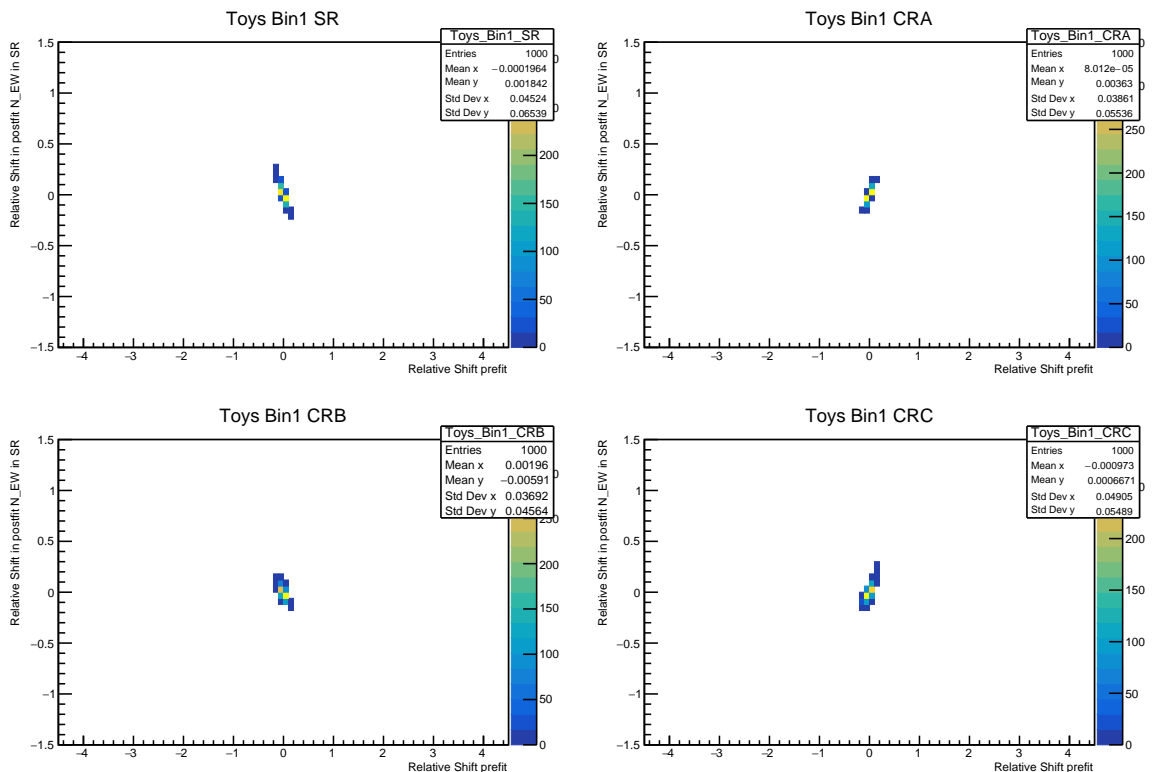
m_{jj} QCD template fluctuations, MG5 QCD in Asimov, Sherpa-2.2.11 QCD template

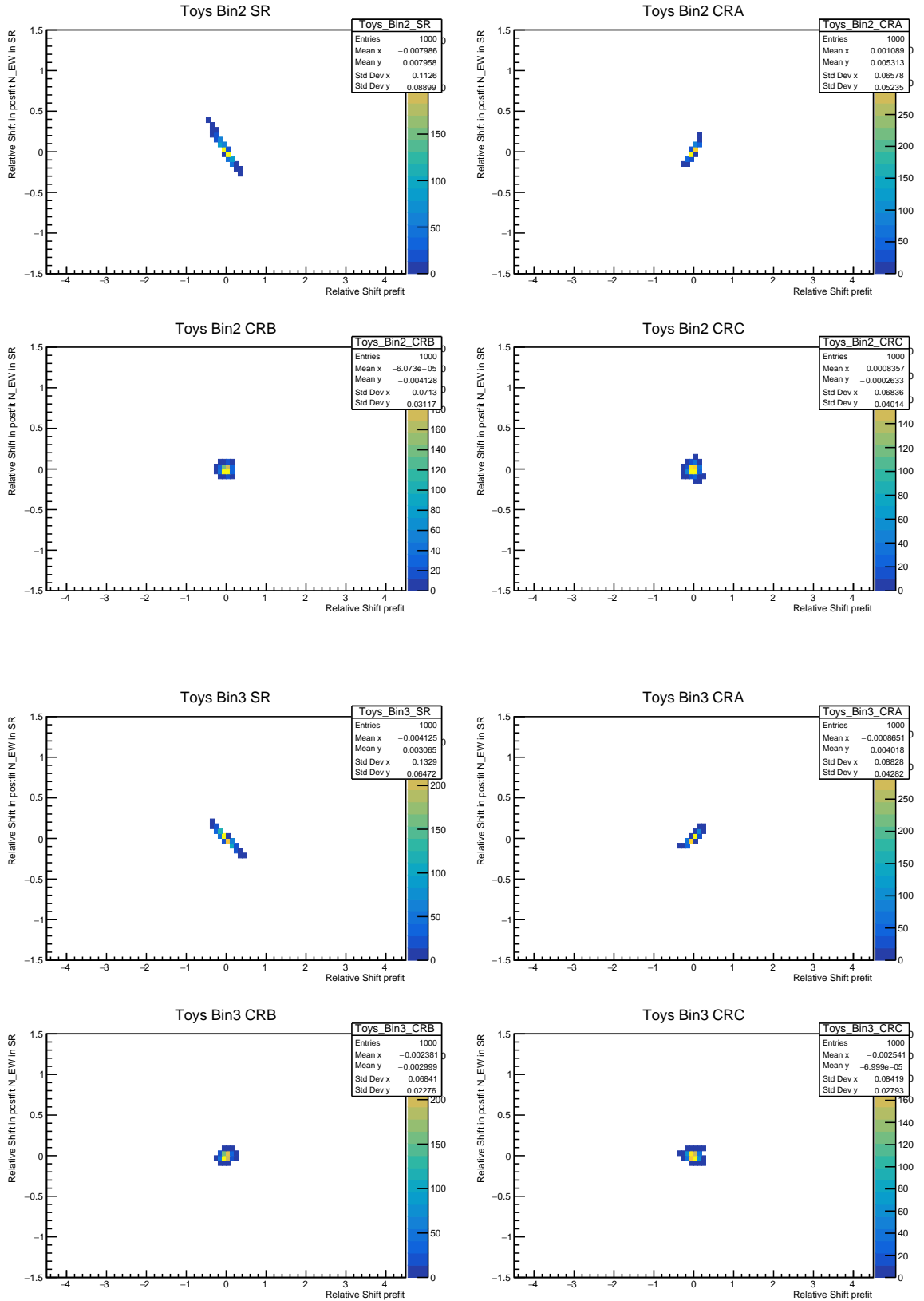


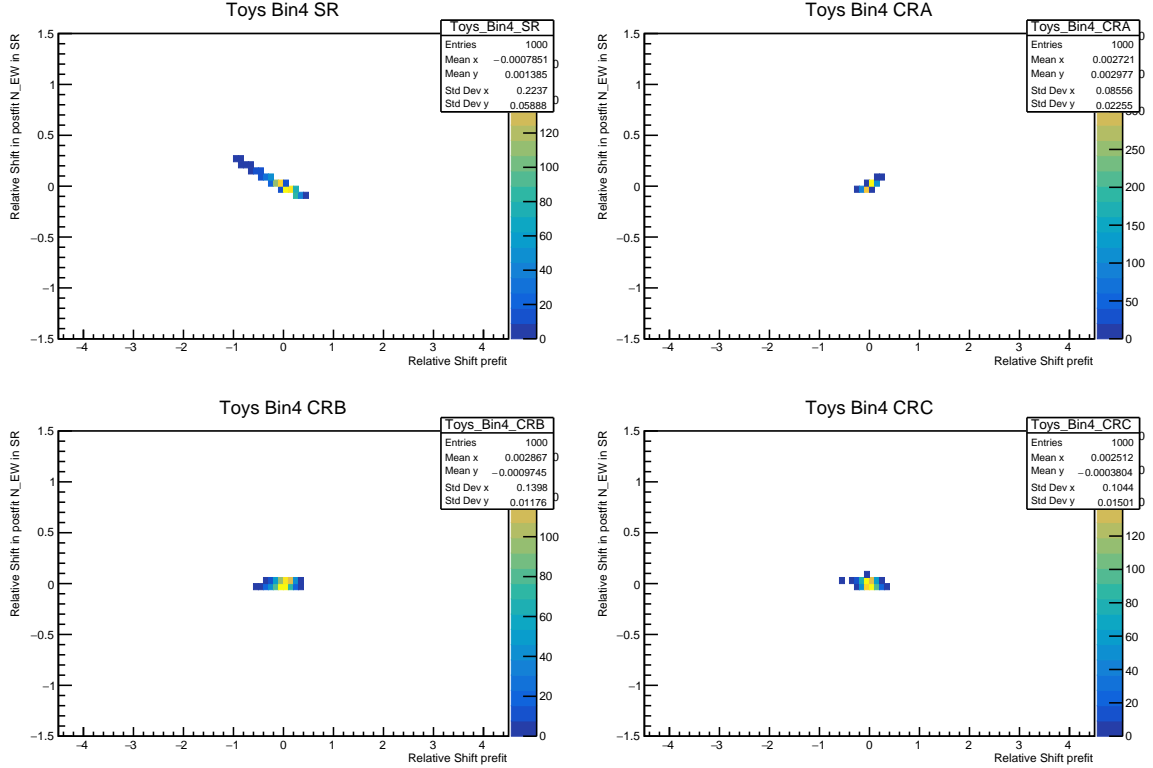




m_{jj} QCD template fluctuations, Sherpa-2.2.11 QCD in Asimov, Sherpa-2.2.11 QCD template

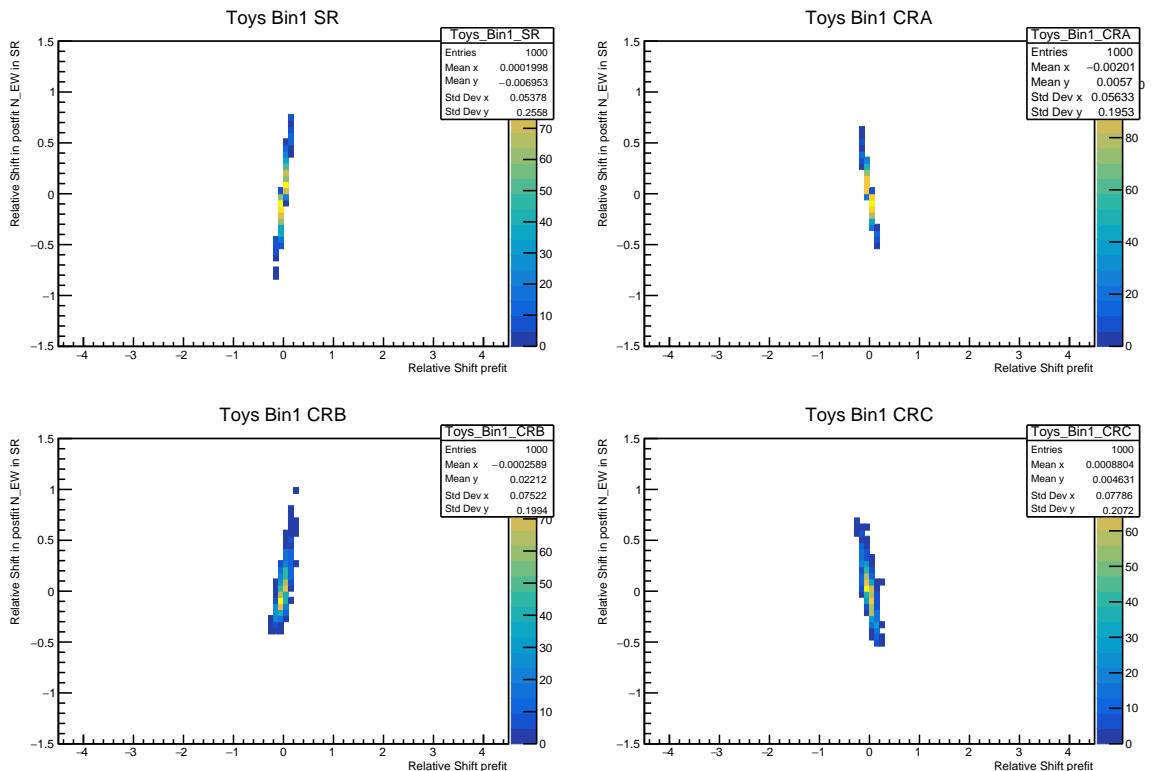


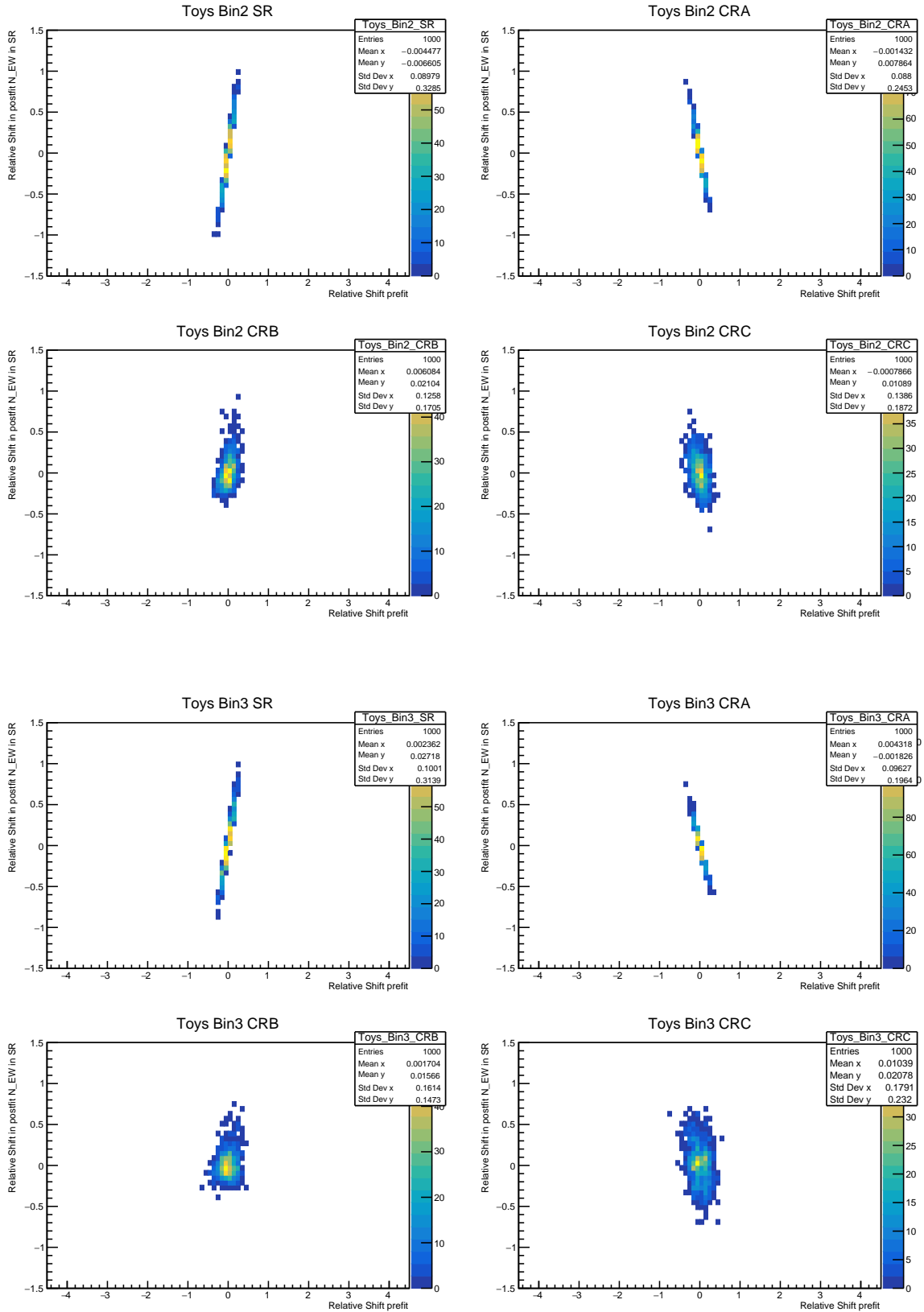


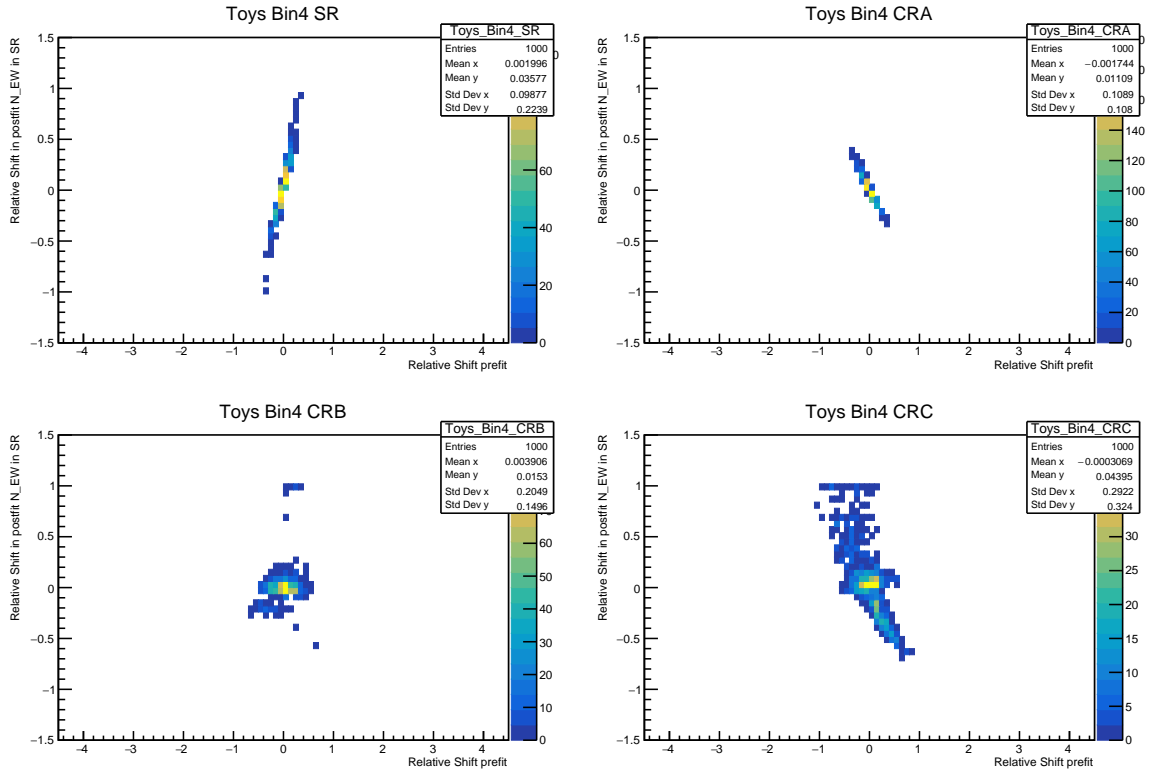


$$\mathbf{B.1.2} \quad f(x_i) = mx_i + c$$

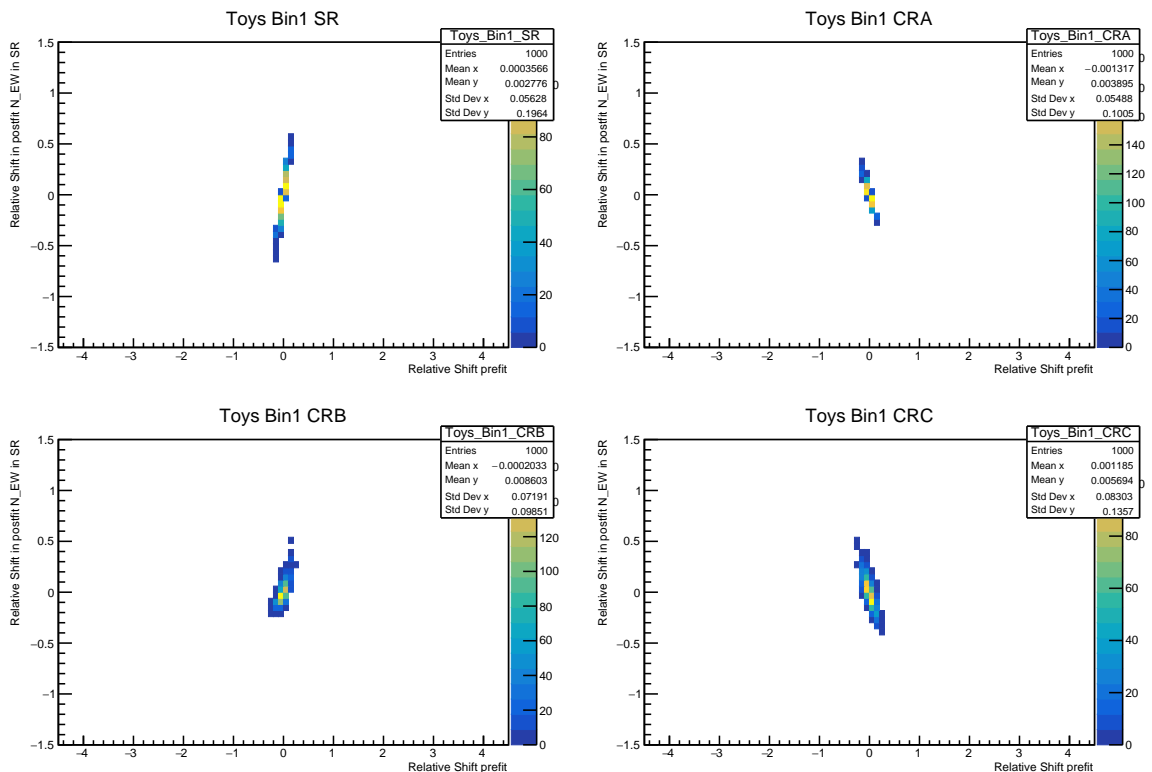
m_{jj} Asimov fluctuations, MG5 QCD in Asimov, MG5 QCD template

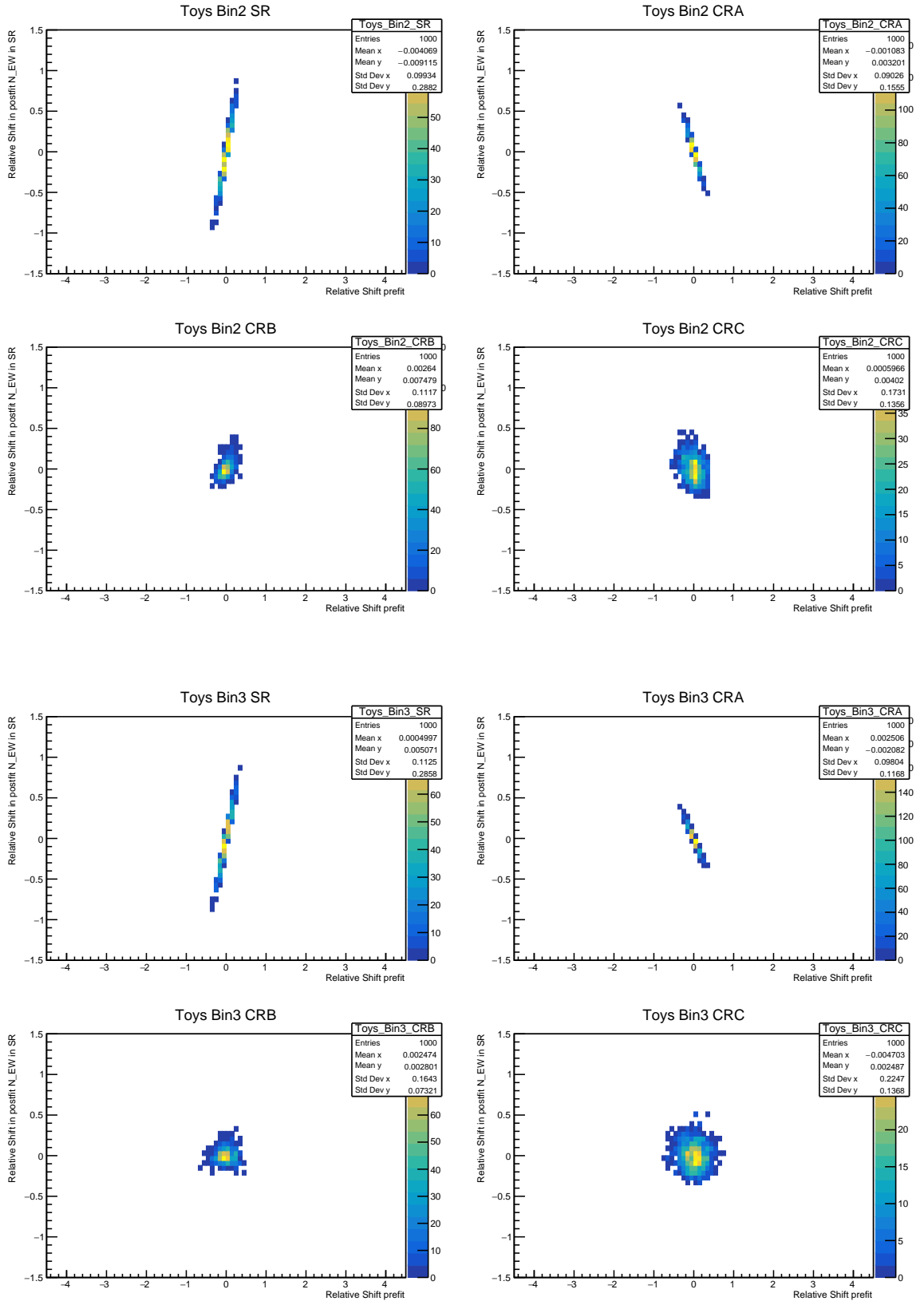


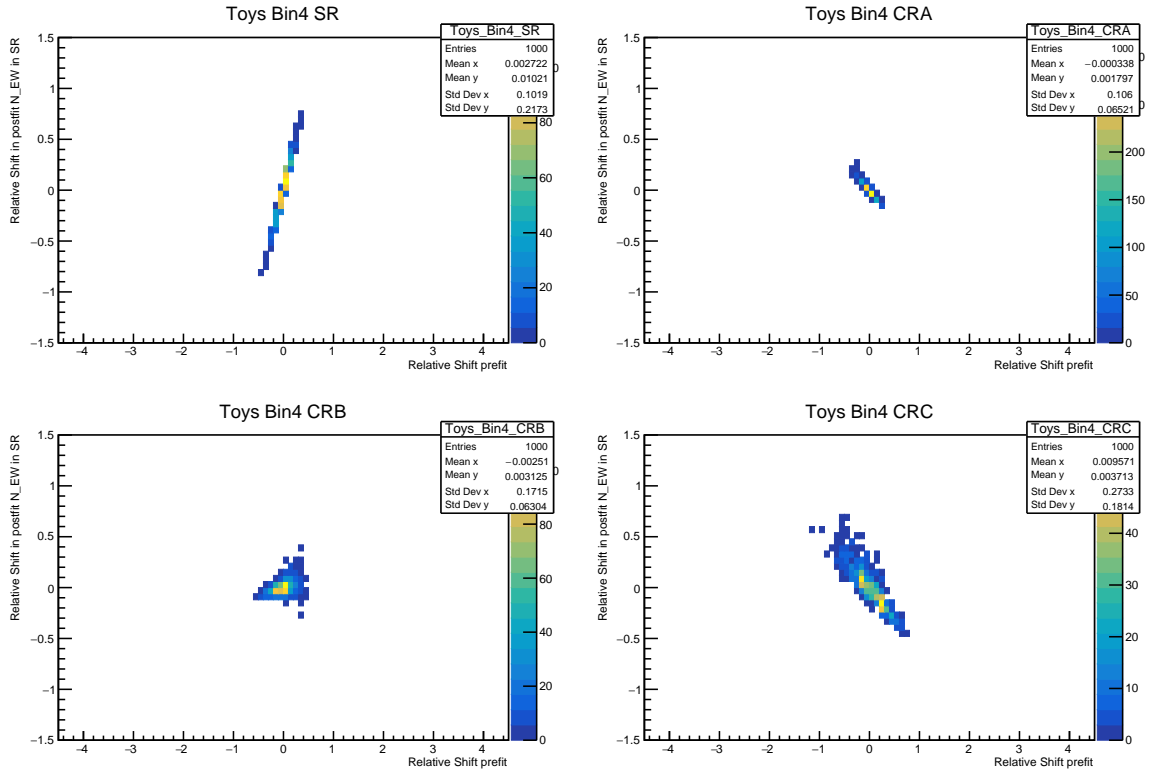




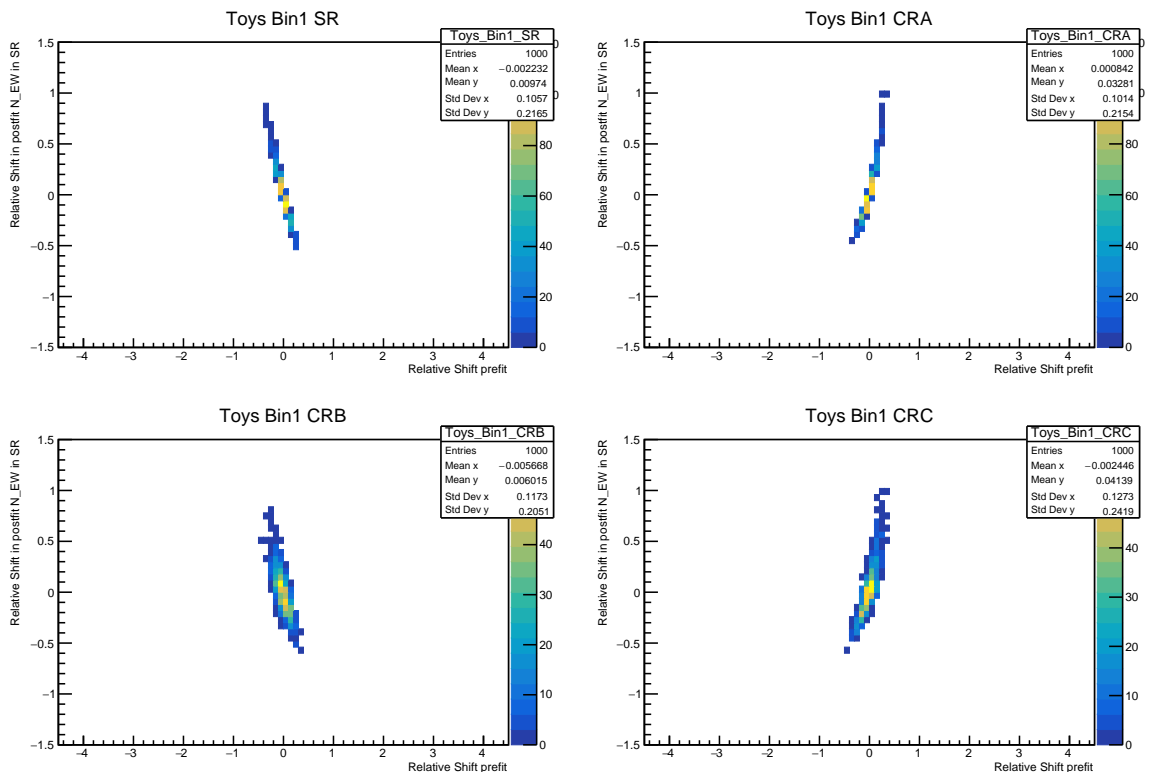
m_{jj} Asimov fluctuations, Sherpa-2.2.11 QCD in Asimov, MG5 QCD template

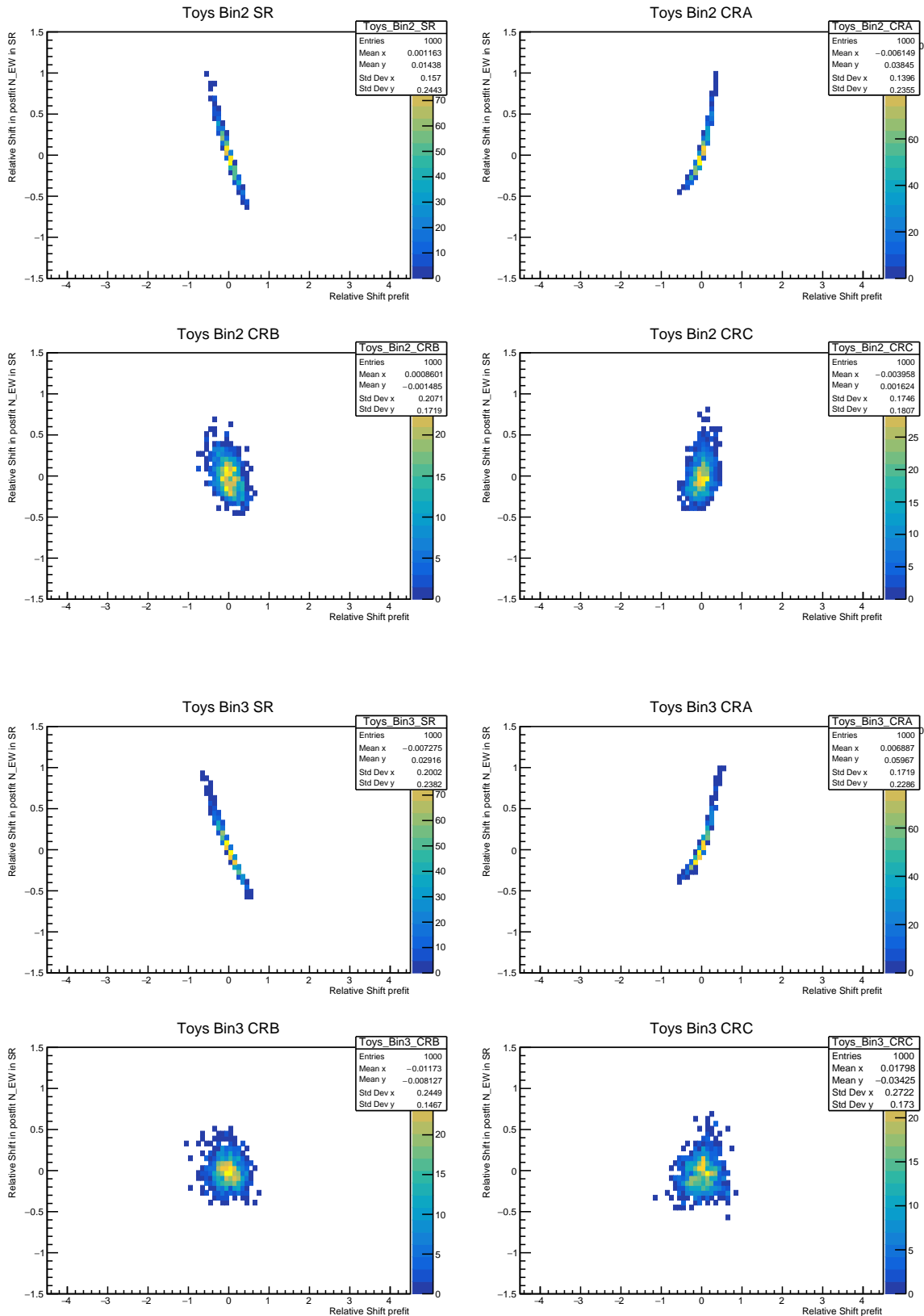


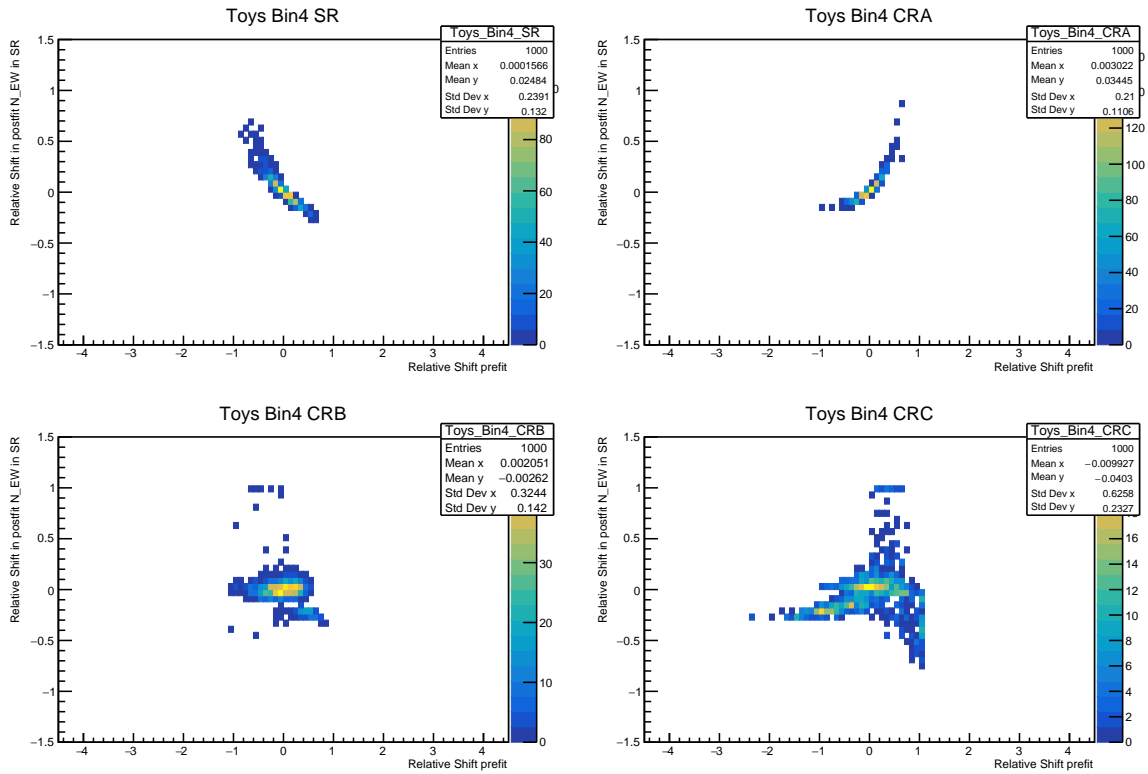




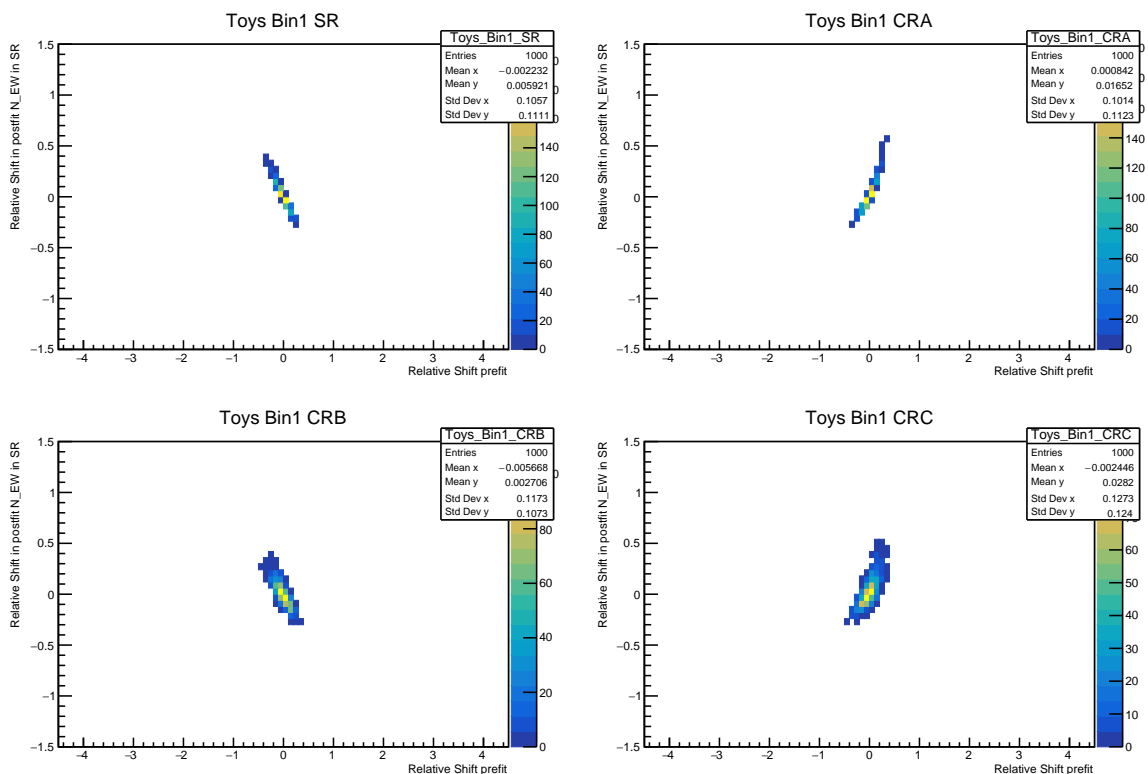
m_{jj} QCD template fluctuations, MG5 QCD in Asimov, MG5 QCD template

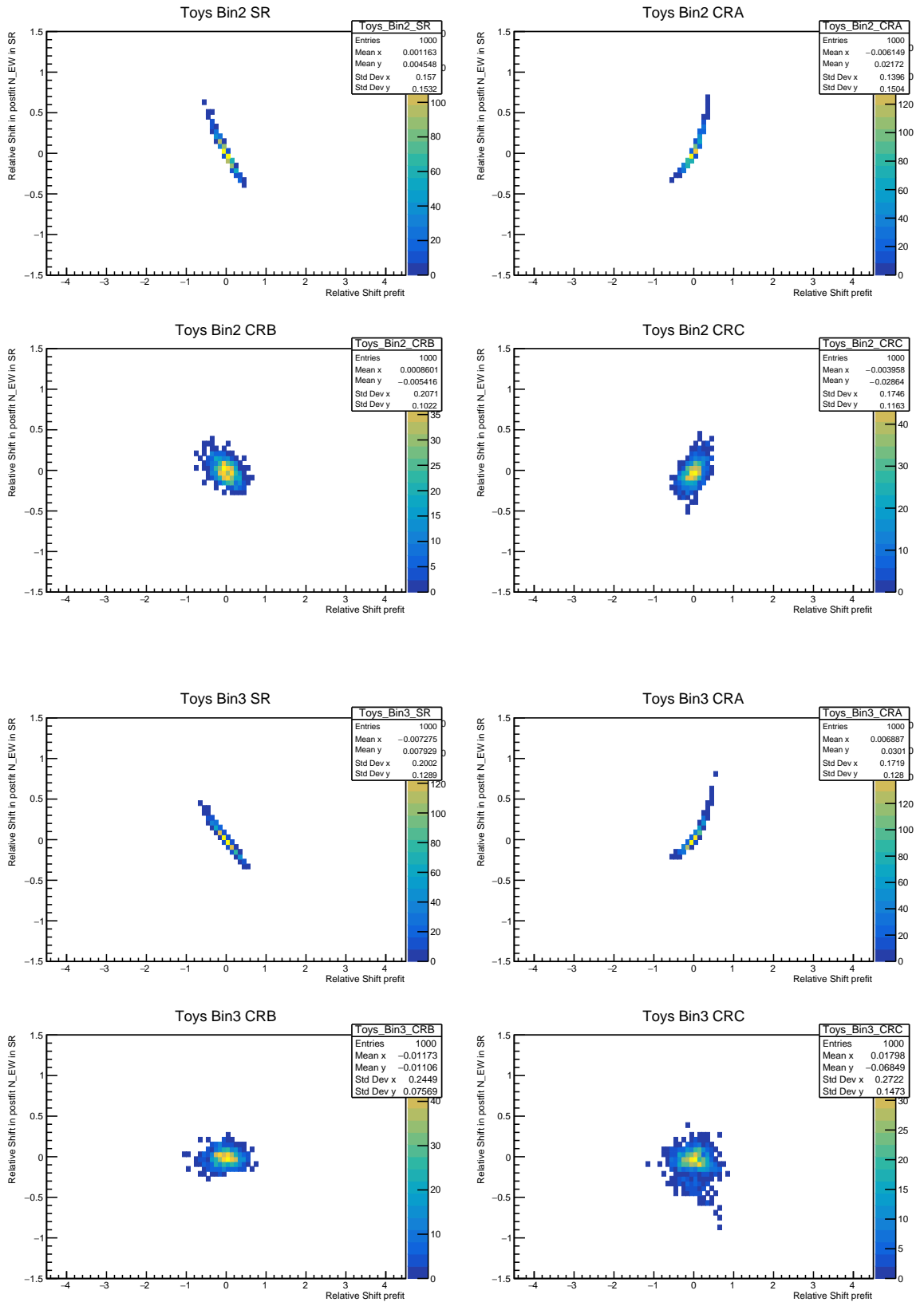


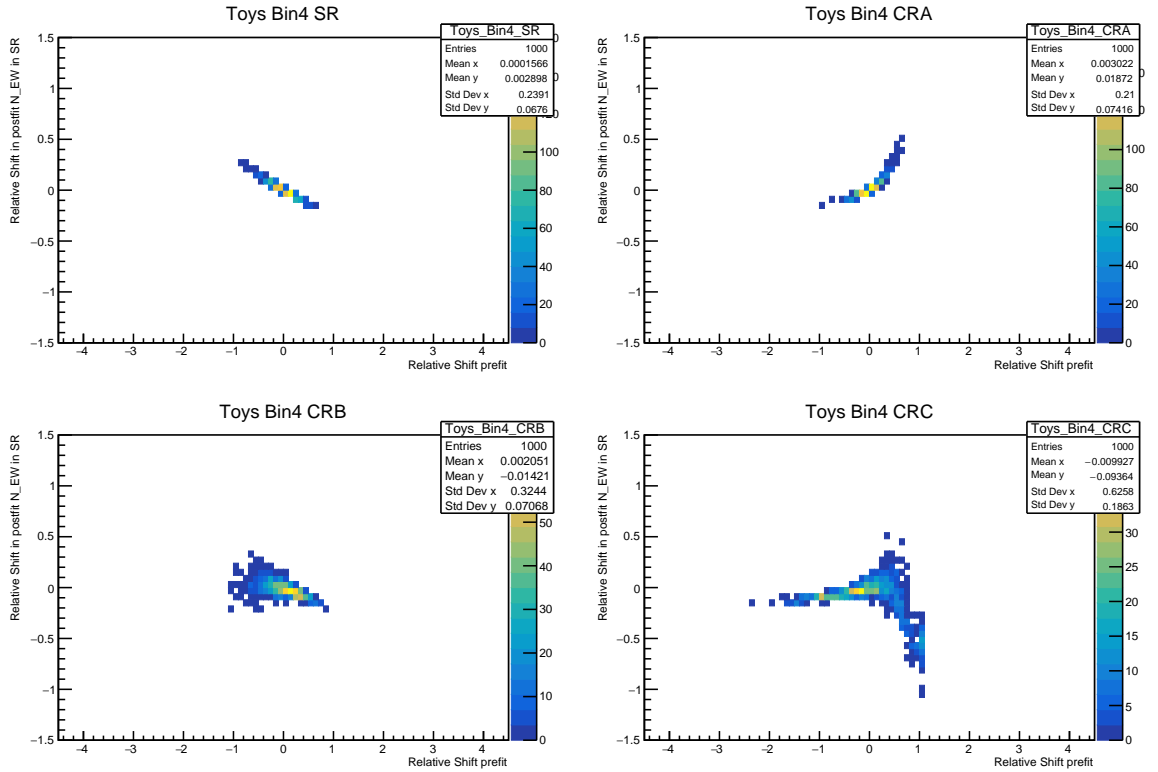




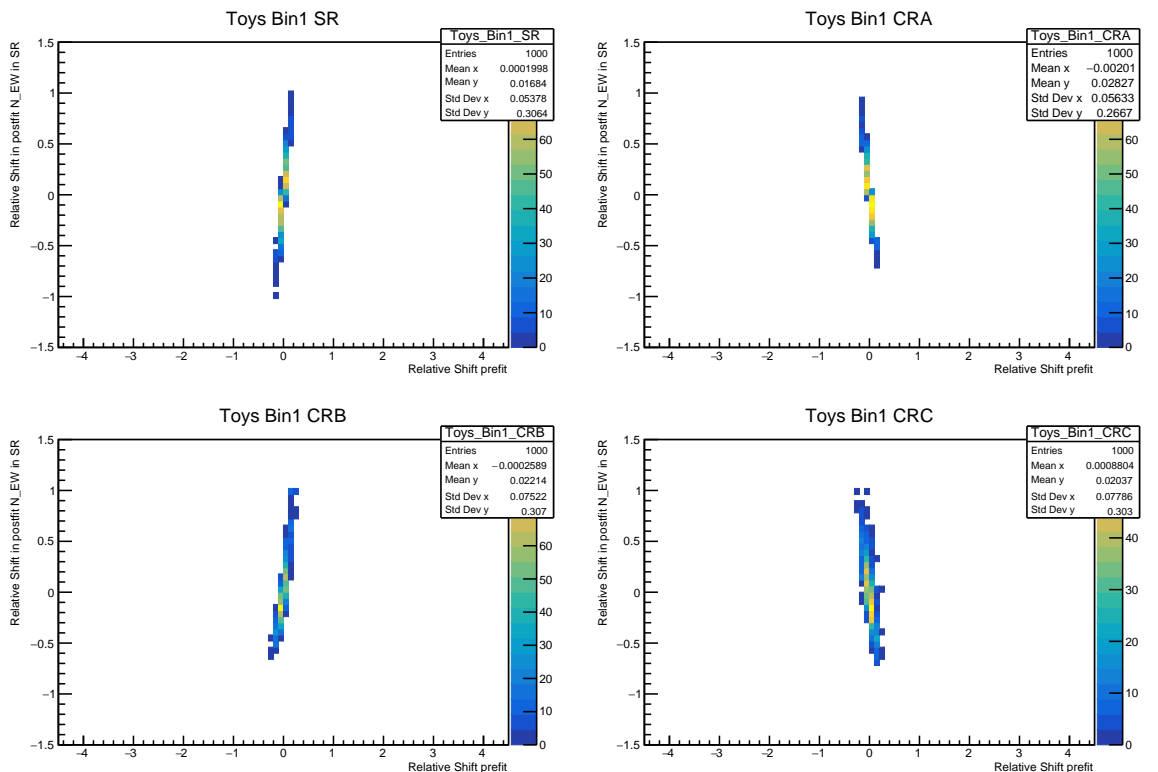
m_{jj} QCD template fluctuations, Sherpa-2.2.11 QCD in Asimov, MG5 QCD template

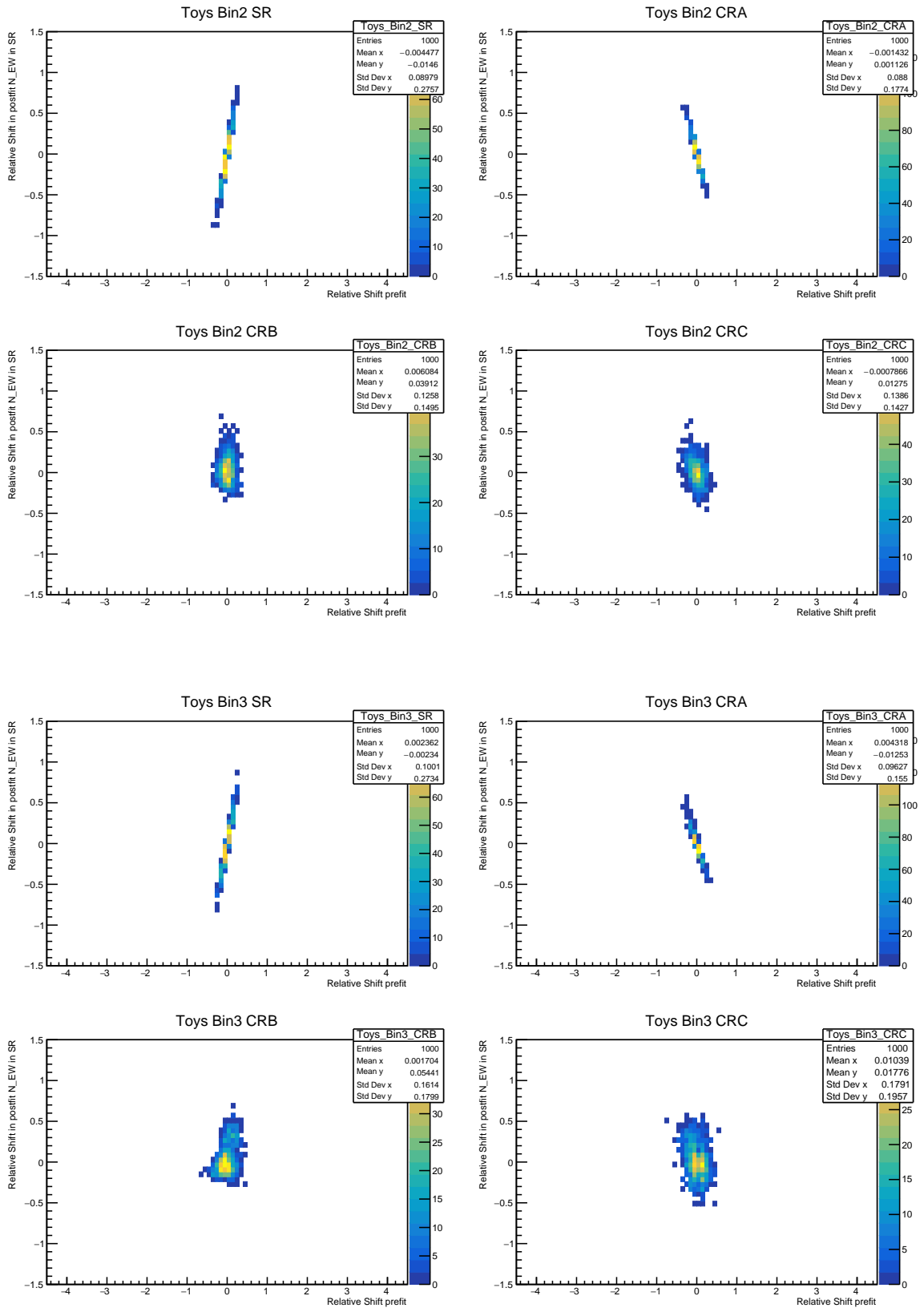


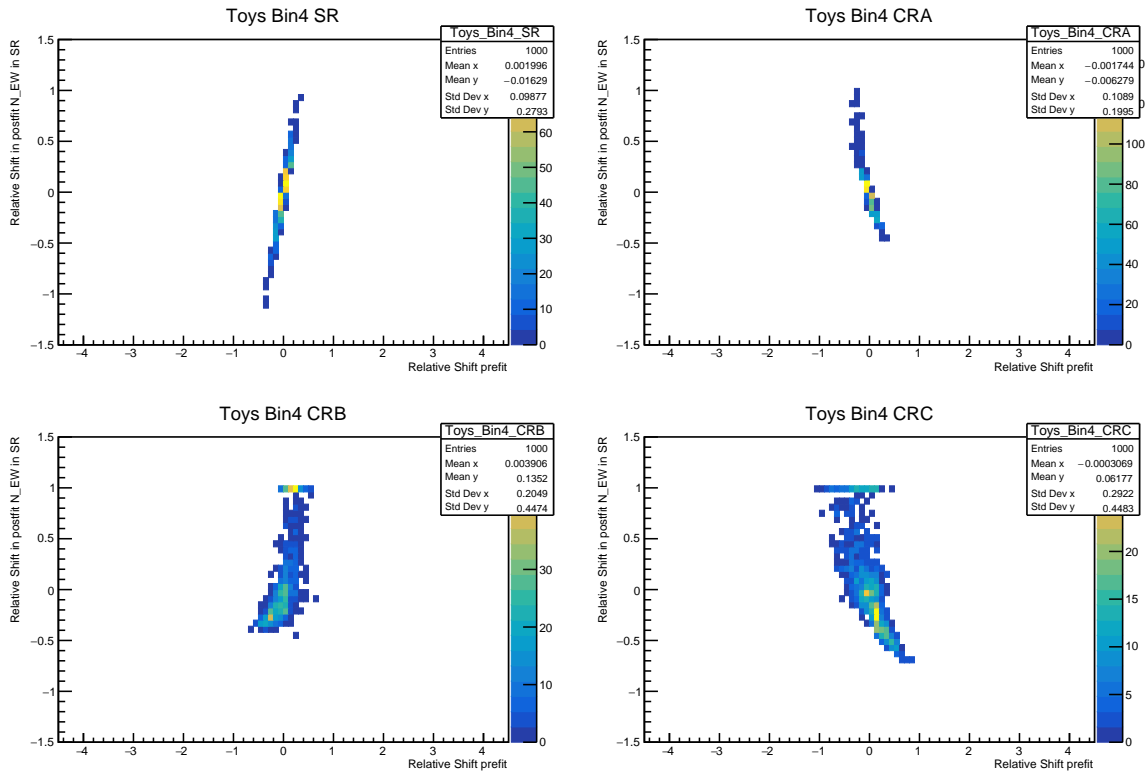




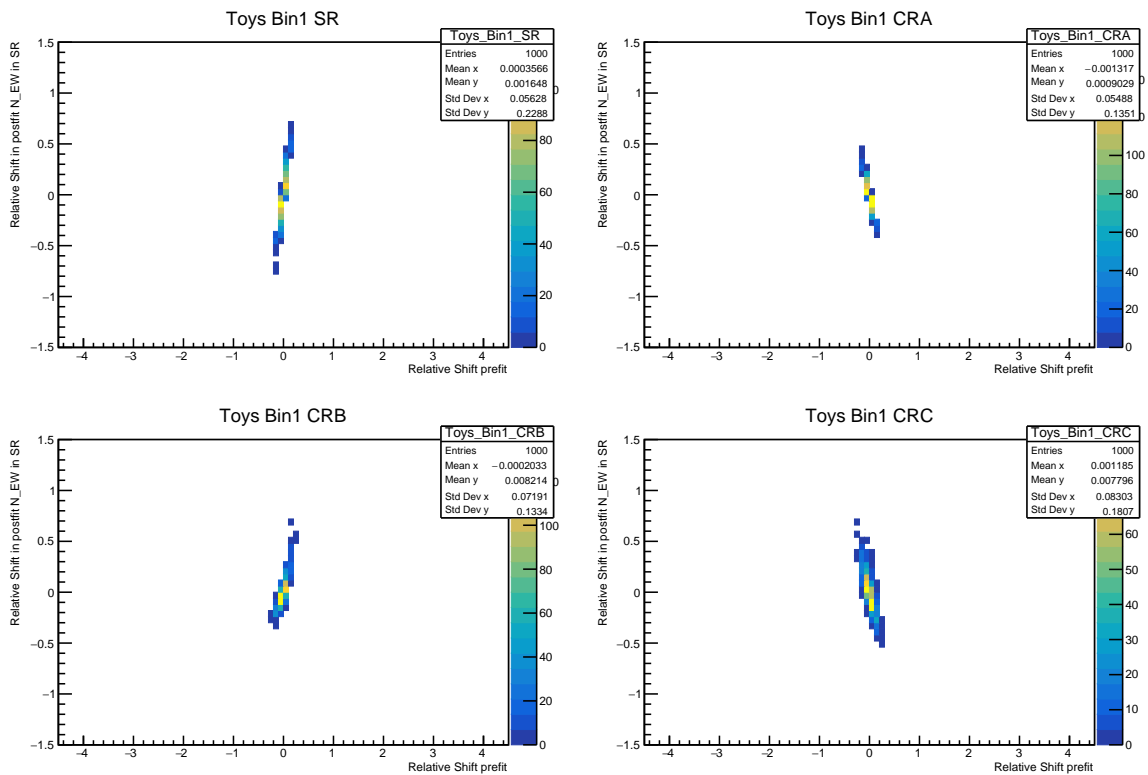
m_{jj} Asimov fluctuations, MG5 QCD in Asimov, Sherpa-2.2.11 QCD template

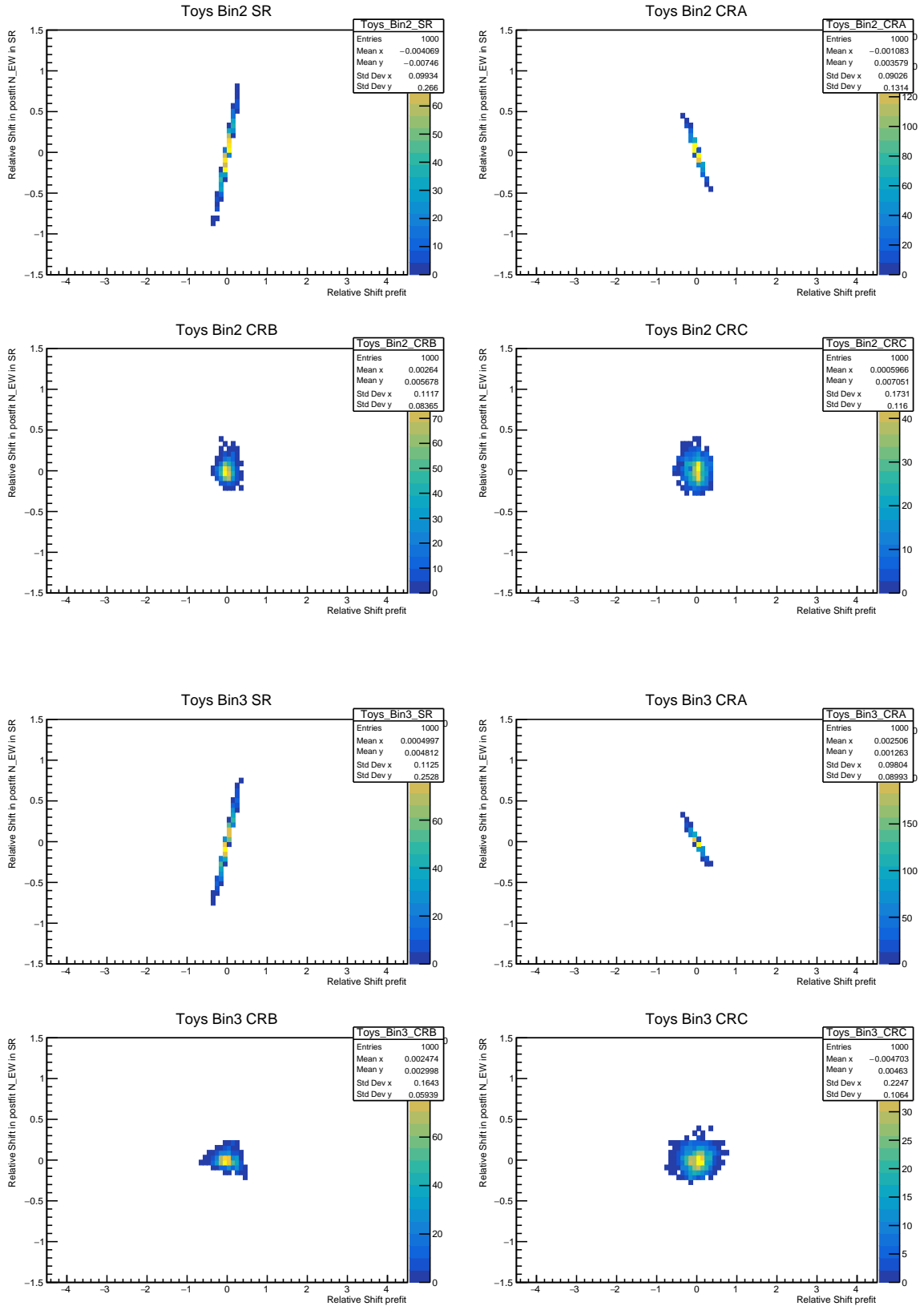


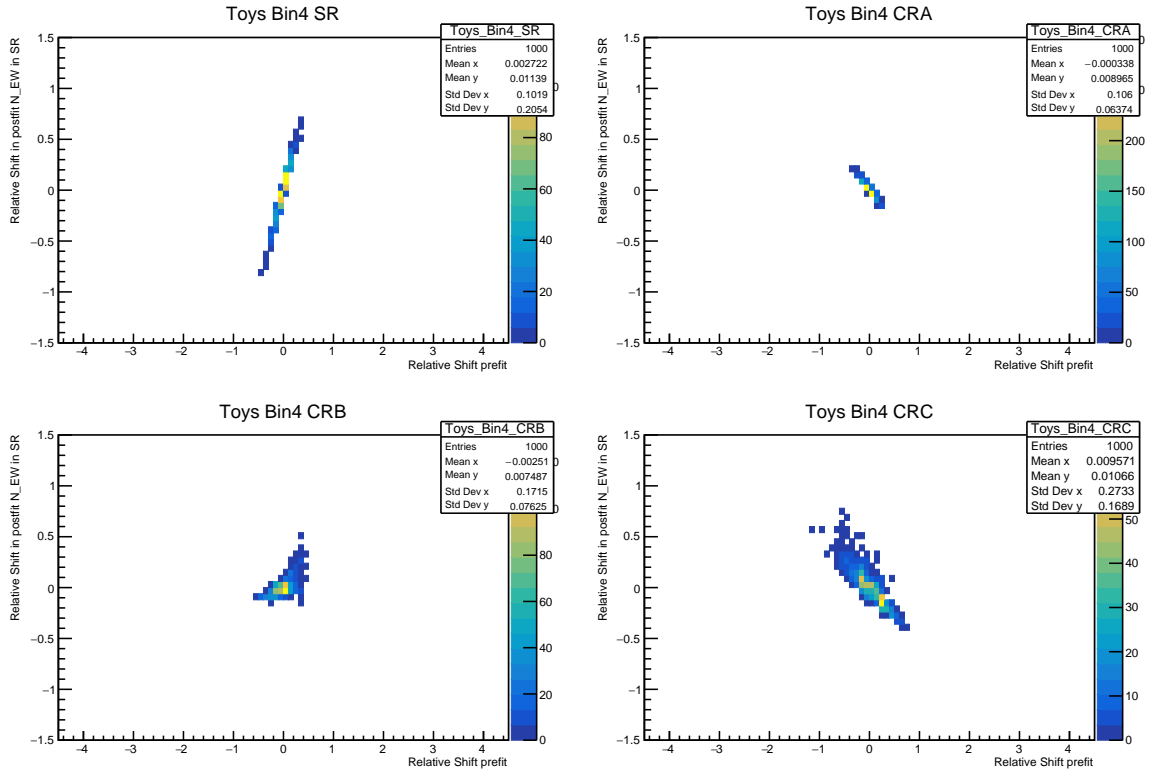




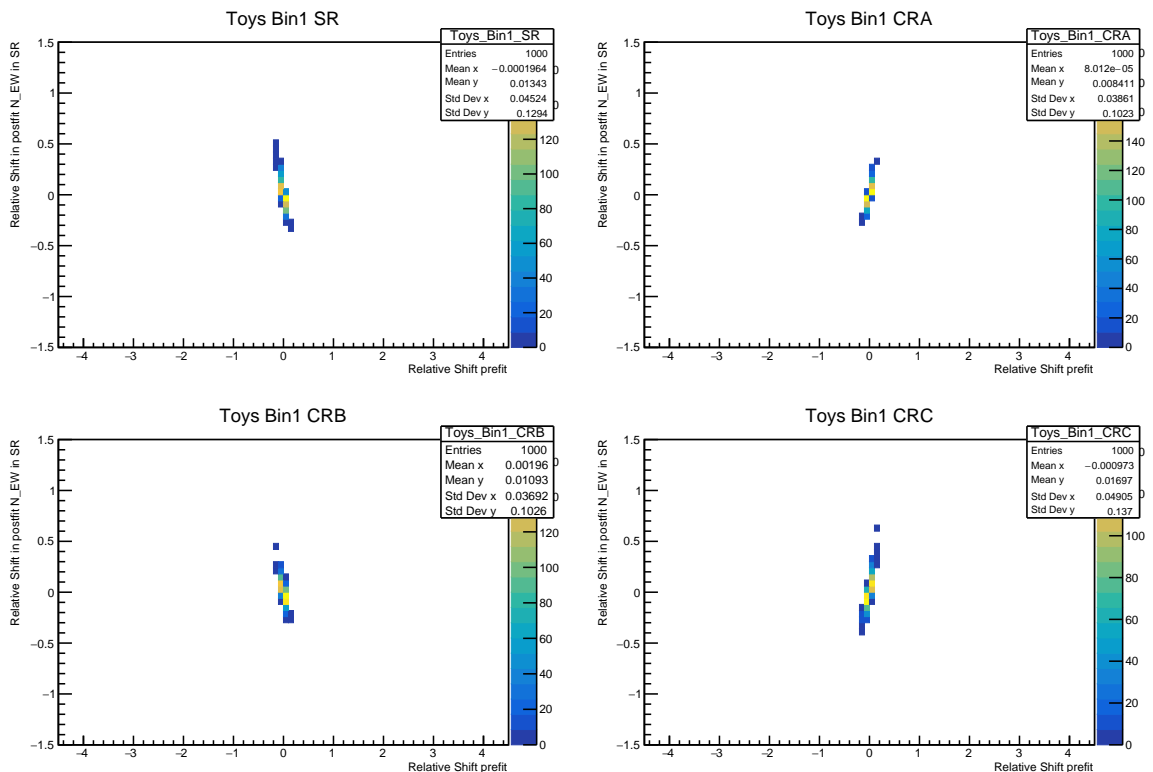
m_{jj} Asimov fluctuations, Sherpa-2.2.11 QCD in Asimov, Sherpa-2.2.11 QCD template

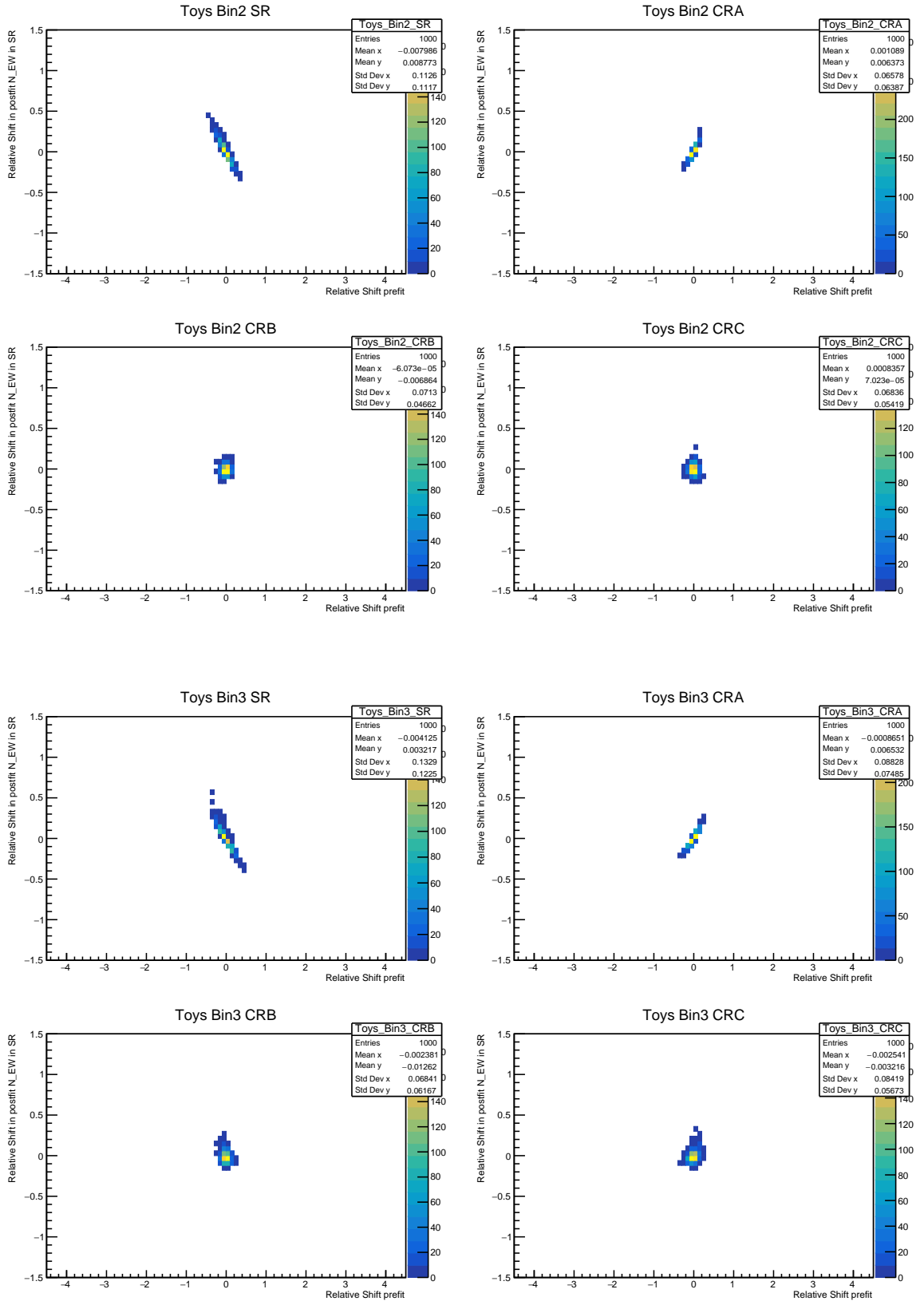


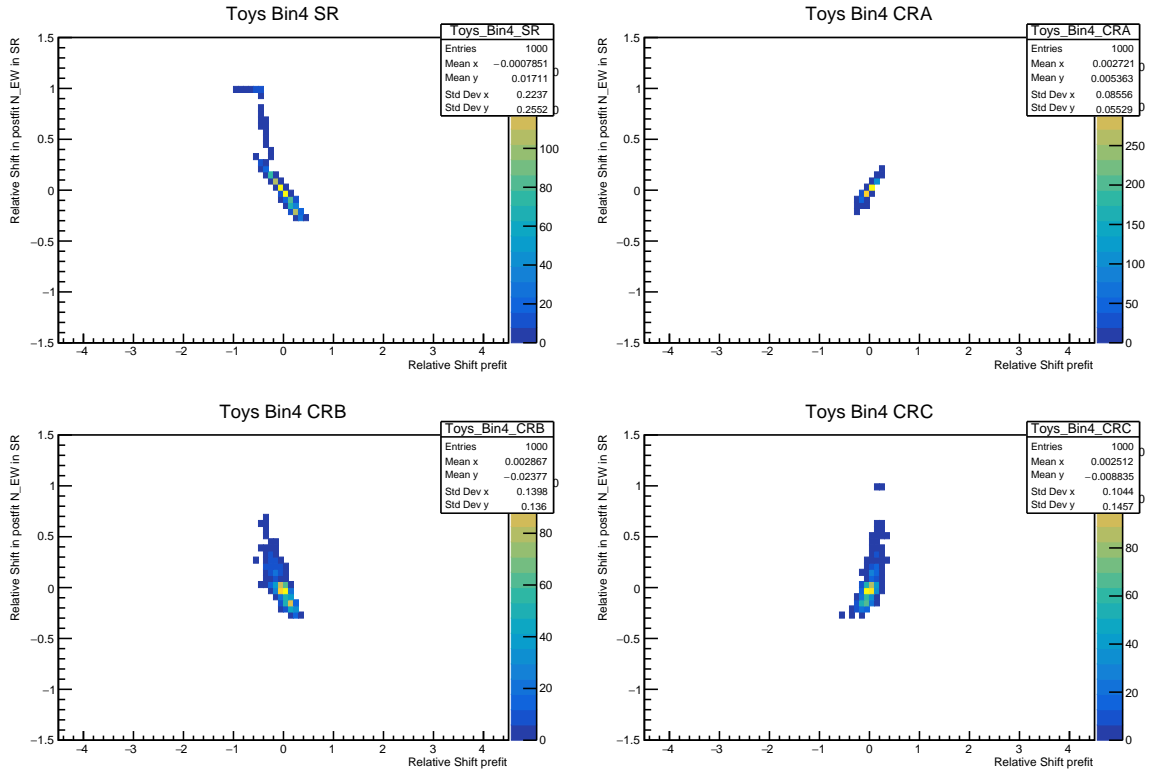




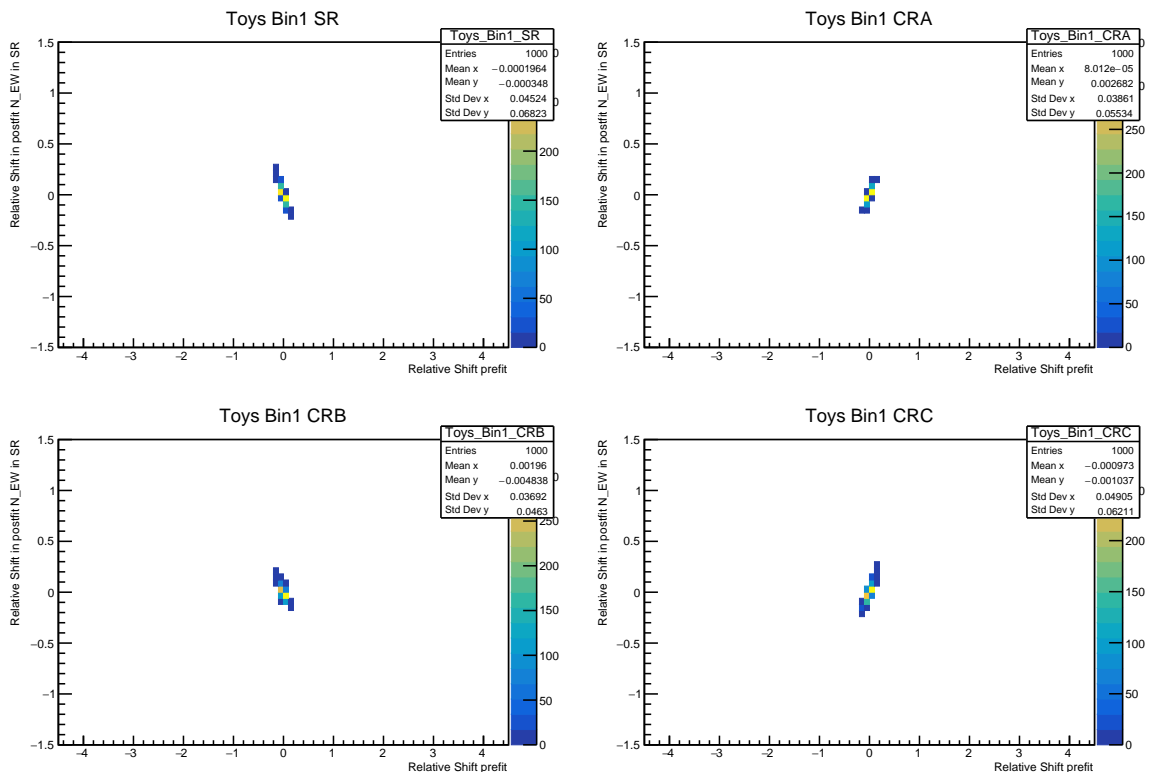
m_{jj} QCD template fluctuations, MG5 QCD in Asimov, Sherpa-2.2.11 QCD template

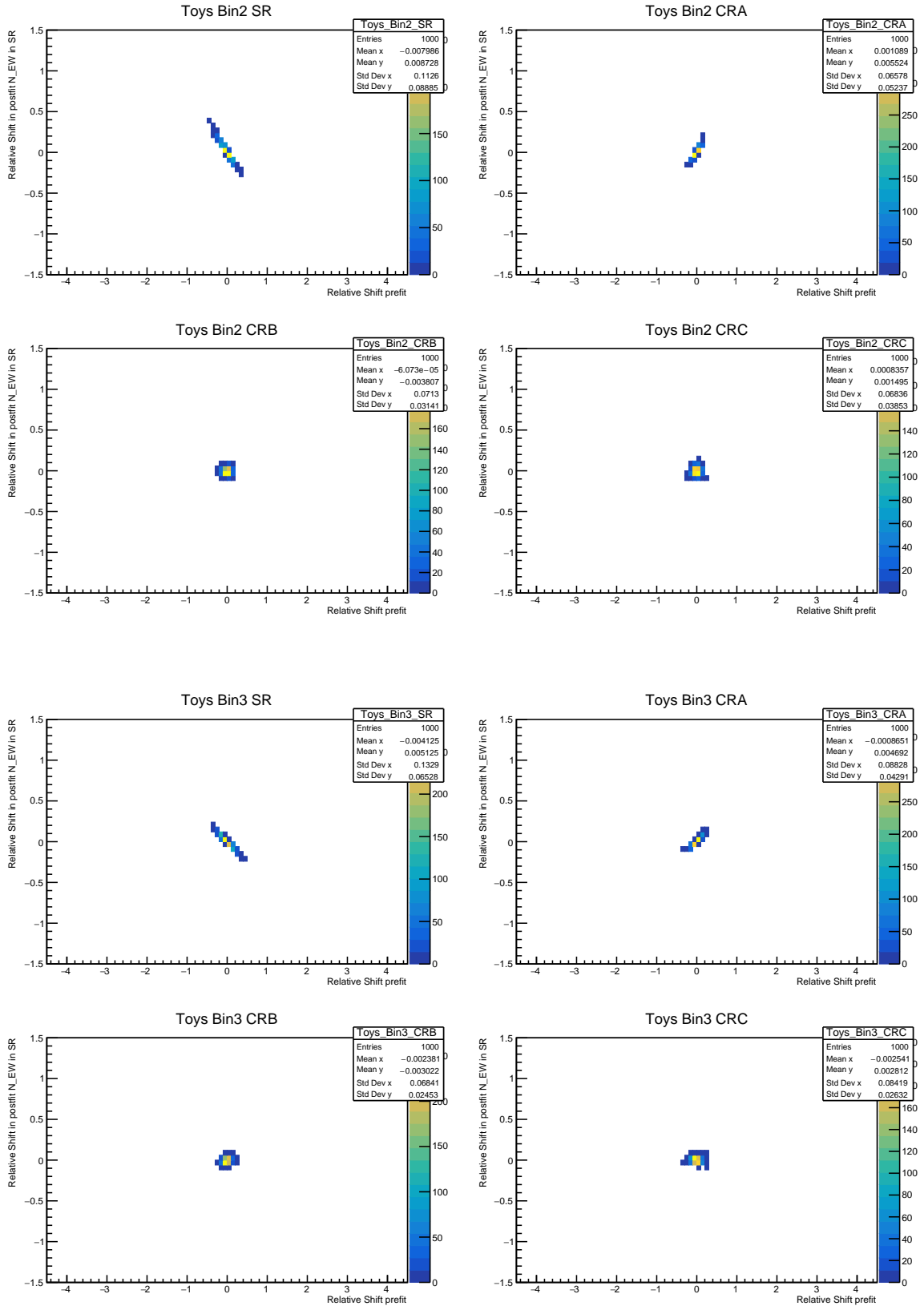


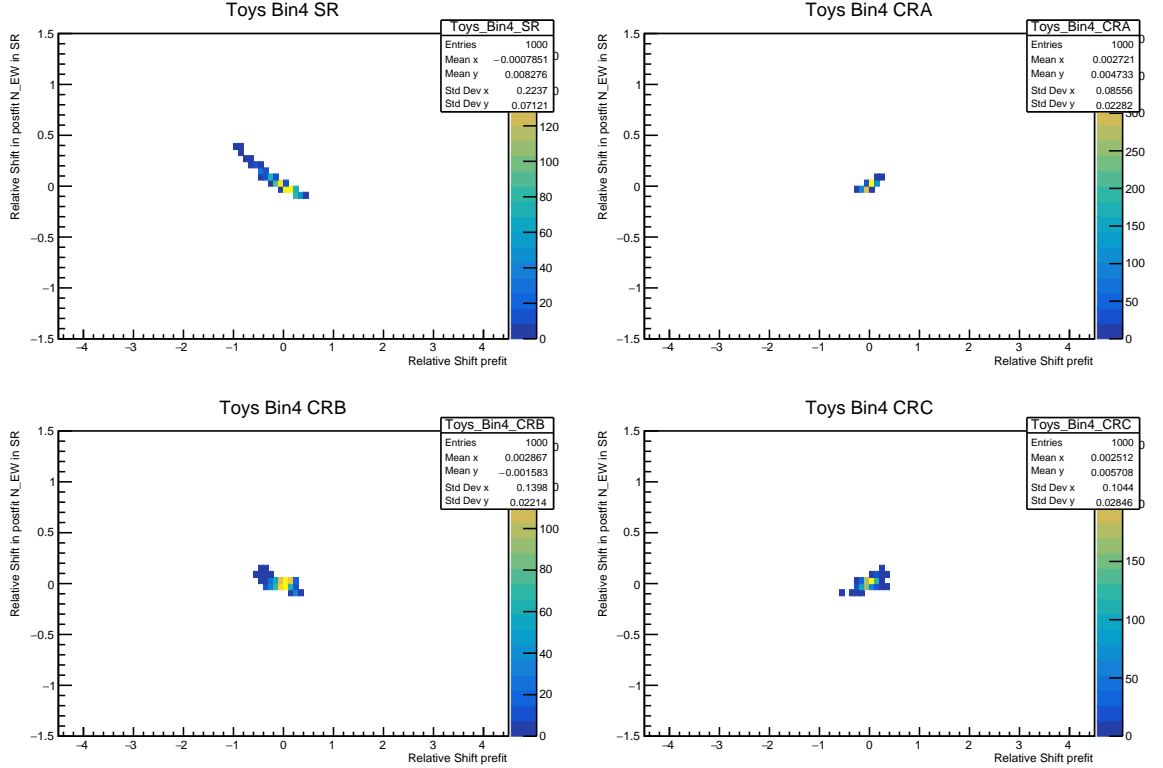




m_{jj} QCD template fluctuations, Sherpa-2.2.11 QCD in Asimov, Sherpa-2.2.11 QCD template







B.2 Different Significance Thresholds

This appendix shows the final systematic uncertainties on $N_{\text{EW}}^{\text{Nom}}$ with significance thresholds set at $\sigma_{\text{thresh}} = 1.0$ and $\sigma_{\text{thresh}} = 1.6$.

B.2.1 $\sigma_{\text{thresh}} = 1.0$

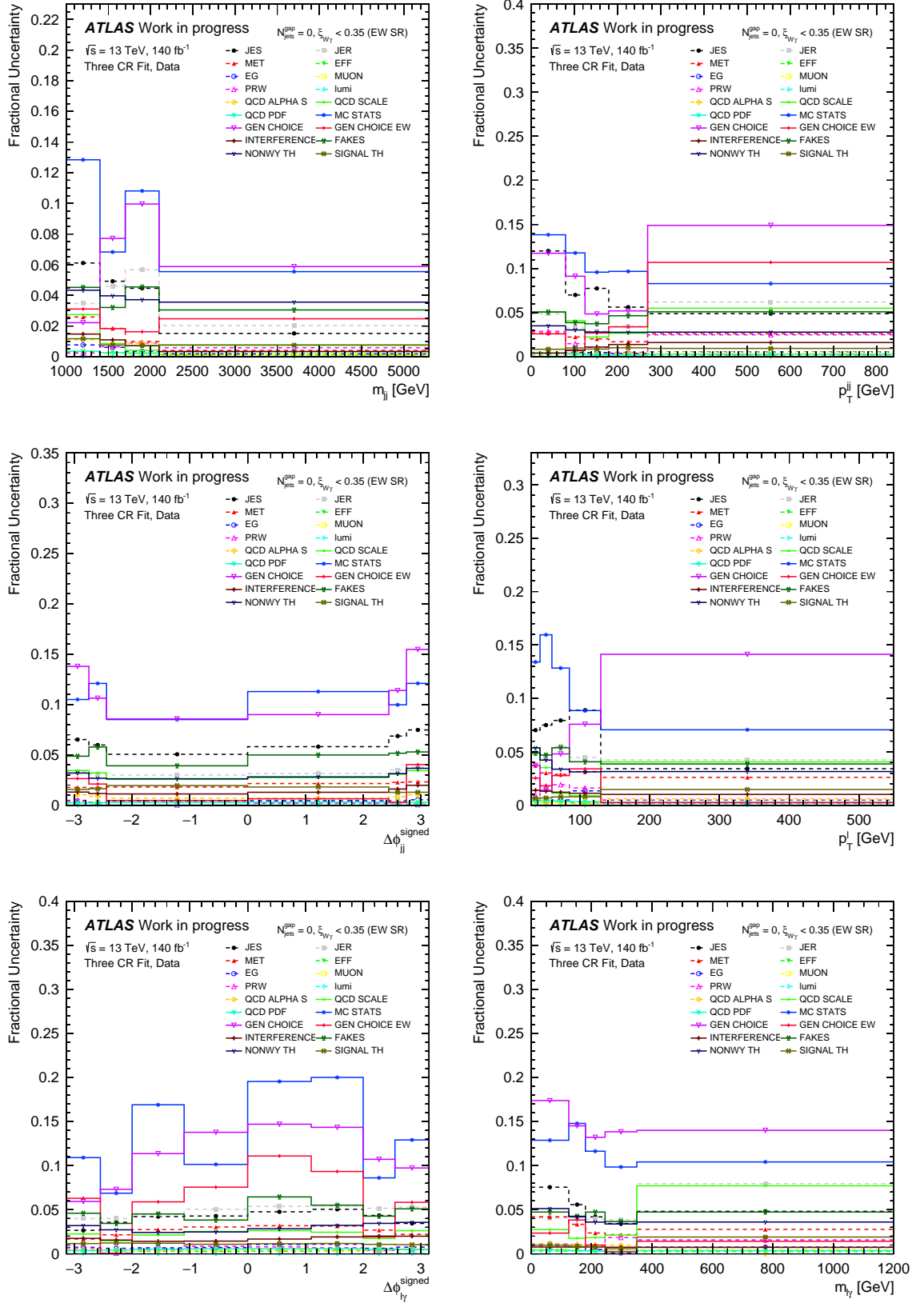


Figure B.1. Systematic uncertainties with significance threshold of $\sigma_{\text{thresh}} = 1.0$.

B.2.2 $\sigma_{\text{thresh}} = 1.6$

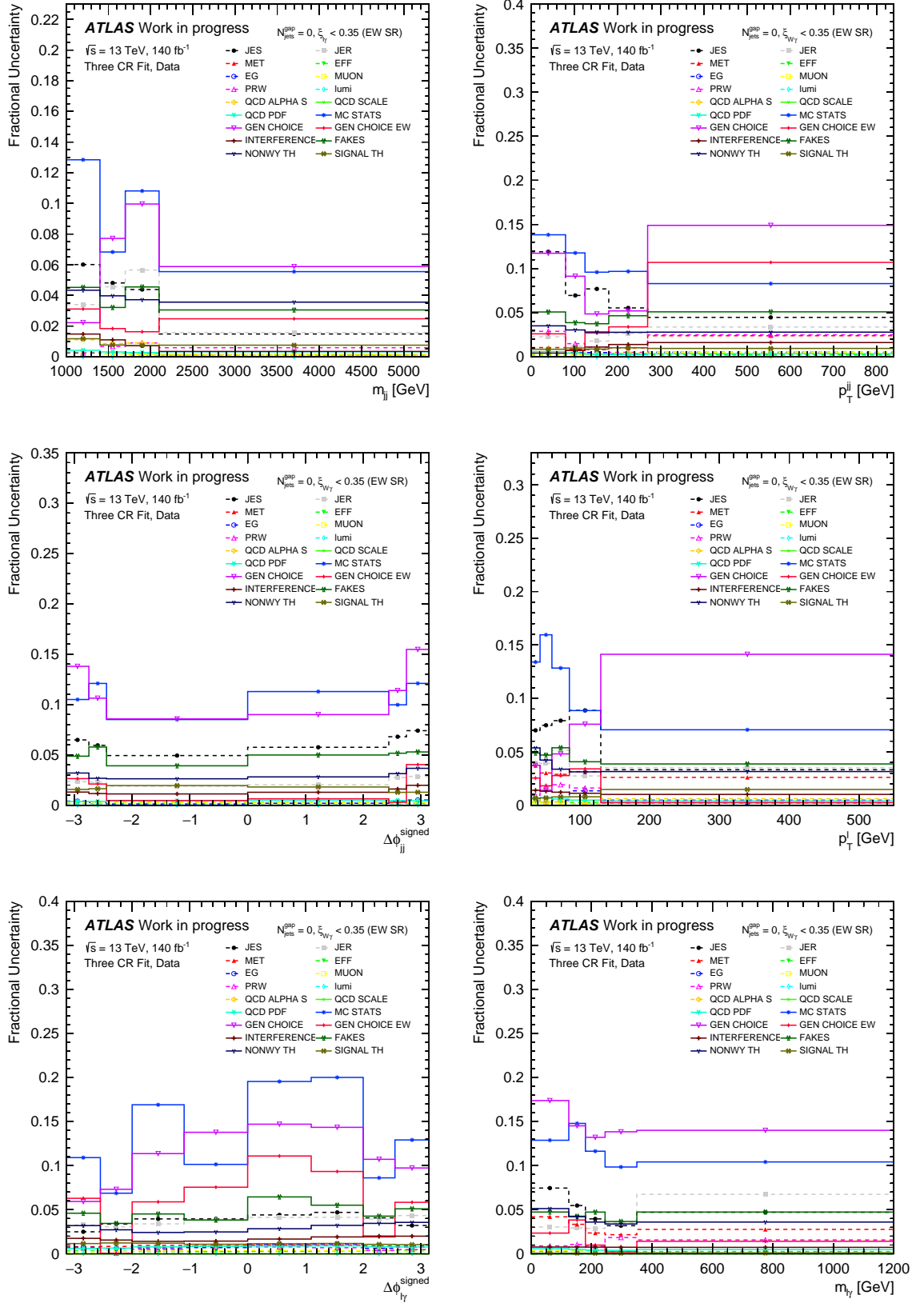


Figure B.2. Systematic uncertainties with significance threshold of $\sigma_{\text{thresh}} = 1.0$.